Institut für Geowissenschaften (IFG)

Eberhard Karls
Universität
Tübingen

Institut für Geowissenschaften (IFG)

TÜBINGER GEOWISSENSCHAFTLICHE ARBEITEN (TGA)

Reihe A: Geologie, Paläontologie, Stratigraphie

Schriftleitung: W. Frisch & J. Kuhlemann

Martina Schmalholz

The amalgamation of the Pamirs and their subsequent evolution in the far field of the India-Asia collision

TGA, A71, 2004

Tübinger **G**eowissenschaftliche **A**rbeiten	A	71	103 S. + App.	34 Abb. 16 Tab.	Tübingen, Juli 2004

Band 71

The amalgamation of the Pamirs and their subsequent evolution in the far field of the India-Asia collision

Martina Schmalholz

Tübingen

2004

Anschrift der Verfasserin: Martina Schmalholz
Inst. für Geowissenschaften, Univ. Tübingen, Sigwartstr. 10, 72076 Tübingen

Key words: Tien Shan, Pamirs, Tibet, geochemistry, U/Pb dating, Ar/Ar dating, fission track thermochronology

Citations of this volume should take the form:

Schmalholz, M. (2004): The amalgamation of the Pamirs and their subsequent evolution in the far field of the India-Asia collision. *Tübinger Geowiss. Arb., Reihe A* **71**, 1-103

Please note that according to German transcription rules, 'Tübinger' transcripts to 'Tuebinger' in case of lack of the character 'ü'.

Library of Congress Cataloging-in-Publication Data

The amalgamation of the Pamirs and their subsequent evolution in the far field of the India-Asia collision / Schmalholz, Martina

p. cm. – (Publication / Geological and Palaeontological Institute, University of Tuebingen, Germany; no. 71)

Includes bibliographical references.
ISSN 0953-4921
1. Geology, Geophysics
I. Title. II. Series.
551.8– dc21

www.uni-tuebingen.de

Printed in Germany

Bisher erschienen in dieser Reihe:

Nr. 1 RING, U. (1989): Tectogenesis of the Penninic/Austroalpine boundary zone: the Arosa Zone (Grisons-Rätikon area, Swiss-Austrian Alps).

Nr. 2 BETZLER, C. (1989): The Upper Paleocene to Middle Eocene between the Rio Segre and the Rio Llobregat (eastern South Pyrenees): facies, stratigraphy and structural evolution.

Nr. 3 HEINZ, W. (1989): Vulkanoklastische Komponenten und deren geodynamische Bedeutung für die Entwicklung der Southern Uplands von Schottland.

Nr. 4 SICK, M. (1989): Paleomagnetism of ophiolite complexes from the southern Middle American Landbridge (Costa Rica and western Panama).

Nr. 5 BRÜCKMANN, W. (1989): Typische Kompaktionsabläufe mariner Sedimente und ihre Modifikation in einem rezenten Akkretionskeil (Barbados Ridge).

Nr. 6 VAVRA, G. (1989): Die Entwicklung des penninischen Grundgebirges im östlichen und zentralen Tauernfenster der Ostalpen – Geochemie, Zirkonmorphologie, U/Pb-Radiometrie.

Nr. 7 SCHWENTKE, W. (1990): Upper Cretaceous tectono-sedimentary and facies evolution of the Basque Pyrenees (Spain).

Nr. 8 RICHTER, C. (1990): The anisotropie of magnetic susceptibility – Numeric models, deformation experiments, and practical application in structural geology.

Nr. 9 HEINZLER-JONCZYK, G. (1992): PTt-Paths in the southeast Tauern Window (Eastern Alps).

Nr. 10 HAIß, N. (1992): Untersuchungen zur Genese von Plagioklasgneisen im Basiskristallin der Ostalpen (Gleinalm- Ötztal- und Silvrettakristallin).

Nr. 11 KRAUS, S. (1992): Stratigraphy and facies of the "Garumnian" – Late Cretaceous to Early Paleogene – in the Tremp region, central southern Pyrenees.

Nr. 12 SFEIKOS, A. (1992): Geology, analysis of deformation and kinematics of the Pelagonian nappe system, Kamvounia mountains (North Thessaly, Greece).

Nr. 13 LIU, G. (1992): Permian to Eocene sediments and Indian passive margin evolution in the Tibet Himalayas.

Nr. 14 BECKER, B. (1993): The Structural Evolution of the Radstadt Thrust System, Eastern Alps, Austria – Kinematics, Thrust Geometries, Strain Analysis.

* Nr. 15 DÜRR, S.B. (1993): The Mid- to Early-Late Cretaceous Xigaze forearc basin (south Tibet); Sedimentary evolution and provenance of clastic sediments. [13 EUR]

* Nr. 16 MICHEL, G. (1993): Neokinematics along the North Anatolian Fault. [15 EUR]

* Nr. 17 HERRMANN, U.R. (1993): The origin of a „Terrane“: U/Pb zircon systematics, geochemistry and tectonics of the Xolapa complex (southern Mexico). [12 EUR]

Nr. 18 GRÄFE, K.-U. (1994): Sequence Stratigraphy in the Cretaceous and Paleogene (Aptian to Eocene) of the Basco-Cantabrian Basin (N. Spain).

Nr. 19 PROKOPH, A. (1994): Zyklische Sedimentation im Oberalb des Norddeutschen Beckens.

* Nr. 20 REICHERTER, K. (1994): The Mesozoic tectono-sedimentary evolution of the Central Betic seaway (external Betic Cordillera, Southern Spain). [15 EUR]

* Nr. 21 RATSCHBACHER, L., SPERNER, B., MESCHEDE, M. & FRISCH, W. (1994): Computer techniques and applications: A program library for stress and strain analysis. [10 EUR]

* Nr. 22 MESCHEDE, M. (1994): Tectonic evolution of the northwestern margin of the Caribbean Plate in the light of the "terrane concept": Structural and geochemical studies in southern Mexico and Costa Rica. [13 EUR]

* Nr. 23 KÖLBL-EBERT, M. (1995): Paläozoische Ganggesteine (Rhyodazite/Dazite und Lamprophyre) des Südschwarzwaldes. [14 EUR]

Nr. 24 JIN, J. (1995): Dynamic stratigraphic analysis and modeling in the south-eastern German molasse basin.

Nr. 25 PATZELT, A. (1996): Palaeo- and rockmagnetism of Cretaceous to Tertiary sediments from the Tethyan Himalaya: evidence for crustal shortening and deformation of the northern Indian margin due to the collision with Eurasia.

* Nr. 26 LÄUFER, A.L. (1996): Variscan and Alpine tectonometamorphic evolution of the Carnic Alps (Southern Alps) – Structural analysis, illite crystallinity, K-Ar and Ar-Ar geochronology. [13 EUR]

* Nr. 27 SPERNER, B. (1996): Computer programs for the kinematic analysis of brittle deformation structures and the Tertiary tectonic evolution of the Western Carpathians (Slovakia). [13 EUR]

Nr. 28 MAYER, H. (1996): Magnetostratigraphic and Cyclostratigraphic Investigations of the Early Cretaceous Biancone Formation at Cismon and Pra da Stua (Southern Alps, Italy) with Palaeoclimatical, Geochronological and Geomathematical Implications.

* Nr. 29 PFÄNDER, Jörg (1996): TWIST – Ein Computerprogramm zur Strainberechnung aus Calcit-Zwillingsdaten und seine Anwendung in der Deformationsanalyse des alpinen Vorlandes. [10 EUR]

* Nr. 30 WINKLER, M. (1996): Genese und geodynamische Stellung der Zentralgneise im Tauernfenster. [13 EUR]

Nr. 31 SCHUSTER, F. (1996): Paleoecology of Paleocene and Eocene Corals from the Kharga and Farafra Oases (Western Desert, Egypt) and the Depositional History of the Abu Tartur Carbonate Platform, Kharga Oasis.

Nr. 32 GÜLDENPFENNIG, M. (1997): Geologische Neuaufnahme der Zone von Badenweiler-Lenzkirch (Südschwarzwald) unter besonderer Berücksichtigung unterkarbonischer Vulkanite und Grauwacken.

* Nr. 33 ZWEIGEL, P. (1997): The Tertiary tectonic evolution of the Eastern Carpathians (Romania): Orogenic arc formation in response to microplate movements. [13 EUR]

* Nr. 34 NOUFAL, A.W. (1997): Geology and tectonic evolution of the Gulf of Suez, West-Central Sinai, Egypt. [15 EUR]

* Nr. 35 GÎRBACEA, R.A. (1997): The Pliocene to Recent Tectonic Evolution of the Eastern Carpathians (Romania) [13 EUR]

Nr. 36 SCHAUER, M. (1998): Dynamische Stratigraphie, Diagenese, und Rohstoffpotential des Oberjura (Kimmeridge 1-5) der mittleren Schwäbischen Alb.

Nr. 37 LEHMANN, J. (1998): Systematic palaeontology of the ammonites of the Cenomanian-Lower Turonian (Upper Cretaceous) of northern Westphalia, North Germany.

Nr. 38 RÖSLER, W. (1998): Magnetostratigraphy of Neogene fluvial sediments: results from a high resolution study and several new sections in the Nepalese Siwaliks.

* Nr. 39 GRÄFE, K. (1998): Exhumation and thermal evolution of the Cordillera de Talamanca (Costa Rica): constraints from fission track analysis, ^{40}Ar-^{39}Ar, and ^{87}Rb-^{87}Sr chronology. [13 EUR]

* Nr. 40 BRÜGEL, A. (1998): Provenances of alluvial conglomerates from the Eastalpine foreland: Oligo-/Miocene denudation history and drainage evolution of the Eastern Alps. [15 EUR]

Nr. 41 HU, S. (1998): A magnetic study on lacustrine sediments from Zoigê Basin, Eastern Tibetian Plateau, China.

* Nr. 42 ELIAS, J. (1998): The thermal history of the Ötztal-Stubai-complex (Tirol; Austria/Italy) in the light of the lateral extrusion model. [15 EUR]

Nr. 43 ASPRION, U. (1998): Ground-penetrating Radar (GPR) analysis in aquifer-sedimentology: Case studies, with an emphasis on glacial systems of SW Germany.

* Nr. 44 FETSCHER, M. (1998): Strukturelle und petrologische Entwicklung des Terraba-Forearcs im zentralen Bereich des flach subduzierten Cocos-Rückens, Süd-Costa Rica.

MORITZ, E. (1998): Interpretation von LWD-Daten mit Hilfe von künstlichen neuronalen Netzen und genetischen Algorithmen (unter Anwendung auf Daten des ODP Leg 170, Costa Rica Convergent Margin). [15 EUR]

* Nr. 45 WALDHÖR, M. (1999): The Small-circle reconstruction in paleomagnetism and its application to paleomagnetic data from the Pamirs. [13 EUR]

* Nr. 46 ABD EL-NABY, H.H. (1999): Geology, petrochemistry and tectogenesis of the Wadi Um Ghalaga area, eastern desert, Egypt. [14 EUR]

Nr. 47 RÖHL, H.-J. (1999): Hochauflösende palökologische und sedimentologische Untersuchungen im Posidonien-schiefer (Lias ε) von SW-Deutschland.

Nr. 48 SCHMID-RÖHL, A. (1999): Hochauflösende geochemische Untersuchungen im Posidonienschiefer (Lias ε) von SW-Deutschland.

* Nr. 49 CHINCHILLA CHAVES, A.L. (1999): Geologie und Struktur des Ophiolith-Komplexes der Nicoya-Halbinsel (Costa Rica). [13 EUR]

* Nr. 50 HUSSIEN MOHAMMED, B. (1999): The geology, structure and geochemistry of the crystalline rocks of the Moyale area, Southern Ethiopia: Implications for the tectogenesis of the Precambrian basement. [13 EUR]

Nr. 51 PÖPPELREITER, M. (1999): Controls on epeiric successions exemplified with the mixed siliciclastic-carbonate Lower Keuper (Ladinian, German Basin).

* Nr. 52 SZÉKELY, B., FRISCH, W., KUHLEMANN, J., & DUNKL, I. (1999): 4th Workshop on Alpine Geological Studies. 21-24 September 1999, Tübingen (Germany). [20 EUR]

* Nr. 53 LÓPEZ, A. (1999): Neo- and paleostress partitioning in the SW corner of the Caribbean plate and its fault reactivation potential. [20 EUR]

Nr. 54 LÖFFLER, S.-B. (1999): Systematische Neubearbeitung und paläoökologische Aspekte der unteroligozänen Molluskenfauna aus den Zementmergeln von Bad Häring (Unterinntal, Tirol).

* Nr. 55 REINECKER, J. (2000): Stress and deformation: Miocene to present-day tectonics in the Eastern Alps. [13 EUR]

Nr. 56 HORNUNG, J. (1999): Dynamische Stratigraphie, Reservoir- und Aquifer-Sedimentologie einer alluvialen Ebene: Der Stubensandstein in Baden-Württemberg (Obere Trias, mittlerer Keuper).

* Nr. 57 SCHNEIDERMEIER, T. (2000): Paläolithische Fundschichten in quartären Lockersedimenten (Südwestdeutschland): Prospektionsmethoden, Stratigraphie und Paläoökologie. [15 EUR]

* Nr. 58 HUBICH, D. (2000): Geodynamische Entwicklung der Karnischen Alpen. [13 EUR]

* Nr. 59 TRAUTWEIN, B. (2000): Detritus provenance and thermal history of the Rhenodanubian flysch zone: mosaicstones for the reconstruction of the Eastern Alps. [13 EUR]

* Nr. 60 SZÉKELY, B. (2001): On the surface of the Eastern Alps – a DEM study. [13 EUR]

* Nr. 61 PAWELLEK, T. (2001):Fazies,- Sequenz-und Gamma-Ray-Analyse im höheren Malm der Schwäbischen Alb (SW-Deutschland) mit Bemerkungen zur Rohstoffgeologie (hochreine Kalke). [30 EUR]

* Nr. 62 CAMPOS BEJARANO, L. (2001): Geology and basins history of Middle Costa Rica: an intraoceanic island arc in the convergence between the Caribbean and the Central Pacific plates. [13 EUR]

* Nr. 63 MOSER, F. (2001): Tertiäre Deformation in den Rumänischen Südkarpaten: Strukturelle Analyse eines Blattverschiebungskorridors am Westrand der Moesischen Plattform. [13 EUR]

* Nr. 64 Dakrory, A.M. (2002): Biostratigraphy, paleoenvironment and tectonic evolution of the Late Cretaceous-Early Paleogene succession on the North African plate (Sinai, Egypt) and a comparison with some European and Asian sections. [20 EUR]

* Nr. 65 Dünkel, I. (2002): The genesis of East Elba iron ore deposits and their interrelation with Messinian tectonics. [15 EUR]

Nr. 66 Most, T. (2003): Geodynamic evolution of the Eastern Pelagonian Zone in north-western Greece and the Republic of Macedonia. Implications from U/Pb, Rb/Sr, K/Ar, $^{40}Ar/^{39}Ar$ geochronology and fission track thermochronology. TOBIAS LIB online

Nr. 67 Most, P. (2003): Late Alpine cooling histories of tectonic blocks along the central part of the TRANSALP- traverse (Inntal-Gardertal): Constraints from geochronology. *Tübinger Geowiss. Arb., Reihe A* **67**, 1-97.

* Nr. 68 Helbing, H. (2003): No suture in the Sardinian Variscides: A structural, petrological, and geochronological analysis. [15EUR]

Nr. 69 Junghans, W.-D. (2003): Fazies, Zyklizität, Petrophysik und Paläomagnetik im Buntsandstein der Bohrung Kraichgau 1002 (SW-Deutschland).

* Nr. 70 Schuller, V. (2004): Evolution and geodynamic significance of the Upper Cretaceous Gosau basin in the Apuseni Mountains (Romania). [15 EUR]

* Nr. 71 Schmalholz, M. (2004): The amalgamation of the Pamirs and their subsequent evolution in the far field of the India-Asia collision. [15 EUR]

Herausgeber: Institut für Geowissenschaften, Universität Tübingen

Sigwartstraße 10, D-72076 Tübingen

ISSN 0953-4921

* zu beziehen über: Dr. Joachim KUHLEMANN, Institut und Museum für Geologie und Paläontologie der Universität Tübingen, Sigwartstraße 10, D-72076 Tübingen, Fax: ++49 7071 5059, e-mail: kuhlemann@uni-tuebingen.de

Aktueller Stand erschienener Bände über: http://www.uni-tuebingen.de/geo/gpi/tga/reihe_a.html

Preise sind ohne Gewähr. Prices are subject to change.

Martina Schmalholz

The amalgamation of the Pamirs and their subsequent evolution in the far field of the India-Asia collision

The highest summit of the Pamir frontal range is the Peak Lenin (7134m, left side). Along the northern orogenic front, the active North Pamir fault cross-cuts the foothills of the range and transfers the Pamirs northward with respect to Eurasia.

Tübingen 2004

The amalgamation of the Pamirs and their subsequent evolution in the far field of the India-Asia collision

Dissertation

zur Erlangung des Grades eines Doktors
der Naturwissenschaften

der Geowissenschaftlichen Fakultät
der Eberhard-Karls-Universität Tübingen

vorgelegt von
Martina Schmalholz (geb. Schwab)
aus Heidelberg

2004

Tag der mündlichen Prüfung: 06.Juli 2004

Dekan: Prof. Dr. Dr. h.c. M. Satir

1. Berichterstatter: Prof. Dr. W. Frisch

2. Berichterstatter: Priv. Doz. Dr. W. Siebel

Wer aber je auf Asiens Erdboden schlief,
wer jemals in Asiens Bergen und Wüsten wanderte,
dessen Seele bleibt diesem geheimnisvollsten aller Erdteile ewig verbunden.

(Philipp Borchers, 1931)

Contents

Figure captions

Fig. 1 Political map of Central Asia with topographical background.

Fig. 2 Sketch map of the Pamirs and West-Turkestan with the main travel routes of the Alpenvereinsexpedition 1913 and the Alai-Pamir-Expedition of 1928 after Finsterwalder (1929).

Fig. 1.1 Topographic and regional tectonic map of the Pamirs and the Tibetan Plateau, showing physiogeographic units and major suture zones after the compilations of Burtman & Molnar (1993) for the Pamirs and Yin & Harrison (2000) for Tibet, and Cenozoic fault systems modified after Yin & Harrison (2000). TFF = Talasso-Ferghana fault, FB = Ferghana basin, AB = Alay basin, TB = Tadzhik basin, KF = Karakorum fault, and ATF = Altyntagh fault. Bold lines outline suture zones with decreasing ages from north to south.

Fig. 2.1 Flow diagram showing the sample preparation and the methods applied.

Fig. 3.1 Raised relief and tectonic map of Afghanistan, the Pamirs, and Tibet with local physiogeographic units from which the names of most structural units are derived. Abbreviations are as follows: r. = range, b. = basin, NP = North Pamirs, CP = Central Pamirs, SWP = south-west Pamirs, SEP = south-east Pamirs, CF = Chaiman fault, KR = Khash Rud, FR = Fahrah Rud, HF = Herat fault, AF = Andarab fault, DF = Darvaz fault, MBF = Middle Badakshan fault, SGF = South Gissar fault, VTAF = Vaksh-Trans-Alay fault, NPF = North Pamir fault, MF = Markansu fault, TFF = Talasso-Ferghana fault, ARF = Aksu-Rankul fault, AMF = Aksu-Murgab fault, KF = Karakorum fault, ATF = Altyntagh fault, MBT = Main boundary fault, MCT = Main Central Thrust, STFS = South Tibetan fault system.

Fig. 3.2 a) Satellite image of the Tien Shan region and northern Tarim margin. b) Outline of the Palaeozoic Tien Shan orogen (modified after Bazhenov et al. 1999) with tectonic units, sutures, strike lines, and sample locations (dots). Abbreviations are as follows: STS = South Tien Shan, YCTS = Yili-Central Tien Shan, NTS = North Tien Shan, TFF = Talasso Ferghana fault, FB = Ferghana basin, AB = Alay basin, YB = Yili basin, JB = Junggar basin, TB = Tarim basin, IKL = Issyk-Kul lake, T s. = Turkestan suture, SG s. = South Gissar suture.

Fig. 3.3 Topographic map of the southernmost Tien Shan and the eastern Pamirs with main faults in black, main sutures in bold grey lines and the sample locations as black dots. NPF = North Pamir fault, STS = South Tien Shan, NP = North Pamirs, CP = Central Pamirs, SP = South Pamirs, RPZ = Rushan Pshart Zone (following Burtman and Molnar 1993), WP = West Pshart, EP = East Pshart (according to Leven 1995).

Fig. 3.4 Geological map of the Altyndara valley with sample locations, main stratigraphic units and structures.

Fig. 3.5 Geochemistry of the magmatic rocks from the South Tien Shan and Pamirs. a) Modal compositions of the plutonic and volcanic rocks with the nomenclature taken from Streckeisen (1976). b) The aluminium saturation index (Molar Al_2O_3/ $CaO+Na_2O+K_2O$) for all rock samples. c) The subdivision of subalkaline rocks using the K_2O vs silica diagram with the boundary lines after Le Maitre et al. (1989). d) The AFM showing the boundary between the calc-alkaline and tholeiitic field for the metavolcanic rocks from the Altyndara valley, Northern Pamirs, after Irvine & Baragar

(1971). Black lines with arrows show typical calc-alkaline and tholeiitic trend lines. e) The Ti-Zr variation diagram shows the fields of volcanic arc basalts, MORB and within-plate basalts for the metavolcanic rocks from the Altyndara valley, Northern Pamirs (after Pearce 1982). f) A La vs Sm plot used to discriminate the tectonic setting of island-arc rocks. g) A tectonic discrimination diagram for the separation of volcanic arc granites (VAG), collision related granites (COLG), within plate granites (WPG), and ocean ridge granites (ORG) after Pearce et al. (1984). h) Zr+Nb+Ce+Y (ppm) vs FeO*/MgO discrimination diagram from Whalen et al. (1987). FG = field for fractionated I-type granitoids. i) The Hf-Rb/30-Tax3 discrimination diagram for granites after Harris et al. (1986), showing the fields for volcanic arc granites, within plate granites, syn-collisional and late to post-collisional granites.

Fig. 3.6 Chondrite-normalised REE abundance patterns (normalised to values given by Masuda et al. 1973) for selected samples from different intrusives from the South Tien Shan (STS) and eastern Pamirs. a) subvolcanic diorites and monzogranites from the STS, b) MORB-type metabasalts, calc-alkaline andesites, dacites, and a rhyolith from the Altyndara valley in black colours; a granodiorite and monzogranites from the Karakul lake batholith are in grey colours, c) Triassic/Jurassic monzogranites from the Central Pamirs and Rushan Pshart Zone and a leucogabbro from the Central Pamirs, and d) Cretaceous monzogranites from the Central Pamirs and Rushan Pshart Zone and a latite-andesite from the Central Pamirs.

Fig. 3.7a-p U/Pb dilution, U/Pb SHRIMP and Pb/Pb zircon ages. See Fig. 3.3 for sample locations and Appendix A, Tab. A7 for data listing. Data points in concordia diagrams with sample names in brackets were excluded from age calculation. TIMS results shown with 2σ error ellipses and discordias as thin lines. SHRIMP results plotted in Terra-Wasserburg concordia diagrams uncorrected for common Pb with 1σ error ellipses. Selected age groups of SHRIMP data are displayed as weighted average diagrams.

Fig. 3.8a-c Rb/Sr whole rock-white mica two-point isochron diagrams. See Fig. 3.3 for sample locations and Appendix A, Tab. A5 for data listing.

Fig. 3.9a-p $^{40}Ar/^{39}Ar$ age spectra, variation of K/Ca, and correlated isotope ratio diagrams ($^{36}Ar/^{40}Ar$ vs $^{39}Ar/^{40}Ar$). See Fig. 3.3 for sample locations and Appendix A, Tab. A3 for data listing. Weighted mean ages (WMA) and weighted mean plateau ages (WMPA) were calculated using shaded steps. TFA is the total fusion age, and IA the isochron age. Uncertainties are 1σ. "Atm." is the $^{36}Ar/^{40}Ar$ of the atmosphere (1/295.5) in the correlated isotope ratio diagram. MSWD is the mean square weighted deviation.

Fig. 3.10a-c Correlated $\varepsilon Nd_{(0)}$ and $\varepsilon Sr_{(0)}$ data versus the age of the samples.

Fig. 3.11 Summary of the geodynamic evolution and amalgamation history of the Pamirs and Tibet. The profile across the Pamirs is based on the geochemical and geochronologycal data and correlations to Tibet and Afghanistan. The Turkestan/North Tien Shan suture is thought to be of Early- to Mid-Palaeozoic age and the Gissar/South Tien Shan sutur of Late Palaeozoic age. The northern Pamirs contain the composite Early Palaeozoic and Late Palaeozoic Kunlun arcs. The southward subducting Jinsha suture is of Late Triassic/Early Jurassic age, whereas the Rushan Pshart suture most likely closed in Mid-Jurassic time. The collision of the Karakorum block with the south-eastern Pamirs is thought along the upper Lower Cretaceous Tirich Mir/Kilik (?)suture.

sample locations and age distribution. (c) presents different structural solutions which might be responsible for the age and track length distribution as well as the cooling paths.

Fig. 4.4 N-S profile of the intramontane Murgab basin, southerly adjacent to the Muzkol dome. The section shows the basin structure and fission track zircon ages (in white frames) and sericite K/Ar ages (grey frames, the data table is documented in Appendix A, Tab. A4) of Palaeogene to ?Neogene sediments of the basin. Obviously the determined ages do not correlate with elevation, but with the distance to the metamorphic dome complex.

Fig. 4.5 N-S profile of the southernmost Tien Shan and eastern Pamirs with the structural units and the summary of the Palaeozoic to Tertiary geochronological evolution of the magmatic belts and basement units. The surface geology is adapted from the geological maps 1:200.000 of Tadzhikistan (1968) and Kyrgyztan (1958). For a better understanding of the subsurface geology see Fig 3.11 (chapter 3). Not all data points are labelled with a sample name and fission track peak ages of sediments are not included.

Prologue

The present doctoral thesis is part of a project financed by the Deutsche Forschungsgemeinschaft (DFG-project Fr 610/11). The aim of the project was to examine the Tertiary to Quaternary tectonics of the Pamirs and to develop a geodynamic model of this region. For this task an international and interdisciplinary team seemed to be most promising, thus following the tradition of previous research expeditions to the Pamirs. Associated were researchers from Germany, USA and Russia and two doctoral students, Martin Waldhör and myself. Prof. Dr. L. Ratschbacher, Freiberg, led structural, geochronological and geodynamic research, Prof. Dr. W. Frisch, Tübingen, represented structural geology and geodynamics, Prof. Dr. M. Strecker, Potsdam, was responsible for neotectonics, and Prof. Dr. E. Appel, Tübingen, focused on palaeomagnetics. Three field excursions to the Pamirs were carried out in 1993, 1996, and 1997. The following thesis is based on data collected in the Pamirs during the last two field seasons. Independent from the project aims, it seemed much more promising to my supervisors and me to constrain the Tertiary history on base of a well defined Pamiran Palaeozoic and Mesozoic geodynamic model. Therefore, in 1999, the thesis subjects were extended. A further impact to the thesis duration was the circumstance that the samples were kept for one year in Tadzhikistan for reasons we never could figure out satisfactorily.

Fig. 1: Political map of Central Asia with topographical background.

The "roof of the world" is what the Persians called the Pamirs. This large mountain region extends over the Tadzhik and Kyrgyz Republics in Central Asia (Fig. 1). In Europe, first descriptions of the Pamirs are related to Marco Polo; he crossed the mountains at Terak Pass in the area of present-day Afghanistan during his legendary journey to northern China in 1271. Owing to his descriptions Marco Polo sheep were later named after him. Beside the Yaks they are often the only visible large animals of the area. In 1866, the first Russian expedition arrived in the Pamirs, led by the naturalist and explorer Fedchenko. He discovered an extensive glacier in the northern Pamirs which has been considered the largest non-polar icefield in the world. The French explorer Pierre Bonvalot completed the first European north-south crossing of the Pamirs in 1886. Other Russian, English and

Swedish expeditions followed. In January 1894, a small caravan led by the famous Swedish explorer Sven Hedin left Tashkent for crossing of the Pamirs to reach Kashgar in China. Sven Hedin was trained in physical geography and on his way he made lot-measurements in the Karakul lake in the north-eastern Pamirs. Lake Karakul is divided into two basins and Hedin discriminated a deeper western (ca. 230 m) and a shallower eastern basin (ca. 50 m). As the Lake Karakul region was one of our main working areas it was exciting to follow Sven Hedin's footsteps.

Towards the end of the 19th century white areas on the maps of Central Asia gradually disappeared as more and more geographic and topographic information was acquired. Sven Hedin again took part in an excursion to the Pamirs in 1928. It was the German-Russian Alai-Pamir expedition (Fig. 2) which produced one of the first scientific compilations about the Pamirs including many geological aspects (Nöth 1932). But the Pamirs remained a wild region with many little known valleys and peaks. During the first research expeditions of the Soviet Academy of Science to the Pamirs between 1928 and 1933 mountaineering exploration began. Tourist expeditions to the Pamirs were first undertaken in the 1950s and since then the Pamirs have been the most popular outdoor mountain region of the former Soviet Union. Unfortunately, today the Pamirs tend to be a more and more remote region again, due to its geopolitical position. In the rear of this, it is even more exciting to elucidate the Pamirs Palaeozoic to Tertiary evolution.

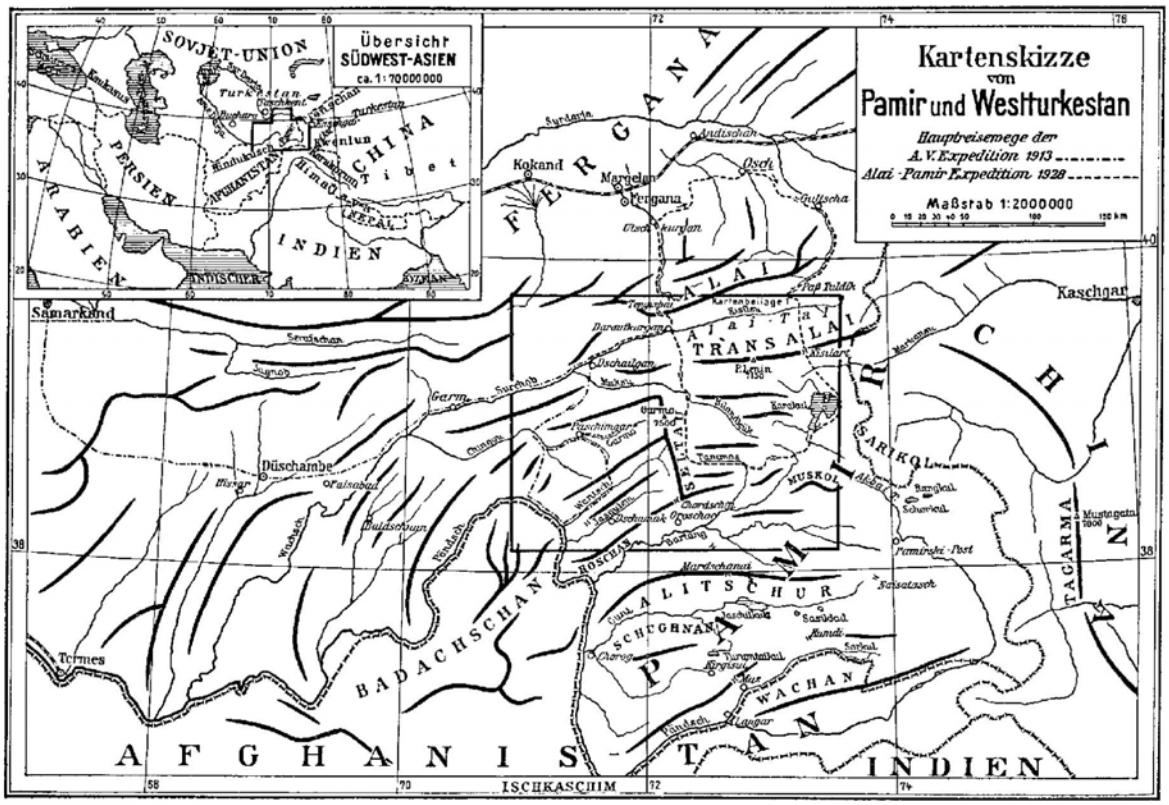

Fig. 2: Sketch map of the Pamirs and West-Turkestan with the main travel routes of the Alpenvereinsexpedition 1913 and the Alai-Pamir-Expedition of 1928 after Finsterwalder (1929).

The amalgamation of the Pamirs and their subsequent evolution in the far field of the India-Asia collision

Abstract

The geodynamic understanding of the Pamir mountains in Central Asia has been hitherto rather fragmentary, despite its importance as one of the linking segments recording the history of the Tethys ocean between southeast Asia and the Alps. A new model for the Pamirs accounts in particular for the structural correlation with the neighbouring Tibetan and Afghan units. Radiometric age dating (U/Pb, Rb/Sr and Ar/Ar) and geochemical provenance analyses of W-E oriented magmatic belts and associated rock assemblages in the southern Tien Shan and eastern Pamirs elucidate the principal geodynamic phases of the region. The events can be comprehended following a N-S transect through the region:

(1) During the early and middle Palaeozoic, an active continental margin existed at the northern margin of the Palaeotethys, striking nearly parallel to the present-day Tien Shan orogen. In the middle and late Palaeozoic, marginal basins were closed and several terranes accreted. Early Permian (~277 Ma), calc-alkaline granitoids from the southern Tien Shan exemplify this development. They correlate with intrusions of the Garm-Turkestan-Alay zone west of the Tien Shan, which is attributed to the northward directed closure of the South Gissar ocean. This closure likely coincided with the disappearance of the South Tien Shan ocean, another marginal basin east of the determined transect. Thereby, the Baysunta and Garm terranes and the Tarim block were accreted.

(2) Southwardly contiguous to the South Tien Shan and the intramontane Alay valley, the northern Pamirs expose metavolcanic rocks (Altyndara section), ~370-330 Ma of age, that represent a possible western extension of the north Kunlun arc of western Tibet. Consecutive late Palaeozoic to Triassic subduction of the Sonpan-Ganze ocean created the southern Kunlun of western Tibet, an equivalent of which is conjectured to exist in the northern Pamirs.

(3) Permo-Triassic volcaniclastic rocks form the Karakul-Mazar accretionary complex in the southern part of the northern Pamirs, which resulted from northward oriented subduction of the Sonpan-Ganze ocean underneath the southern Kunlun arc (see above) and southward oriented subduction along the Tanymas suture underneath the area now represented by the northern edge of the Central Pamirs. This cryptic southern suture correlates with the Tibetan Jinsha suture and the Central Pamirs corresponds to the Qiangtang block. The post-tectonic massive Lake Karakul batholith was emplaced into the accretionary units of the northern Pamirs at ~227 Ma, roughly coinciding with similar granitoids of northwest Tibet (~227-199 Ma). Comparable Permo-Triassic volcaniclastic successions and Triassic plutonites are reported from the western Badakshan, western Hindu Kush, and Feroz Koh of Afghanistan.

(4) Medium to high grade metamorphites of the Sonpan-Ganze ocean floor and its mainly Triassic mélange compose basement domes in the Central Pamirs, which have been exhumed in the Tertiary. In the Qiangtang block of Tibet, basement domes of analogous composition have been exhumed already in the late Mesozoic. It is

postulated that the Safed Khers area of Afghanistan hosts similar basement domes, and the Band-e Bayan and Farah Rod zones of that country correlate with the Mesozoic Central Pamirs and Qiangtang cover sequences.
(5) Calc-alkaline granitoids (~190-150 Ma) cut the southern Central and northern Southeast Pamirs. They intruded into the eastern Pshart oceanic basin-arc sequence and formed the Rushan Pshart arc. The Farah Rod zone of Afghanistan likely represent the western continuation of this setting and granitoids of the southern Qiangtang block of Tibet (~170-160 Ma) epitomize its eastern prolongation. These successions and intrusives of the Rushan Pshart zone record the closure of probably several small, laterally arranged transpressive basins reaching into the Bangong-Nujiang zone between the Qiangtang and Lhasa blocks in Tibet. These basins were finally consumed by Mid-Jurassic times.
(6) Zircons of Late Miocene xenoliths and of Cretaceous plutons from the central and southern Pamirs suggest a prolonged magamtic history of the region comprising four main phases: Cambro-Ordovician (~575-410 Ma); Triassic (~250-200 Ma), related to subduction along the Jinsha suture and/or Triassic rifting; Jurassic (~200-150 Ma), related to subduction along the Rushan Pshart suture; and Cretaceous. The Cretaceous activity may comprise peaks at ~120 Ma and ~80 Ma, reflecting arc activity prior to accretion of the Karakorum block probably along the Tirich Mir fault and flat-slab subduction along the Shyok suture north of the Kohistan-Ladakh arc respectively.

The above outlined accretion history is supported by fission track ages of detrital apatites and zircons depicting four major phases of tectonic activity:
(a) Age populations of ~370 Ma from Tertiary sedimentary basins of the northern Pamirs and northern Central Pamirs are interpreted to be related to the first, northern Kunlun arc stage.
(b) A Permo-Triassic cluster ranging from ~266 to 242 Ma was detected in all studied regions from the southern Tien Shan to the eastern Pamirs. These ages argue for Triassic rifting and/or Triassic southward subduction along the Jinsha suture.
(c) Jurassic age populations from 170-145 Ma occur in Tertiary sedimentary rocks of the South Tien Shan, Kunlun, southern Qiangtang, and Rushan Pshart zone. They are attributed to the Rushan Pshart arc formation and Rushan Pshart basin closure in Mid-Jurassic, which entailed the collision of the Central Pamirs and southeast Pamirs. The coincident collision of the Qiangtang and Lhasa blocks caused for instance Mid-Jurassic compressive deformation in the Kunlun mountains.
(d) Late Cretaceous fission track ages were determined on apatites of Tertiary intramontane basin sediments from the South Tien Shan and on zircons from intrusive rocks of the northern and southern Central Pamirs. These ages may reflect limited exhumation induced by underthrusting of the southeastern Pamirs beneath the southern margin of the Central Pamirs and by intracontinental subduction of the Karakul-Mazar and Jinsha lithosphere underneath the northern margin of the Central Pamirs. This compression was probably triggered by flat-slab subduction along the Shyok suture, between the Karakoum and Kohistan-Ladakh terranes.

The protracted accretion history came to a close with the final collision between India and Eurasia ~55 Ma ago, establishing the Pamirs into an intracontinental position. Deformation did not propagate continuously from south to north, but it might have instead concentrated in rheologically weakened zones, like the Central Pamirs. There, intracontinental subduction along the Jinsha suture and Rushan Pshart zone may have favoured deformation, generation of melt, and the emplacement of the prominent Muzkol and Sares domes. Their exhumation between 25 to 15 Ma seemed to have heated southerly contiguous Tertiary intramontane basins. Coevally, the northern margin of the Karakul-Mazar belt was exhumed along the right-lateral transpressional Markansu fault. Apatite fission track analyses across the Karakul lake batholith gave ages from 56 to 18 Ma with a younging towards the north. Early Miocene exhumation was followed by eastward lateral extrusion and uplift along large (Karakorum, Markansu) and conjugated (southern Tien Shan margin, frontal Pamirs, southern Central Pamirs margin) strike-slip faults, thus compensating for continuous N-S compression between India and Asia; these zones are active at least since 11-10 Ma.

Zusammenfassung

Die paläozoische bis tertiäre geodynamische Entwicklung des Pamir Gebirges in Zentralasien war bisher nur unvollständig rekonstruiert. Dabei handelt es sich bei der Region um einen Schlüsselbereich im Verständnis der lateralen Tethysentwicklung von den Alpen bis nach Südostasien. In der vorliegenden Arbeit wird ein neues, vollständiges geodynamisches Modell entwickelt, das mit den strukturellen Einheiten Afghanistans korreliert und sich sehr gut in existierende Modelle Tibets einfügt.

Mit Hilfe von radiometrischen Altersdatierungen (U/Pb, Rb/Sr und Ar/Ar) und geochemischen Herkunftsbestimmungen an magmatischen Gesteinen W-O streichender magmatischer Gürtel und assoziierter Gesteinsabfolgen lassen sich die wichtigsten paläohistorischen Phasen der Region rekonstruieren. Entlang einem N-S Profil vom südlichen Tien Shan bis östlichen Pamir werden die geodynamischen Ereignisse wie folgt zusammengefaßt:

1) Während des frühen und mittleren Paläozoikums existierte ein aktiver Kontinentalrand im Norden der Paläotethys, etwa entlang dem heutigen Tien Shan Gebirge. Im mittleren und späten Paläozoikum schlossen sich Randbecken und kleinere Terranes amalgamierten. Dies ist beispielsweise entlang des Profils durch die unterpermischen (~277 Mio. Jahre) kalk-alkalinen Granitoide des südlichen Tien Shan belegt. Diese Intrusionen sind mit der westlich angrenzenden Garm-Turkestan-Alay Zone vergleichbar und zeigen die nordwärts gerichtete Schließung des Süd-Gissar Ozeans an. Dieses Ereignis entspricht der Schließung des Süd Tien Shan Ozeans, einem weiteren Randbecken östlich des Profils. Dabei wurden von West nach Ost die Baysunta und Tadjik Terranes sowie der Tarim Block amalgamiert.

2) Südlich schließt sich im bearbeiteten Profil nach dem Süd Tien Shan und dem intramontanen Alaytal der Nordpamir an. Dort belegen ~370-330 Mio. Jahre alte metavulkanische Gesteine (Altyndara Profil) einen magmatischen Bogen, der mit dem nördlichen Kunlun Bogen Westtibets korrelierbar ist. Die spätpaläozoische/triassische Subduktion des Sonpan-Ganze Ozeans führte in Westtibet zur Ausbildung des südlichen Kunlun Bogens. Ein äquivalenter triassischer magmatischer Bogen läßt sich im Nordpamir vermuten.

3) Gut belegt sind permotriassische vulkanosedimentäre Abfolgen im Nordpamir (in der Karakul See Region), die den Karakul-Mazar Akkretionskomplex aufbauen. Dieser entwickelte sich im Sonpan-Ganze Ozean zwischen nordwärts gerichteter Subduktion unter den magmatischen Kunlun Bogen und südwärts gerichteter Subduktion entlang der Tanymas Sutur am Nordrand des Zentralpamirs. Die kryptische, pamirische Tanymas Sutur ist mit der tibetischen Jinsha Sutur korreliert und der Zentralpamir mit dem Qiangtang Block. In die verschiedenen Subduktions- und Akkretionseinheiten des Nordpamirs intrudierte der massige, triassische/jurassische, posttektonische Karakul See Batholith. Der ~227 Mio. Jahre alte Granitoid ist mit gleich alten (~227-199 Mio. Jahre) posttektonischen Granitoiden in Nordwest-Tibet korrelierbar, die den Karakul-Mazar Komplex zusammenfügen. Vergleichbare Plutonite und permotriassische vulkanosedimentäre Abfolgen werden aus dem westlichen Badakshan, westlichen Hindu Kush, und der Feroz Koh Region in Afghanistan beschrieben.

4) Im Zentralpamir sind Basement-Antiformen aufgeschlossen, die hauptsächlich aus im Tertiär exhumiertem, mittel- bis hoch metamorphen Sonpan-Ganze Ozeanboden und

triassisch/jurassischer Sonpan-Ganze Mélange bestehen. Im Qiangtang Block Tibets sind ebenfalls Basement-Dome, die aus den gleichen Einheiten bestehen, allerdings schon im Mesozoikum exhumiert wurden, bekannt. Möglicherweise ist in der afghanischen Safed Khers Region ähnliches Basement in Antiklinoria aufgeschlossen und die Band-e Bayan und Fahrah Rod Zonen Afghanistans können mit der mesozoischen Bedeckung des Zentralpamirs und dem Qiangtang Block korreliert werden.

5) Kalk-alkaline Granitoide (~190-150 Mio. Jahre) durchschneiden den südlichen Zentralpamir und nördlichen Südost-Pamir. Sie intrudierten die östliche Pshart Ozeanbecken-Inselbogen Sequenz und bauen den magmatischen Rushan Pshart Bogen auf. Die Fahrah Rod Zone in Afghanistan ist die vermutete westliche Fortsetzung und Granitoide des südlichen Qiangtang Blocks (170-160 Mio. Jahre) bilden die östliche Verlängerung dieser Zone. Die Abfolgen und Intrusionen der Rushan Pshart Zone belegen die Schließung mehrerer lateral aneinander gereihter Becken, die sich vermutlich in einem transpressiven Milieu gebildet haben. Diese Becken setzen sich bis in die Bangong-Nujiang Zone an der Grenze zwischen dem Qiangtang Block und Lhasa fort und wurden im mittleren Jura geschlossen.

6) Kretazische Plutone, die in den zentralen und südlichen Pamir intrudierten, belegen eine lang anhaltende magmatische Geschichte. Ihre Zirkone, sowie Zirkone aus spätmiozänen Xenolithen, belegen, daß die magmatische Hauptaktivität in vier Phasen erfolgte: vom Präkambrium bis Ordovizium (~575-410 Mio. Jahre); in der Trias (~250-200 Mio. Jahre), durch Subduktion entlang der Jinsha Sutur und/oder triassischem Rifting; im Jura (~200-150 Mio. Jahre), durch Subduktion entlang der Rushan Pshart Sutur; in der Kreide. Die kretazische Aktivität hatte möglicherweise zwei Höhepunkte, um ~120 Mio. und ~80 Mio. Jahre. Das frühere Kreide-Ereignis spiegelt Inselbogen-Aktivität vor der Akkretion des Karakorum Blocks wider, eventuell entlang der Tirich Mir Störung. Der spätkretazische Magmatismus könnte ein Hinweis auf flach einfallende Subduktion entlang der Shyok Sutur nördlich des Kohistan-Ladakh Bogens sein.

Apatit- und Zirkon-Spaltspurenalter unterstützen die oben dargestellte Akkretions-geschichte. Vier Hauptphasen tektonischer Aktivität sind durch Spaltspurenalter an detritischen Apatiten und Zirkonen belegt:

(a) Alterspopulationen von ~370 Mio. Jahren wurden in tertiären Sedimentbecken des Nordpamir und nördlichen Zentralpamir gefunden. Diese Alter deuten auf das nördliche, erste Kunlun-Inselbogen-Stadium hin.

(b) Permotriassische Altersgruppen (~266-242 Mio.) wurden in allen untersuchten Gebieten vom Süd Tien Shan bis zum östlichen Pamir gefunden. Diese Alter wurden als Ausdruck triassischen Riftings und/oder triassischer, südwärts gerichteter Subduktion entlang der Jinsha Sutur interpretiert.

(c) Jurassische Alter (~170-145 Mio. Jahre) kommen in tertiären Sedimentgesteinen des südlichen Tien Shans, Kunlun, südlichen Qiangtang, und in der Rushan Pshart Zone vor. Sie sind mit der Rushan Pshart Inselbogen-Entwicklung und Rushan Pshart Becken-Schließung im mittleren Jura korrelierbar, die zu der Kollision des Zentral-pamirs mit dem Südost-Pamir führte.

(d) Oberkreide Spaltspurenalter wurden an Apatiten von Sedimentgesteinen tertiärer intramontaner Becken des Süd-Tien Shan bestimmt. Gleiche Alter erzielten Zirkone magmatischer Gesteine des nördlichen und südlichen Zentralpamirs. Diese Alter reflektieren möglicherweise schwache Exhumierung, verursacht durch die beginnende Unterschiebung des südöstlichen Pamirs unter den Südrand des Zentralpamirs und durch intrakontinentale Subduktion der Karakul-Mazar- und Jinsha-Lithosphäre unter den Nordrand des Zentralpamirs. Diese Einengung und Hebung wurde wahrscheinlich durch die flach einfallende Subduktion und Kompression entlang der Shyok Sutur zwischen den Karakorum und Kohistan-Ladakh Terranes ausgelöst.

Mit der finalen Kollision von Indien mit Eurasien vor etwa 55 Mio. Jahren endete die lang andauernde Akkretionsgeschichte und der Pamir kam in eine intrakontinentale Position. Augenscheinlich schritt die post-kollisionale Deformation nicht kontinuierlich von Süden nach Norden voran, sondern hat sich in rheologisch geschwächten Zonen wie dem Zentralpamir konzentriert, wo wahrscheinlich intrakontinentale Subduktion entlang der Jinsha- und Bangong-Nujiang Sutur Deformation und Schmelzbildung erleichtert hat. Daher ist das stärkste Exhumierungsereignis in den Muzkol- und Sares-Domen des Zentralpamirs dokumentiert. Die Exhumierung der Dome bewirkte zwischen 25 und 15 Mio. Jahren die Aufheizung tertiärer intramontaner Becken entlang der Südseite des Doms. Ein Apatit-Spaltspurenprofil über den Karakul-Batholith ergab Alter von 56 bis 18 Mio. Jahren mit einer Verjüngung in Richtung Norden. Gleichzeitig mit der Dom-Exhumierung im Süden, wurde auch der nördliche Rand des Karakul-Mazar Gürtels entlang der dextralen, transpressiven Markansu-Störung exhumiert. Die frühmiozäne Exhumierung geht über in laterale Extrusion entlang großer (Karakorum, Markansu) und konjugierter (Südrand Tien Shan, frontale Pamirkette, Südrand Qiangtang Block) Seitenverschiebungen und kompensiert so die anhaltende Nord-Süd-Verkürzung zwischen Indien und Asien. Diese Lokalitäten sind seit mindestens 11-10 Mio. Jahren aktiv.

1 Introduction

Until the 1990s, geological surveying of the Pamirs focused on Precambrian geology and ore exploration. At the same time, the neighbouring Himalayas and Tibet (Fig. 1.1) were studied applying modern mountain building theories. Despite the shortage of modern data, several scientists were successfully placing the Pamirs' geologic history into a plate tectonic framework (e.g. Zonenshain et al. 1990, Burtman & Molnar 1993). In accordance with the tectonic history of other Central Asian regions, the Pamir crust amalgamated over several orogenic cycles during the Palaeozoic and Mesozoic. Although attempts have been made to correlate Palaeozoic and Mesozoic sutures in the Tien Shan and Pamirs with those in Tibet and Afghanistan, mapping of ophiolites and related rocks has not sufficiently highlighted the sutures. Likewise is the structural relationship, number, identity, and evolution of intervening blocks in the Central Asian region still poorly known. Attempts to correlate Palaeozoic and Mesozoic sutures from Tibet or Afghanistan across the Pamirs are problematic. This is by virtue of northward deflection of the Pamirs relative to the neighbouring areas in the east and west. Another difficulty arises from significant post-collisional shortening during the Cenozoic India-Asia collision. Although this collision occurred approximately 1000 km south of the Pamirs, it has dramatically reshaped the Pamirs until recently. Much of the research in Central Asia of the last two decades focused on Tibet and on the tectonic activity post-dating the India-Asia collision (e.g. Tapponnier & Molnar 1977; Dewey et al. 1989, Yin & Harrison 2000 and several others). By contrast, only little is published about the post-collisional history of the Pamirs (Arrowsmith & Strecker 1999; Burtman & Molnar 1993; Coutand et al. 2002; Ducea et al. 2003; Frisch et al. 1994a, 1994b; Hubbard et al. 1997, 1999; Pavlis & Hamburger 1997; Ratschbacher & Schwab 1999; Ratschbacher et al. 1996, 1997; Schwab et al. 1997, 1999, 2000; Strecker et al. 1994a, 1994b, 1995a, 1995b, 2003). Nevertheless, reconstructions of Cenozoic deformation resulting from the India-Asia collision are considered preliminary owing to insufficient knowledge of the pre-collisional geometry of Central Asia. Identification of pre-Cenozoic sutures can provide crustal markers which aid in unravelling Cenozoic shortening and displacements. This in turn facilitates understanding and reconstruction of tectonic events that were affecting the Pamirs.

The aim of this study is to elucidate the Pamirs' pre- and post-collisional tectono-thermal evolution and to help understanding the development of the Pamir-Tibet orogenic setting, responsible for constructing one of the Earth's largest mountain belts. Data collection was concentrated across E-W striking magmatic belts and along a N-S traverse from South Tien Shan (STS) through the eastern Pamirs.

The following main questions are addressed:

- What is the age and origin of the E-W striking magmatic belts and what was their role in the crustal formation of the Pamirs?
- What are the eastern and western equivalents to Pamiran sutures and crustal blocks?
- Where is intracontinental deformation, caused by the India-Asia collision, concentrated in the southern Tien Shan and eastern Pamirs? How does

deformation propagate from the plate margins to the interior of the continent?

- What is the Cenozoic to recent thermotectonic response of the crust to the ongoing contraction across the Tien Shan and Pamir regions?

Based on the acquired data, their interpretation in relation to the evolution of the Pamirs, this thesis comprises the following main chapters:

- Crustal assemblage of the Pamirs: age and origin of magmatic belts from the southern Tien Shan to the eastern Pamirs (chapter 3).
- Cenozoic exhumation history of the South Tien Shan and eastern Pamirs (chapter 4)

Finally, this study results in a redefined age zonation and amalgamation history of the Pamirs and provides the first comprehensive research project about the Tertiary low-T evolution post-dating the India-Asia collision.

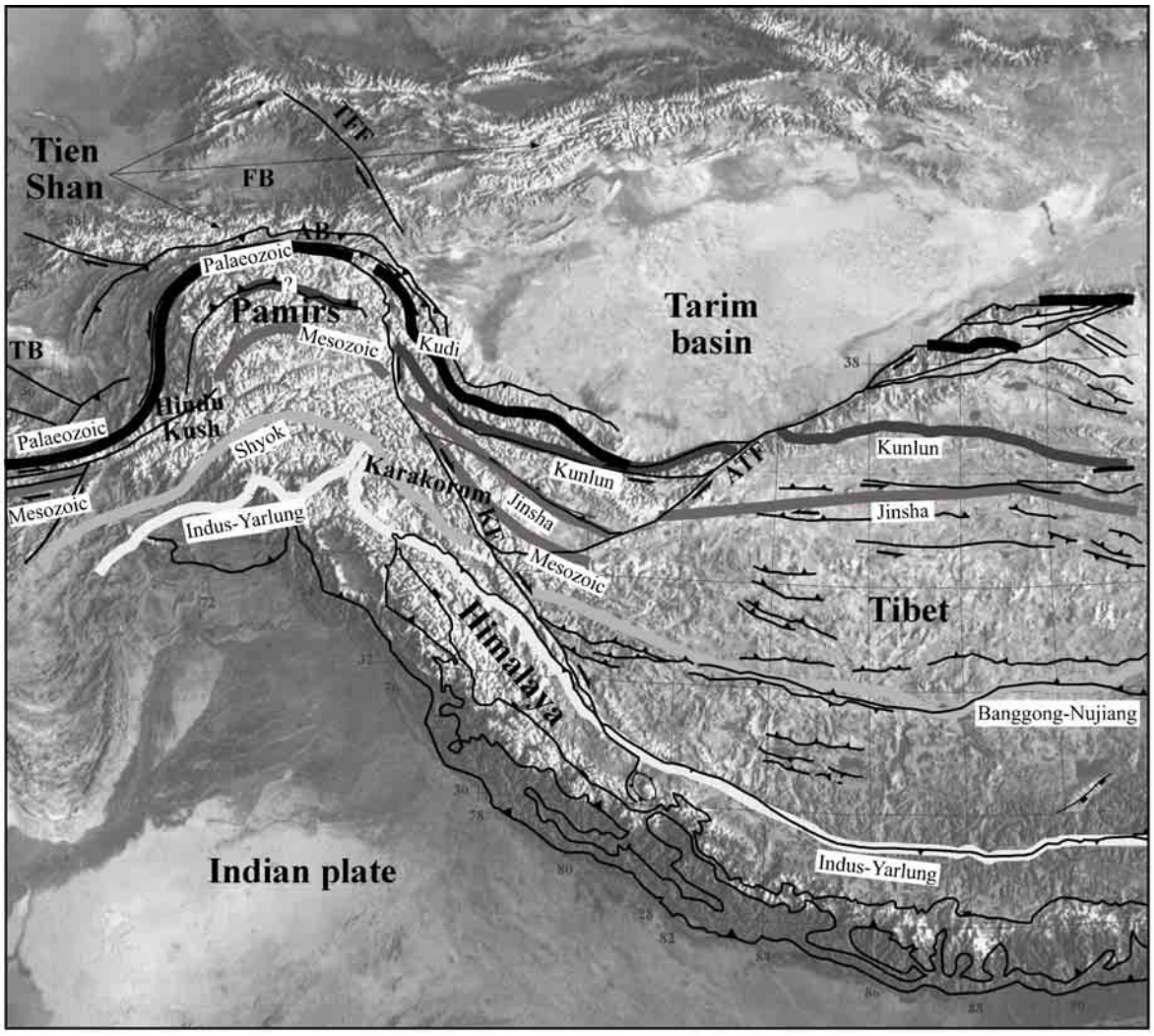

Fig. 1.1: Topographic and regional tectonic map of the Pamirs and the Tibetan Plateau, showing physiogeographic units and major suture zones after the compilations of Burtman & Molnar (1993) for the Pamirs and Yin & Harrison (2000) for Tibet, and Cenozoic fault systems modified after Yin & Harrison (2000). TFF = Talasso-Ferghana fault, FB = Ferghana basin, AB = Alay basin, TB = Tadzhik basin, KF = Karakorum fault, and ATF = Altyntagh fault. Bold lines outline suture zones with decreasing ages from north to south.

2 Sample preparation and analytical techniques

2.1 Sampling strategy

In this study, a combination of petrology, geochemistry and geochronology was used to identify and characterise the timing, correlation in space and time, and the tectonic environment of magmatic arcs in the southernmost Tien Shan and north-eastern Pamirs. Petrological and geochemical data were used for standard classification of magmatic rocks and to estimate their origin and the tectonic environment in which they were placed. It was further aimed to estimate by isotopic data like εNd-values, if there was any changing influence of lower and upper crustal compositions to melting processes. U/Pb geochronology was applied to obtain the first reliable crystallisation and metamorphic dates and to constrain whether new crustal material was generated or older crustal components were reworked inferred by inherited components. Rb/Sr and Ar/Ar data were used to determine metamorphic and cooling ages. These medium-T ages support the U/Pb ages or serve as minimum estimates for crystallisation ages when U/Pb ages were not determined. To constrain the latest stage of mountain building the fission track thermochronology as a low-temperature geochronological method was applied. With the aid of fission track analyses and in combination with the medium-T geochronology the long term cooling history and erosional behaviour of the mountain range was determined. Furthermore, zircon and apatite fission track ages and the fission track length study in apatites was used to constrain the temperature history of sedimentary basins. Peaks in the age spectrum of sediments defined the input of different

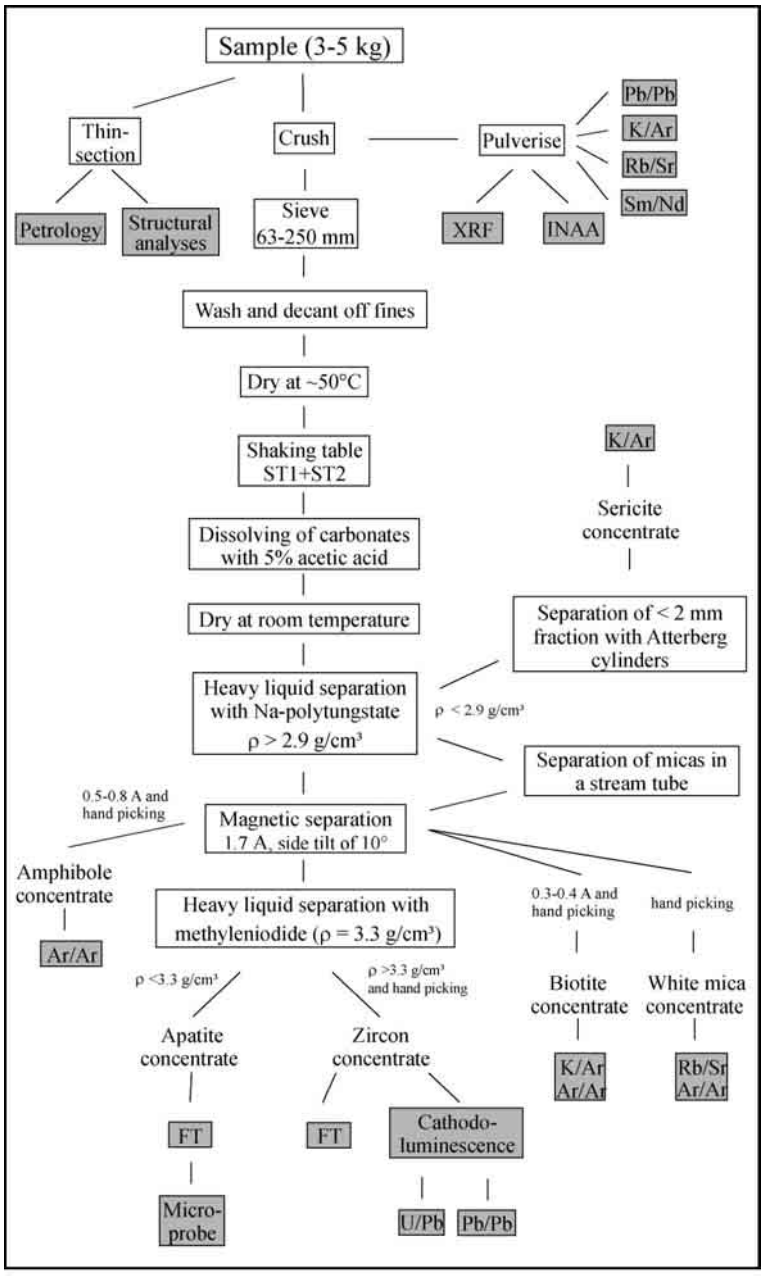

Fig. 2.1: Flow diagram showing the sample prepration and the methods applied

source terrains, changes in the sedimentation pattern, and the cooling history of the hinterland. Figure 2.1 shows the work routine, which was applied to the rock samples and Appendix A, Tab. A1 summarises sample descriptions and locations.

2.2 X-ray fluorescence spectroscopy (XRF) and Instrumental Neutron Activation Analysis (INAA) on whole rock

Major and trace element concentrations of 38 rock samples were measured by XRF (X-ray fluorescence spectrometry) at the Institut für Geowissenschaften, Universität Tübingen, Germany, with a Siemens S 200 spectrometer. Three basalt samples were analysed on a Philips PW 2400 spectrometer at the University of Fribourg, Switzerland. Pulverised sample material was dried at 110°C to remove adsorbed water (H_2O^-). Sample tablets were formed by melting of 7.5 g lithium metaborate and 1.5 g whole rock powder. The weight of crystal water (H_2O^+) was determined on 1 g sample powder at 1050°C after 15 hours.

INAA was performed on 38 samples by Activation Laboratories Ltd. in Ancaster, Ontario, Canada. A 0.5-2.0 g sample was weighed into a small custom-made polyethylene vial to totally fill the vial. For every 11 samples, a CANMET MRG-1 standard was co-irradiated with flux wires at a thermal neutron flux of 7 x 10^{12} neutron/cm^2s for 15 minutes in the RIFLS site of the McMaster Nuclear Reactor. After 7 days of decay time the samples were counted on a high purity co-axial Ge Detector with a resolution of > 1.7 keV for the 1332 keV Co-60 photopeak. The data were corrected for decay and compared with a calibrated value developed from multiple international reference materials (approximately 50) using the flux wire monitors. The CANMET standard MRG-1 was used solely for verification of the procedure and not for calibration purposes. Selected samples were recounted and compared with the original as part of the QA/QC procedure. Gamma-ray energies are listed in Hoffman (1992). A summary of XRF and INAA is given in Appendix A, Tab. A2. For chondrite normalised rare earth element (REE) diagrams, normalisation values for the Sedy meteorite of Masuda et al. (1973) were used. Ocean ridge granite (ORG) REE patterns are normalised with values after Pearce et al. (1974).

2.3 Mica and amphibole separation for K/Ar, Ar/Ar and Rb/Sr dating

Sericites of low-grade metamorphic clastic sediments were measured from the fraction < 2 μm. For sericite separation the samples were ground for 20 s in an agate-mill. Rocks containing small amounts of carbonate were treated with 5% acetic acid. The insoluble residue was washed several times with distilled water. Separation of the < 2 μm clay-fraction was achieved in Atterberg cylinders. If necessary, sodium (Calgon®) was used as dispersing agent. Biotite and white mica were separated using streaming tubes (Mica Jet), heavy liquids (sodium polytungstate, ρ = 2.9 g/cm^3) and magnetic separation. Quality of separation was enhanced by paper sticking and handpicking. Amphibole separation was performed by crushing, sieving, magnetic separation, and handpicking. Yury D. Pushkarev, Institute of Geology and Geochronology of the Precambrian, Russian Academy of Sciences, St. Petersburg, Russia, performed the K/Ar age determinations. All basalt whole rock samples were crushed for destruction of bubbles, which may contain excess ^{40}Ar. The content of

radiogenic ^{40}Ar was measured by isotope dilution. ^{38}Ar was used as an isotope tracer. Potassium was determined by flame photometry; its concentration was determined twice in each sample. Ar/Ar ages were determined on amphibole, white mica, biotite and K-feldspar.

Samples for $^{40}Ar/^{39}Ar$ dating were crushed and the >63 μm size mica fraction extracted using standard mineral separation techniques. The separates were cleaned by ultrasound and later purified by hand picking; the largest, inclusion-free grains were used for dating. The separates were packaged in pure Cu-foil, stacked in a pure SiO_2 vial together with foil-packaged neutron fluence monitors, and irradiated in different irradiations at the Oregon State University TRIGA reactor. Taylor Creek sanidine (USGS standard 85G003; Dalrymple & Duffield 1990) with an assigned age of 27.92 Ma was used as a neutron flux monitor. Lothar Ratschbacher performed Ar extraction at the Ar/Ar laboratory at Stanford University, USA. 1-2 mg of each monitor were analysed with a 6-W Spectra-Physics continuous Ar-ion laser operating in TEM_{00} mode in 6 groups of 3-5 grains to determine the irradiation parameter *J*. An uncertainty of 0.5% (at 1σ) was used for *J* for all samples. Resistance furnace analyses were conducted in a double-vacuum Staudacher-type resistance furnace. The evolved gas was purified during extraction by SAES ST-172 and ST-101 getters and a stainless steel cold finger and analysed on a MAP 216 mass spectrometer fitted with a Baur-Signer ion source and a Johnston MM1 multiplier with a sensitivity of approximately 2×10^{-14} mol/V. Analyses were corrected for system blanks and instrumental mass discrimination using the program EyeSoreCon, written by B.R. Hacker. Laser blanks were typically 2×10^{-16} moles for m/e 40, and resistance furnace blanks varied from $\sim 1 \times 10^{-16}$ mol at 800°C to $\sim 1 \times 10^{-15}$ at 1400°C.

Rb/Sr ages were determined on granites by whole rock analyses and on white mica of fraction 125-250 μm. For all Rb/Sr analyses the isotope dilution method was applied. The whole rock powders were dissolved overnight with HF-$HClO_4$ in 15ml Savillex® beakers at 120°C for 2-3 days. Mineral decomposition was done in Teflon bombs at 180°C for one week. White mica samples were spiked with $^{87}Rb/^{84}Sr$ isotope tracer solution before decomposition. Mass spectrometer measurements on a Finnigan MAT 262 were performed by Elmar Reitter at the Geochemisches Zentrallabor, Universität Tübingen, Germany. For the age calculation the software Isoplot/Ex Version 2.49 (Ludwig 2001) was used. The results of Ar/Ar, K/Ar, and Rb/Sr dating are summarised in Appendix A, Tab. A3, A4, and A5.

2.4 Preparation of whole rock samples for Sr and Nd isotopic composition

For Sr and Nd isotope analyses, samples (whole rock powder) were dissolved in 52% HF for four days at 140°C. Digested samples were dried and re-dissolved in 6N HCl, dried again and re-dissolved in 2.5N HCl. Sr and light rare-earth elements (LREE) were isolated on quartz columns conventional ion exchange chromatography with a 5 ml resin bed of Bio Rad AG 50W-X12, 200-400 mesh. Nd was separated from REEs using quartz columns with 1.7 ml Teflon® powder coated with di(2-ethyl-hexyl)ortho-phosphoric acid (HDEHP) as cation exchange medium.

Isotopic measurements of granitic and basement rocks were made applying Thermal Ionisation Mass Spectrometry, on a Finnigan MAT 262 mass spectrometer at the

Geochemisches Zentrallabor, Universität Tübingen, Germany. Sr was loaded with a Ta-HF activator on pre-conditioned W filaments and measured in single-filament mode. Nd was loaded as phosphate on pre-conditioned Re filaments and measurements were performed in a Re double filament configuration. The $^{87}Sr/^{86}Sr$ isotope ratios were normalised to $^{86}Sr/^{88}Sr = 0.1194$ and the $^{143}Nd/^{144}Nd$ isotope ratios to $^{146}Nd/^{144}Nd = 0.7219$. Analyses of 24 separate loads of Ames metal (Geological Survey of Canada, Roddick et al. 1992) gave a $^{143}Nd/^{144}Nd$ of 0.512125 ± 0.000010 (errors are 2σ of the mean) and within the same period the NBS 987 Sr standard yielded a $^{87}Sr/^{86}Sr$ of 0.710259 ± 0.000012 (n = 28). Total procedural blanks (chemistry and loading) were < 200 pg for Sr and < 50 pg for Nd. Sm and Nd isotopic ratios of 17 samples are given in Appendix A, Tab. A6.

2.5 U/Pb isotope dilution and Pb/Pb evaporation age determination methods on zircons

For conventional U/Pb analyses zircon populations consisting of a few morphologically identical grains were washed in hot 6 N HCl and hot 7 N HNO_3 prior to dissolution to remove surface contamination. A mixed $^{205}Pb/^{235}U$ tracer solution was added to the grains. Dissolution was performed in PTFE vessels in a 1900 psig (130 bar) PARR acid digestion bomb (Parrish 1987) according to the vapour digestion method (Wendt & Todt 1991). The bomb was placed in a temperature-controlled oven at 200°C for one week in 22N HF and for one day in 6N HCl to assure re-dissolution of the fluorides into chloride salts and avoid U/Pb fractionation (Mattinson 1994). Separation and purification of U and Pb were carried out on Teflon columns with a 40 µl bed of AG1-X8 (100-200 mesh) anion exchange resin following the procedure described in Poller et al. (1997). Further details on U/Pb analytical techniques are given in Chen et al. (2000).

Thermal Ionization Mass Spectrometry was applied for isotopic measurements of 11 samples on a Finnigan MAT 262 mass spectrometer at the Geochemisches Zentrallabor, Universität Tübingen, Germany. The measurements were performed by Fukun Chen, Wolfgang Siebel, and myself. Four samples were measured at the Isotope Geochemistry Lab of the University of Washington, USA, by Bruce K. Nelson. Pb was loaded onto a pre-conditioned Re filament according to the Si-gel method (Cameron et al. 1969) and measured at ~1300°C in single-filament mode. U was loaded with 1N HNO_3 onto a pre-conditioned Re filament and was measured in double-filament configuration. Total procedural blanks were < 10 pg for Pb and < 2 pg for U. A factor of 1‰ per mass unit for instrumental mass fractionation was applied to all Pb analyses, using NBS SRM 981 as reference material. Initial common Pb remaining after correction for tracer and blank was corrected using values from the Stacey & Kramers (1975) model. The decay constants for U are those given in Jaffey et al. (1971). U/Pb discordia intercepts were calculated using regression treatment (Wendt 1986).

The single zircon Pb-evaporation analyses were made by Fukun Chen following the procedures of Kober (1986, 1987), Körner & Todt (1988), Cocherie et al. (1992), Klötzli (1997) and Kröner & Hegner (1998). Untreated whole zircon grains or fragments were analysed using a double Re filament configuration. The motif behind this method is the assumption that the Pb with the highest activation energy, i.e. the highest evaporation

temperature, resides in the undamaged crystalline domains of the zircon which have not lost any Pb. The Pb residing in zircon domains with radiation damage (metamict domains) has a low activation energy and it evaporates from the grain at low temperature. The $^{207}Pb/^{206}Pb$ ages, in a strict sense, must be interpreted as minimum ages in cases when no inherited Pb is present. In many studies, it is assumed that the $^{207}Pb/^{206}Pb$ ratios obtained at high temperatures reflect the primary ratio, not affected by Pb-loss, and the corresponding dates are interpreted as concordant. Comparison between different geochronological methods showed that careful application of the evaporation method provides reliable ages for zircons from magmatic and metamorphic rocks (e.g. Kober et al. 1986, Kober 1987, Cocherie et al. 1992, Ansdell & Kyser 1993, Chen 1999). The measurement of the isotopic abundance was performed in a dynamic mode with mass sequences 206-207-204-206-207 or 206-207-207-206-204 using an ion-counter. Data collection started at 1400°C, and the temperature increased by 20°C to 30°C after each evaporation-deposition cycle. The ages were calculated from $^{207}Pb/^{206}Pb$ ratios obtained on a stable ion beam, and only ratios with $^{207}Pb/^{206}Pb$ ratios > 5000 were used for further processing. A correction for common Pb was performed according to Cocherie et al. (1992) using a Pb composition with a two-stage evolution (Stacey & Kramers 1975). The errors on the ages are reported as $2\sigma_{mean}$ of the population of weighted $^{207}Pb/^{206}Pb$ ratios. The results of 15 analysed U/Pb and Pb/Pb samples are summarised in Appendix A, Tab. A7 and A8.

2.6 U/Pb SHRIMP measurements on zircon

SHRIMP-analysis of zircon was done by Lothar Ratschbacher at the SHRIMP-RG facility at Stanford University, USA. Data are collected in Appendix A, Tab. A9. Zircons and standard grains were deposited onto and pressed into two-sided tape, covering approximately a 1.5 cm^2 square in the centre of a 25.4 mm circle. A 25.4 mm cylindrical Teflon mould was positioned so that it surrounded the grains, and a thoroughly blended mixture (25:3 by weight) of Struers EPOES Resin and EPOAR Hardener was poured over them to a thickness of 1-1.5 cm. The epoxy was left to cure for 12-24 hours. The sample mount was put in an slow (60°C) oven for about 2 hours and then cooled. The mould was removed and the epoxy plug was trimmed on a lathe to form a disc about 6 mm thick. The back (non-specimen) side was polished so the specimens can be seen from the back. Finally, the embedded specimen side was polished to exposure of individual grains (1500 grit wet/dry sandpaper, followed by 6 μm, then 1 μm diamond powder slurries on a Struers LabPol5 rotary polisher). Cathodoluminescence electron and optical images were prepared to reveal the internal structure (e.g., age heterogeneity expressed by core and rims and growth zonation) of all zircons and was used to guide the subsequent analyses. Prior to placing the mount in the instrument, it was cleaned in a 1M HCl solution, thoroughly rinsed in de-ionised water, baked in a slow oven for approximately one-half hour, and then coated with roughly 10 nm of gold in a sputter coater.

The zircon runtable consisted of the species Zr_2O, ^{204}Pb, background, ^{206}Pb, ^{207}Pb, ^{208}Pb, ^{238}U, ThO-248, and UO-254. Pb isotope ratios were taken as measured following the removal of the background. Pb/U ratios were calibrated against the concomitant UO/U ratio, and an overall normalisation relating ion intensity to actual ratio was taken at the

mean UO+/U+ and Pb+/U+ value. Since the age of the standard and its actual Pb/U is known, unknown parameters can be calibrated against the standard. Data reduction was carried out through versions of PRAWN and Lead, data reduction programs based on routines developed at ANU. PRAWN (Playing Retrospectively Around With Numbers) produces isotope ratios from the observed intensities, while lead carries out the renormalisation against the standard.
The Stanford SHRIMP-RG incorporates a different mass analyser in comparison with that used on the SHRIMP II models. Double-focusing mass spectrometers consist of an electrostatic analyser (ESA) and a magnetic sector. The purpose of the ESA is to remove velocity dispersion from the mass filtered beam by producing an equal and opposite dispersion to that produced in the magnet. The double focusing refers to the refocus of the ion beams of a single mass without any dispersion from the angular trajectory of the ion beams or the velocity of the ions. When the ESA precedes the magnet, it is referred to as having a forward geometry. By contrast, a magnet positioned before the ESA is reverse geometry. In a reverse geometry mass spectrometer, mass separation occurs relatively early in the beam path and so only one mass is passed through to the collector. Because the analyser is only transmitting a single mass ion beam, the abundance sensitivity (the degree to which scattered ions interfere with the peak of interest) is much increased because any neighbouring intense ion beam is rejected well out of sight of the collector. Perhaps the biggest advantage of the SHRIMP-RG is the larger magnet dispersion afforded by the reverse geometry. Given similar source and collector slits, SHRIMP-RG yield four times the mass resolution of the SHRIMP-FG designs with the same sensitivity.

2.7 Cathodoluminescence of zircons

The cathodoluminenscence (CL) technique is a high resolution method to determine the internal crystal growth structure of zircons. This method has been often employed in recent years to support the interpretation of U/Pb zircon ages (e.g. Chen 1999a, Poller et al. 1997, Vavra et al. 1996). Studies of Marshall (1988) and Sommerauer (1976) showed the correlation between colour and brightness of the luminescence and variations in the concentration of certain trace elements. The variation of the chemical composition in minerals will be therefore simply reflected in CL zoning. As shown by Frank et al. (1982), a boundary between two successive zones reveals the shape of the crystal corresponding to a particular time in its growth history. Furthermore, irregular boundaries record stages of growth interrupted by some degree of solution. For the CL analyses zircons were attached to the bottom of a vessel and fixed with Epofix® resin for polishing. The luminescence was determined by an energetic electron beam on a JEOL JXA Superprobe at the Institut für Geowissenschaften, Universität Tübingen, Germany. The Superprobe is equipped with a cathodoluminescence (CL)-detector at an acceleration voltage of 15 kV. Note that the zircons used for the Pb-evaporation and conventional U/Pb analyses are not identical with those taken for the CL studies, however they are supposed to be representative. Cathodoluminescence images of zircons are presented in Appendix B, plates B1-B5.

2.8 Preparation and irradiation of apatite and zircon samples for fission track dating

The preparation of mineral mounts from sedimentary and magmatic rocks was carried out at the fission track laboratory at the Institut für Geowissenschaften, Universität Tübingen. After crushing and sieving the samples, the <250 μm fraction was further separated using a GEMINI shaking table. The two fractions richest in heavy minerals were treated by 5% acetic acid to dissolve the carbonates and then further processed by heavy liquid separation (Sodium polytungstate, ρ = 2.9 g/cm^3 and methyleniodide, ρ = 3.3 g/cm^3) and magnetic separation. Apatite grains were embedded in ARALDITE-D epoxy resin on glass slides. Zircons were mounted on FEP (polyfluorethylene) Teflon or PFA (tetrafluorethylene-perfluoroalkoxyethylene copolymer) Teflon (Gleadow et al. 1976, Tagami et al. 1988). Mineral mounts were ground using emery papers with 1200 and 2500 mesh grain size and water as lubricant. The mineral surfaces were polished using 9 μm, 3 μm and 1 μm oil-based diamond suspension. Apatite mounts were etched with 1% HNO_3 for 2 min 45 s to 3 min 30 s at room temperature or with 5.5M HNO_3 for 20 s at 21°C. For the etching of the zircon mounts, a KOH-NaOH eutectic melt was used at 215°C (Gleadow et al. 1976). Zircon mounts of hardrocks were etched for 21 to 34 h, those of sediments were etched for 21 to 107 hours depending on the track density and the grade of metamictisation of the zircon grains.

Apatite and zircon fission track dating was carried out using the external detector method (EDM) (Hurford and Green 1983). Mineral mounts, glass dosimeters and standards of known age were covered with low-U muscovite sheets that served as detectors for the induced fission tracks of the samples. The dosimeter glasses are distributed by J. Scheurs, Corning, USA. CN5 with 12 ppm natural uranium (Hurford & Green 1983) was used for apatite and CN2 with 38 ppm natural uranium (Hurford & Green 1983) for zircon. The mounts were packed using foam, polyethylene and parafilm and were irradiated either at the nuclear reactor RISØ in Roskilde, Denmark, or at the Oregon State University TRIGA reactor, USA. The neutron flux was 3.5 x 10^{15} n/cm^2 for apatite and 1.2 x 10^{15} n/cm^2 for zircon. To analyse the homogeneity of the neutron fluence, the two dosimeter glasses and the age standards were placed on each end of the sample package. The following age standards were used for apatites: (a) Fish Canyon volcanic tuff (Colorado, USA) with an age of 27.8±0.7 Ma (Hurford & Hammerschmidt 1985) and (b) Durango (Cerro de Mercado/Mexico) with an age of 31.4±0.6 Ma (McDowell & Keizer 1977). Zircon age standards are the following: (a) Fish Canyon volcanic tuff (Colorado, USA), (b) Buluk Member of the Bakate Formation/Kenia with an age of 16.2±0.2 Ma (Hurford & Watkins 1987), and (c) Tardree rhyolite (Northern Ireland, U.K.) with an age of 58.7±1.1 Ma (Hurford & Green 1983). After irradiation the muscovite sheets and dosimeter glasses were etched with 40% HF for 35 min or with 50% HF for 20 min. Fission track etching was finished by rinsing mineral mounts, muscovite sheets and dosimeter glasses with distilled water.

2.9 Determination and interpretation of fission track data

Counting of spontaneous and induced fission tracks was performed under a Zeiss optical microscope (Axioscope) with a 1000x magnification. Spontaneous tracks in

apatites and zircons were counted using immersion oil, whereas the induced tracks in the muscovites were counted under dry objective. Data were collected with a positioning tablet controlled by the computer program "FT Stage" (version 3.11) developed by Dumitru (1993). The calculation of fission track ages was performed with the computer program TRACKKEY 4.0 of Dunkl (2002). The apatite ξ-factor of 401.21 ± 9.89 was determined from 10 apatite standards and the zircon ξ-factor of 122.91 ± 2.09 is based on 7 zircon standards (Appendix C, Tab. C2 and C3). The χ^2 test was used to determine whether a fission track grain age distribution is homogeneous or discordant (Galbraith 1981). Discordance is defined as grain ages with a variance greater than expected for an analytical error alone. Mixed distributions can arise from (a) sediments with unreset fission track ages, (b) differential resetting of grains with different annealing properties due to variable compositions, or (c) variable alpha-damage. If the χ^2 test of the probability of grains counted in a sample is $>5\%$, a "pooled age" is determined that depicts that the grains belong to a single age population. If χ^2 is $<5\%$, a "mean age" is determined that in most cases assesses only an "over-dispersed" distribution relative to the expectation for count statistics for fission processes (Galbraith 1981). Galbraith and Laslett (1993) introduced the "central age" to represent the estimated age of a discordant distribution taking into account random errors caused by the analyst. The fission track data of apatites are summarised in Appendix C, Tab. C4, and of zircons in Appendix C, Tab. C6.

2.10 Fission track length distributions in apatites

Fission track lengths are reduced or completely annealed by elevated temperature. The individual track-lengths distribution of an apatite sample can be used for the interpretation of the apparent fission track age of the sample with respect to its time-temperature history. Track lengths are measured on horizontal tracks that are completely contained within the host mineral, i.e., so called "confined tracks" (Gleadow et al. 1986). The annealing process is not a linear process; this is best illustrated over geological time scales: in the total annealing or instability zone (TAZ) at >125°C for apatite, tracks anneal immediately after their formation. No accumulation of tracks occurs and the fission track age is zero. Between 60°C and 125°C a transitional zone of partial track shortening exists. This zone is called partial annealing zone (PAZ). Track-length reduction proceeds with increasing rates at higher temperature. At temperatures <60°C, in the so called stability zone, hardly any reduction of the fission tracks can be observed. It follows, that the pattern of track shortening is characteristic for the cooling through the PAZ. Confined track lengths were measured in the same apatite mounts used for the age determinations. Identification and counting of confined tracks was performed under an oil objective with 1000x magnification (same microscope set-up and data collection as for track-density measurements) by a projection tube and a digitising tablet arrangement. Track-length data are included in Appendix C, Fig. C2.

2.11 Electron microprobe analyses on apatites

Electron microprobe analyses were applied to obtain information about the chemical composition of apatites dated by the fission track method. Chemical

compositions of apatites affect the track annealing kinetics. In general, Cl-apatites anneal at higher temperatures than F-apatites (e.g., Green et al. 1986, 1989). For precise reconstructions of T-t paths measurements the chemical compositions of apatites are therefore required. These have been carried out at the Mineralogisches Institut, Universität Heidelberg, using a Cameca SX 51 microprobe. The measurements were done with an acceleration voltage of 15 kV, a probe current of 20 nA, and a defocused spot of 20 μm. Mineral standards for machine calibration were manufactured by Micro-Analysis Consultant Ltd (MAC), Cambridgeshire, UK. The chemical composition of each dated apatite grain in selected fission track samples was determined. The Durango apatite standard was used to calibrate P, Ca, and F. A scapolite mineral standard was used for the calibration of chlorine, and a wollastonite standard for the calibration of silica. The OH-content has been calculated stochiometrically. Electron microprobe analyses of the apatites are summarised in Appendix C, Tab. C5.

2.12 Thermal modelling of the fission track age and length distribution in apatites

Apatite fission track data provide not only age information but also an estimate of the thermal history of host rocks. The annealing of fission tracks is an important aspect of the fission track thermochronometer. Thermal histories can be reconstructed from forward modelling of time-temperature histories and through comparison of predicted and measured fission track ages and lengths based on the understanding of annealing kinetics in apatite (Green et al. 1986 and 1989, Laslett et al. 1987, Crowley et al. 1991). The fission track age and track length distribution determine the cooling below the respective closure temperature of each mineral and the cooling rate. In case of fission tracks, the closure temperature is defined as effective retention temperature at which 50% of the original number of fission tracks are preserved. For apatites, a closure temperature of 100±20° C is generally assumed (Wagner 1968, Naeser & Faul 1969, Hurford 1986), whereas the zircon closure temperature has been determined as 240±50° C for slow cooling rates (Hurford 1986). For cooling rates >10° C/Ma, as in alpine regions, a value of 225±25° C has been proposed by Hurford et al. (1989, 1991).
The computer program AFTSolve (Ketcham et al. 2000) was used to model the thermal histories of selected samples with sufficient track length data. The program combines "forward modelling", in which fission track parameters for hypothetical thermal histories are predicted, with "inverse modelling" that reconstructs thermal histories based on input of measured fission track data. AFTSolve (1) generates a large number of forward models, (2) compares predicted apatite fission track parameters including apparent age and length distribution with measured values for each forward model, and (3) uses the good and acceptable forward models to provide quantitative constraints on time-temperature histories that are permitted by the measurements. Input parameters for the program are the apparent fission track age, the fission track length distribution, and the chlorine content or d_{par} (etch pit diameter) of the apatites. Time-temperature constraints, such as geochronologic data of other minerals, or known burial and erosion history can be incorporated in the model. The program uses a Monte Carlo algorithm to generate a best fit thermal evolution path for an apatite sample with known apparent age and track length distribution. The operator can determine the

number of simulation runs and the modelled output parameters are compared with the input parameters. The correlation of input and modelled output data is statistically evaluated with the Kolmogorov-Smirnov test. The program provides a graphic display of the modelling results showing the best fit thermal evolution and statistically acceptable limits. The best fit thermal history may neither be geologically meaningful nor unique. The annealing model of Ketcham et al. (2000) was chosen with the measured chlorine data as input for the chemical composition. None of the modelled samples defined selected kinetic populations as all apatites were fluorapatites. Each sample was modelled in 50.000 simulation runs. The modelled time-temperature paths are shown in Appendix C, Fig. C3.

2.13 Decomposition of zircon fission track grain age distributions

Single fission track grain age spectra of sedimentary samples that are not thermally overprinted or reset, mirror the provenance ages of their source area. The decomposition of the mixed fission track grain age distribution of a sample yields age populations. These populations reflect low-temperature cooling phases during the geological history of the hinterland from which the sediment was eroded. The decomposition of the age spectra can be approximated statistically. The computer program BINOMFIT (Brandon 2002) was used, which is based on the binomial peak-fitting method of Galbraith and Green (1990). The binomial peak-fitting method is based on the maximum likelihood method which determines the best-fit solution by directly comparing the distribution of the grain data to a predicted mixed binomial distribution (Brandon 2002). The entire grain age distribution is decomposed into a finite set of component binomial distributions, each of which is defined by a unique mean age, a relative standard deviation, and an estimated number of grains in the component distribution. The initial guesses for peak ages are generated from the probability density plot for the fission track grain age distribution. The quality of the fit for each solution is scored using the χ^2 test (Brandon 2002). To test the number of underlying distributions and to define the minimum number of binomials needed, an *F*-ratio test (Bevington 1969) is introduced to judge whether the reduction of χ^2, due to the addition of a new peak, is only by chance. When *F* is large the improvement in fit, associated with the additional peak is considered significant. The *F* distribution is used to assign a probability P(*F*), which is the probability that random variation alone could produce the observed *F* statistics. Brandon (2002) considers P(*F*) $<$ ~5% to indicate that the improvement in fit is significant. Thus, the optimal number of significant peaks can be found by adding peaks until one gets a value of P(*F*) $>$ ~5%. Results of fission track data and calculated age clusters using the computer program BINOMFIT are illustrated in Appendix C, Tab. C7 and the decomposed fission track age spectra in Appendix C, Fig. C5.

3 Crustal assemblage of the Pamirs: age and origin of magmatic belts from the southern Tien Shan to the north-eastern Pamirs

The purpose of this chapter is (1) to introduce existing ideas about the formation of the Pamirs, (2) to describe the geological setting, and (3) to present a new and compiled set of geochemical and geochronological data of magmatic rocks from southernmost Tien Shan and the north-eastern Pamirs. Geochemical data characterise magmatic arc and postcollisional magmatites and therefore assess the nature and limits of continental margins and linear collisional orogens (e.g. Sengör et al. 1993). Based on radiometric ages of the different magmatic rock assemblages, the age zonation of the magmatic belts can be defined. (4) Finally, correlations with magmatic belts in Tibet and Afghanistan led to a new geodynamic model for the Central Asian region, which elaborates on previous scenarios.

3.1 Introduction

The Pamirs were formed by accretion of continental fragments of Gondwana to the southern margin of Eurasia. Magmatic arcs and island arcs of the Palaeotethys and Tethys oceans and their marginal basins contributed significantly to that process. The Pamirs were subdivided into a northern, central, and southern part (Fig. 3.1, and 3.3) based mainly on rock assemblages and their stratigraphic age (e.g., Burtman & Molnar 1993, Zonenshain et al. 1990, Kravchenko 1979). However, it remains unclear how many of these subduction and collision phases moulded the Pamirs, when they occurred and how they can be correlated from Afghanistan (W) through the Pamirs into Tibet (E). Geodynamic models from neighbouring China (e.g., Yin & Nie 1996) show how large-scale strike-slip faults and truncation of structures at the margin of the Tarim basin hampered along strike correlation of sutures and magmatic belts across the Tibetan plateau and to the Pamirs. A detailed and quantitative model of the Palaeozoic and Mesozoic evolution of the Pamirs is basically missing and peculiarities of the Pamirs compared with neighbouring regions were hitherto poorly envisaged.

3.2 Geological setting

Tien Shan

The Tien Shan orogen is one of the most impressive mountain belts in Central Asia. It extends east-west for at least 2500 km with peaks exceeding 7400 m (e.g. Peak Popedy 7439 m). The orogenic belt was formed in late Palaeozoic times (e.g., Burtman 1975, Coleman 1989, Carroll et al. 1990, Windley et al. 1990, Allen et al. 1993, Gao et al. 1995), but the present-day mountain range is a major product of the Tertiary India-Asia collision (Molnar & Tapponnier 1975, Tapponnier & Molnar 1979). Geological studies were focused mainly on the Chinese Tien Shan (e.g., Windley et al. 1990, Allen et al. 1993, Carroll et al. 1995, Gao et al. 1998), and the westernmost part of the Tien Shan (e.g., Brookfield 2000 and Russian literature therein). The whole Tien Shan belt is segmented by the NW-SE striking Talasso-Ferghana fault, which separates a western from an eastern part (Fig. 3.2).

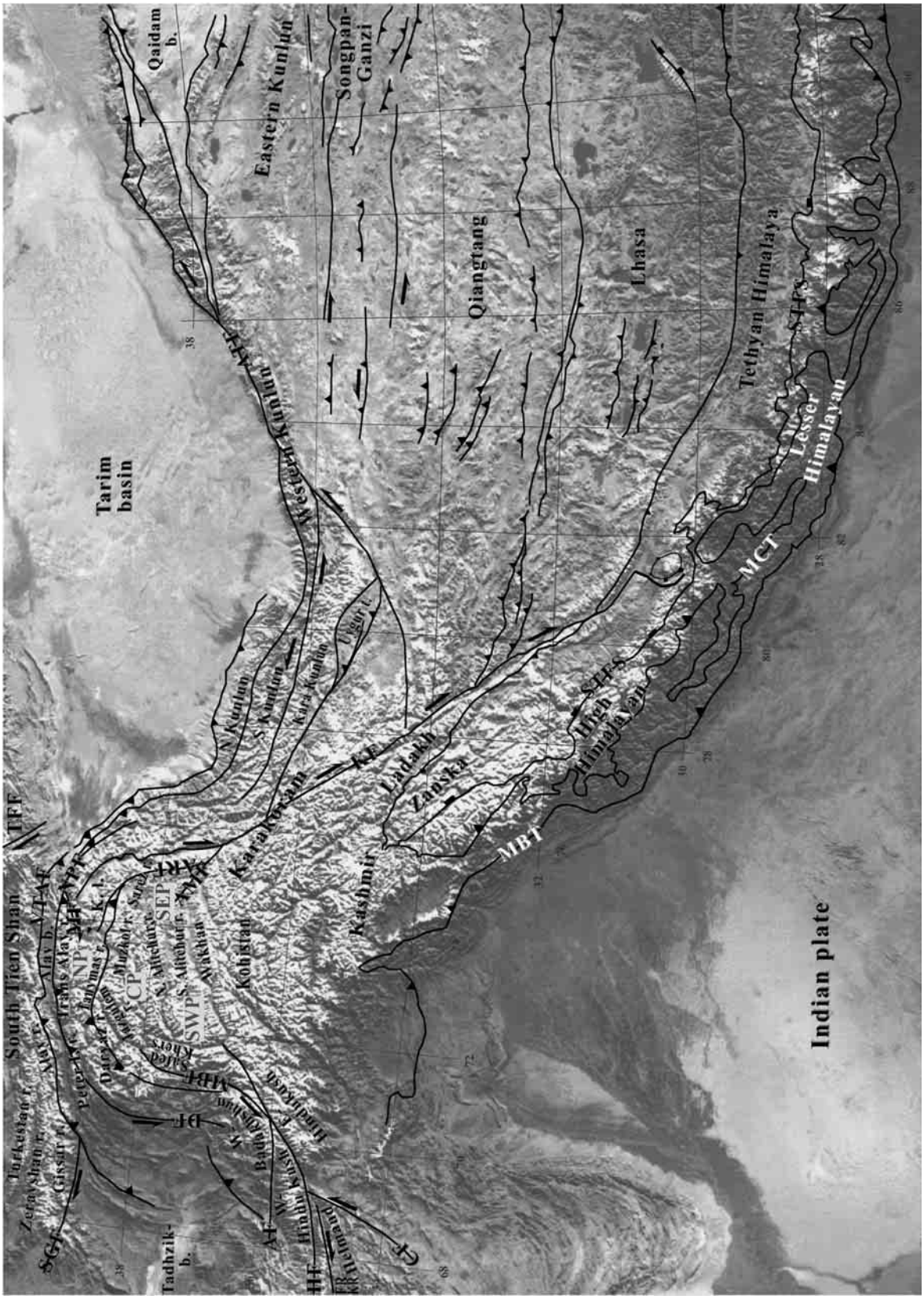
Qaidam b.
Eastern Kunlun
Songpan-Ganzi
Tarim basin
Western Kunlun
Qiangtang
Lhasa
Tethyan Himalaya
STFS
Lesser Himalayan
MCT
MBT
Indian plate
South Tien Shan
TFF
Turkestan r.
Zeravshan r.
Gissar r.
Alay b.
ATAF
Trans Ala
Peter the
Darvaz f.
Muzkol r.
Karakul
Altyn
Altyn
Kohistan
Karakoram
KF
Ladakh
Zanska
Kashmir
Ulrch
Himalayan
Tadhzik-b.
HF
Hindu Kush
Badakhshan
Wakhan
SWP
SEP
MBT
DF
Khots
Alfoc
Kyrgyzstan
Tajikistan
Afghanistan
Pakistan
China
India

Two Palaeozoic sutures divide the Chinese Tien Shan into three tectonic entities: the South Tien Shan (STS), Yili-Central Tien Shan (YCTS), and North Tien Shan (NTS) (e.g., Windley et al. 1990, Allen et al. 1993). From the Late Ordovician to the Early Carboniferous, the STS documents the evolution of an oceanic basin, established between the passive N-Tarim continental margin and the active STS margin. The STS ocean subducted towards the north underneath the YCTS and created an island arc with volcanic rocks of Late Silurian to Early Carboniferous age. Palaeozoic high T/P and high P/T metamorphic belts with syncollisional granites formed on the southern side of the YCTS block (Gao et al. 1995). The YCTS consists of Precambrian basement and was separated from the Junggar plate in the north by the Late Cambrian to Early Carboniferous palaeo-Junggar ocean, which is suggested by the rock associations of the NTS and the Junggar and Turpan basins (e.g., Carroll et al. 1990). This ocean was subducted southward under the northern margin of the YCTS where early Palaeozoic island arc volcanic rocks and granitoids occur (Chen et al. 1985, Hopson et al. 1989, Allen et al. 1993). The closure of the Junggar ocean was in Late Carboniferous time (e.g., Carroll et al. 1990). The NTS is dominated by Devonian to Carboniferous calc-alkaline volcanic rocks, deep marine volcanogenic sedimentary rocks, and scattered ultramafic rocks and radiolarian cherts.

The western segment of the South Tien Shan is part of the Gissar-, Zeravshan-, and Turkestan-Alay ranges (Fig. 3.1 and 3.2) and consists mainly of Palaeozoic sedimentary strata, Precambrian basement, remnants of oceanic crust, and volcanic arcs. Here, a Silurian to Lower or Middle Devonian calc-alkaline volcanic arc developed during the successive closure of an Early Palaeozoic ocean basin (Turkestan ocean) (Brookfield 2000). Further to the south, adjacent to the Tadzhik basin, Brookfield (2000) reported a second island arc of Early Carboniferous age. He suggested that the so-called Gissar island arc had been active only for the short time period of the Early Carboniferous and thus the Gissar basin, which was subducted northward along the Gissar arc, could have been only a very small basin.

No post-Palaeozoic igneous rocks are found in the Tien Shan and north of it. South of the Tien Shan, in the Tadzhik depression, Leith (1982) documented a south-facing mainly Mesozoic passive continental margin.

The South Tien Shan (STS) is separated from the Pamirs by the Alay basin. Currently, this basin being closed from W to E by an anticlockwise rotation of India against Eurasia (Le Pichon et al. 1992). The Alay basin developed from a foreland basin of the rising Pamir orogen to an intramontane molasse basin.

Fig. 3.1: Raised relief and tectonic map of Afghanistan, the Pamirs, and Tibet with local physiogeographic units from which the names of most structural units are derived. r. = range, b. = basin, NP = North Pamirs, CP = Central Pamirs, SWP = south-west Pamirs, SEP = south-east Pamirs, CF = Chaiman fault, KR = Khash Rud, FR = Fahrah Rud, HF = Herat fault, AF = Andarab fault, DF = Darvaz fault, MBF = Middle Badakshan fault, SGF = South Gissar fault, VTAF = Vaksh-Trans-Alay fault, NPF = North Pamir fault, MF = Markansu fault, TFF = Talasso-Ferghana fault, ARF = Aksu-Rankul fault, AMF = Aksu-Murgab fault, KF = Karakorum fault, ATF = Altyntagh fault, MBT = Main boundary fault, MCT = Main Central Thrust, STFS = South Tibetan fault system.

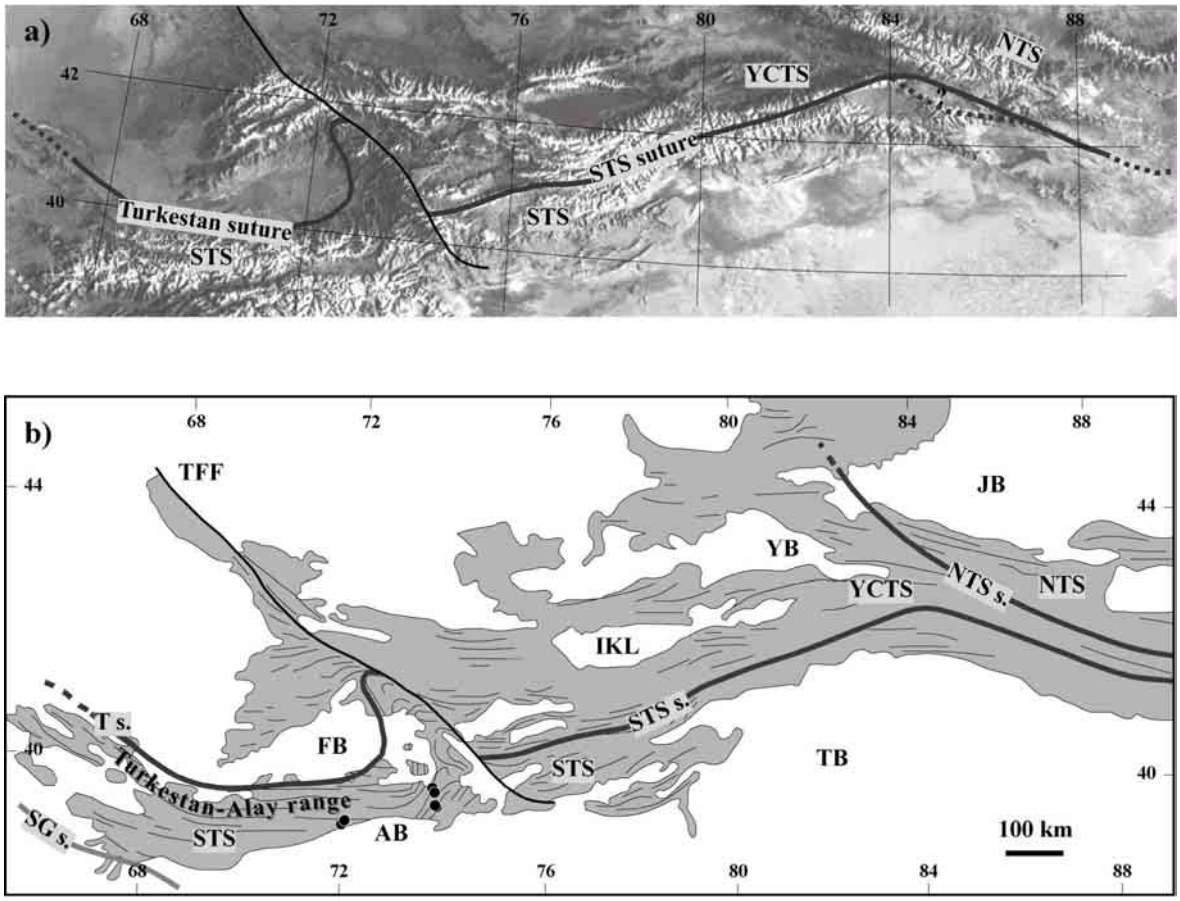

Fig. 3.2: a) Satellite image of the Tien Shan region and northern Tarim margin. b) Outline of the Palaeozoic Tien Shan orogen (modified after Bazhenov et al. 1999) with tectonic units, sutures, strike lines, and sample locations (dots). Abbreviations are as follows: STS = South Tien Shan, YCTS = Yili-Central Tien Shan, NTS = North Tien Shan, TFF = Talasso Ferghana fault, FB = Ferghana basin, AB = Alay basin, YB = Yili basin, JB = Junggar basin, TB = Tarim basin, IKL = Issyk-Kul lake, T s. = Turkestan suture, SG s. = South Gissar suture.

Northern Pamirs

A model from Burtman & Molnar (1993) comprises three east-west trending suture zones in the Pamirs defining the margins of three individual terranes: the Northern, Central, and Southern Pamirs (Fig. 3.1). The following description of the units and the data presentation follows this division. Deformation in these main tectonic belts of the Pamirs occurred in the Late Palaeozoic, Late Mesozoic and Cenozoic (Burtman & Molnar 1993).

The Northern Pamirs are composed of different tectonic subunits: the northernmost external part of the Pamirs comprises imbricated Palaeozoic metasedimentary and metavolcanic rocks, as well as Mesozoic and Cenozoic sedimentary strata. Along this northern orogenic front the Pamirs as a whole are translated northward with respect to Eurasia. This is indicated by seismic activity at the active Main Pamir fault, the northward propagation of thrusting and the progressive annihilation of the intramontane Alay basin (Strecker et al. 1995b). A micro-continent with Proterozoic basement is documented in the north-western part of the northern Pamirs. On the northern rim, this basement is locally overlain from an Early to Middle Carboniferous

igneous and sedimentary rock sequence deposited in an oceanic environment (Geological map of Tadzhik SSR 1983, Ruzhentsev and Shvol'mann 1982). This cover encloses volcanic rocks (Burtman & Molnar 1993), which are unconformably overlain by flysch-greywacke sequences of Middle to Upper Carboniferous and Permian age. All strata were deformed in the latest Palaeozoic, during the closure of the Palaeotethys.
The southern subzone consists predominantly of Late Palaeozoic flysch and molasse sediments and a narrow band of Middle to Upper Triassic basaltic andesites belonging to a calc-alkaline series (Burtman & Molnar 1993). These volcanic rocks unconformably overlie the Palaeozoic rocks. In the Lake Karakul area large batholiths of Triassic age are widespread. This area represents a large depression dominantly filled with Quaternary lacustrine and glacial deposits (Strecker et al. 1995b). In the eastern part of the Northern Pamirs, the active Markansu fault in the north and the Aksu-Rangkul fault in the south document dextral strike-slip; intervening is the rift structure of the Karakul area. In the southern part of the Northern Pamirs thrust faults are south vergent. This southern margin of the Northern Pamirs documents the Late Palaeozoic accretion of the Central Pamirs (Burtman & Molnar 1993). Neither the exact closing time of the suture nor an intervening oceanic basin are well constrained. Based on oceanic rock assemblages, the Late Palaeozoic suture can be traced from the southern margin of the Northern Pamirs, where it is called Tanymas suture, into the northern Hindu Kush in Afghanistan, and into the Kunlun in Tibet (Burtman & Molnar 1993).

Central Pamirs, Rushan Pshart Zone, and South Pamirs

The Late Palaeozoic and Mesozoic history of the Central Pamirs, Rushan Pshart zone (RPZ), and of the South Pamirs (Fig. 1.1 and 3.1) has been much debated. In tectonic and palaeogeographic reconstructions, Karapetov et al. (1975), Shvol´man (1978), Pashkov & Shvol´man (1979) and Shvol´man & Pashkov (1986) interpret the RPZ as a major tectonic suture extending into Afghanistan and Tibet, and marking the consumption of a Permo-Triassic ocean that closed during the Jurassic. In some palaeotectonic reconstructions, the oceanic basin is thought to have been more than 2000 km wide in the Triassic (Sengör 1990).
Burtman & Molnar (1993) pointed out that the Khas Rud ophiolite in Afghanistan is likely an equivalent of the RPZ. Late Palaeozoic to Mesozoic sedimentary sequences of the Farah Rud basin in Afghanistan were apparently deposited on a passive continental margin and can be correlated to sequences near the southern edge of the Central Pamirs. The eastward continuation of the Farah Rud and RPZ to Tibet is more problematic: two ophiolite belts are commonly interpreted as Mesozoic sutures in Central Tibet. One lies south of the Kunlun mountains (e.g. Pearce & Deng 1988, Sengör 1984) extending to north-eastern Tibet. The other one is the Banggong suture (e.g. Matte et al. 1992) in western Tibet. Burtman & Molnar (1993) aligned the west Kunlun suture with the RPZ and the Banggong suture with the Shyok suture. The Shyok and Indus-Tsangpo ophiolite belts mark the suture between India and Eurasia and intervening island arcs; in latest Mesozoic the Karakoram, Kohistan and Ladakh were incorporated and in early Cenozoic time India was involved (e.g., Petterson & Windley 1985, Coward et al. 1987).

In detail, the Central Pamirs are only about 50 km wide and consist of units, the description and dating of which have varied significantly: Burtman & Molnar (1993) describe shallow water siliciclastic and carbonate sequences of Late Palaeozoic to Jurassic age, which suggest the presence of a platform or passive continental margin. In most areas Cretaceous and Palaeogene sedimentary rocks were deposited conformably. In some areas the sequence is nearly complete from the Late Carboniferous to the Paleogene, but in others Late Jurassic and Early Cretaceous rocks are missing (Ruzhentsev 1970). Ruzhentsev (1970) describes a local unconformity with Late Cretaceous limestones above intensely folded Triassic and Jurassic sandstones and slates in the Muzkol range. However, there is no evidence for large thrusts between Late Carboniferous and Palaeogene time. Leven (1995) documented the Upper Triassic/Lower Jurassic Vomar Formation, which reflects continental to coastal marine conditions.

Whereas Pashkov & Shvol´man (1979) suggested the existence of an oceanic basin between the south-eastern Pamirs and the East Pshart zone (a subunit of the Rushan Pshart zone, Fig. 3.3), Leven (1995) concluded that the Permo-Triassic volcano-sedimentary sequences in the East Pshart zone are related to rifting processes between the West Pshart and the East Pshart zones. Thereby the passive continental margin successions of the West Pshart correlates with the Central Pamirs, whereas the East Pshart corresponds to the south-eastern Pamirs. Gaetani (1997) suggested that sedimentary cycles of the Karakoram might be analogous to those of the Central and south-eastern Pamirs. Furthermore, except for the Cretaceous there are similarities between the Karakoram and eastern Hindu Kush. Gaetani (1997) described successions of the Central Pamirs composed of Cambrian to Middle Carboniferous strata unconformably overlain by the usually well represented ?Late Carboniferous-Early Permian to Middle Triassic marine cycle. Predominantly terrigenous rocks, including conglomerates of Late Triassic to early Jurassic age follow. In the southeastern Pamirs, the oldest rocks are of ?Late Carboniferous to Early Permian age indicating a rifting episode in the earliest Permian (Grunt & Novikov 1994, Gaetani 1995). Montenat et al. (1986), Girardeau et al. (1989), Sengör (1990), Brookfield (1993) and Stampfli & Pillevuit (1993) considered the ocean that formed during this rifting period as the link between the Waser-Panjao ocean, which opened in Central Afghanistan north of the Helmand Block, and the Banggong-Nujiang ocean which opened north of the Lhasa Block in Tibet (Girardeau et al. 1984). This seaway closed during the Late Triassic. Gaetani (1997) interpreted the Alitchur Mountain region between the south-western and south-eastern Pamirs (Fig. 3.1) to be the collision zone between two blocks within the western extension of the composite Lhasa terrane. This is evidenced by a Upper Triassic flysch in the Alitchur and marginal south-eastern Pamirs (Norin 1976, Dronov & Leven 1990), which is separated from underlying Permo-Triassic basinal sediments by an angular unconformity, furthermore by the existence of Late Triassic granitoids in this area (Budanov 1990) and by a gabbro-harzburgite complex described by Shvol´man & Pashkov (1986) and Shvol´man (1980).

Also Kravchenko (1979) saw a close relationship between the Central Pamirs and parts of the Rushan Pshart zone (RPZ) and the southeastern Pamirs during the Permian and Triassic time as these regions recorded a rifting phase from Carboniferous to Middle

Triassic and the formation of an island arc in the Late Triassic-Jurassic. According to Kravchenko (1979) flysch, andesites, gabbro and plagiogranite intrusions represent the island arc, whereas molasse deposits and granite intrusions associated with weak folding document major activity during the Late Jurassic and Early Cretaceous.
In the eastern Central Pamirs Precambrian basement rocks are exposed in the E-W striking Muzkol- and Sares antiforms. The intensity and age of the tectonothermal history and associated granite intrusions of the basement remain unclear.
From the above it becomes clear that there is a strong need for a better defined age zonation and geochemical classification of magmatic belts in the Pamirs. In a N-S profile across the Pamirs only the Shyok suture is better constrained by geochemical and geochronological studies (e.g. Fraser et al. 2001, Rolland et al. 2000).

3.3 Petrology and geochemistry

The following part deals with the typology of the studied plutons, particularly with regards to their geochemical and petrological aspects. New own data help to characterise the magmatic belts and to constrain their first-order setting. Published data from the Tien Shan, Afghanistan and Tibet will be included into the interpretations of the geotectonic setting. The sample locations (Fig. 3.3) are summarised in Appendix A, Tab. A1.

3.3.1 Petrology

Southernmost Tien Shan

Six samples collected at four localities (Fig. 3.2 and 3.3) comprise plutonic or subvolcanic rocks of granitic and dioritic compositions (Appendix A, Tab. A2). The samples intruded into Lower to Middle Carboniferous host rocks. Samples TS12a, TS12b, TS18a, and TS20a contain amphiboles, which are in the latter two samples intergrown with biotites and/or clinopyroxenes. Some biotites show chloritisation and feldspar is partly sericitized. Accessory minerals are apatite, zircon and opaque phases. Calcite is abundant in some samples as a secondary mineral. Widespread fault- and thrust tectonics caused cataclastic to weakly ductile deformation and mineral alteration in samples TS1, TS12b and TS20a.

North Pamirs (NP)

Two sections in the Northern Pamirs have been examined: (1) a N-S transect along the Altyndara valley in the external part of the Pamirs and (2) around the Karakul lake in the north-eastern part of the North Pamirs (Fig. 3.3 and 3.4).

Altyndara valley

The stratigraphically lowermost rocks of Carboniferous age are distributed in the southern part of the Altyndara section. Massive metavolcanic successions predominate. These subalkaline series range from basaltic to rhyolitic in composition (Appendix A, Tab. A2). The Carboniferous rocks are progressively deformed towards the north. The volcanic rocks are metamorphosed under greenschist facies conditions and intercalated with clastic sedimentary layers. The middle part of the section is dominated by Mesozoic clastic and carbonate rocks with a major mylonitic zone, where

Palaeozoic units are thrust northward over Mesozoic rocks. Into the Mesozoic units volcanic rocks of unknown age are intercalated, but it is not clear if they are in stratigraphic or tectonic contact The northern part of the section is composed of Tertiary units and comprises the so-called North Pamir Fault, an active thrust front over the Eurasian plate, that steeply dips southward. The collected samples comprise either metavolcanics, volcanoclastic or clastic metasediments. Ten metavolcanic whole rock samples were geochemically analysed and the geotectonic setting was interpreted. Most of the samples revealed deformed textures and altered mineral compositions. Acidic metavolcanic rocks show a foliated texture with micro-quartzitic matrix, large K-feldspar and plagioclase phenocrysts. Some feldspars portray weak sericitisation and strain shadows. Biotites are often chloritised.

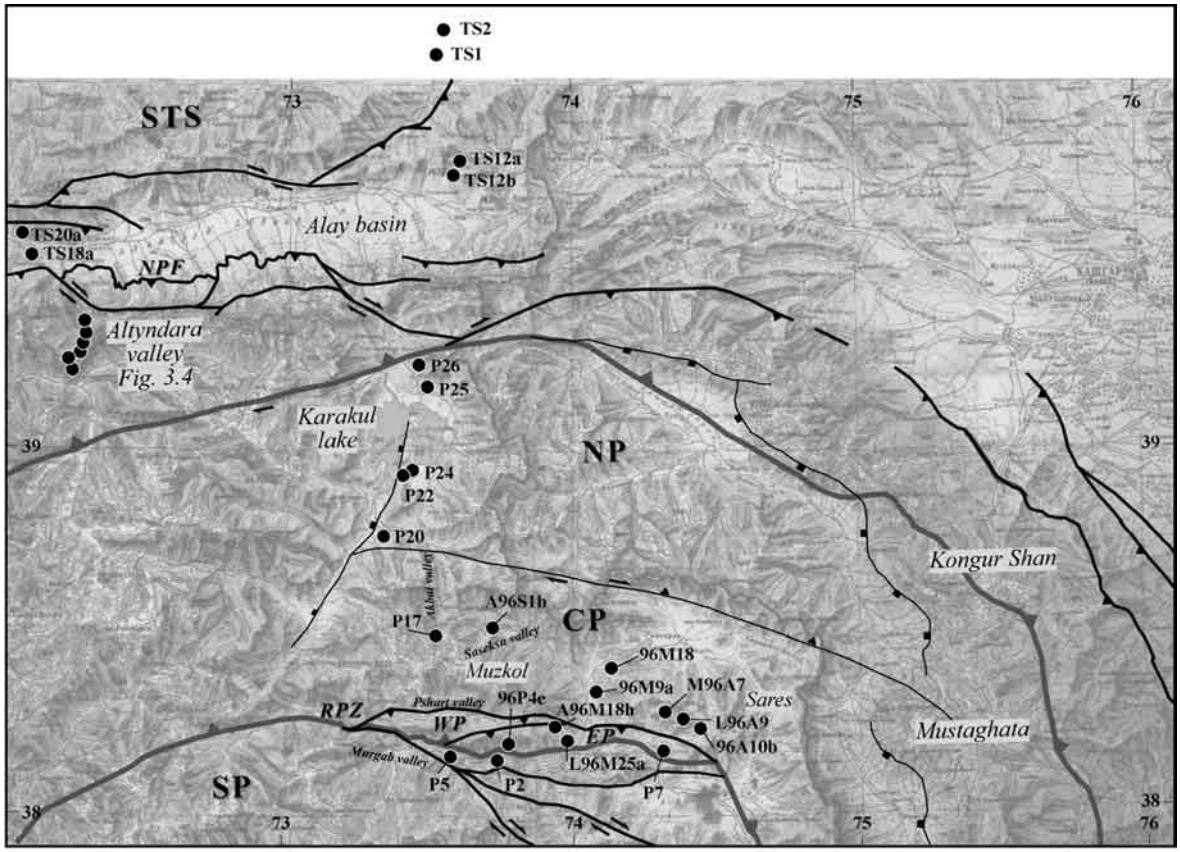

Fig. 3.3: Topographic map of the southernmost Tien Shan and eastern Pamirs with main faults in black, main sutures in bold grey lines and the sample locations as black dots. NPF = North Pamir fault, STS = South Tien Shan, NP = North Pamirs, CP = Central Pamirs, SP = South Pamirs, RPZ = Rushan Pshart Zone (following Burtman & Molnar 1993), WP = West , EP = East Pshart (according to Leven 1995).

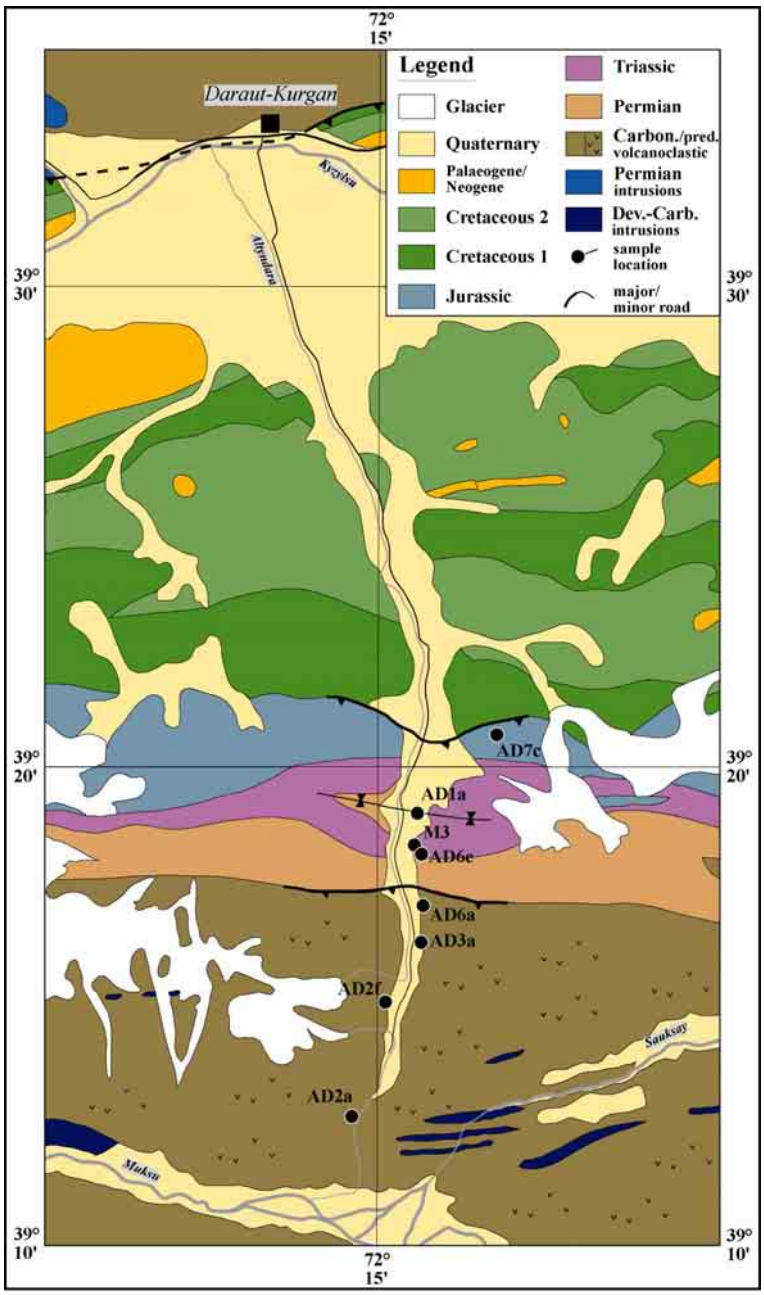

Fig. 3.4: Geological map of the Altyndara valley with sample locations, main stratigraphical units and structures.

Lake Karakul

The Lake Karakul area (Fig. 3.3) is dominated by an east-west trending belt of undeformed granodiorites and monzonites-granites. The granitoids intruded into Carboniferous to Permian metaclastic and meta-volcanic rocks, locally accompanied by gabbroic intrusives. The granite samples are either two-mica granites (P20) or biotite granites (P22, P24, P25 and P26) with zoned plagioclase, K-feldspars and in some samples epidote.

Central Pamirs (CP) and Rushan Pshart Zone (RPZ)

The basement of the Central Pamirs consists of highly deformed, middle to high grade metamorphic rocks, interpreted to constitute another Precambrian-Palaeozoic continental fragment that collided with Asia probably in the Permian (Burtman & Molnar 1993). The central and eastern part of the Central Pamirs are structurally occupied by the Muzkol- and Sares domes, which are interpreted as Precambrian antiforms by Russian geologists. Most parts of the antiforms consist of monotonous biotite-gneisses and amphibolites, which are intruded along their southern margin by small bodies of gabbroic and dioritic rocks. The basement is structurally overlain by metamorphosed and deformed Palaeozoic siliciclastic and Triassic to Jurassic platform-type clastic and carbonate rocks. Based on previous studies (e.g., Ratschbacher et al. 1996, 1997; Ratschbacher & Schwab 1999, Schwab et al. 1997) and new data it is concluded, that the domes are a Tertiary feature. In the Central Pamirs and the Rushan Pshart zone, magma series of different ages and types are widely distributed (Fig. 3.3). The following samples were examined:

(1) P17, an undeformed aplite dike, crops out along the northern margin of the Muzkol dome and cuts high-grade, locally migmatitic basement biotite-gneiss and Early Cretaceous non-metamorphic red beds.
(2) A series of Late Cretaceous, probably Early Tertiary intrusive bodies crops out along the northern margin of the Muzkol dome. One sample (A96S1b) is a subalkaline to alkaline subvolcanic latite-andesite with actinolithe, clinopyroxene, plagioclase, K-feldspar and relatively little quartz.
(3) In the easternmost part of the Muzkol dome several small gabbro-bodies intrude basement biotite-gneisses. Sample 96M9a is a leucogabbro with a considerable amount of alkali-feldspar with perthitic segregation and primary magmatic plagioclase, which is replaced by epidote and a second generation of plagioclase. Epidote is overgrown by vesuvianite (idocrase) and both minerals are graphically intergrown with plagioclase. Accessory minerals are titanite and high amounts of zircon. Titanite contains some grains of rutile. Green biotite and amphibole are sometimes intergrown, and biotite encloses apatite. In summary, the leucogabbro represents a highly fractionated late-magmatic intrusion, metamorphosed under amphibolite facies or probably under high-pressure conditions (rutile).
(4) Sample 96M18a is from a fine-grained clastic layer within massive dolomites of likely Silurian age cropping out along the northern margin of the Muzkol and Sares domes.
(5) At the junction of the Pshart- and Murgab valleys a further granite intrusion is exposed. Sample L96M25a is a biotite-granite with chloritised biotite, sericitised K-feldspar, microcline and weakly deformed quartz, intruding a possible Permo-Triassic meta-volcaniclastic sequence.
(6) Further to the west in the Pshart valley, a granitoid pebble (96P4e) from a likely Miocene intramontane basin conglomerate is determined as a slightly deformed two-mica granite.
(7) At the northern side of the Pshart valley, a ?Carboniferous chlorite-muscovite-staurolite-garnet schist (A96M18h) was sampled at the base of the Permo-Triassic sequence.
Along the northern margin of the Aksu valley occurs a W-E to NW-SE striking belt of granites: (8) sample L96A9 is a biotite granite intruding a possible Early to Late Palaeozoic sequence west of the Sares dome, (9) sample P7 is a white mica granite, and (10) M96A7 a two-mica granite that intruded into likely Palaeozoic sequence or Jurassic rocks.
(11) A very small intrusive granitoid was sampled in the south-eastern part of the Aksu valley (96A10b) that was determined to be a biotite granite.

Northernmost South Pamirs

In the northern part of the south-east Pamirs, a series of granites and granodiorites intrude Late Palaeozoic to Jurassic rocks in blocks rimmed by Cenozoic dextral transpressional faults. These blocks were thrust northward onto the Rushan Pshart zone, north-west of Murgab. Two granodioritic intrusions (P2 and P5) were sampled in the Murgab valley, where they cut a passive margin sequence of Late Palaeozoic to Jurassic age.

3.3.2 Major and trace elements

Major and trace element concentrations of all samples are compiled in Appendix A, Tab. A2. Plutonic rocks of the South Tien Shan (STS) were identified as monzogranites, and the subvolcanic rocks as granodiorites (Fig. 3.5a). Metavolcanic rocks of the northern Pamirs (Altyndara valley) have basaltic to rhyolitic compositions, batholiths of the Lake Karakul area are monzogranites and granodiorites, whereas most plutons of the Central Pamirs (CP) and the Rushan Pshart Zone (RPZ) are monzogranites. Further sampled rock types in the Central Pamirs are a leucogabbro (96M9a) and a latite-andesite (A96S1b).

Igneous rocks from the STS belong to sub-alkaline respectively high-K calc-alkaline, mainly peraluminous I-types (Fig. 3.5b, h), and only the northernmost sampled rocks TS1 and TS2 are transitional to S-type series. The latter two samples imply a higher degree of crustal contamination as indicated by the lack of hornblende, more K-feldspar megacrysts, and the higher A/CNK ratio and SiO_2 content (Fig. 3.5b). All rock samples are interpreted as volcanic arc related (Fig. 3.5f-i), but with probably more fractionated rock types to the northeast. Chondrite-normalised rare earth element (REE) patterns of the South Tien Shan samples (Fig. 3.6a) show strong fractionation of the LREE (La_N/Sm_N = 4-6) and only a weak negative Eu-anomaly (Eu* was determined from interpolation of REE patterns between Sm and Tb). The HREE are most fractionated in samples TS12a,b and less fractionated in the subvolcanic rock samples TS18a, TS20a.

The North Pamirs metavolcanic rocks from the Altyndara valley have low- to medium-K character (Fig. 3.5c) and are metaluminous (Fig. 3.5b). Although all samples show a clearly calc-alkaline trend (Fig. 3.5d), the basalt samples plot into the MORB field (Fig. 3.5e). The rock-types with MORB affinity were formed in an oceanic or early arc setting, whereas all other samples represent normal volcanic arc rocks (Fig. 3.5f). This is also reflected in the chondrite-normalised REE patterns (Fig. 3.6b): the oceanic or early-arc volcanic rocks show flat, typical MORB patterns; normal arc samples and samples with increasing SiO_2-contents show steeper LREE fractionation patterns. Only the samples AD2a and AD6b display a distinctly negative Eu-anomaly.

The Lake Karakul batholiths are peraluminous, mainly S-type monzogranites (Fig. 3.5b), and have high K-contents. In context with their petrological features, they are classified as post-tectonic granitoids with an arc to late-/post-collisional geochemical signature (Fig. 3.5f-i). The rocks show a consistent strong fractionation from La to Sm and the magnitude of the negative Eu-anomaly (Eu/Eu* = 0.62-0.74) increases with increasing SiO_2-contents (Fig. 3.6b).

The leucogabbro 96M9a (dark grey circle) intrudes schists and gneisses in the eastern part of the Muzkol dome. It has low K-contents (Fig. 3.5c), a metaluminous character (Fig. 3.5b), and seems to be secondarily enriched in SiO_2. The REE pattern is generally enriched with La_N/Lu_N = 20.6 and shows a positive Eu-anomaly (Eu/Eu* = 1.2), probably due to plagioclase enrichment.

The Triassic/Jurassic monzogranites (dark grey circles) are heterogeneous in their major- and trace element contents. Sample L96M25a is a metaluminous I-type monzogranite with high K-contents like the other samples of this group (Fig. 3.5a-c). The rock is interpreted as volcanic arc related (Fig. 3.5f-i) with an overall depletion of HREEs and a weakly negative Eu-anomaly (Fig. 3.6c). The two Jurassic samples L96A9

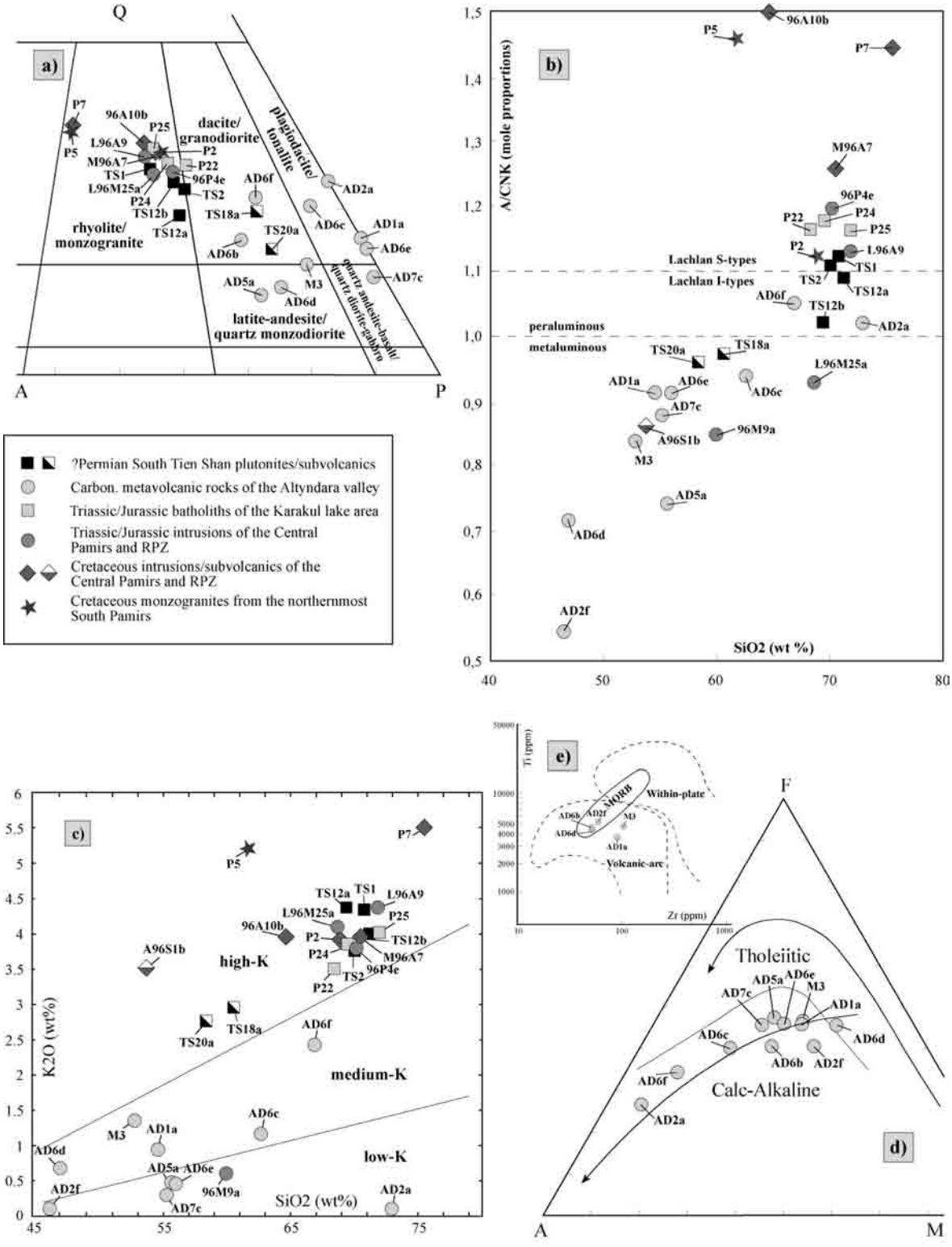

Fig. 3.5: Geochemistry of the magmatic rocks from the South Tien Shan and Pamirs. a) Modal compositions of the plutonic and volcanic rocks with the nomenclature taken from Streckeisen (1976). b) The aluminium saturation index (molar $Al_2O_3/CaO+Na_2O+K_2O$) for all rock samples. c) The subdivision of subalkaline rocks using the K_2O vs silica diagram with the boundary lines after Le Maitre et al. (1989). d) The AFM diagram showing the boundary between the calc-alkaline and tholeiitic field for the metavolcanic rocks from the Altyndara valley, Northern Pamirs, after Irvine & Baragar (1971). Black lines with arrows show typical calc-alkaline and tholeiitic trend lines. e) The discrimination diagram for volcanic-arc basalts, MORB and within-plate basalts based upon the log scale Ti-Zr variations (after Pearce 1982).

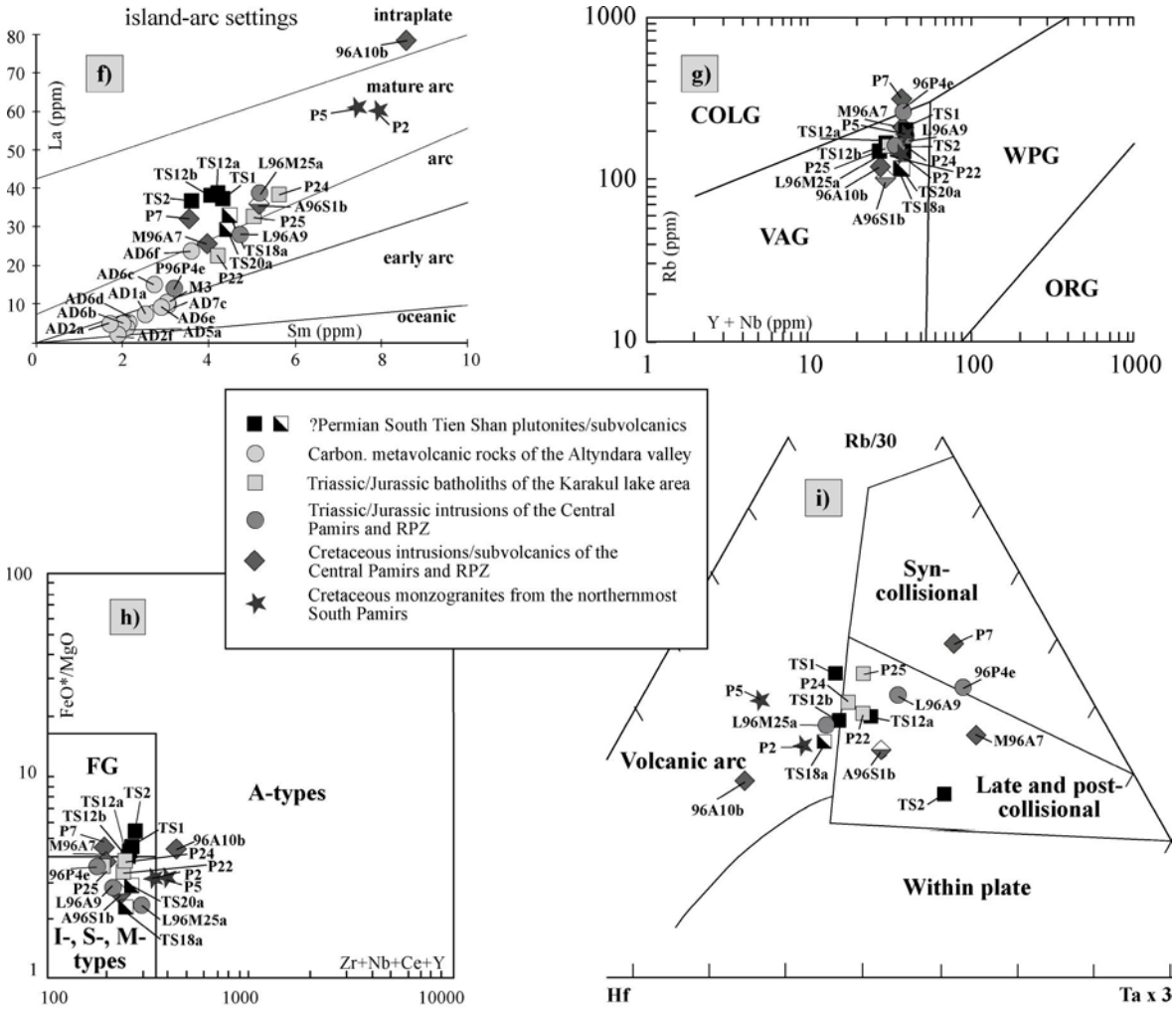

Fig. 3.5 continued: f) A La vs Sm plot used to discriminate the tectonic setting of island-arc rocks. g) A tectonic discrimination diagram for the separation of volcanic arc granites (VAG), collision related granites (COLG), within plate granites (WPG), and ocean ridge granites (ORG) after Pearce et al. (1984). h) Zr+Nb+Ce+Y (ppm) vs FeO/MgO discrimination diagram from Whalen et al. (1987). FG = field for fractionated I-type granitoids. i) The Hf-Rb/30-Tax3 discrimination diagram for granites after Harris et al. (1986), showing the fields for volcanic arc granites, within plate granites, syn-collisional granites, and late to post-collisional granites.*

and 96P4e resemble high-K, peraluminous S-type granitoids (Fig. 3.5b-c). Rb-mobility may cause a transitional position between volcanic arc and collision-related tectonic setting (Fig. 3.5f-i). The rock samples show different degrees of REE enrichment with La_N/Lu_N = 16.7 (L96M25a), 13.0 (96P4e), and 7.8 (L96A9) (Fig. 3.6c).

The Cretaceous monzogranites from the Central Pamirs, RPZ and northernmost South Pamirs are all high-K, highly peraluminous S-type intrusions. There is some diversity in this group, probably due to some element mobility of K and Rb. Nevertheless, some samples are petrologically identified as S-type monzogranites (e.g. the two mica granite P7). The subalkaline to alkaline subvolcanic latite-andesite A96S1b has a metaluminous character (Fig. 3.5a-c). The tectonic classification is heterogeneous from volcanic arc to collisional setting (Fig. 3.5f-i). In chondrite-normalised REE abundance diagrams all samples show a concave-upward pattern with the highest La_N/Lu_N values

of 26-40 for samples P2, P5, and 96A10b. The other two samples M96A7 and P7 have lower REE concentrations of rock/chondrite in respect to the other samples of this group and have a higher negative Eu-anomaly, most likely due to higher plagioclase fractionation. The chondrite-normalised REE pattern of sample A96S1b shows no Eu-anomaly and is comparable to the REE pattern of sample 96M9a. The La_N/Lu_N of the latite-andesite is 13, resembling typical alkaline REE distributions.

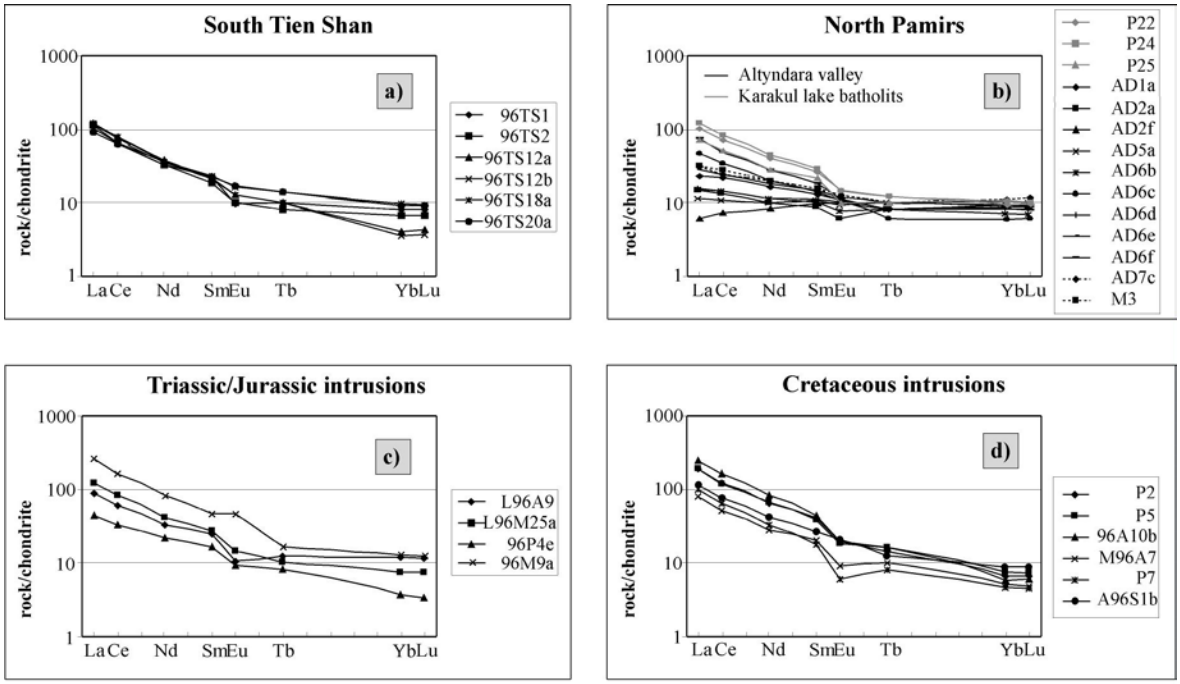

Fig. 3.6: Chondrite-normalised REE abundance patterns (normalised to values given by Masuda et al. 1973) for selected samples from different intrusives from the South Tien Shan (STS) and eastern Pamirs. a) subvolcanic diorites and monzogranites from the STS, b) MORB-type metabasalts, calc-alkaline andesites, dacites, and a rhyolith from the Altyndara valley in black colours; a granodiorite and monzogranites from the Karakul lake batholith are in grey colours, c) Triassic/Jurassic monzogranites from the Central Pamirs and Rushan Pshart Zone and a leucogabbro from the Central Pamirs, and d) Cretaceous monzogranites from the Central Pamirs and Rushan Pshart Zone and a latite-andesite from the Central Pamirs.

3.4 Geochronology

3.4.1 U/Pb isotope dilution, SHRIMP U/Pb and Pb-evaporation zircon ages

The results of U/Pb isotope dilution analyses of 50 single zircon fractions from 15 magmatic rock samples are given in Appendix A, Tab. A7. In average 5-10 zircon grains were analysed per fraction. The radiogenic $^{207}Pb/^{206}Pb$ evaporation method was conducted on 2 single zircon grains of sample 96M9a (Appendix A, Tab. A8). Appendix A, Tab. A9 shows the isotopic ratios of single zircon SHRIMP analyses performed on zircons of 5 different samples. Concordia diagrams with the U/Pb isotopic data, the histogram of the radiogenic $^{207}Pb/^{206}Pb$ ratios obtained by the evaporation method, and weighted mean age diagrams of SHRIMP data are shown in Fig. 3.7.

Northern Pamirs/Altyndara valley

AD2a: From AD2a, the Altyndara metarhyolite, three zircon fractions were analysed. The zircons show elongated magmatic habitus with longer (fraction F1) and smaller prisms (F3 and F5). The zircons are < 200 μm in size, corners are sometimes rounded and many grains are broken. Most grains show magmatic zonation (cathodo-luminescence images, Appendix B, plate B1), but some are also metamict with diffuse internal parts. In some cases embayments can be seen at the outer margin but also at margins of cores. Frequently sector zoning is observable. Based on the external morphology of the zircons, the grains plot in the calc-alkaline and sub-alkaline fields of a Pupin diagram (Pupin 1980). Two data points are concordant at 329 ± 5 Ma, which is interpreted as crystallisation age, and one data point plots above the concordia (Fig. 3.7a).

AD6c: An andesite-dacite sample from the metavolcanic unit of the Altyndara valley has only few and small (80-150 μm) zircons and only one fraction (F2) was dated. The U/Pb isotopic ratios were plotted into the same diagram as sample AD2a (Fig. 3.7a), due to its close association within the same Palaeozoic metavolcano-sedimentary succession. Fraction 2 (AD6c) plots slightly below the concordia close to the fractions of sample AD2a, and it is concluded that AD6c has the same late Early Carboniferous age than AD2a. All fractions from both samples have identical $^{207}Pb/^{235}U$ ages. In cathodoluminescence images (Appendix B, plate B1) these zircons reveal magmatic zoning with low-angle truncations dominating over high-angle truncations. In comparison with sample AD2a, AD6c zircons have only small or no cores. In some zircons magmatic or fluid resorption is visible.

Northern Pamirs/Karakul lake

P26: From the P26 granite three zircon fractions were analysed with the U/Pb isotope dilution method (Fig. 3.7b). This sample yielded ambiguous results. Data are neither concordant nor colinear. One fraction (2b) plots above the concordia, possibly suggesting an analytical problem due to U loss during wet-chemical treatment. Embedding of more common lead into the lattice during zircon alteration could be an alternative explanation. A minimum U/Pb age of about 216 ± 2.0 Ma is suggested. To constrain the age of this sample more precise SHRIMP analyses were performed on 10 single zircon grains. The weighted mean $^{206}Pb/^{238}U$ age is 227.0 ± 4.1 Ma. Most likely

some of the zircons suffered Pb loss after crystallisation, what explains why data points plot below the concordia and the obtained minimum age of 216 ± 2.0 Ma. To evaluate the complexity of this sample, SHRIMP analyses were performed on 12 single zircon grains. Cathodoluminescence images show spectacular, multiple growth and resorption facets; inner grain portions are sometimes metamict (Appendix B, plate B2). No cores have been detected. At several grains core and rim portions were probed but yielded identical ages within error. One grain gave an imprecise Devonian age (~ 400 Ma); the weighted mean of 14 spot ages, excluding the youngest grain (~ 189 Ma), is 227 ± 4.1 Ma (Fig. 3.7c).

P22: Two zircon fractions were analysed from this granite. Cathodoluminescence images (Appendix B, plates B1, B2) of zircons from this sample show grains with a fine magmatic zonation and often large cores, which show also magmatic zonation. Fraction 1 is long prismatic (150-250 μm), colourless and clear. The other fraction (F2) is prismatic and shorter (80-200 μm), also clear but more brownish. In the concordia diagram (Fig. 3.7b) one fraction (F2) lies above the concordia, whereas F1 has a concordant age of about 215 ± 1.5 Ma. Samples P22 and P26 were measured in two different laboratories but show both the phenomena of data points plotting above the concordia. The real reason is unclear, but it is most likely to result in similar Pb diffusion behavior. As all fractions plot on or near the concordia between 200-225 Ma, this age range is interpreted as minimum crystallisation time span for these batholiths.

Central Pamirs/Muzkol dome

P17: Two fractions were available for analyses from this granite (Fig. 3.7d). One fraction (D2) has very small (63-80 μm) zircon grains, the other fraction (DE2) has grains in the range of 80-125 μm. Assuming a simple crystallisation and recent partial Pb loss model for these two fractions the age interpretation is at 531 ± 30 Ma. A better MSWD-value can be obtained assuming a Pb loss around 41 Ma ± 22 Ma with an upper interception age at 539 ± 5 Ma. SHRIMP analyses of 14 grains aimed to probe possible Tertiary rims. The zircons are exceedingly complex internally and inclusion rich (Appendix B, plate B2). Spot ages range from 561 to 424 Ma; no younger rims have been detected. The weighted mean of 14 spot ages, excluding the youngest spot (~ 424 Ma), is 536 ± 18 Ma (Fig. 3.7e).

96M9a: Four fractions were extracted from this sample with big (around 200 μm), euhedral zircons. F1 comprises elongated, brownish-pink zircons, F2 consists of smaller clear and pinkish zircons, F4 has also pinkish medium sized zircons and F5 contains the largest yellow-brownish to pinkish and short prismatic zircons. Many of the zircons show optically dark inclusions. The cathodoluminescence images (Appendix B, plate B2) reveal mainly long prismatic grains with large, well rounded cores. The cores show oscillatory zoning and have embayments likely caused by resorption of inclusions in the igneous melt. Most of the zircons illustrate sector zoning along the prismatic long axis. Many of the grains are fractured but not broken. The four measured fractions are all discordant (Fig. 3.7f). Since F2 has a too low $^{206}Pb/^{204}Pb$ ratio (< 100), the fraction was excluded from the discordia calculation. The fractions F1, F3 and F5 show a linear

arrangement with a lower intercept at 169 +6/-8 Ma and an upper intercept at 828 ± 95 Ma. The lower intercept age is interpreted as minimum age for magmatic crystallisation.
The radiogenic $^{207}Pb/^{206}Pb$ evaporation method was applied on two zircon grains of this sample (Appendix A, Tab. A8, Fig. 3.7g). Both grains yielded identical ages with 231 ± 10 Ma (grain 1, 226 ratios) and 228 ± 10 Ma (grain 2, 260 ratios). Grain 1 was evaporated in two temperature steps and grain 2 in one evaporation step.

Central Pamirs/Rushan Pshart Zone

L96A9: This sample offered five datable zircon fractions (Fig. 3.7h). Fractions F1, F3, and F5 contain clear pinkish zircon grains of different size, whereas F2 and F4 are composed of huge euhedral prismatic grains with a brownish, unclear colour due to internal fractures. All fractions plot below the concordia and no discordia can be drawn through all fractions. In combination with the SHRIMP data (Fig. 3.7i) a meaningful age interpretation is possible by drawing a discordia through the fractions F1, F3 and F5 to get a maximum age estimate for a lower intercept age which is 205 ± 1.9 Ma. A discordia through fractions F1, F2 and F4 results in a minimum age estimate for the lower intercept age which is 179 ± 44 Ma. The latter two fractions show very low $^{206}Pb/^{204}Pb$ ratios of 176.9 (F2) and 129.0 (F4) and therefore might be less reliable for age interpretation. SHRIMP analyses on 12 grains probed core and rim regions and zoning patterns (Appendix B, plate B3). Three cores cover 194-202 Ma and the corresponding rims are between 154-171 Ma. Assuming that an older group of spot ages represents ages typified by these cores, the weighted mean of 13 measurements of this group is 201 ± 4.4 Ma. A younger group, possibly typifying rim ages, is 170 ± 6 Ma; the youngest rim is ~146 Ma, the oldest spot ~217 Ma. In the Pupin-diagram most of the zircon grains plot into the alkaline and peralkaline mantle differentiates, and a minority into the field of hybrid calc-alkaline magmas. The CL images reveal two different types of zircon grains. Some show complete magmatic zoning, sometimes with a resorption phase, others have large inherited cores which are mainly metamict.

L96M25a: The four fractions from this sample plot below the concordia (Fig. 3.7j). A heterogeneous source for this zircons is concluded, followed from the distribution and non linear arrangement of the data points in the concordia plot. The emplacement occurred approximately between 167 and 235 Ma; the lower estimated age was determined with a discordia through fractions F2 and F4 and the upper estimated age with a discordia through fractions F4 and F5. In the Pupin-diagram the fractions plot into the calc-alkaline to subalkaline area. The cathodoluminescence (Appendix B, plate B3) depict long prismatic grains and huge inherited, mainly metamict cores. The zircons have a magmatic zonation which is interrupted by a well rounded resorption rim in most of the grains.

M96A7: The zircons from this sample are most complex ones. Five zircon fractions were determined by the conventional U/Pb dilution method (Fig. 3.7k). Owing to a lack of concordance and colinearity, this sample yielded ambiguous results. Most reliable is a lower intercept age at 131.1 ± 1.6 Ma connecting fractions F2, F3, F4, and F5. As the

fractions are situated close to the lower intercept, the Early Cretaceous age is interpreted as formation age of the zircons with older inherited components. This is confirmed by the CL images, which show zircons with large cores. Sometimes in the cores a second, older core is included. The cores are either metamict or have a magmatic zonation. The older core type is well rounded, whereas the younger core generation shows only abrasion at the corners. Some zircons seem to reveal a younger rim. SHRIMP analyses (Fig. 3.7l) of 24 grains aimed to probe the core types and rims (Appendix B, plate B4). Three different core ages have been detected: one spot yielded 2187 ± 13 Ma, four spots of rounded metamict cores and one weakly zoned inner grain spot range from 250 to 214 Ma (weighted mean 221 ± 24 Ma), and four rounded, metamict (one weakly zone) cores range from 182 to 156 Ma (weighted mean 162 ± 18 Ma). The majority of spots probed spectacularly zoned idiomorphic grains with spot ages ranging from 130 to 104 Ma (weighted mean of 17 spots 113 ± 3.4 Ma); four spots of idiomorphic, well-zoned grains, and outermost idiomorphic rims of grains with cores yielded even younger ages (94 to 77 Ma, weighted mean 90 ± 10 Ma).

96A10b: The sample yielded three zircon fractions for conventional U/Pb dating (Fig. 3.7m). Two of the fractions (F1 and F2) plot on the concordia. As fraction F3 has a very small analytical uncertainty but plots below the concordia, Pb loss can be assumed. This might be also true for fraction F1. No older Pb component seems to be inherited. Only one intercept could be calculated which is interpreted as the crystallisation age at 126 ± 50 Ma.

A96S1b: Six fractions were selected from this subvolcanic latite-andesite (Fig. 3.7n). All fractions consist of small zircons (~63-80 μm). One half is long prismatic, transparent without inclusions. The other half shows transparent whitish to yellowish tabular zircons. Many zircons are broken. Zircons plot into the field of calc-alkaline and subalkaline magma series in the Pupin-diagram. Two fractions (F6 and F7) plot close but above the concordia and fractions F2 and F3 close but below the concordia. These four fractions are interpreted to approximate the crystallisation age, whereas fraction F8 might include inherited cores. Fraction F5 might have lost Pb. The lower intercept age is 74.2 ± 0.7 Ma.

Northernmost South Pamirs

P2: As only one zircon fraction was analysed, which is discordant, no age interpretation could be made (Fig. 3.7o). SHRIMP analyses on 15 zircons (Fig. 3.7p) reveal ages on well rounded cores (Appendix B, plate B4) of about 1624 Ma, 902 Ma, 417 Ma, 355 Ma, and 196 Ma; one 158 Ma spot is from a nodular inner grain portion. 15 spots from rims and multi-faced, idiomorphic grains range from 126 to 102 Ma with a weighted mean age of 117.9 ± 3.7 Ma; one grain is as young as 78 ± 5 Ma.

P5: The two analysed zircon fractions plot close to the lower discordia interception (Fig. 3.7o). Therefore one could choose a simple model of crystallisation with some minor inheritance. Assuming no subsequent Pb loss, the crystallisation age is 74.5 ± 8.8 Ma with Precambrian zircon inheritance (i.e. ~710 Ma). The two fractions of sample P5

plot nearly at the same place in the U/Pb concordia diagram as the fraction from sample P2. Both samples belong to nearby calc-alkaline intrusions in the Murgab valley. Assuming that the weighted mean age of sample P2 is also representative for sample P5, one can conclude from the discordia plot, that both samples (P2 and P5) have inheritance and suffered some Pb loss, as they plot just below the assumed concordia age calculated by the SHRIMP data.

Northern Pamirs

Altyndara valley

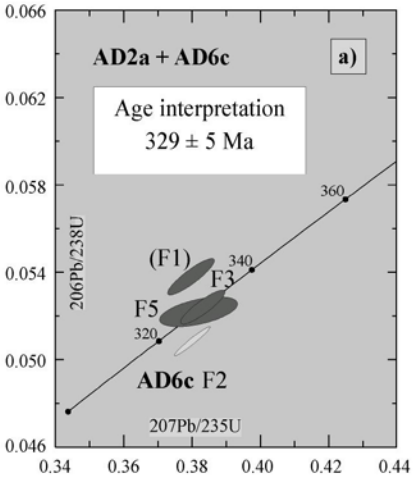

Fig. 3.7a-p: U/Pb dilution, U/Pb SHRIMP and Pb/Pb zircon ages. See Fig. 3.3 for sample locations and Appendix A, Tab. A7 for data listing. Data points in concordia diagrams with sample names in brackets were excluded from age calculation. TIMS results shown with 2σ error ellipses and discordias as thin lines. SHRIMP results plotted in Terra-Wasserburg concordia diagrams uncorrected for common Pb with 1σ error ellipses. Selected age groups of SHRIMP data are displayed as weighted average diagrams.

Karakul lake batholiths

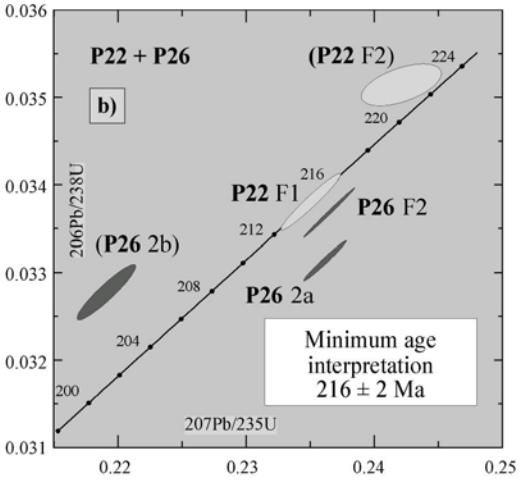

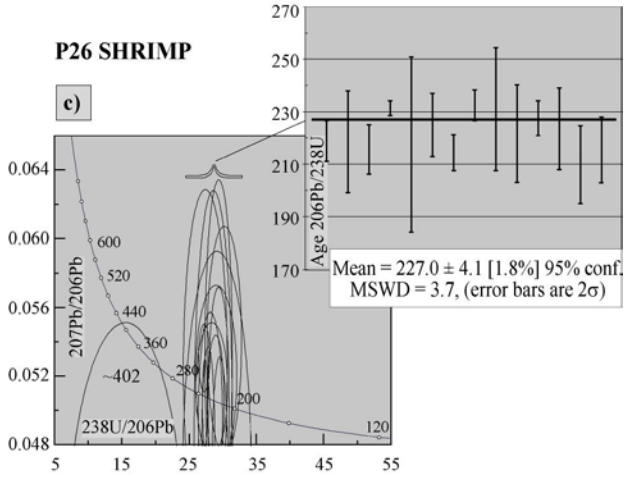

Central Pamirs

Muzkol dome

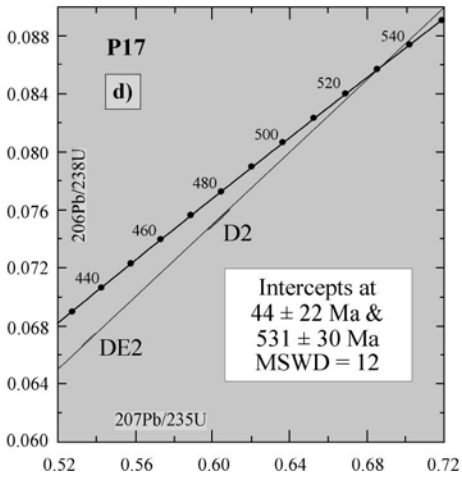

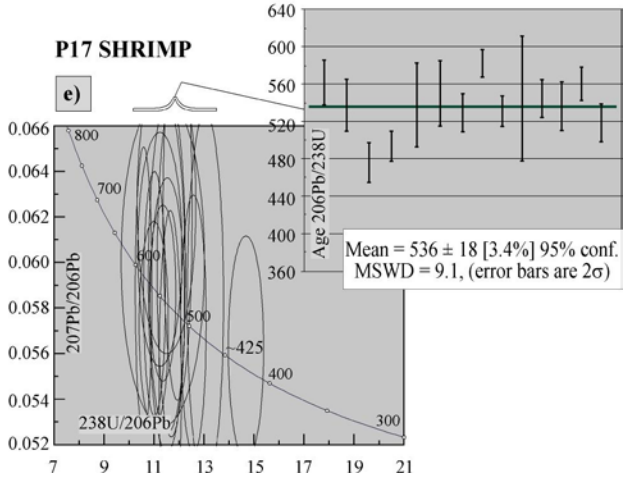

Central Pamirs

Muzkol dome

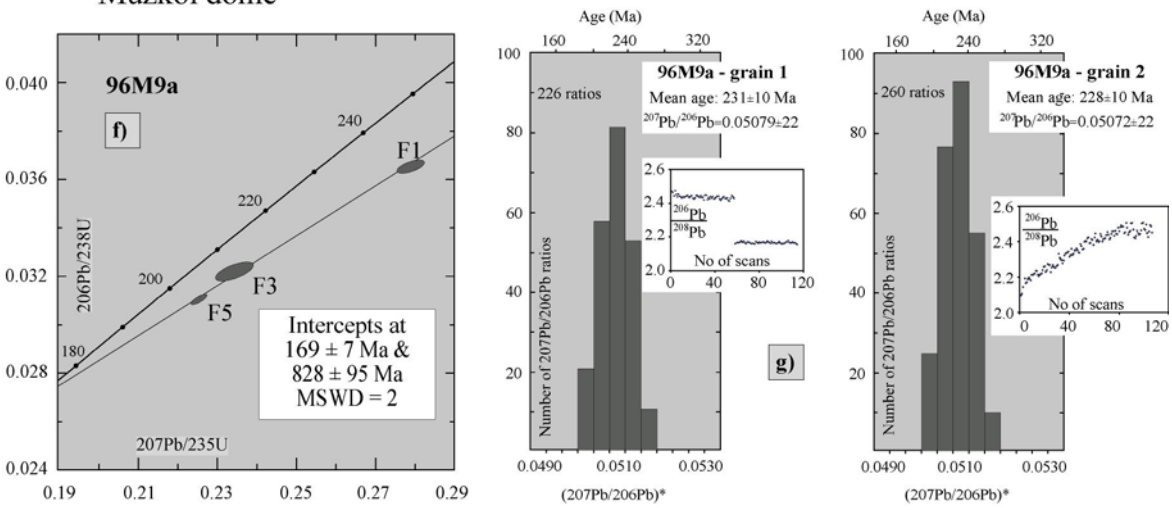

Central Pamirs/Rushan Pshart Zone

Aksu valley

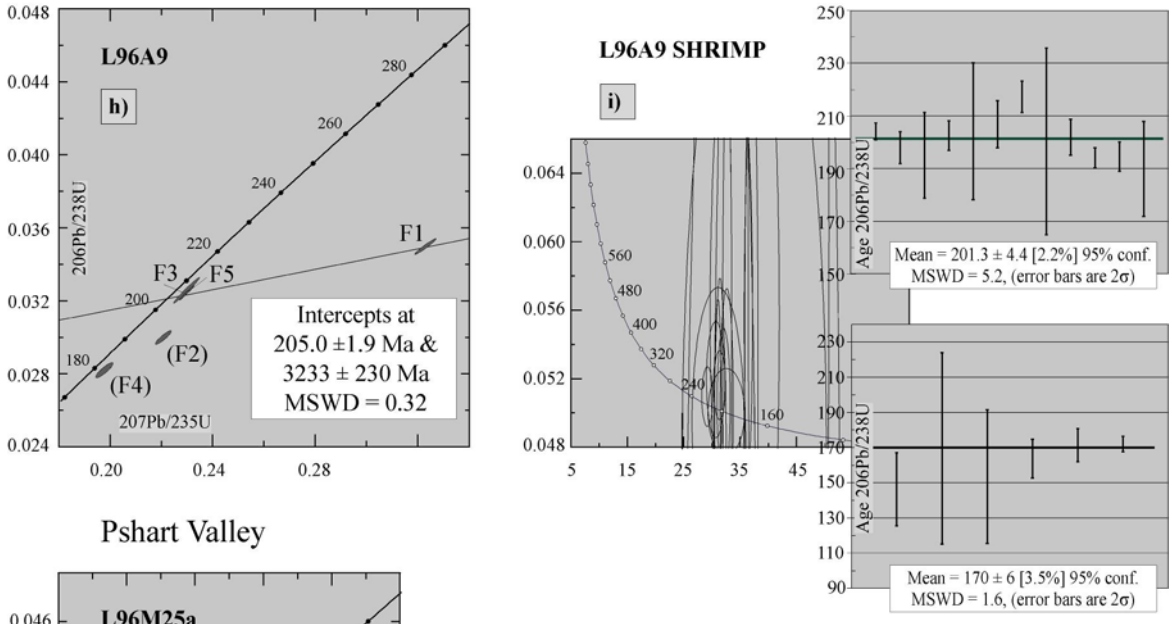

Pshart Valley

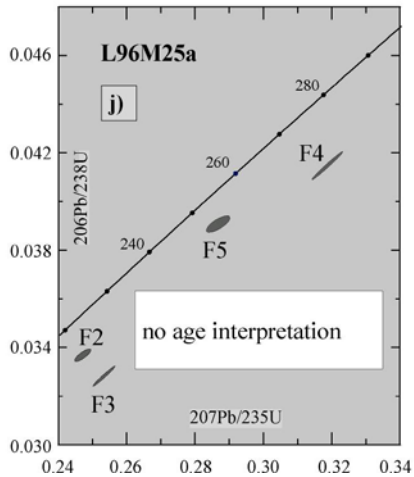

Central Pamirs/Rushan Pshart Zone

Aksu valley

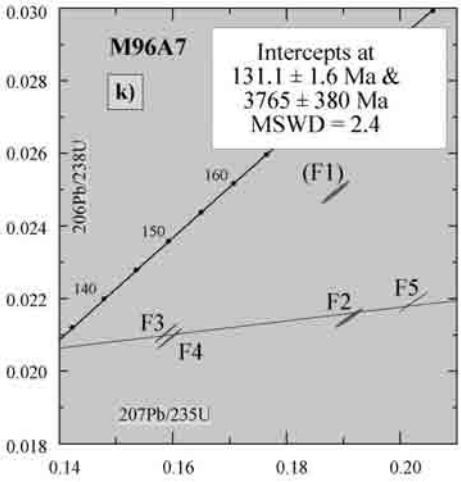

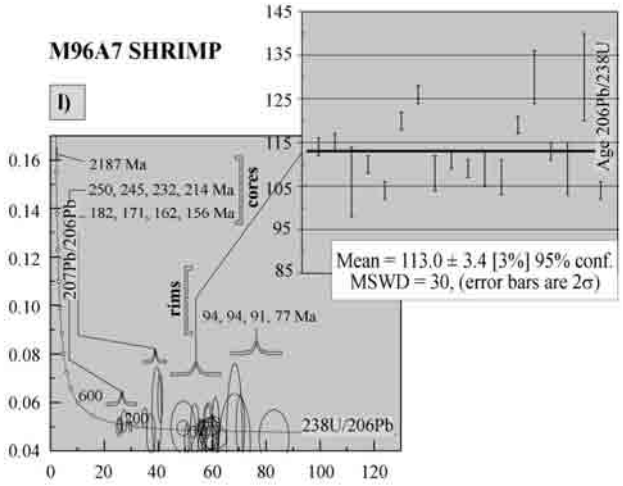

Aksu valley

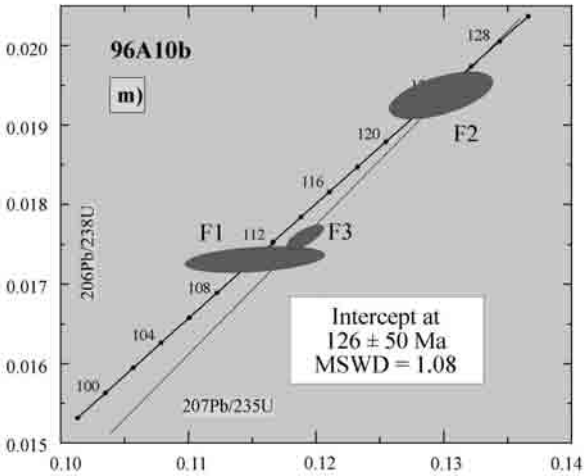

Saseksu valley

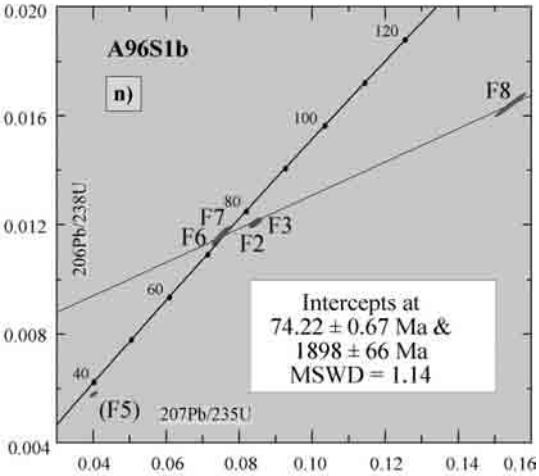

Northernmost South Pamirs

Murgab Valley

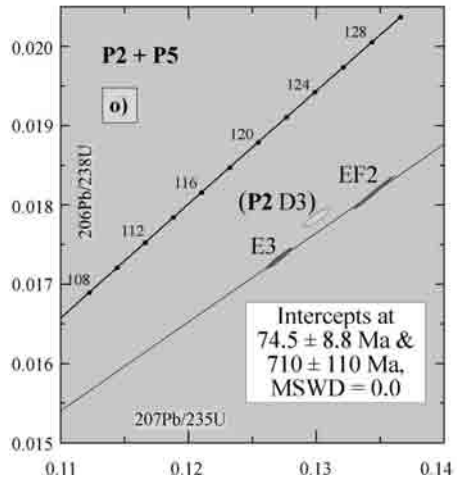

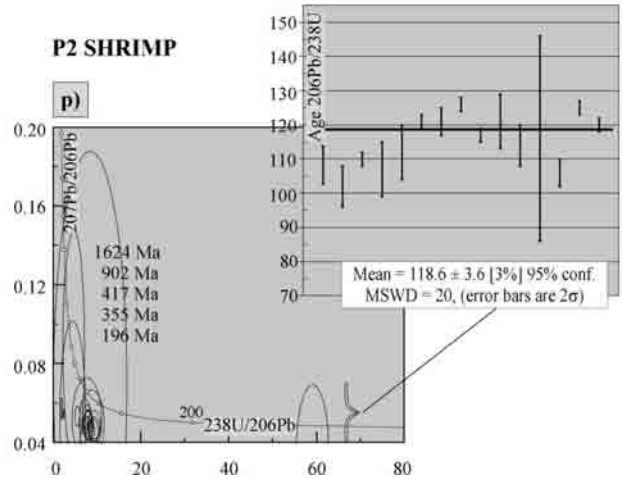

3.4.2 Rb/Sr dating

The Rb/Sr mineral ages of granites and basement rocks were determined by isotope dilution on whole rock samples and muscovites. The data are listed in Appendix A, Tab. A5 and the two-point isochron plots are presented in Fig. 3.8. For sample locations see Fig. 3.3.

The granite sample M96A7 has a late Early Cretaceous Rb/Sr mineral age of 103.6 ± 1.1 Ma (Fig. 3.8a). Also sample P7 yielded a Cretaceous Rb/Sr mineral age of 111.2 ± 1.1 Ma (Fig. 3.8b). Sample 96P4e, the granite pebble from a ?Miocene conglomerate of a Central Pamiran Tertiary intramontane molasse basin (southerly adjacent to the Muzkol dome) yielded a Rb/Sr mineral age of 188.4 ± 1.9 Ma (late Early Jurassic) (Fig. 3.8c).

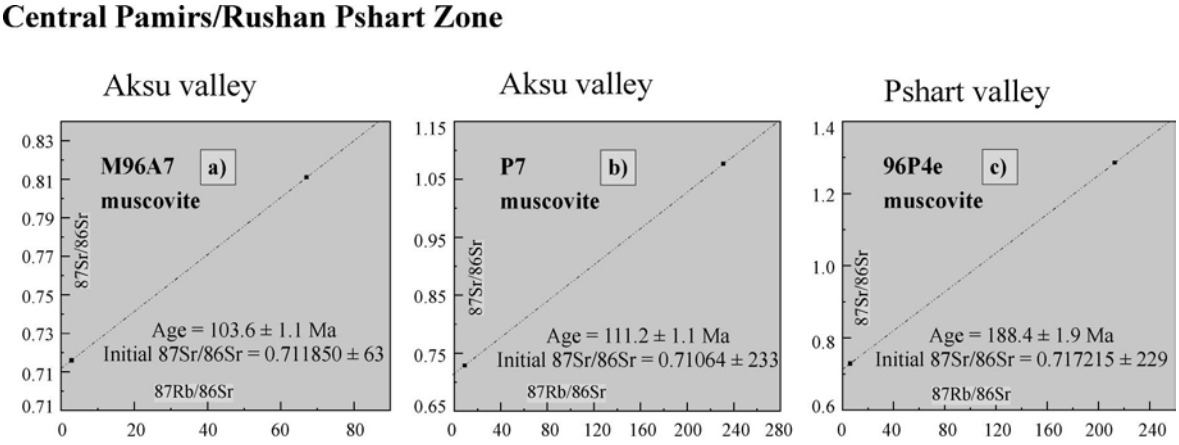

Fig. 3.8a-c: Rb/Sr whole rock-white mica two-point isochron diagrams. See Fig. 3.3 for sample locations and Appendix A, Tab. A5 for data listing.

3.4.3 Ar/Ar dating

The results of Ar/Ar dating are listed in Appendix A, Tab. A3 and the age spectra are depicted in Fig. 3.9. For sample locations see Fig. 3.3.

To assess the age of the STS magmatic rocks $^{40}Ar/^{39}Ar$ biotite cooling ages of samples TS12b and TS20a were obtained (Fig. 3.9a,b). The K/Ca ratio and age spectra of sample TS12b suggest the existence of a composite mineral, eventually by the appearance of chlorite. Both samples gave identical Early Permian ages of 277 Ma, although they are separated by around 100 km in an E-W direction.

From the Northern Pamirs two hornblende samples from the Altyndara metaandesites gave Early Carboniferous ages. Sample AD2e has excess Ar in the mid-T steps and shows Ar loss in the low-T steps; the probable age is 350 ± 20 Ma (Fig. 3.9c). From the hornblende-rich metaandesite AD6b (Fig. 3.9d), a total fusion age (TFA) of 319.9 ± 4.6 Ma was calculated; the highest-T step gives 354.7 ± 2.2 Ma, compatible with the age of hornblende from sample AD2e.

Samples from the Karakul lake area give very consistent Late Triassic/Early Jurassic muscovite and biotite $^{40}Ar/^{39}Ar$ cooling ages. The age spectra show no disturbance and the calculated ages range from 207 to 191 Ma (Fig. 3.9e-j).

South Tien Shan

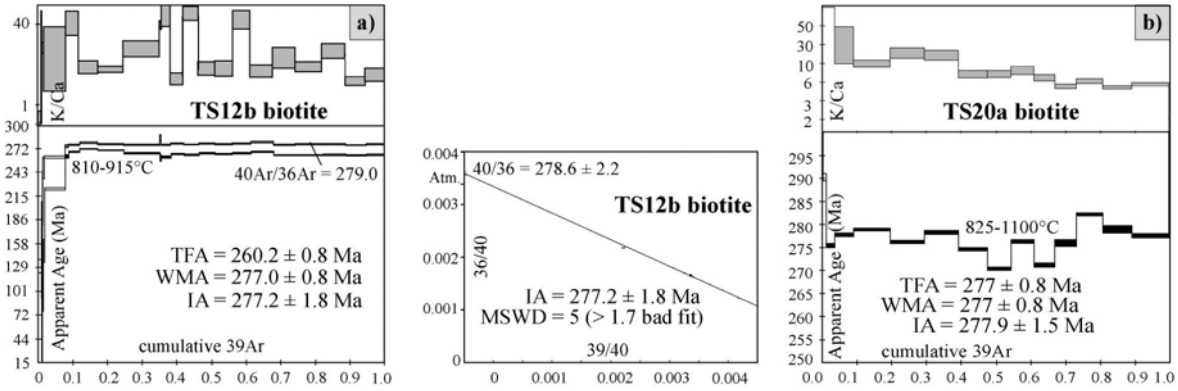

Northern Pamirs

Altyndara valley

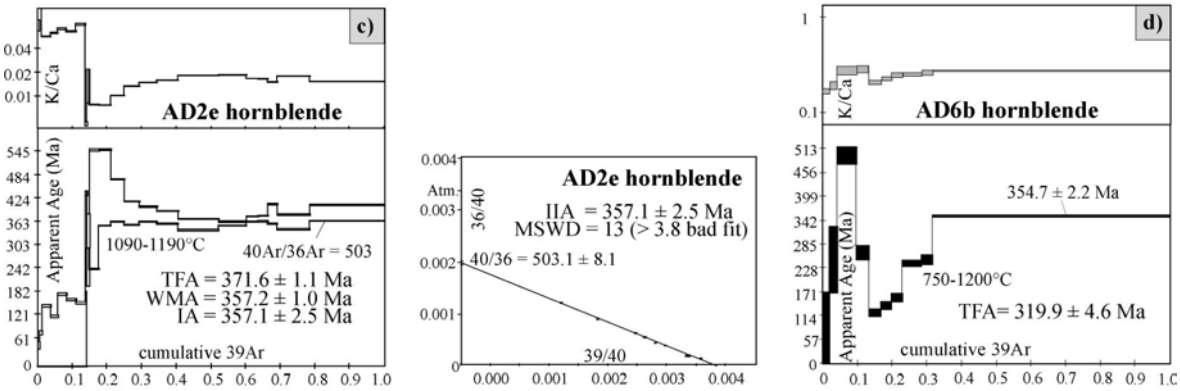

Karakul lake batholiths

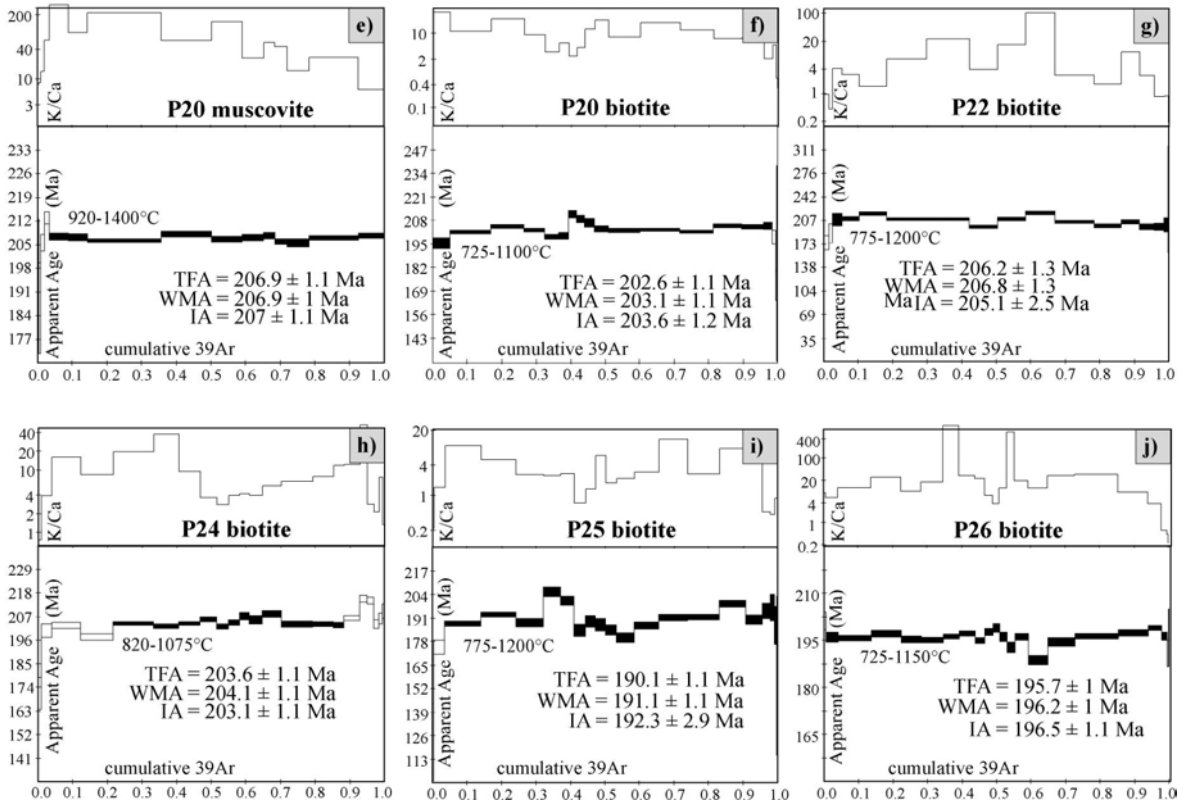

Central Pamirs/Rushan Pshart Zone

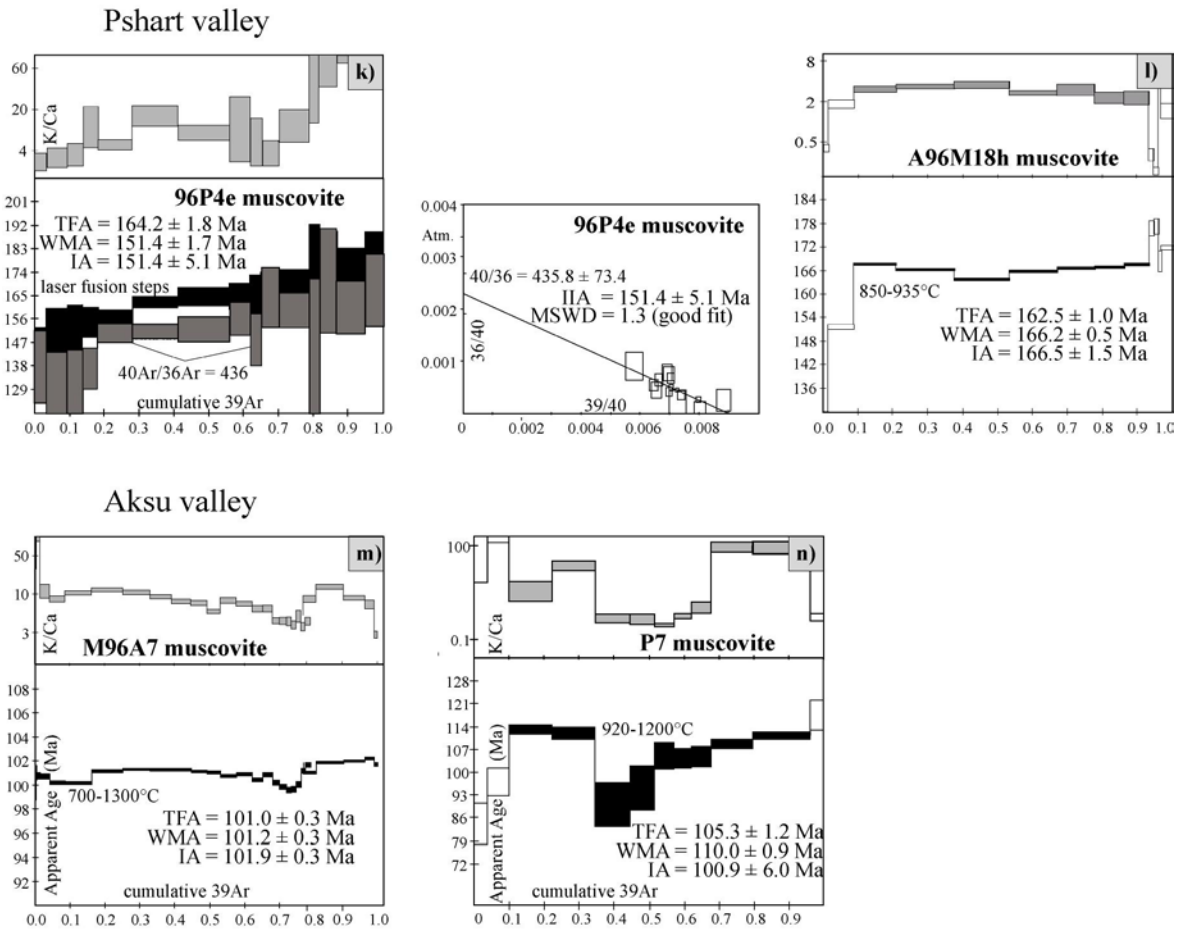

Northernmost South Pamirs

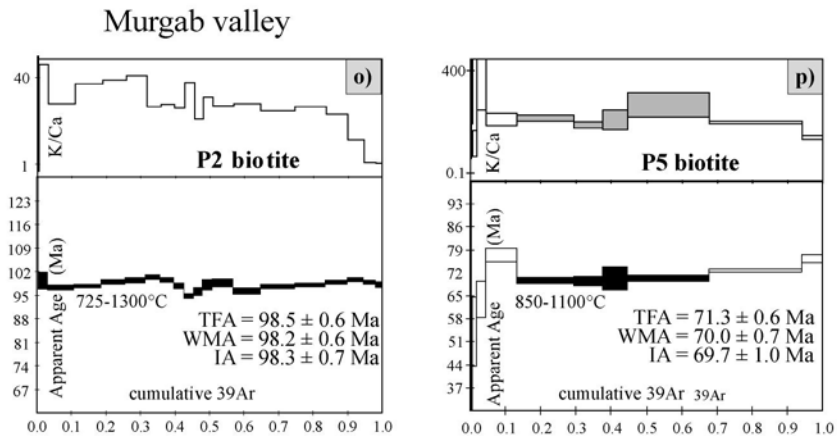

Fig. 3.9a-p: 40Ar/39Ar age spectra, variation of K/Ca, and correlated isotope ratio diagrams (36Ar/40Ar vs. 39Ar/40Ar). See Fig. 3.3 for sample locations and Appendix A, Tab. A3 for data listing. Weighted mean ages (WMA) and weighted mean plateau ages (WMPA) were calculated using shaded steps. TFA is the total fusion age, and IA the isochron age. Uncertainties are 1σ. "Atm." is the 36Ar/40Ar of the atmosphere (1/295.5) in the correlated isotope ratio diagram. MSWD is the mean square weighted deviation.

A granite pebble from a ?Miocene conglomerate in the Pshart valley (96P4e) gave a Late Jurassic $^{40}Ar/^{39}Ar$ age of 151.4 ± 1.7 Ma (Fig. 3.9k). $^{40}Ar/^{39}Ar$ dating of muscovite from a basement rock north of Murgab (A96M18h) yielded an age of 166.2 ± 0.5 Ma (Fig. 3.9l).

Cretaceous intrusions of the Central Pamirs and RPZ gave late Early Cretaceous $^{40}Ar/^{39}Ar$ cooling ages of ~105 and ~101 Ma (samples M96M7 and P7, respectively; Fig. 3.9m,n) and $^{40}Ar/^{39}Ar$ cooling ages from two intrusions of the northernmost South Pamirs spread from ~98 Ma (P2) to ~70 Ma (P5) (Fig. 3.9o,p).

3.5 Sr and Nd isotope compositions of the granitoids

Correlated isotopic compositions of the Sm/Nd and Rb/Sr systems have been used to obtain information about the magma sources and to determine crustal formation ages. Twelve igneous samples have been analysed (Appendix A, Tab. A6) from the Northern and Central Pamirs and the Rushan Pshart Zone. In general, model ages assess the time at which a rock separated from its mantle source region. For igneous and meta-igneous rocks this is a good estimate of the crust formation age.

Most of the Pamiran granitoids were derived by the melting of older continental crust (S-type granites). Therefore model ages will be indicative of the age of the crustal source. This is possible because the intracrustal fractionation process does not greatly disturb the Sm/Nd ratio of the source. Often, however, granites are a mixture of crustal and mantle sources. When this is the case, calculated model ages may give very misleading results (Arndt & Goldstein 1987). In this study, model ages were calculated with the equation of Liew & Hofmann (1988) with a two component reservoir of continental crust (CC) and depleted mantle (DM).

Initial Sr-ratios are lowest for the Carboniferous metavolcanic rocks of the Northern Pamirs (Altyndara valley) with $(^{87}Sr/^{86}Sr)_i$ = 0.705264 to 0.705642 and for the Triassic leucogabbro ($(^{87}Sr/^{86}Sr)_i$ = 0.705311). All other Sr-initials from Triassic/Jurassic granitoids range from 0.706974 to 0.709310, indicating crustal contamination. The Cretaceous granitoids have initial Sr-ratios between 0.709745 and 0.711105, implying even more crustal involvement. Such increasing contribution of crustal material in Cretaceous granites correlates with the low initial Nd-values of 0.512001 to 0.511820. The highest $(^{143}Nd/^{144}Nd)_i$ values obtained the metavolcanic rocks from the Altyndara valley, which range from 0.512191 to 0.512508. The leucogabbro shows also a high $(^{143}Nd/^{144}Nd)_i$ value of 0.512477, whereas the rocks of the Lake Karakul batholith fall into a very narrow range between 0.512148 and 0.512159. The Triassic/Jurassic samples have slightly lower values around 0.512050. Cretaceous granites show the lowest $(^{143}Nd/^{144}Nd)_i$ values . The $\varepsilon Nd_{(0)}$ values of the Cretaceous granites fall within the range of -11 to -12, those of the Triassic/Jurassic granitoids of the Central Pamirs and Rushan Pshart zone around -8 with the exception of the leucogabbro with an $\varepsilon Nd_{(0)}$ value of -0.3. $\varepsilon Nd_{(0)}$ values of the Karakul lake batholith are -6 to -7. The metavolcanic rocks show a wider spread of $\varepsilon Nd_{(0)}$ values from +4.5 to -3.4. Model ages for these rocks mirror this variety with ages increasing from 0.6 Ga for the southern samples to 1.1 Ga for the northern samples. The model ages of the Lake Karakul batholith are about 1.3 Ga, whereas the Triassic/Jurassic plutons are very consistent in the range of 1.4 Ga.

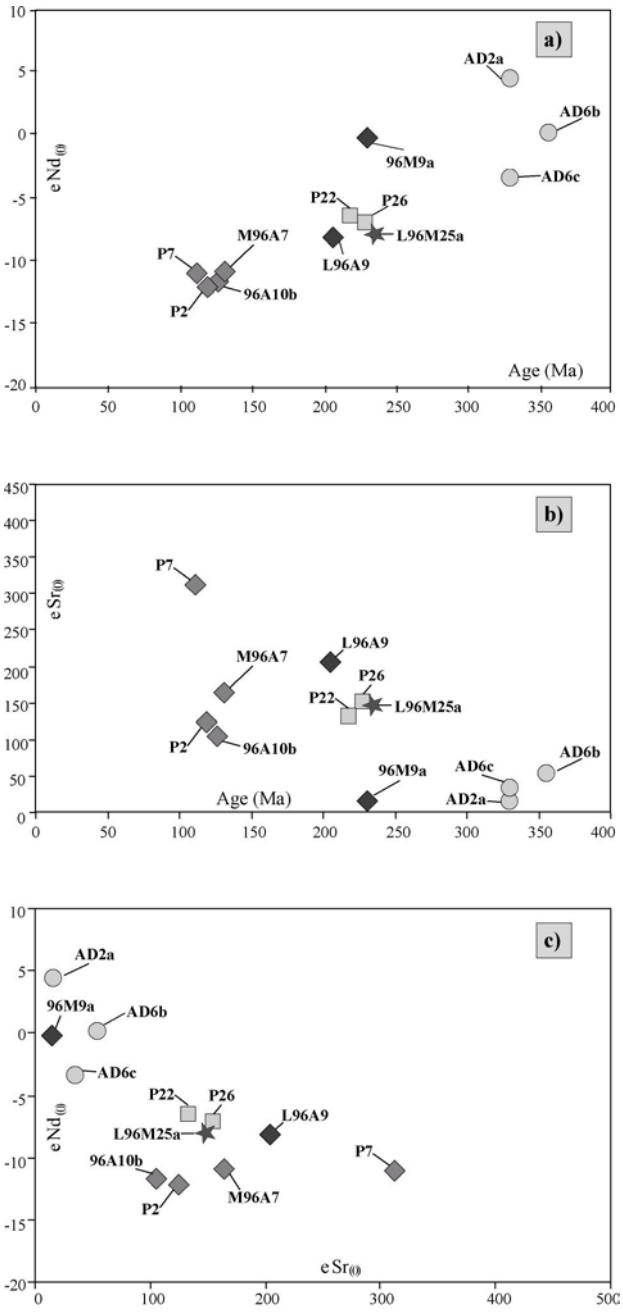

Fig. 3.10a-c: Correlated eNd(0) and eSr(0) data versus the age of the samples.

The Cretaceous plutons show model ages of around 1.7 Ga. Two outliners are represented by a much younger model age of 0.7 Ga for the leuco-gabbro, and by the oldest model age of around 2.0 Ga of sample P2, a Cretaceous granite. This granite has a very high $^{147}Sm/^{144}Nd$-ratio, implying a high degree of fractionation, due to the likely presence of garnet in the magma source. From Fig. 3.10c one can conclude a source region for the gabbro bodies of the north-eastern part of the Murgab dome (sample 96M9a) close to the standard reference reservoir which has $\varepsilon Nd_{(0)}$ and $\varepsilon Sr_{(0)}$ values of 0. In a similar range are the metavolcanic rocks from the Altyndara valley. The amount of crustal contamination increases from the upper left to the lower right. DePaolo & Wasserburg (1979) pointed out that mixing of two magma sources, respectively the contamination with crustal material, would create mixing relations dominated by a large variation of $\varepsilon Sr_{(0)}$ values with relatively stable $\varepsilon Nd_{(0)}$ values. This is also obvious from Fig. 3.10c: the Cretaceous samples show a range of $\varepsilon Sr_{(0)}$ values from ~100 to ~350 with $\varepsilon Nd_{(0)}$ values of about -11 to -12. Triassic and Jurassic rock samples from the Lake Karakul and Rushan Pshart zone show $\varepsilon Nd_{(0)}$ values of about -6 to -8 and the $\varepsilon Sr_{(0)}$ values spread from ~150 to ~200. The Karakul batholith seem to have a higher amount of mantle component or less crustal contamination than the other Triassic/Jurassic samples from the Rushan Pshart zone and the Cretaceous samples.

3.6 Geotectonic interpretation and correlation of the magmatic belts

In the following, the detailed geochemical and geochronological analyses are used to develop a regional syntheses of the geotectonic setting in which the magmatic belts of the southern Tien Shan and eastern Pamirs evolved (Fig. 3.11 and 3.16).

South Tien Shan

In the South Tien Shan (STS), the determined Late Palaeozoic (~277 Ma) granites are interpreted either as mature arc-related intrusions or syn- to post-collisional granites. The intrusions correspond westward along strike to the Turkestan Alay and South Gissar zones at the northern margin of the Tadzhik basin (Fig. 3.11, 3.16). Mid-Carboniferous volcanic rocks of the south Gissar range are interpreted as island arc tholeiites (Portnyagin et al. 1974). The volcanic rocks are spatially associated with granitic and granodioritic intrusions of the same age. The whole rock assemblage is in fault contact to the south with sheared and thrusted blocks of carbonates, turbidites and olistostromes, clastic molasse and a basal ophiolite melange. Portnyagin et al. (1974) interpreted this rock association as the "south Gissar marginal suture". Northward increasing differentiation of the igneous rocks of the STS, which testifies for a north-dipping subduction zone, can not only be inferred from this study, but also across the Gissar range (Leith 1982).

In a section across the easternmost Chinese South Tien Shan (Fig. 3.11), Allen et al. (1993) report the deposition of a stable marine platform on the northern margin of the Tarim block, developed over Precambrian continental basement. Through much of the Late Palaeozoic, the same region was a north-facing passive continental margin (Windley et al. 1990, Graham et al. 1990) similar to the Gissar region at that time. The destruction of the passive margin must have been completed by the end of the Early Permian, as the final episode of marine sedimentation occurred at this time. The closure of the oceanic basin resulted in the collision of the Tarim block with the Central Tien Shan along the southern Tien Shan suture (Allen et al. 1993). Regional granitoids belong either to volcanic arc or syn- to post-collisional settings. Limited regional knowledge does not allow a clear distinction between a supra-subduction or syn- to post-collisional origin for these granites (Allen et al. 1993), a situation very similar to the results of this study. Undeformed Late Palaeozoic calc-alkaline lamprophyre dykes intrude the Kyrgyz South Tien Shan, the Gissar range and the southern side of the southern Tien Shan suture in the Chinese Tien Shan (Mogarovskiy 1986, Allen et al. 1993). Allen et al. (1993) tended towards an interpretation of the dykes following

Fig. 3.11: Summary of the geodynamic evolution and amalgamation history of the Pamirs and Tibet. The profile across the Pamirs is based on the geochemical and geochronological data and correlations to Tibet and Afghanistan. The Turkestan/North Tien Shan suture is thought to be of Early- to Mid-Palaeozoic age and the Gissar/South Tien Shan sutur of Late Palaeozoic age. The northern Pamirs contain the composite Early Palaeozoic and Late Palaeozoic Kunlun arcs. The southward subducting Jinsha suture is of Late Triassic/Early Jurassic age, whereas the Rushan Pshart suture most likely closed in Mid-Jurassic time. The collision of the Karakorum block with the south-eastern Pamirs is thought along the upper Lower Cretaceous Tirich Mir/Kilik (?)suture. Finally, due to approaching India the Kohistan-Ladakh arc was sutured at ~80 Ma along the Shyok arc to the Karakorum. The amalgamation was completed with the India-Asia collision along the Indus-Yarlung suture at about 55 to 50 Ma.

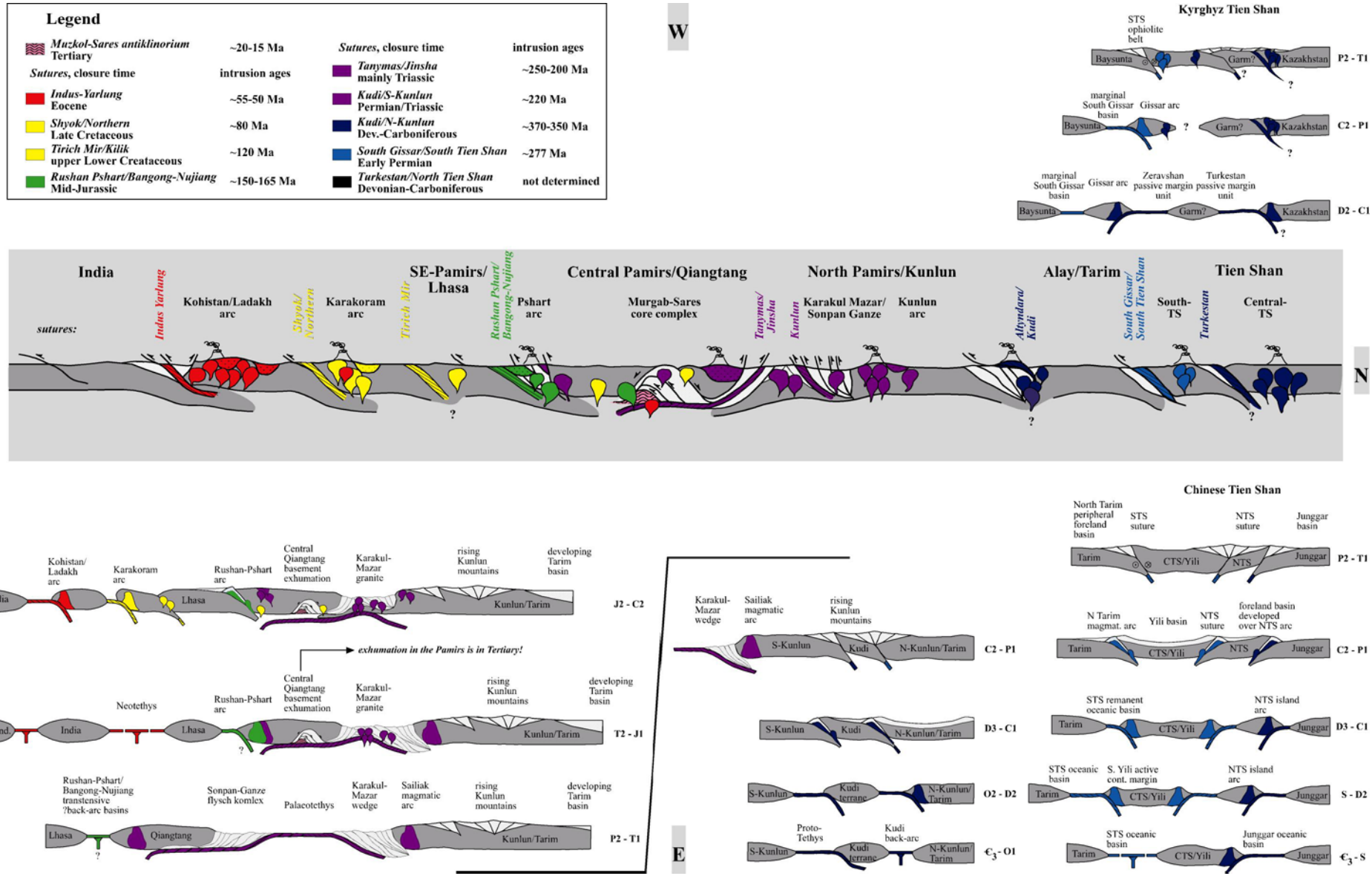
Legend
Muzkol-Sares antiklinorium Tertiary ~20-15 Ma
Sutures, closure time intrusion ages
Indus-Yarlung Eocene ~55-50 Ma
Shyok/Northern Late Cretaceous ~80 Ma
Tirich Mir/Kilik upper Lower Creataceous ~120 Ma
Rushan Pshart/Bangong-Nujiang Mid-Jurassic ~150-165 Ma
Sutures, closure time intrusion ages
Tanymas/Jinsha mainly Triassic ~250-200 Ma
Kudi/S-Kunlun Permian/Triassic ~220 Ma
Kudi/N-Kunlun Dev.-Carboniferous ~370-350 Ma
South Gissar/South Tien Shan Early Permian ~277 Ma
Turkestan/North Tien Shan Devonian-Carboniferous not determined
W
Kyrghyz Tien Shan
STS ophiolite belt
Baysunta
Garm?
Kazakhstan
P2 - T1
marginal South Gissar basin
Gissar arc
C2 - P1
Zeravshan passive margin unit
Turkestan passive margin unit
D2 - C1
India
SE-Pamirs/ Lhasa
Central Pamirs/Qiangtang
North Pamirs/Kunlun
Alay/Tarim
Tien Shan
sutures:
Indus Yarlung
Kohistan/Ladakh arc
Shyok/ Northern
Karakoram arc
Tirich Mir
Rushan Pshart/ Bangong-Nujiang
Pshart arc
Murgab-Sares core complex
Tanymas/ Jinsha
Kunlun
Karakul Mazar/ Sonpan Ganze
Kunlun arc
Altyndara/ Kudi
South Gissar/ South Tien Shan
South-TS
Turkestan
Central-TS
S
N
Kohistan/ Ladakh arc
Karakoram arc
Rushan-Pshart arc
Central Qiangtang basement exhumation
Karakul-Mazar granite
rising Kunlun mountains
developing Tarim basin
India
Lhasa
Kunlun/Tarim
J2 - C2
exhumation in the Pamirs is in Tertiary!
Neotethys
Gond.
T2 - J1
Rushan-Pshart/ Bangong-Nujiang transtensive ?back-arc basins
Sonpan-Ganze flysch komlex
Palaeotethys
Sailiak magmatic arc
Qiangtang
P2 - T1
E
Karakul-Mazar wedge
Sailiak magmatic arc
S-Kunlun
Kudi
N-Kunlun/Tarim
C2 - P1
D3 - C1
Kudi terrane
O2 - D2
Proto-Tethys
Kudi back-arc
ϵ_3 - O1
Chinese Tien Shan
North Tarim peripheral foreland basin
STS suture
NTS suture
Junggar basin
Tarim
CTS/Yili
NTS
Junggar
P2 - T1
N Tarim magmat. arc
Yili basin
foreland basin developed over NTS arc
C2 - P1
STS remanent oceanic basin
NTS island arc
D3 - C1
STS oceanic basin
S. Yili active cont. margin
S - D2
Junggar oceanic basin
ϵ_3 - S

Thompson et al. (1984), who see calc-alkaline lamprophyres as melts of enriched sub-continental lithosphere, frequently associated with orogenic belts, but post-dating the peak of compressional deformation and rather associated with varying degrees of contemporary extension. On the other hand, there are also lamprophyres known in an Andean-type continental margin setting (Carlier & Lorand 1997). In the Central Tien Shan, in the Chinese sector, a high volume of granite intrusions is exposed, which increases to the west. Hu et al. (1986) obtained a variety of ages from 350 Ma to 250 Ma by both U/Pb and K/Ar methods. Hopson et al. (1989) recorded four phases of plutonic magmatism in the Tien Shan: from 415 to 398 Ma (Late Silurian/Early Devonian), ~365 Ma (Late Devonian), ~334 Ma (Early Carboniferous), and ~261 Ma (Permian). A section of the western part of the Chinese Tien Shan (Fig. 3.11), described by Chen et al. (1999), confirms a north-facing passive continental margin along the northern Tarim margin during the Early Palaeozoic, separating the Tarim block from the Central Tien Shan (e.g. Yili block). Along the northern margin of this south Tien Shan oceanic basin was an active continental margin established, at least from the Silurian to the Middle Devonian, subducting northward beneath the Yili microcontinent. Isotopic ages of the south Tien Shan ophiolites and island arc granites show a considerable variation along strike (Chen et al. 1999): in the eastern segment of the South Tien Shan suture, oblique collision is documented for the Late Devonian/Early Carboniferous, leaving a remnant oceanic basin to the west. Subduction ceased in the western segment in the Late Carboniferous/Early Permian, creating an Early Permian magmatic arc along the northern Tarim margin and probably in the Kyrgyz South Tien Shan. This magmatic arc existed for only a short time during the Early Permian.
Here, it is concluded that the obtained Early Permian Ar/Ar ages of the southernmost Tien Shan can either be interpreted as denudational cooling ages close to the crystallisation age, and therefore as evidence for final Early Permian subduction of this remnant basin or that the obtained ages reflect cooling related to an Early Permian extensional event, documented in some regions along the northern Tarim margin. In the area of the northern Tarim basin a Late Permian/Early Triassic peripheral foreland basin and a foreland deformation belt developed (e.g., Bazhenov et al. 1993, Caroll et al. 1995) (Fig. 3.11).

North Pamirs-Altyndara metavolcanic rocks

The studied magmatic rocks from the Trans-Alay range (Fig. 3.3-3.4) of the northernmost Pamirs are mafic to acid, greenschist grade and deformed metavolcanic rocks. The age of the volcanic rocks is ~370-320 Ma and likely extends into the Triassic. Based on major, trace, and isotope geochemistry two different geotectonic environments could be distinguished: the southernmost part of a N-S section in the Altyndara valley consists of tholeiitic basalts which are interpreted to represent either oceanic crust or primitive island-arc basalts. Northward, more evolved calc-alkaline basalts, andesites and rhyolites of early arc stages are exposed. Pospelov (1987), Budanov & Pashkov (1988) and Leven (1981) recorded magmatic rocks belonging to an oceanic environment north of the Lake Karakul area, which are herein interpreted as likely correlatives of the Altyndara section. Furthermore, in the western part of the Northern Pamirs is the lower part of sections also composed of oceanic volcanics, but

the upper part varies: in some places tholeiitic compositions dominate, in others the volcanic rocks belong to island arc series (Pospelov 1987, Pospelov & Sigachev 1989). Based on biostratigraphic determinations (Budanov & Pashkov 1988, Leven 1981, Ruzhentsev & Shvol'man 1981, Ruzhentsev et al. 1978, and Pospelov 1987) Burtman & Molnar (1993) conclude a pre-Late Carboniferous ocean basin and its closure in the Late Carboniferous. Following stratigraphic interpretations (Ratschbacher 2003, pers. comm.; Schwab et al. in review), the base of the oceanic sequence is dominated by mafic lavas of likely Lower Carboniferous age, whereas the Upper Carboniferous is heterogenous. The magmatic-arc sequence is capped by limestones reaching into the Permian and is laterally replaced by thick greywacke, which is in turn overlain by molasse.

In summary, it is concluded that the Lower Carboniferous to ?Triassic Altyndara metavolcanic and volcanoclastic rocks, which are exposed in the Trans-Alay mountains of the Northern Pamirs, are part of an oceanic basin succession and a magmatic arc complex of which lateral continuations should be identifiable.

Similar Lower to Middle Palaeozoic belts to the east might be found in the western Kunlun, south of the Tarim basin. The western Kunlun (Fig. 3.1, 3.11-12, 3.14) is divisible into the North Kunlun, South Kunlun and Kara-Kunlun (or Mazar terrane, part of the Taxkorgan-Tianshuihai terrane) (e.g., Pan et al. 1992, Mattern et al. 1996, Yang et al. 1996, Xiao et al. 2002). The basement of the North Kunlun is interpreted to document Sinian rifting along the southern Tarim margin with ocean spreading during the later Sinian and Lower Palaeozoic, resulting in the formation of the Proto-Tethys Ocean (Mattern & Schneider 2000). The consumption of the Proto-Tethys is documented by arc-type granitic rocks of Lower to Middle Palaeozoic age. The basement of the South Kunlun consists of gneisses, amphibolites and migmatitic gneisses. Protoliths of the migmatites south of Kudi seem to be of Proterozoic age (Mattern et al. 1996). $^{40}Ar/^{39}Ar$ age spectra on K-feldspars of 380-350 Ma were interpreted by Matte et al. (1996) as the minimum age for metamorphism. Zhang et al. (1992) distinguished two arc granitoid belts in the South Kunlun, an older Palaeozoic one in the north, and a younger, Late Palaeozoic to Mesozoic one in the south. Both, the North and South Kunlun show a pre-Devonian stratigraphic gap which exists between the Sinian rift sequence (North Kunlun) respectively the Proterozoic metamorphic rocks (South Kunlun) and the unconformably overlying Upper Devonian terrestrial red molasse deposits, followed by Permo-Carboniferous shallow marine carbonates.

The Lower to Middle Palaeozoic Wuyitake (Oytag)-Kudi-Subasi ophiolite belt (e.g., Pan 1993, Pan 1994, Deng 1995, Mattern et al. 1996, and Yang et al. 1996) is proposed as the suture zone between the North and South Kunlun (Fig. 3.12) (Jiang et al. 1992, Pan 1994, Deng 1995, Mattern et al. 1996, Yang et al. 1996) and is here interpreted as eastward continuation of the volcanic arc sequence of the Altyndara section.

Only very few rocks have been analysed and dated from the Oytag suture, but more data are available from the Kudi suture. From the Oytag region, plagiogranites intruding basic lavas of an ophiolite suite were determined geochemically; the Sm-Nd model ages of the basic volcanic rocks are 970-690 Ma (Deng 1995) and the Sm-Nd isochron age of dunite, pyroxene peridotite, gabbro and plagioclase in the gabbro is 651±53 Ma (Ding et al. 1996). The plagiogranites are determined as ocean ridge

granites and have Sm-Nd model ages of 629.9 Ma and 599.8 Ma (Yaohui et al. 2001). Calculated εNd-values for the plagiogranites and mafic rocks are 4.34 and 4.87 respectively, whereas the $Sr_{(i)}$ and εSr of the plagiogranites are 0.702588 and -16.1 (Yaohui et al. 2001). These data are comparable to the data from this study about the acid and mafic metavolcanic rocks from the Altyndara section (e.g. AD2a, a metarhyolite, with $Sr_{(i)}$ of 0.705384, $\varepsilon Nd_{(0)}$ of 4.51, and a Sm-Nd TDM model age of 600 Ma).

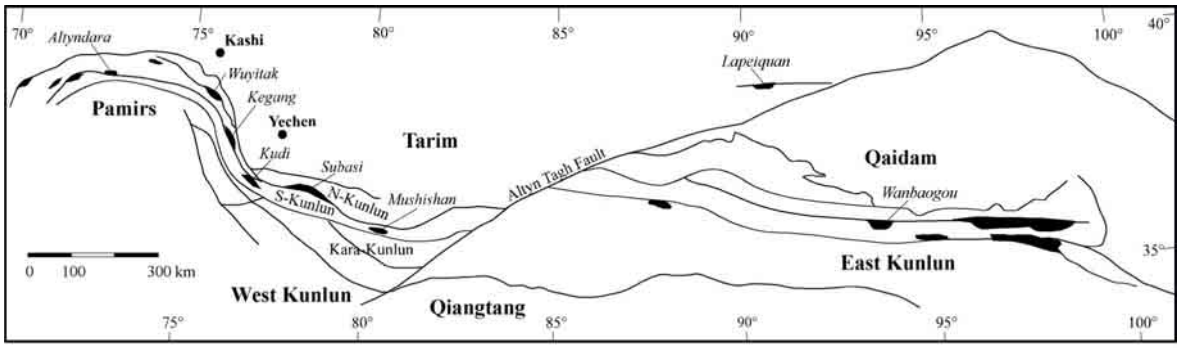

Fig. 3.12: Schematic map of the Kunlun region with the distribution of ophiolite rock assocciations. Compiled after Yang et al. 1996 and Sobel & Arnaud 1999.

Southeast of the Oytag suture, parallel to the strike of structures, the Lower Palaeozoic Kudi suture (Arnaud 1992, Matte et al. 1996) crops out. The suture belt includes Tarim basement on the north side with 2261 +95 –76 Ma old gneiss (U/Pb on zircon), crosscut by dolerite dikes and overlain by Riphean limestones. To the south, Lower Palaeozoic oceanic crust includes pillow lavas and radiolarian cherts (Sobel & Arnaud 1999). Gabbro from this crust as well as Proterozoic mafic volcanic rocks were intruded by ~460 Ma granodiorites (U/Pb on zircon). These units are associated with migmatitic gneisses, probably derived from Proterozoic basement with an ~1800 Ma Sm/Nd model age (Sobel & Arnaud 1999). Subsequent metamorphism is dated ~420 Ma and 350 Ma by $^{40}Ar/^{39}Ar$ on biotite and K-feldspar, respectively; the latter age is probably an underestimate (Sobel & Arnaud 1999). The entire sequence is crosscut by undeformed post-tectonic granites dated at ~380 Ma (U/Pb on zircon, Rb/Sr on whole rocks and biotites, and $^{40}Ar/^{39}Ar$ on biotite; Sobel & Arnaud 1999). Also Xu et al. (1994) dated the southern posttectonic granites at 384±1.9 Ma (U/Pb on zircon) and at 384.7±5.2 Ma ($^{40}Ar/^{39}Ar$ on biotite). The calc-alkaline North Kudi pluton is dated at 404 Ma (U/Pb on zircon) with $\varepsilon Nd_{(t)}$ values ranging from -2.4 to -9.6 (Yuan et al. 1999). Other subduction-related diorites located north of the Kudi lavas have U/Pb zircon ages of 458±2.5 Ma and $^{40}Ar/^{39}Ar$ amphibole and biotite ages of 475.5±8.8 Ma and 449±24 Ma, respectively (Xu et al. 1994). Recent studies have reached a consensus view, that the Kudi ophiolite formed in a supra-subduction zone setting (Wang et al. 2000, 2001; Zhang & Zhou 2001). Intensive geochemical studies on the different types of extrusive rocks of the Kudi ophiolite (Wang et al. 2002) depicted a new and detailed geodynamic model for the evolution of the Kudi ophiolite belt. The authors illustrate the evolution of a first-stage arc system and a subsequent evolution of a back-arc basin. It must be improved, whether this model can be adapted for the evolution of the metavolcanic sequence of the Altyndara valley in the Northern Pamirs. However, the Altyndara section seem to

represent a slightly younger evolutionary stage of an oceanic basin and the generation of a primitive island arc than further east – or the section documents probably the younger back-arc stage. Further geochemical and structural studies have to reveal this.

Continuing east along the central portion of the Altyn Tagh, Sobel & Arnaud (1999) described two transects across the Altyn Tagh range which include the possible continuation of the early to middle Palaeozoic sutures described above. The published oldest rocks in the Altyn Tagh range are considered to be Tarim basement, represented by the Miran Group of gneiss, granulite and amphibolite. The rocks are dated at 2462 Ma (U/Pb on zircon, Wang et al. 1993) and yielded Sm/Nd ages of 2787±151 Ma and 2792±208 Ma on granulite and amphibolite, respectively (Che et al. 1995). A gabbro from a mafic magmatic unit in the centre of the range is dated as 1883±110 Ma by the Rb/Sr method (Wang et al. 1993). Biotite from granitic gneisses of the Miran Group at Lapeiquan (Fig. 3.12) yielded a WMPA age of 1741±24 Ma (Sobel & Arnaud 1999); this might reflect a cooling age related to the emplacement of the crosscutting mafic dikes. In the area just south of the North Altyn Tagh fault, bimodal volcanics, interpreted to represent a rift, are dated at 1793±270 Ma by Sm/Nd on basalt. The same region contains a granulite dated at 1704±105 by Sm/Nd. These ages of the Tarim basement are comparable to the ages found in the Kudi section. Only few Palaeozoic intrusions are documented across the transects of the Altyn Tagh range; a 424±8 Ma Rb/Sr age was obtained from an acidic volcanic unit near Lapeiquan (Che et al. 1995). A metamorphosed granite gneiss yielded an age of 472.8±10.4 Ma, mica schists on the south side of the range yielded a WMPA of 453.4±8.7 Ma on muscovite, and a foliated leucogranite a WMPA of 431.5±7.8 Ma on muscovite. Undeformed porphyritic biotite granite yielded an Rb/Sr age on biotite of 426 Ma (no error given; Xu et al. 1996); another undeformed granodiorite of the area yielded an WMPA of 413.8±8.0 Ma on biotite (Sobel & Arnaud 1999). Pegmatites 430 km to the east were dated at 431.6±7.6 Ma on muscovite. Basalt from a dismembered ophiolite suite south from the Altyn Tagh fault at Mangnai is dated 481±53 Ma by an eight point Sm/Nd isochron (Sobel & Arnaud 1999). From these data Sobel & Arnaud (1999) suggest the existence of a suture zone in the Altyn Tagh range, which is most clearly developed near Lapeiquan: an early Palaeozoic basin with likely oceanic crust closed post-Early Silurian and pre-Middle Devonian. Basin closure may have resulted in high-pressure metamorphism and is therefore also interpreted as a suture zone which might be correlated with the Wuyitake (Oytag)-Kudi-Subasi ophiolite belt and the northern Pamirs belt. Jolivet et al. (1999) dated a further granite of this region by the U/Pb zircon method at 441±9 Ma. A five point Rb/Sr isochron age was obtained at 327±7 Ma with an initial $^{87}Sr/^{86}Sr$ ratio of 0.7095±0.0036 (±2σ).

Correlation of this suture further east can be only tentatively drawn, as available data cannot reliably distinguish between similar igneous-metamorphic belts recognised in this area (Sobel & Arnoud 1999). Candidates include the East Kunlun Shan, the northern margin of the Qaidam basin, and the Bei Shan.

Westward of the Northern Pamirs, Middle Palaeozoic sutures should continue into Afghanistan (Fig. 3.13). Unfortunately, several years of war hindered scientific research in this region and therefore only limited geological data are available from Afghanistan. One of the latest compilations of typology, age and geodynamic setting of plutonic rock

associations in Afghanistan is from Debon et al. (1987). As concluded from the tectonic position, likely candidates of magmatic rock associations representing the continuation of the Middle Palaeozoic suture might be cropping out in the Western Badakhshan, Western Hindu Kush, and Feroz Koh regions. Stöcklin (1977) correlated the Northern Pamirs with the Feroz Koh (Paropamisus), the Western Hindukush and northern Kunlun. Much of the western Hindu Kush is made up of Silurian radiolarian slates, Palaeozoic volcanic rocks, including spilites and ultrabasites, associated with slates, quartzites and greywackes of supposed Lower Carboniferous age. These rocks are strongly folded, metamorphosed, intruded by granites (e.g., the pre-Namurian Khinjan granite), and overlapped disconformably by carbonatic, detrital and partly volcanic rocks of Late Carboniferous to Permian age. According to the compilation of Debon et al. (1987), no Lower to Middle Palaeozoic magmatic rock associations were detected in the Western Badakhshan, Western Hindu Kush, and Feroz Koh regions. Here in this thesis, it is proposed that large parts of traces of the Early to Middle Palaeozoic suture zone are truncated by the sediments of the Tadjik basin, which follows just north and north-west of the Western Badakhshan, Western Hindu Kush, and Feroz Koh regions. The Tadjik basin area was affected by strong subsidence continued through Permian into Triassic time and was accompanied by widespread basic and acid volcanic effusions.

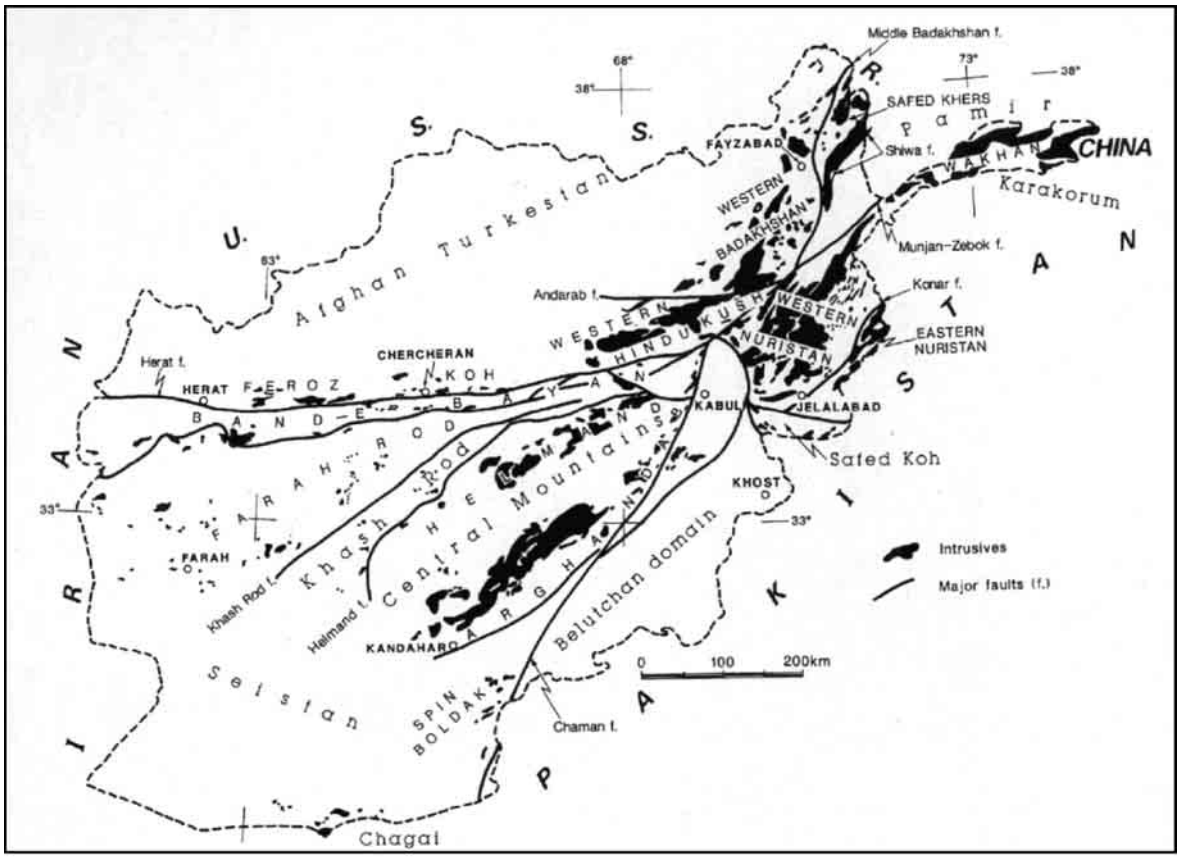

Fig. 3.13: Schematic map of the intrusives in Afghanistan. From Debon et al. (1987) after the adaption of Stazhilo-Alekseev et al. (1973) and Chmyriov & Salah (1976).

North Pamirs-Karakul lake batholith

The herein presented E-W trending Karakul lake batholith is characterised by undeformed granodiorites to monzogranites, which intrude Carboniferous to Permian, possibly Triassic metaclastic and metavolcanic rocks, locally accompanied by gabbroic intrusives. U/Pb zircon ages of the batholith are interpreted as minimum crystallisation ages at about 215.0±1.5 Ma. This age is supported by $^{40}Ar/^{39}Ar$ biotite and muscovite ages in the range of 207 to 191 Ma, interpreted as cooling ages close to the crystallisation age. The rocks are characterised as high-K, calc-alkaline, transitional I- to S-type intrusive rocks with $Sr_{(i)}$=0.707623 (P22) and 0.706974 (P26). $\varepsilon Nd_{(t)}$ values are around –4 and the depleted mantle model ages are ~1.3 Ga. The batholith is interpreted as post-tectonic intrusion through relatively thin crust with less crustal contribution to the magma source than determined from other Pamiran magmatic rocks (see chapter 3.5).

Intrusions of similar age are reported in the western Kunlun: Yuan et al. (1999) dated the Akarz mountain pluton, which is located southwest of Kudi and which intrudes a Proterozoic basement group in the north and a lower Permian magmatic arc (Sailiyak magmatic arc) in the south. The Akarz mountain pluton covers an area of more than 2800 km^2, and is truncated to the south by the Mazar-Kangxiwar fault (southern margin of the South Kunlun). Like in the Karakul lake area, the magmatic rocks are mainly granodiorites and monzogranites, with some quartz-diorites. The U/Pb zircon age is 214.9±1.5 Ma (Yuan et al. 1999), identical to the data from the Karakul lake batholith. The $\varepsilon Nd_{(t)}$ values show a wide variety between –3.2 to –11.9 (5 samples), indicating that the magma source is heterogeneous with involved continental crust. The depleted mantle model ages are between 1.29 to 2.08 Ga (Yuan et al. 1999). A gneissic granite, located 22 km north-east of Mazar yielded a biotite Ar/Ar isochron age of 211.8±10.8 Ma age (Xu et al. 1996, Pan 1996) supporting, like the Ar/Ar ages of the Karakul batholith, the crystallisation age. A red porphyry volcanic rock situated close to the granite yielded a Rb/Sr whole rock age of 180±10 Ma (Matte et al. 1996).

The Kara Kunlun or Mazar terrane consists of different subduction complexes (Fig. 3.14), which are subdivided into three units: (1) the northern Bazar Dara subduction complex with imbricated blocks of sandstone, calc-arenite, limestone, and metavolcanic blocks in a matrix of weakly metamorphosed Triassic deep-sea turbidites (Xiao et al. 2002). This zone has Ordovician to Permian fossils and is situated south of the Sailiyak magmatic arc. (2) The southern Heweitan mélange is composed of a slate-phyllite matrix with blocks of limestone, turbidite, and radiolarite with Permian to Triassic fossils (Gaetani et al. 1990, Pan 1996, Xiao et al. 2002). The Konggashankou-Qogir fault is the southern limit of the Heweitan subduction complex; the fault separates Gondwana cool-water fauna in the south from Cathaysian warm-water fauna in the north (Li et al. 1995). Thus, a suture is supposed along the Konggashankou-Qogir fault, which can be correlated with the Jinsha suture to the east (Li et al. 1995). Xiao et al. (2002) interpret the Heweitan rocks as a subduction complex near the trench of a north-dipping subduction zone. (3) The Qitai forearc basins of Late Triassic turbidites and intercalated carbonates overlie the Bazar Dara and Heweitan subduction complexes. The sediments of the Qitai forearc basin were derived from both the adjacent Sailiyak arc and the subduction complex. Xiao et al. (2002) conclude that the

Kara Kunlun or Mazar accretionary prism formed by subduction-accretion processes during closure of the Palaeotethyan ocean and the final docking of the Gondwana Karakoram-Qiangtang block to the Eurasian Kunlun block.

Granitic intrusions into the Bazar Dara and Qitai complexes yielded Rb/Sr biotite isochron ages of 190 Ma (Zhang & Xie 1989), suggesting that by the Late Triassic to Early Jurassic the locus of magmatism had migrated from north (Sailiyak magmatic arc) to south. $^{40}Ar/^{36}Ar$ plateau ages of biotite, determined by Xu et al. (1992), range between 215 and 185 Ma, whereas the lower interception U/Pb zircon ages for different intrusions in the Kara Kunlun range between 199 and 192 Ma. A K/Ar biotite cooling age of 171.5±5.4 Ma was reported by Gaetani et al. (1991) for the Mazar pluton located west of Mazar. The emplacement and cooling ages of the Karakul lake batholith presented in this study, are very well correlatable to ages of the western Kunlun range and are herein summarised as the Karakul-Mazar belt.

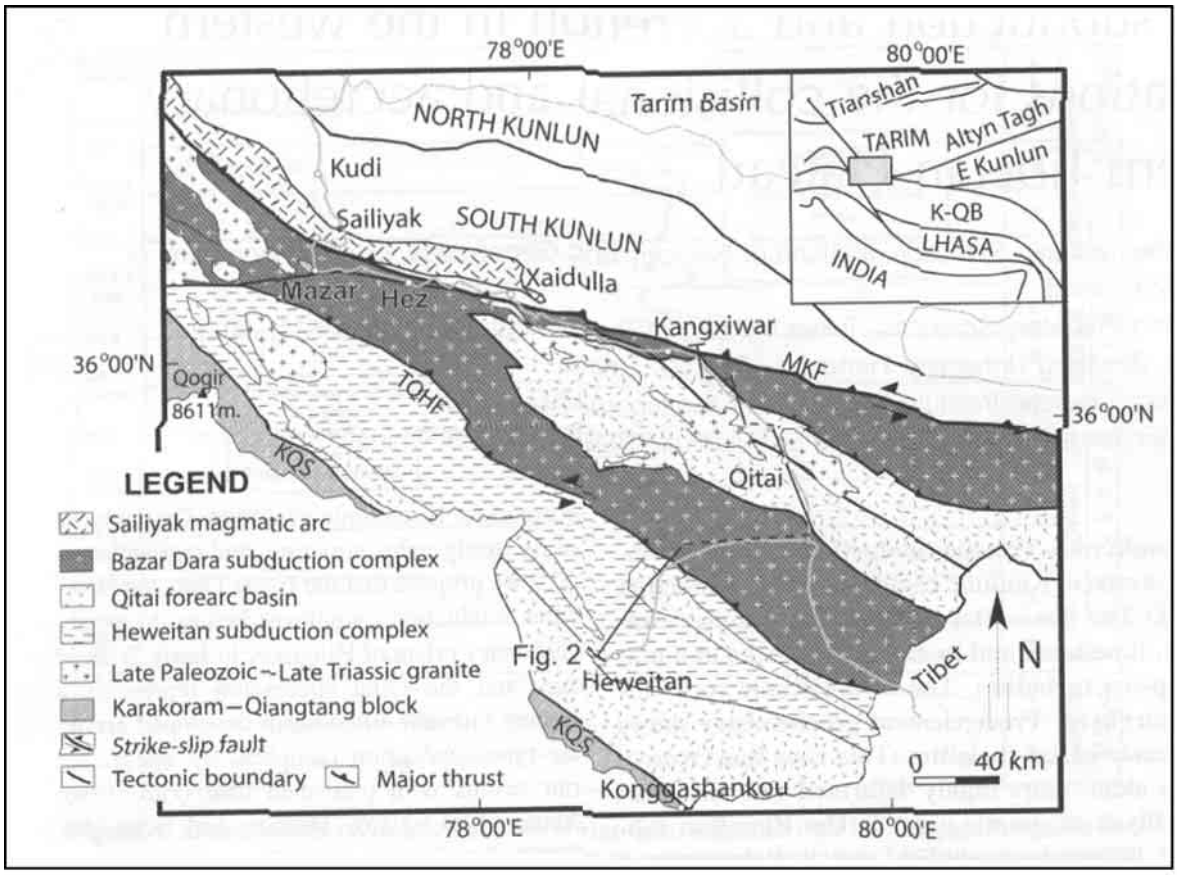

Fig. 3.14: Schematic tectonic map of the Kunlun orogen (adapted after Xiao et al. 2002). MKF = Mazar-Kangxiwar fault, TQHF = Taaxi-Qiertianshan-Hongshanhu fault, KQS = Konggashankou-Qogir suture. For clarity, Jurassic and Cretaceous units are not shown.

Correlation of the Karakul lake batholith to the west leads to the eastern and south-eastern margin of western Badakshan and western Hindu Kush, and to the southern margin of Feroz Koh in Afghanistan (Fig. 3.1, 3.13). Extensive granite intrusions of Early Mesozoic age are documented in the area of the Salang pass (Stöcklin 1977). The lateral extent of such Triassic intrusions, mainly granodiorites of calc-alkaline character, is more than 500 km along strike and associated with volcanic activity (Debon et al. 1987).

The granodiorites of western Badakshan and western Hindu Kush have $Sr_{(i)}$-ratios of 0.7044±4 and a whole rock Rb/Sr isochron age (9 samples) of 234±12 Ma (Debon et al. 1983). Rb/Sr biotite ages of 8 samples are in the range of 224-192 Ma (Desio et al. 1964). Samples from the Feroz Koh region gave K/Ar ages on biotite of 212 Ma (Wittekindt 1973) and K/Ar on whole rock of 247-192 Ma (Debon et al. 1986). Debon et al. (1983) suggested that the magmatic arc intrusions have been formed by ocean subduction to the south. Other authors inferred northward subduction, either of the Palaeotethys located immediately south of the western Badakshan and western Hindu Kush (remnants of which being assumed to occur along the Herat fault (e.g. Mattauer et al. 1980, Tapponnier et al. 1981) or south of the Farah Rod ocean (e.g., Bassoullet et al. 1980).
The Late Triassic/Early Jurassic transitional I- to S-type intrusions of the Lake Karakul area find widespread correlatives to the east and west and are interpreted as syn- to late-collisional intrusions stitching together the Late Palaeozoic Kunlun arc formed by northward subduction of the Palaeotethys and the mid-Jurassic Jinsha suture formed by southward subduction of the Palaeotethys along the northern margin of the Qiangtang terrane. The Late Palaeozoic to Triassic volcanoclastic successions around the Lake Karakul area are interpreted in this study as equivalents to the Mazar accretionary prism in the western Kunlun (Xiao et al. 2002). Further eastward, these rock associations are correlatives to the Songpan-Ganze melange of northern Tibet.

Central Pamirs

In the Central Pamirs, different tectono-stratigraphic units are constrained by diverse intrusions of different age and geochemical composition. As pointed out from the discussion in chapter 3.2, no unique and complete geological description exists from the Central Pamirs. Formerly, three main structural units were characterised, namely (1) Precambrian basement, covered by (2) Mesozoic units and overlain by several (3) Tertiary intra-montane molasse basins.

Central Pamiran basement rocks

Ratschbacher et al. (1999), Schwab et al. (2000) and this thesis could demonstrate, that the basement antiforms are a young Cenozoic feature. The regional structure is a normal fault bounded anticlinorium exposed in the Muzkol and Sares domes. The metamorphic rocks cropping out in these windows are metamorphosed to greenschist or amphibolite facies conditions with local migmatisation. The rocks are mainly biotite-gneiss, phyllitic quarzite, flysch-like metaclasitic rocks, amphibolite, and greenschist.
The oldest intrusion of the Central Pamirs dated in this study, is an aplitic dike (sample P17) cutting high-grade biotite-gneiss in the Muzkol dome. The upper interception U/Pb zircon age of this sample is about 535 Ma and SHRIMP spot ages range from 561 to 424 Ma (see chapter 3.3).
Similar extensional metamorphic core complexes to a much larger extend with like aged basement rocks are found in the Central Qiangtang block (Kapp et al. 2000). The metamorphic rocks are interpreted to represent the Songpan-Ganzi accretionary wedge system created by southward subduction of the Palaeotethys along the Jinsha suture and below the Qiangtang block. Mélange-exhumation was triggered by Late Triassic-

Early Jurassic low-angle normal faulting and thus earlier than in the Central Pamirs, but coeval with ongoing subduction (Kapp et al. 2000). A sliver of garnet-amphibole gneiss of the blueschist-bearing Gangma Co mélange derived zircon U/Pb ion-microprobe ages in the range of 556 to 419 Ma (Kapp et al. 2000) comparable to the data of sample P17 of the Central Pamirs. Such basement slivers are constrained as Pan-African basement that was eroded from the base of the Qiangtang block and incorporated into the mélange during low-angle subduction (Kapp et al. 2000). Like the mélange rocks in Central Qiangtang, the characteristic rock associations of the Central Pamiran domes are monotonous siliciclastic and volcanoclastic rocks, as well as mafic volcanic rocks, which are interpreted as a subduction-accretion association (Schwab et al. in press).

The gabbro sample 96M9a, a representative for Triassic-Jurassic gabbros intruding the biotite-gneisses in the Muzkol and Sares domes, has an upper intercept age at around 830 Ma; the most common age population of detrital zircons in the sedimentary rocks of the Qiangtang mélange is between 1200-800 Ma (65% of all zircons, Kapp et al. 2003) and around 830 Ma old granites constitute the basement of the Songpan-Ganze system in eastern Tibet. These granites are interpreted as part of the South China craton (Roger & Calassou 1997). The Pamiran gabbros and their likely equivalents in Central Tibet indicate oceanic crust of Late Triassic/Early Jurassic age subducting southward beneath the Central Pamirs and Qiangtang block. The Nd model age of 0.7 Ga from the leucogabbro 96M9a is younger then all other determined model ages from the Qiangtang and is more indicative for Kunlun and Karakul-Mazar affinity. The final closure of the oceanic basin and the intervening Songpan-Ganze mélange was along the Jinsha suture in Tibet and along the Tanymas suture in the Pamirs. The cryptic Tanymas suture is therefore thought to be the westward continuation of the Jinsha suture. Further similarities are granitoids intruding the Qiangtang block in the Pamirs and in Central Tibet (see below).

Triassic/Jurassic intrusions of the Central Pamirs

Granitoids intruding the Qiangtang block have different ages or ion probe age components of ~230-200 Ma and/or of ~200-160 Ma in the Pamirs and in Tibet. Some of these intrusions with a major Triassic age component are herein attributed to early Mesozoic southward subduction of oceanic crust along the Jinsha suture. Sample L96M25a may received a lower intercept age of ~235±11 Ma, , whereas the mean of 12 SHRIMP spot ages of sample L96A9 is about ~201±4 Ma. A granitoid of a Qiangtang core complex in Tibet yielded a comparable weighted mean $^{206}Pb^*/^{238}U$ ion-mircroprobe zircon age of 220±1 Ma (Kapp et al. 2000). According to Kapp et al. (2000) the closure between the Qiangtang and Kunlun blocks was in the Late Triassic/Early Jurassic. The exhumation of the Songpan-Ganze mélange in the extensional metamorphic core complexes in the central Qiangtang block occurred in an intracontinental setting by Late Triassic-Early Jurassic. Consequently, intrusions with a major mid-Jurassic age component are interpreted to characterise basin closure in the Rushan Pshart zone, probably with subduction of oceanic lithosphere below the southern margin of the Qiangtang block. This suggests, that in the area of the narrow Qiangtang block of the Central Pamirs a younger 200-160 Ma southern magmatic belt may have overprinted an

older 230-200 Ma magamtic arc along the northern margin of the Qiangtang block (Tanymas-Jinsha suture). The Sr-initials of the Triassic/Jurassic intrusions are in the range of 0.706974 to 0.709310 and therefore indicate only limited crustal contamination in comparison to the Cretaceous granites (see below) and thus only limited crustal stacking. The rock types are mainly biotite granites or two mica granites into Triassic-(?)Jurassic siliciclastic host rocks. As the samples L96M25a, L96A9, M96A7, 96P4e, and A96M18h do all show mid-Jurassic lower intercept ages or SHRIMP spot ages and only in case of the first two samples also Triassic age components, these samples are interpreted to belong to mid-Jurassic basin closure along the Rushan Pshart zone.

Rushan Pshart Zone

During most of the Permo-Triassic, the southern margin of the Qiangtang terrane was under extension. The Rushan-Pshart zone, a transitional zone between the Central Pamirs and the South Pamirs, is built of Upper Palaeozoic to Jurassic volcano-sedimentary successions probably representing a rift-margin and/or an oceanic basin – (?)arc sequence. Some earlier models postulated the existence of a vast Permo-Triassic ocean, closed during the Jurassic (e.g. Sengör 1990). Leven (1995) is more arguing for a narrow sea-way, which separated the West Pshart from the East Pshart instead of interpreting the Rushan Pshart zone as a continuous suture zone between the Central and South Pamirs.

Across the Tibetan plateau, the Bangong-Nujiang zone (BNZ) separates the Qiangtang block in the north from the Lhasa block in the south. Several ophiolite-bearing basins are aligned along the BNZ, which are of Mesozoic age (Yu et al. 1991). The average width is between 10 to 20 km, but can locally reach up to 200 km. The interpretation of the Bangong-Nujiang zone is very controversial. Most authors interpreted the BNZ as a collisional suture (e.g. Pan & Zheng 1983, Zheng et al. 1984, Coulon et al. 1986). Girardeau et al. (1985) considered Late Jurassic to Early Cretaceous ophiolite obduction associated with long-range thrusting of >100 km. Xu et al. (1985) assumed a mid-Jurassic collision. Pearce & Deng (1988) and Hsü et al. (1995) suggested that different ophiolite units of the BNZ may represent different types of lithosphere. However, according to Schneider et al. (2003) the views of what may be forearc or backarc lithosphere are inconsistent. As discussed earlier, Gaetani (1997) deny a correlation of the Waser-Panjao ocean (opened in Central Afghanistan north of the Helmand block), the Rushan Pshart zone, and the Bangong-Nujiang ocean as the Waser-Panjao and Bangong-Nujiang oceans closed mainly in Jurassic time whereas he suggests, that the Rushan Pshart oceanic basin closed already in Late Triassic. In the central part of the SE Pamirs, as well as in the Karakorum, no major episodes of deformation are recordable at the end of the Triassic although terrigenous, and sometimes even continental sediments rest on older marine successions. This is also true for the Central Pamirs, where predominantly terrigenous rocks including conglomerates of Late Triassic to Early Jurassic age are found (Gaetani 1997). As a consequence, Gaetani (1997) follows an interpretation of the BNZ as a back-arc basin and connects the BNZ to the Shyok back-arc, and links them both to the Kohistan and Ladakh-Gangdese oceanic arcs.

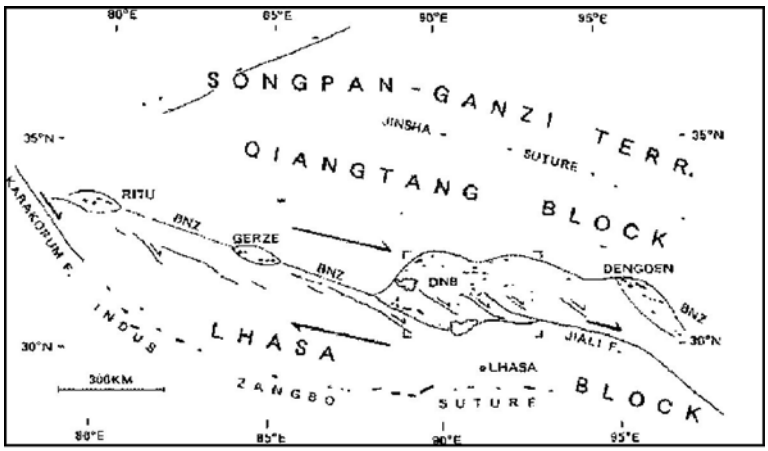

Fig. 3.15: Tibetan ophiolites (black) and basins along the Bangong-Nujiang zone (adapted from Schneider et al. 2003). BNZ = Bangong-Nujiang zone, DNB = Dongqiao-Naqu basin.

Coward et al. (1988) pointed out some problems concerning the BNZ as Mid-Late Jurassic collisional suture because typical collision related deformation, thickening, mountain building, as well as related molasse formation are lacking. Schneider et al. (2003) found an interpretation for the eastern BNZ solving most of these problems. Based on detailed basin analyses of the Dongqiao Naqu basin (DNB), one of several scattered basins along the BNZ, Schneider et al. (2003) explain the DNB as a polycyclic basin. The rift flank sequences indicate transtensional basin formation (Permian to Late Triassic) with rifting via oceanisation (Late Triassic to Early Jurassic) to transpression of a remnant basin. Partial basin closure of the DNB, indicated by ophiolite thrusting to the south, was during the early Mid- to Late Jurassic. Whether the eastern Qiangtang block was affected by arc magmatism is unclear; thus Schneider et al. (2003) characterise the Late Jurassic to Early Cretaceous DNB as a remnant basin. In summary, their model explains the occurrence of similar prerift sequences on the Lhasa and Qiangtang blocks and the regional linear ophiolite belts distribution pattern within strike-slip zones and between continental blocks as parautochthonous rather than allochthonous units (Schneider et al. 2003). Some of the transpressional and transtensional strike-slips which are suppositional for their model, were probably initiated in the Late Jurassic and are evident for the Late Cretaceous to Tertiary. During Neogene and Quaternary some faults were reactivated (Schneider et al. 2003).

Coming back to the Rushan Pshart zone and the in this study preferred correlation with the BNZ, the following concept can be drawn: The revised (Leven 1995), isolated, lens-shaped tectonic blocks of the Rushan, Pshart and Dunkeldyk may be considered as transtensional basins accompanied by rifting associated basaltic volcanism on the northern Gondwana margin. Only in the (?)Rushan block, East Pshart, and south-eastern Pamirs is the Carboniferous and Lower Permian recorded. Like in the Qiangtang and Lhasa it is dominated by clastic deposits (Leven 1995, Schneider et al. 2003). The Upper Permian is charcetrised by siliceous sediments interbedded with calcereous sediments in the East Pshart, and south-eastern Pamirs. Basalts occur in the Upper Permian of the East Pshart, whereas basaltic tuffs, probably derived from the East Pshart are deposited in the south-eastern Pamirs. The Upper Permian/(?)Triassic of the Rushan block contains fusulinids and corals, proposing a carbonate platform. According to Leven (1995) the Permian of the Central Pamirs and West Phart are characterised by limestones and dolomite which may be part of a former carbonate platform. The same facies is recorded from the Central Qiangtang and Lhasa blocks

(Leeder et al. 1988, Yin et al. 1988, Taner & Meyerhoff 1990). In the Central Pamirs, the Upper Triassic to Lower Jurassic terrigenous Vomar Formation is interpreted as continental to coastal marine, similar to the Jurassic near-coastal environment described by Schneider et al. (2003) for the Qiangtang block. The Dunkeldyk block differs in rock composition and palaeo-environment: The block is divided into a northern zone of Carboniferous to Permian crystalline rocks in amphibolite facies with schists, marbles, mafic volcanic rocks and cherts. The total thickness is 2500m or more. The rocks are overlain by black shales, marbles, and metabasalts and are probably comparable to the Permian carbonate-chert sequence of the West-Pshart (Leven 1995). The southern zone of the Dunkeldyk block consists of a clastic Carboniferous to Early Permian succession, followed by cherts and cherty schists with Permian conodonts, limestones and basalts. The Triassic is composed of a thick sequence of volcano-sedimentary rocks comparable to the East-Pshart zone. Unfortunately, the Jurassic is not described and can't be related to the Qiangtang and Lhasa blocks.

In summary, I conclude, that the Gondwana northern margin developed a much differentiated Permo-Triassic extensional margin. In a transtensional setting evolved several basins, striking E-W between the Central Pamirs/Qiangtang and SE Pamirs/Lhasa. Such basins or basin fragments are described from the DNB (Schneider et al. 2003) and the Rushan Pshart zone (Leven 1995). These basins were fragmented into deeper basin segments with in some places oceanic crust, cherts, and flysch deposits and shallow marine carbonate accumulations at structural highs. Locally, these structural highs are composed of continental gneissic rocks as the Amdo massif in the eastern BNZ and probably the northern Dunkeldyk block in the eastern RPZ. Probably, the difficulties to correlate the stratigraphic sections, ages, and palaeo-environments of the Rushan Pshart zone arose from the disrupted, incomplete or repeated sections and the lack of an underlying image of a structural and palaeoenvironmental diverse basin. If the initiation of the basin formation was in an back-arc basin setting as discussed for the BNZ couldn't be figured out for the Rushan Pshart zone. Like in the Amdo region, where the ophiolites were thrusted southwards onto the Lhasa block, ophiolites related to the Rushan Pshart zone were found in the south-eastern Pamirs (Chatyrtash and Gurumda sections in Schwab et al. in press).

As mentioned above, there are several intrusive rocks along the southern margin of the Central Pamirs which may be attributed to the closure of these basins. The magmatic rocks show magmatic arc signiture and are therefore interpreted to represent the Mid-Jurassic arc along the southern Qiangtang margin. Middle Jurassic age groups characterise samples L96A9 (170±6 Ma) and M96A7 (~182-156 Ma). The ~169 Ma lower intercept of sample 96M9a may indicate a mid-Jurassic disturbance in the ~239 Ma zircons. In the eastern Qiangtang, Girardeau et al. (1984) and Chang et al. (1989) set the emplacement of the ophiolites into the Jurassic. Mid-Jurassic thrusting affected the Amdo massif, where biotite-grade shear zones and later brittle thrusts accommodated tectonic transport towards the south (Coward et al. 1988). The Amdo gneiss yields a mid-Jurassic lower intercept age for sphene of 171±6 Ma (Xu et al. 1985), which dated the regional metamorphism linked to Jurassic shortening (Chang et al. 1989). An Jurassic arc in the eastern Qiangtang was only speculative. However, Allègre et al. (1984) and Pearce & Deng (1988) suggest northward subduction below

oceanic crust for the consumption of the DNB basin. The arc is likely represented by Jurassic volcanic rocks north and south-west of the Amdo massif (Pearce & Mei 1988, Pearce & Deng 1988). This model accounts for the zonation of rock types such as fore-arc ophiolites, volcanic arc rocks, and back-arc amphibolites from south to north. So far, igneous rocks north of the BNZ are scarce and not much determined. The description and recognition of the mid-Jurassic Rushan Pshart arc along the southern margin of the Central Pamirs/Qiangtang on base of the herein presented geochemical and geochronological data is therefore exceptional.

The correlation of the Karakul-Mazar, Qiangtang and Rushan Pshart zone to Afghanistan is difficult, due to the strong alpine overprint. Furthermore, there are only limited radiometric data, mainly Rb/Sr and K/Ar data, from these regions available (e.g. Debon et al. 1987). Most of them yield Tertiary ages and the truly emplacement ages are obscured. Correlation is more related to the rock associations than to geochemical and geochronological data and the most likely candidates are the Band-e Bayan, Farah Rod, Khas Rod and Safed Khers domains (Fig. 3.1, 3.13).

The Band-e Bayan area is a very poorly known area; it is made up of metamorphic, sedimentary and volcanic formations ranging in age from (?)Precambrian to Cretaceous (Debon et al. 1987). It can only be speculated if these rock associations may be correlatives to the Karakul-Mazar belt in the Central Pamirs. The Band-e Bayan contains small plutonic outcrops. The most common rock types are granodiorites, granites and adamellites, and to a lesser extend trondhjemites. The general character is peraluminous and light, dark or two mica types. In the eastern part, the rocks are transitional to metaluminous types. Most of the rocks are calc-alkaline or sub-alkaline. Like in the Central Pamirs most of the rocks obtained Tertiary and subordinate Lower Cretaceous ages by Rb/Sr and K/Ar dating. Unfortunately no U/Pb ages are available to constrain the crystallisation ages of these intrusions.

The Farah Rod and Khas Rod domains are quite different and tectonically separated by the Khas Rod fault (Fig. 3.13). The Farah Rod domain is probably made up of continental basement overlain by Upper Mesozoic sediments and by dominantly Eocene-Oligocene volcanic rocks. Numerous stocks and small plutons, often associated with volcanic rocks occur. The dominant intrusive types are metaluminous and peraluminous granodiorites, granites and adamellites of subalkaline character. Like in the Central Pamirs there occur transitional to alkaline intrusions with quartz syenites or quartz monzonites. The Khas Rod is an ophiolitic complex associated with spilite-diabas stocks of assumed Early Cretaceous age. Several authors (Karapetov et al. 1975, Bassoullet et al. 1980, Vachard 1980, Mattauer et al. 1981, Tapponnier et al. 1981, Debon et al. 1987) have suggested that the Khas Rod domain is probably the continuation of the Rushan Pshart zone. According to Blaise et al. (1978), the Khas Rod domain represents remnants of a Triassic/Jurassic oceanic basin which closed in Early Cretaceous. Subduction direction was probably to the south, beneath the Central Afghanistan mountains. Like in the Band-e Bayan only Tertiary and Lower Cretaceous K/Ar ages were determined (Debon et al. 1987).

The Safed Khers domain (Fig. 3.1, 3.13) is bounded in the north-west by western Badakhshan and to the south-east by the Axial batholith zone of Pakistan and by the Wakhan zone. Precambrian gneisses and metasedimentary formations (black slates) of

possibly Upper Jurassic and older ages crop out (Debon et al. 1987). These rock associations may be likely equivalents to the metamorphic mélange rocks of the Central Pamirs. Like in the before described Afghanistan regions, there are no crystallisation ages of the plutonic rocks known, but as in the Central Pamirs, there are widely spread and different isolated plutons distributed in the Safed Khers region. In Debon et al. (1987) there are two types described: (1) "a dominant, alumino-cafemic association, either light-coloured subalkaline or transitional to a calc-alkaline or tholeiitic type", or (2) "less commonly, an aluminous, quartz-poor and leucocratic association." The latter rock group may be relatable to the small gabbro intrusives of the Central Pamirs. I wonder, if the Precambrian gneisses would show the same structural features like in the Central Pamirs and Qiangtang block and if they are also composed of mainly accretionary wedge rocks comparable to the metamorphosed Songpan-Ganze mélange of the Central Pamirian and Qiangtang domes.

Southern Pamirs

In the northernmost South Pamirs a series of granites and granodiorites intrude late Palaeozoic to Jurassic rocks in blocks rimmed by Tertiary dextral transpressional faults. These blocks were thrust northward onto the Rushan Pshart zone northwest of Murgab. The determined samples P2 and P5 are high-K, peraluminous S-types, and likely represent mature-arc to late- and post-collisional granitoids. These rocks show LREE enrichment in respect to HREE and La_N/Lu_N ratios of 26-28. They offer the highest Sr-initial values of around 0.711105 and lowest initial Nd-values of around 0.5118197. This likely suggests the highest amount of crustal contamination of all determined samples. The age of these samples is determined by SHRIMP spot ages at about ~119±4 Ma, whereas the lower intercept age, determined by conventional U/Pb dating, is at ~75±9 Ma.

Few magmatic rocks from the Central Pamirs and Rushan Pshart zone yielded also Cretaceous U/Pb ages or age components. The currently northernmost Cretaceous intrusion of this study is latite-andesite A96S1b of the northern Qiangtang block. This sample yielded a lower intercept age of ~74±1 Ma, but more characteristic for its position above the Karakul-Mazar complex is its inherited component of ~1.9 Ga. This ages trace a major age component of detrital zircon ages in the Songpan-Ganze system of eastern Tibet (Bruguier et al. 1997), and a major intrusion period in the Tarim (Kapp et al. 2003, Gehrels et al. 2003). The sample shows also a close geochemical relationship to the central Qiangtang leucogabbro 96M9a. The other samples showing Cretaceous ages or age components are granitoid intrusions into the southern margin of the Qiangtang or Rushan Pshart zone. Sample M96A7 shows a major Mid-Cretaceous age component of 113±3 Ma, determined by the SHRIMP method. Sample 96A10b yielded a lower intercept age of ~126 Ma, whereas the Rb/Sr age of sample P7 is at about 111 Ma.

In Tibet, along the BNZ, a bimodal suite of metaluminous tonalite-granodiorite and two-mica granites occur, which were emplaced around 140 to 80 Ma in a post-collisional setting (Xu et al. 1995, Harris et al. 1988). During the Early Cretaceous to Mid-Eocene, the Dongqiao-Naqu basin (DNB) became again a back-arc basin, while continuing to be a remnant basin (Schneider et al. 2003). Certain Cretaceous and

Palaeogene volcanic rocks of central and southern Tibet show arc affinities (Coulon et al. 1986) and Ar/Ar ages ranging between 110 and 80 Ma in the north and between 60 to 50 Ma in the south. Coulon et al. (1986) relate this ages to north directed subduction beneath Lhasa, with shallow subduction until 80 Ma, followed by steeper subduction. The plutonic Gangdese/Transhimalaya belt of the southern margin of Lhasa is the manifestation of this subduction zone (e.g. Schärer et al. 1984, Harris et al. 1988, Miller et al. 2000). Miller et al. (2000) compared several own and published age data of magmatic rocks from different parts of the whole Transhimalayan magmatic belt and could define two major intervals of calc-alkaline magmatism: a mid-Cretaceous peak at about 120-90 Ma and a Palaeocene and Eocene time interval at around 60 to 40 Ma. The first interval fits very well the findings of this study, even so in the Pamirs it is concluded that the Cretaceous magmatism may have been bimodal with peaks at ~120 Ma and ~75 Ma.

The amalgamaltion history beween the Indus –Yarlung and the Rushan Pshart sutures is in many aspects speculative (e.g. Hildebrand et al. 2000, Fraser et al. 2001). South of the southern Pamirs and Lhasa follow the Wakhan, eastern Hindu Kush, and Karakoram blocks. Whereas the South Pamirs comprises mainly undifferentiated Cretaceous and Tertiary intrusives, the Karakorum is composed of metamorphic and sedimentary rocks intruded by subduction related granitoids with predominately Early Cretaceous and locally Jurassic ages. The boundary between the East Hindu Kush block and the Karakorum is supposed along the Rich Gol Metamorphic Complex (RGMC), a narrow strip along the Tirich Mir fault (Zanchi et al. 1997). The RGMC is composed of high-grade metabasites with serpentinites and metapelites. Zanchi et al. (1997) conclude, that the East Hindu Kush and Karakorum share a common history at least since Mid-Cretaceous, as both blocks are intruded by the East Hindu Kush granitoids. One of these, the Tirich Mir pluton, records a Rb/Sr whole rock age of 115±4 Ma (Desio et al. 1964), but is probably poorly constrained (Hildebrand et al. 2000). The Kafiristan pluton yield a Rb/Sr whole rock age of 480 Ma (Debon et al. 1987), which is a typical Gondwanan age. Within the Tirich Mir fault, pegmatite dikes crosscut staurolith schists; the latter yield U-Pb monazite ages of 135-126 Ma near Gharam Chasma. U-Pb dating of uraninites from one of these pegmatites revealed an age of 114±2 Ma (Hildebrand et al. 2001). Thrusting along the Tirich Mir fault took place during the Cretaceous (Hildebrand 1998). The southern margin of the eastern Hindu Kush region was discriminated by a continental margin type above a north-dipping Tethyan oceanic subduction zone. The collision between the Karakorum and the southerly adjacent Kohistan-Ladakh arc was about ~80 Ma along the Shyok/Northern suture (e.g. Chandra et al. 1999). Finally, India collided with the amalgamated Eurasia at about 55-50 Ma. A major phase of crustal continental melting in the South Pamirs, East Hindu Kush, and Karakorum regions led to the emplacement of leucogranites, like the Gharm Chasma pluton (~24 Ma) in the Hindu Kush and the Baltoro granite in the central and eastern Karakorum (Hildebrand et al. 2001).

Zircon geochronology of Cretaceous and Cenozoic granitoids from the southern Qiangtang to northern South Pamirs and from crustal xenoliths erupted from 90-100 km depth in the south-eastern Pamirs during the Miocene (Ducea et al. 2003) chronicles multiple Phanerozoic additions to a Proterozoic crust derived from Gondwana. The

most distinct magmatic events occured during the Cambro-Ordovician (575-410 Ma; Qiangtang and South Pamirs), Triassic (250-200 Ma; Qiangtang, by southward subduction along the Tanymas/Jinsha suture), Mid-Jurassic (200-150 Ma; Qiangtang and Rushan Pshart zone, by northward subduction along the Rushan Pshart/Bangong-Nujiang suture), Mid-Cretaceous (~120 Ma; Qiangtang, Rushan Pshart, and South Pamirs, by probably northward subduction along the Tirich Mir/Kilik (?)suture), and Late Cretaceous (~80 Ma; Qiangtang, Rushan Pshart, and South Pamirs, by subduction along the Shyok suture).

3.7 Conclusions

Based on new own and published data it is for the first time possible to develop a comprehensive model of the amalgamation history of the Pamirs and to integrate and correlate this model into existing geodynamic models from Tibet and Afghanistan. This thesis closes the gap of the Palaeo- and Neo-Tethyan closure history from the Alps to Eastern Asia. Suture zones offer a variety of tectonic contexts from subduction to collision to mountain building. Diachronous development of structures produced by these processes provides a unique overview of Tethyan closure since in many cases several stages exist simultaneously in the suture zone (Fig. 3.11, 3.16) and can be directly compared. Detailed regional studies about the structure of crustal, lithospheric, or whole-mantle scale, on the P-T-t evolution of metamorphic domains, on magmatic and volcanic products related to the Tethyan closure, and on Tethyan marginal and continental basin evolution form the basis for a useful synthesis of Tethyan and Central Asian mountain belt tectonics. The detailed analyses and regional syntheses of the Pamiran amalgamation are pertinent to the modelling of the large-scale general structures and form the basic understanding for the Tertiary deformation and exhumation history.

The Early Permian, calc-alkaline South Tien Shan samples described in this study, are correlated with the Garm-Turkestan-Alay zone granitoids, and correspond to a mature calc-alkaline arc north of the South Gissar suture. The Baysunta and Garm basements, which crops out in the Gissar range and Garm-Turkestan-Alay zone may be interpreted as part of the Tadjik continental block that connects with the Tarim block underneath the northern Pamirs. It follows, that any westward extension of Early Paleozoic sutures of northern Tibet, e.g. the Kudi suture, must be located south of the Tadjik massif.

The northern Pamirs and north-western Tibet contain the north-facing Kunlun suture, the south-facing Jinsha suture, and the intervening Carboniferous to Triassic Karakul-Mazar subduction-accretion system; the latter is correlated with the Sonpan-Ganze mélange of Tibet. The Kunlun arc is the juxtaposition of an Early Palaeozoic (north Kunlun) and a Late Palaeozoic-Triassic (south Kunlun) arc. In the northern Pamirs, the ~370-320 Ma old metavolcanic Altyndara rocks are representatives of the north Kunlun arc. Arc activity most likely extended into a Triassic back-arc basin setting.

Fig. 3.16: Distribution and correlation of sutures across the Pamiran-Tibetan regions. Bold line outline the suture zones with decreasing ages from north to south. The Turkestan/North Tien Shan suture (in black) is thought to be of Early- to Mid-Palaeozoic age and the Gissar/South Tien Shan sutur of Late Palaeozoic age (in light blue). The northern Pamirs contains the composite Early and Late Palaeozoic Kunlun arcs (in dark blue). The southward subducting Jinsha suture (in violett) is of Late Triassic/Jurassic age, whereas the Rushan Pshart suture (in green) most likely closed in Mid-Jurassic time. The collision of the Karakorum block with the south-eastern Pamirs is supposed to be along the upper Lower Cretaceous Tirich Mir/Kilik (?)suture (in yellow). Finally, due to approaching India, the Kohistan-Ladakh arc was sutured at ~80 Ma along the Shyok arc (in yellow) to the Karakorum. The amalgamation was completed with the India-Asia collision along the Indus-Yarlung suture (in red) at about 55 to 50 Ma.

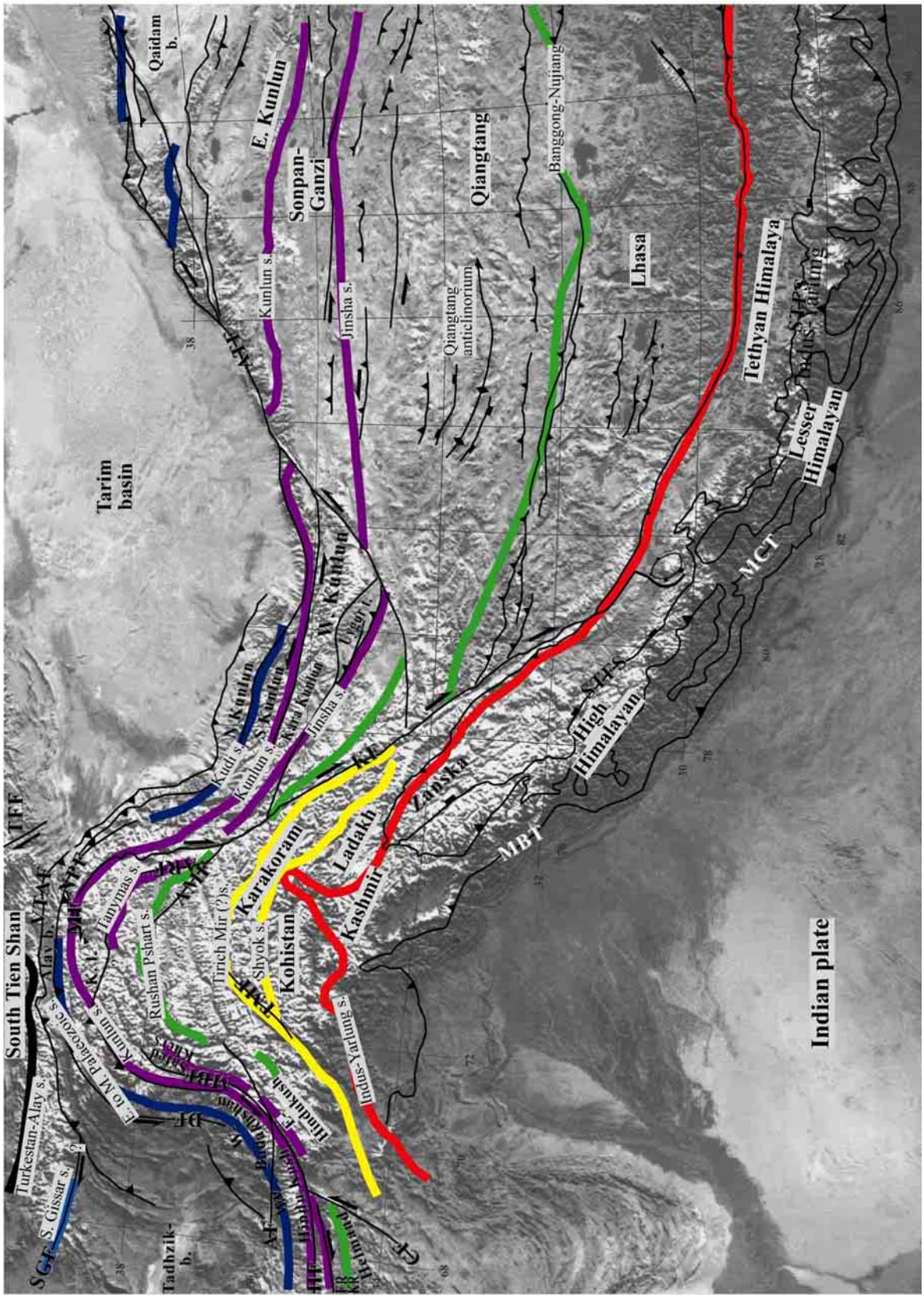
South Tien Shan
Turkestan-Alay s.
S. Gissar s.
Alay b.
Tadzhik-b.
Tarim basin
Qaidam b.
E. Kunlun
Sonpan-Ganzi
Kunlun s.
Jinsha s.
Qiangtang
Qiangtang anticlinorium
Banggong-Nujiang
Lhasa
Tethyan Himalaya
Lesser Himalayan
Indian plate
TFF
ATF
KTF
MKT
KF
MBT
MCT
STDS
Karakoram
Ladakh
Kohistan
Kashmir
Zanska
High Himalayan
Indus-Yarlung s.
Tanymas s.
Rushan Pshart s.
Shyok s.
Tirich Mir (?)s.
Kudi s.
Kara Kunlun
Uygur t.
Hindukush
Pamir
Helmand
Chaman

The Permo-Triassic volcano-siliciclastic sediments of the Lake Karakul area constitute the Karakul-Mazar/Sonpan-Ganze accretionary wedge rocks. The Late Triassic/Jurassic Karakul lake batholith is stitching together the Kunlun arcs and are correlated to the western Kunlun (Akarz mountain pluton, (?)Sailiyak magmatic belt) and to the western Badakshan, western Hindu Kush, and Feroz Koh regions (e.g. at Salang pass).

South of the northern Pamirs/Kunlun, the cryptic Tanymas/Jinsha suture evidence mainly Triassic southward subduction of the Karakul-Mazar/Sonpan-Ganze ocean beneath the Central Pamirs/Qiangtang block. The basement antiforms of the Central Pamirs and Qiangtang, formerly interpreted to be of Precambrian age, are mainly composed of exhumed medium to high-grade metamorphic Tanymas/Jinsha ocean floor and Triassic/Jurassic basin associations. Eventually, in the Safed Khers related basement domes are exposed and the Band-e Bayan and Farah Rod can be correlated with the Central Pamirs and Qiangtang.

The southern margin of the Central Pamirs and the Rushan Pshart zone are intruded by several granitoids of diverse composition and with distinct age groups or age components from 250-200 Ma and 200-150 Ma. The first group is attributed to the southward subduction along the Jinsha suture, whereas the latter group represent the Rushan Pshart arc, which developed by Jurassic northward subduction of oceanic lithosphere of the Rushan Pshart basin. A similar zone is found along the Bangong-Nujiang zone in Central Tibet. As in the Pamirs, the closure of scattered oceanized basins along the Rushan Pshart and Bangong-Nujiang zones led to the collision of the Central Pamirs/ Qiangtang block with the SE Pamirs/Lhasa blocks. South of the SE Pamirs/Lhasa terranes, a new active margin established. Probably upper Lower Cretaceous (~120 Ma) collision of the Karakorum with the eastern Hindu Kush and SE Pamirs along the Tirich Mir/Kilik (?)suture and Late Cretaceous (~80 Ma) collision of the Kohistan/Ladakh arc with the Karakorum along the Shyok suture caused bimodal intrusion of granitoids as far as to the northern Central Pamirs.

This study suggests a relatively simple first-order crustal structure for the Pamirs and Tibet. From the Kunlun arc in the north to the southern Qiangtang block in the south, the Pamirs and Tibet have a dominantly (meta)sedimentary crust, characterised by the Karakul-Mazar/Sonpan-Ganze accretionary wedge rocks. The crust south of the southern Qiangtang block is likely of granodioritic composition, reflecting long-lived subduction, arc formation and Cretaceous-Cenozoic underthrusting of arc segments beneath the Qiangtang block.

4 Cenozoic exhumation history of the southernmost Tien Shan and eastern Pamirs

4.1 Introduction

In the previous chapter it was suggested that the Pamirs assembled by orogenic processes from Late Palaeozoic to Mesozoic times, i.e. by the development of successively southward-stepping Andean-type plate margins. In contrast, the Recent Pamirs mountain range is a result of the Tertiary India-Asia collision, which brought the Pamirs into an intra-continental plate position.

So far, no comprehensive study exists about the Tertiary thermal evolution of the Pamirs. Regional studies define an important Tertiary tectonothermal event in the south-western Pamirs (Hubbard et al. 1999) and eastern Central Pamirs (Ratschbacher & Schwab 1999, Schwab et al. 1999, 2000), but it remains an open question where exactly Cenozoic deformation and related exhumation is located in the Pamirs and when exhumation started. Several Tertiary intramontane basins along the southernmost Tien Shan, the margins of the external Pamirs, and in the Central Pamirs are indicative for active erosion during the Tertiary.

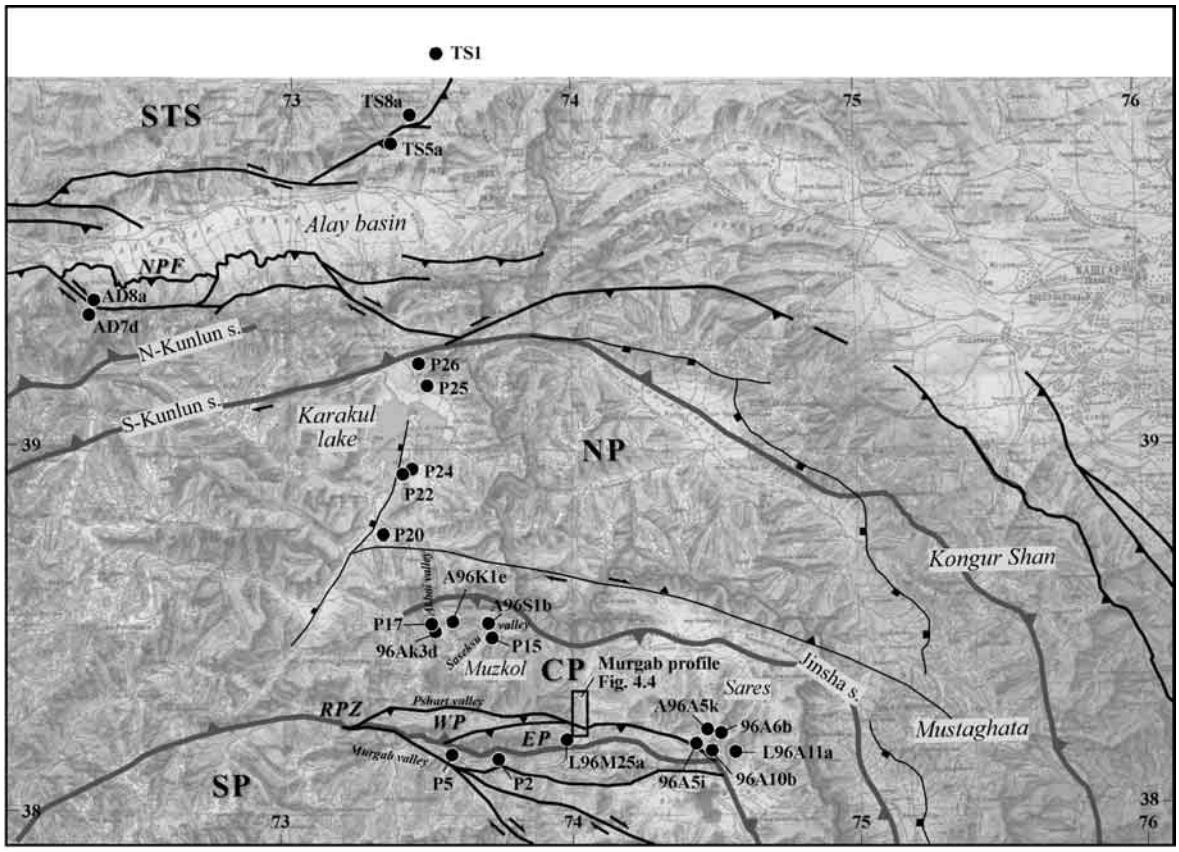

Fig. 4.1: Location map of samples determined for the Tertiary cooling history. Black lines constrain the main faults, bold grey lines the main sutures and black dots the sample locations. NPF = North Pamir fault, STS = South Tien Shan, NP = North Pamirs, CP = Central Pamirs, SP = South Pamirs, RPZ = Rushan Pshart Zone (following Burtman & Molnar 1993), WP = West Pshart, EP = East Pshart (according to Leven 1995).

Fission track thermochronology is a low-temperature geochronological method and a well-established and powerful tool to constrain the thermal evolution of the upper crust. Thus, the method enables to constrain the latest stage of mountain building in the Pamirs. It allows the reconstruction of the onset and rate of cooling. Assuming that the geothermal gradient is known, cooling rates can be transformed into denudation rates which in turn can be related to tectonic activity.

4.2 Results

Fission track dating

The sample locations and the list of fission track samples are summarised in Fig. 4.1 and Appendix C, Tab. C1. Zircon and apatite fission track ages were determined on 25 samples. The analytical data of apatites and zircons are listed in Appendix C, Tab. C4 and C6, respectively. The data for apatites are illustrated in Appendix C, Fig. C1, those of zircons are shown in Appendix C, Fig. C3. The regional distribution of the fission track ages is shown in Fig. 4.2-4.5. The results of the decomposed fission track ages of sediment samples are listed in Appendix C, Tab. C7 and Fig. C4.

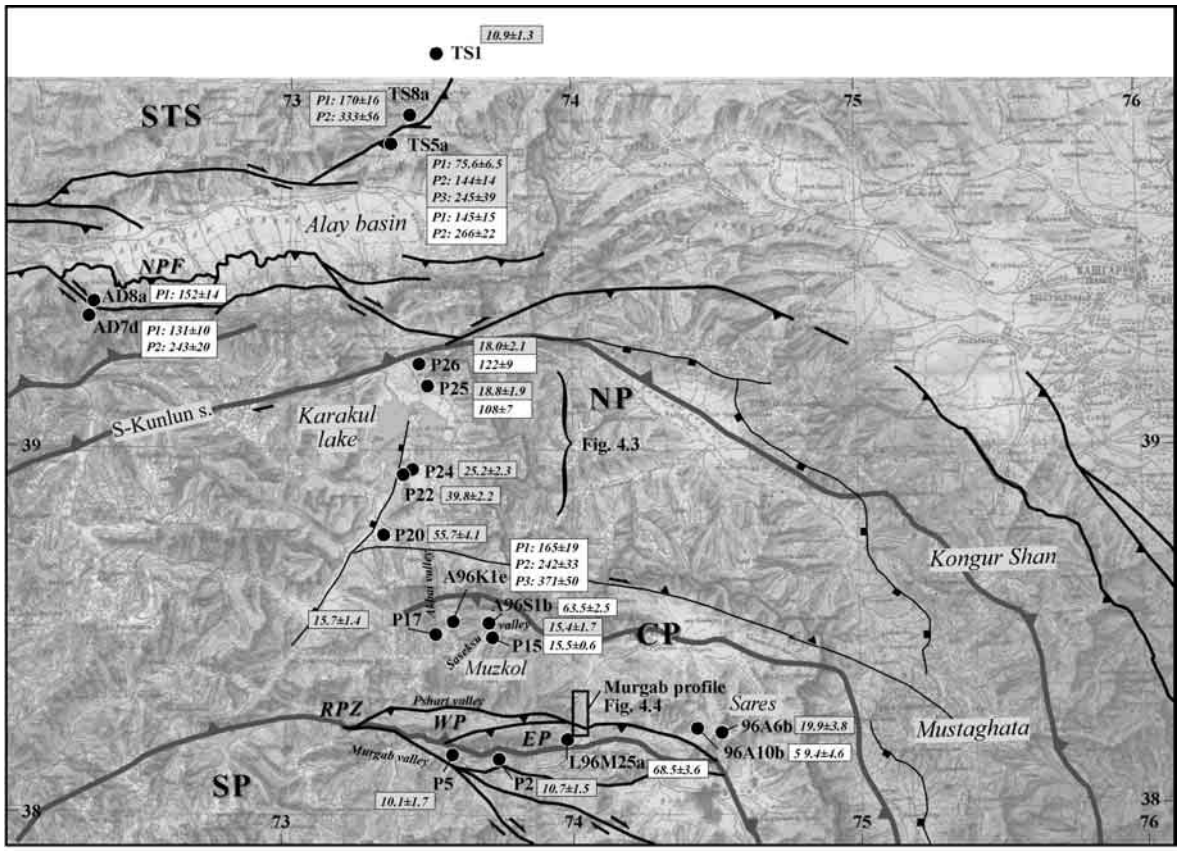

Fig. 4.2: Distribution of zircon and apatite fission track ages of the southernmost Tien Shan and eastern Pamirs. Gray boxes refer to apatite fission track ages, white boxes to zircon fission track ages. In case of sediment samples, the decomposed fission track grain ages are documented as peak ages P1, P2, P3. All other ages are Central ages and belong to hardrock samples. All errors refer to 1σ confidence level. Black lines constrain the main faults, bold grey lines the main sutures and black dots the sample locations. NPF = North Pamir fault, STS = South Tien Shan, NP = North Pamirs, CP = Central Pamirs, SP = South Pamirs, RPZ = Rushan Pshart Zone (following Burtman & Molnar 1993), WP = West Pshart, EP = East Pshart (according to Leven 1995).

Southern Tien Shan

One Permian granite sample (TS1) and two sandstone samples (TS5a, TS8a) from a SW-NE striking Tertiary intramontane basin of the southernmost Tien Shan have been dated (Fig. 4.2). The apparent apatite fission track age of hardrock sample TS1 is 10.9±1.3 Ma. Sample TS5a was probed from ?Neogene sediment strata, sample TS8a from ?Lower Palaeogene strata (Geological map 1:200.000 of Kyrgyz SSR, 1958). The apatite and zircon fission track samples of the sandstones do not pass the χ^2 test and therefore denote the occurrence of multiple age populations within the samples. Modelled peak ages (Appendix C, Tab. C7, Fig. C4) are Lower Carboniferous (333 Ma, TS8a apatite), Permian (266 Ma, TS5a zircon; 245 Ma, TS5a apatite), Middle to Late Jurassic (170 Ma, TS8a apatite; 144-145 Ma, TS5a zircon and apatite), and Late Cretaceous (76 Ma, TS5a apatite).

Northernmost Pamirs, N-Kunlun

Two sandstone samples (AD7d, AD8a) were probed from a Tertiary intramontane basin along the northern flanks of the Pamirian frontal range (Fig. 4.2). From both samples zircon fission track grain ages could be determined. Sample AD7d shows again a non-reset grain age distribution with modelled peak ages at ~243 Ma and ~131 Ma (Appendix C, Tab. C7, Fig. C4). The sample AD8a offered only 6 datable grains, which seem to represent only one single age population with a central age of ~152 Ma.

Karakul-Mazar granitoids, Northern Pamirs

Five different granitoid locations (P20, P22, P24, P25, and P26) were probed across the Karakul-Mazar batholith belt (Fig. 4.2). Two zircon fission track samples P25 and P26 yield apparent ages of 108 Ma and 122 Ma, respectively. Apparent apatite fission track ages range from Eocene to Miocene (56-18 Ma) with a trend to younger ages towards the north (Fig. 4.3).

Qiangtang block, Central Pamirs

For a better understanding of the sample localities, the structural units and lithologies of the Central Pamirs are shortly repeated here: (1) A pre-Late Palaeozoic Qiangtang basement is inferred from inherited zircons of granitoid sample P17 and correlations with Tibet. (2) Triassic-Jurassic meta-siliciclasic and metavolcanic rocks are exposed in the Muzkol and Sares domes and were metamorphosed and deformed during the Tertiary. They are interpreted to correspond to the Karakul-Mazar-Sonpan-Ganze accretionary wedge rocks, associated with the subduction of the Jinsha oceanic crust. Likely remnants of this oceanic crust are small Triassic/Jurassic gabbro bodies within the Muzkol and Sares domes. (3) Few Cretaceous magmatic rocks are exposed in the Qiangtang block (e.g., 96A10b, A96S1b). Late Cretaceous sample A96S1b from the northern margin of the Qiangtang block shows geochemical affinity to the Central Qiangtang gabbros and to the Karakul-Mazar substratum. Sample 96A10b is of upper Lower Cretaceous age and from the southern margin of the Qiangtang block. Rock generation is probably more related to subduction processes along the Shyok arc. The sample A96S1b yielded a central zircon fission track age of ~64 Ma, whereas sample 96A10b obtained a mean zircon fission track age of ~59 Ma, probably suggesting that the zircon grains might be partly reset (Fig. 4.2). (4) The Muzkol and Sares domes provide an outstanding example for India-Asia post-collisional intracontinental deformation within Central Asia. The domes represent an antiformal structure,

previously defined by Russian geologists as a Precambrian to Palaeozoic basement window (Burtman and Molnar 1993, and Russian reference cited therein; Geological map of Tadzhik SSR 1:500 000). This thesis and Schwab et al. (in press) demonstrated that these basement rocks were formed mainly in Triassic/ Jurassic times during subduction of the Jinsha oceanic crust and flysch sedimentation in the intervening Sonpan-Ganzi basin. In contrast, the exhumation of the domal structure is a Tertiary feature. Miocene apatite fission track ages were obtained from the Early Palaeozoic intrusion P17 (~16 Ma), from the Tertiary intrusion P15 (~15 Ma), and from the Tertiary aplitic dyke 96A6b (~20 Ma). The zircon fission track age of the sample P15 is around 16 Ma (Fig. 4.2). (5) Sandstone samples from Teriary intramontane basins along the southern and northern margins of the Muzkol dome define different Tertiary histories on both sides of the dome: (a) The zircon fission track grain age distribution of the Palaeogene sandstone sample A96K1e of a Tertiary basin north of the Muzkol dome is not reset. Hence, the age spectrum defines several age populations (Appendix C, Tab. C7, Fig. C4): The oldest peak is around 370 Ma, a further peak is in Early Triassic around 242 Ma, and the youngest peak age clusters around 165 Ma (Fig. 4.2). (b) Two sandstone samples from an intramontane basin south of the Muzkol dome, the herein called 'Murgab section' (Fig. 4.4), yielded single zircon fission track grain age populations with central ages of ~20 Ma and ~19 Ma (M96A6b and A96M4b, respectively).

Rushan Pshart arc

Triassic/Jurassic arc-type intrusions and a Triassic oceanic-basin-arc sequence in the eastern Pshart constitute the Rushan Pshart arc. Sample L96M25a, a monzogranite, yielded an zircon fission track age of 68.5±3.6 Ma (Fig. 4.2).

Shyok arc

Late Cretaceous granodiorites (P2 and P5) are the southernmost samples dated in this study and are related to the Shyok arc. Apatite fission track ages of these samples are around 10 Ma and so far the youngest fission track ages in the Pamirs (Fig. 4.2).

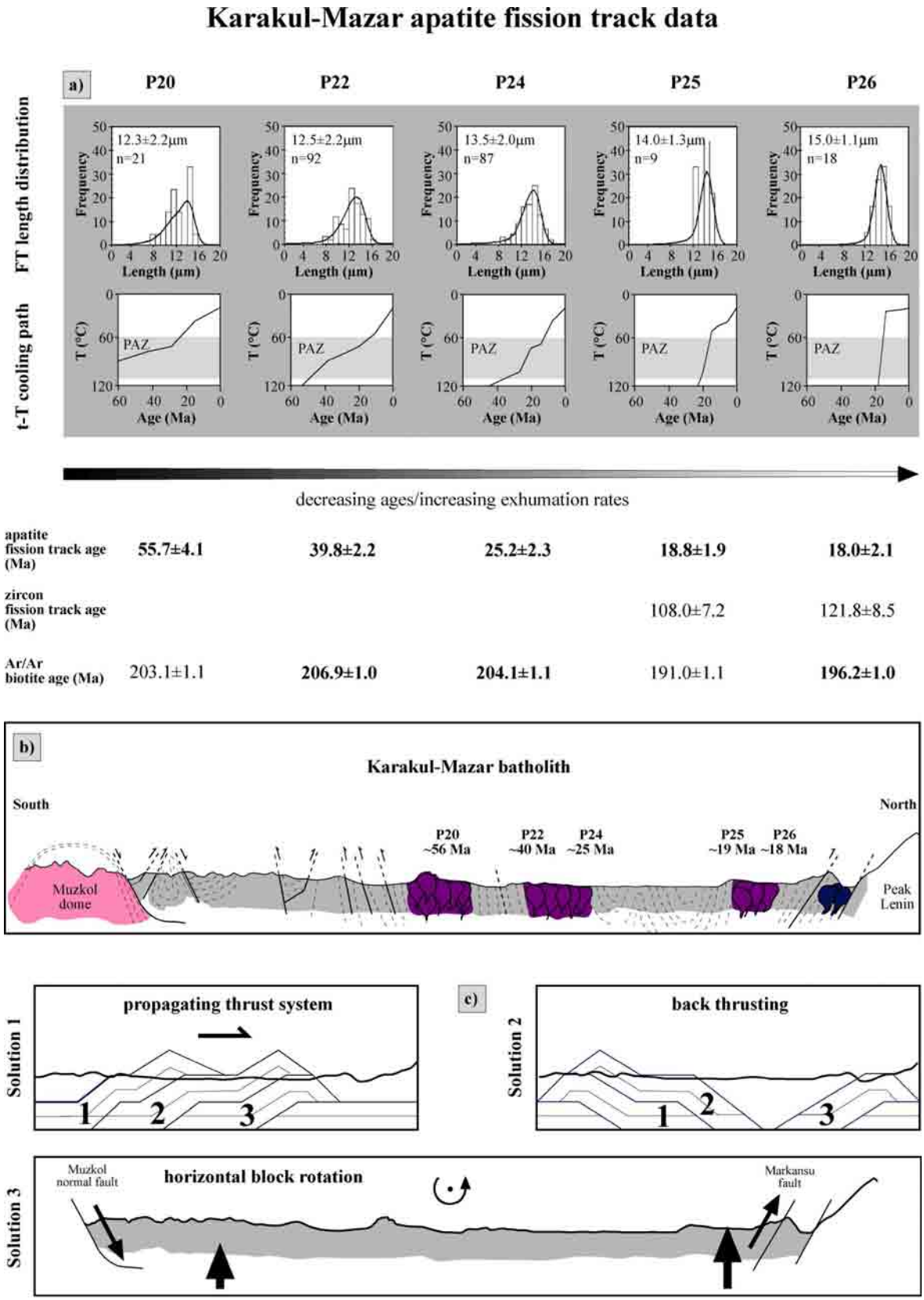

Fig. 4.3: Summary of the fission track data from the Karakul-Mazar belt. (a) shows the track length distribution and final cooling through the apatite partial annealing zone (PAZ). The t-T paths were modelled with the program AFTSolve (Ketcham et al. 2000). Bold ages confirm the northward decreasing age trend. (b) gives an overview of the sample locations and age distributions. (c) presents different structural solutions which might be responsible for the age and track length distribution as well as the cooling paths.

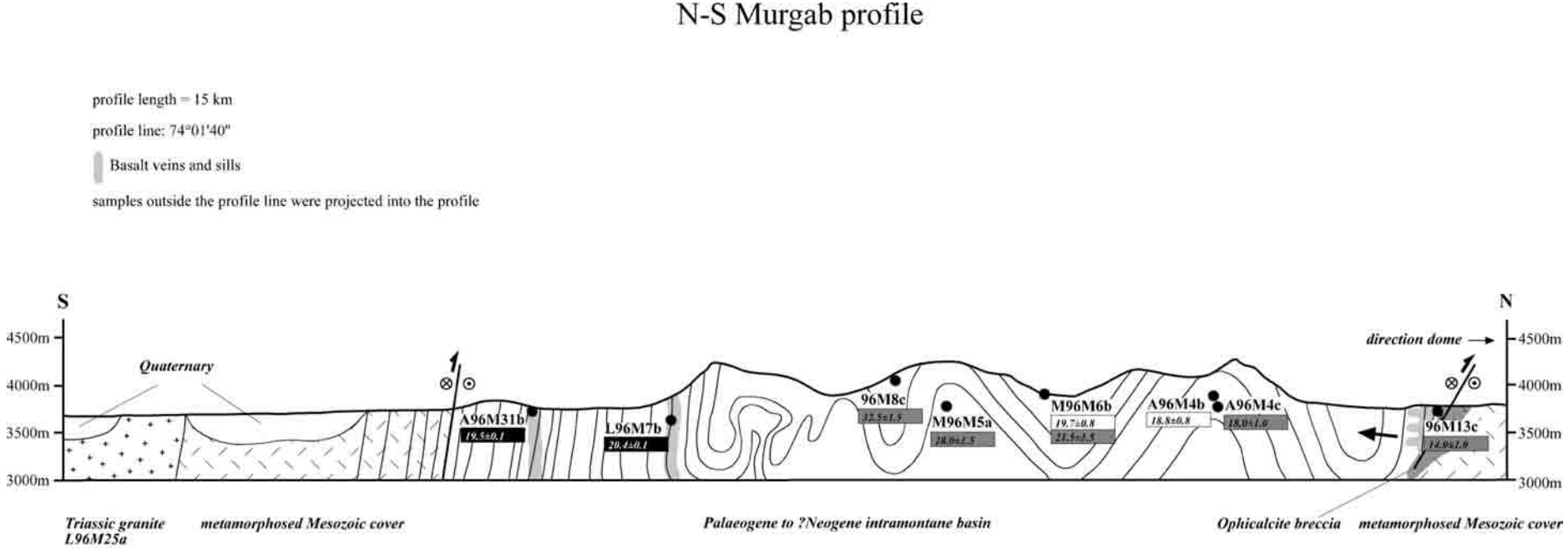

Fig. 4.4: N-S profile of the intramontane Murgab basin, southerly adjacent to the Muzkol dome. The section shows the basin structure and fission track zircon ages (in white frames) and sericite K-Ar ages (grey frames, the data table is documented in Appendix A, Tab. A4), of Palaeogene to ?Neogene sediments of the basin. Ar/Ar whole rock ages from basalts cutting the section are in black frames (the data table is documented in Appendix A, Tab. A3).

Thermal modelling

The results of the thermal modelling are graphically illustrated in Appendix C, Fig. C2a-k. Modelling was performed on samples having enough measurable confined track length, which is dependent on the U-content and the age of the sample. Hence, not in all regions the latest cooling history could be modelled. AFTSolve models the temperature range of the apatite partial annealing zone, thus the temperature range of around 60°C to 110°C. All suggested cooling paths above or below the PAZ temperatures are therefore only inferred from the modelling results, but are not modelled themselves.

To model the time-temperature history of the granite samples from the Karakul-Mazar belt, the Ar/Ar data and zircon fission track ages were also considered. Modelling was started at the maximum boundary temperature of the program at 325°C with the Ar/Ar biotite age of the sample. The southerly samples P20 to P24 have mean track lengths between 12.4 μm to 13.4 μm indicating slow cooling through the partial annealing zone (Fig. C2a-c). In contrast, samples P25 and P26 have mean track lengths of 14.4 μm and a narrow track length distribution, suggesting fast cooling in Miocene times (Fig. C2d-e). Cooling through the PAZ increases from 0.5°C/Ma in the south (P20) to 25°C/Ma in the north (P25). From the modelling it is inferred that after passing the PAZ, the samples show cooling rates in the range of 1.7°C/Ma to 3.2°C/Ma until reaching the present day surface temperature of 20°C. The samples left the PAZ from ~23 Ma to ~12.5 Ma. In the modelling, the zircon fission track ages of 122 Ma (P26) and 108 Ma (P25) were also considered and similar zircon fission track ages around 120 Ma were assumed for the other 3 samples. The modelled cooling histories offer different best-fit time-temperature paths during Mesozoic times for the samples: P20 shows a Mid to Late Jurassic cooling event from about 300°C to 110°C, sample P22 Late Cretaceous cooling in the same temperature range, whereas for sample P25 cooling from 300°C to 110°C is inferred for Eocene times. Samples P24 and P26 show constant moderate cooling from about 1.2°C/Ma for the temperature range >110°C. Other modelling attempts considered constrains around 150 Ma and 80 Ma, as these thermal events are suggested from sediment samples from adjacent regions. Modelling solutions did not show any difference in the goodness of the statistical parameters of modelled age and track length nor was a mid-Jurassic cooling event well detectable from the cooling paths.

Samples P17 and P15 from the Muzkol dome have apparent fission track ages around 15 Ma with track lengths between 14.1 μm to 14.7 μm suggesting fast cooling (Fig. 2f-g). The best fit models suggest nearly identical time-temperature evolutions for both samples with very rapid cooling before entering the PAZ. Sample P17 cooled between 23 to 14 Ma with an inferred rate of 24.4°C/Ma. Cooling through the PAZ was modelled with a rate of 14.3°C/Ma and final cooling to surface temperatures, starting around 11 Ma, is again inferred from the model with a rate of 3.6°C/Ma. Sample P15 cooled very rapid at 16-15 Ma: the Ar/Ar biotite and potassium-feldspar ages and the zircon and apatite fission track dates are within errors nearly identical. Upon entering the PAZ, cooling seemed to have decreased to a rate of 18.5°C/Ma. Upon leaving the PAZ at ~12.3 Ma, the rate decreased to 3.3°C/Ma until reaching the today's surface temperature. In summary, the samples of the Muzkol dome show the highest average

cooling rates of all samples.

Samples P2 and P5, the Late Cretaceous intrusions of the northernmost South Pamirs, were difficult to model, due to their low number of confined track length (<10). The track length distribution of both samples is different: Sample P2 has a mean track length of 14.0±1.7 μm suggesting fast cooling, whereas sample P5 has a mean track length of 11.0±3.2 μm suggesting slow cooling. The track length distribution of sample P5 implies a bimodal distribution, but might be not representative due to the low amount of tracks. Nevertheless, the time-temperature histories of sample P2 and P5 were modelled in two ways: (1) Like for the other samples, a simple cooling history was assumed (Fig. C2h,j). In this case, from the best fit time-temperature path it is inferred that sample P2 cooled continuously from 98-10 Ma with an average cooling rate of 2.4°C/Ma. Cooling through the PAZ from ~10-7.5 Ma was with an increased rate of 20°C/Ma. Final cooling from latest Miocene to recent occurred at 5.3°C/Ma. The time-temperature path of sample P5 is different. In the best-fit solution sample P5 remains in the assumed Ar/Ar biotite retention zone until the onset of the India-Asia collision (~55 Ma). Then, the sample cools to the lower temperature boundary of the APAZ at 110°C at 40 Ma with a high cooling rate of 6.7°C/Ma. From about 40-5 Ma the sample P5 remained into the APAZ and cooled very slowly with 1.3°C/Ma. The model suggests that cooling increased after leaving the PAZ to an average rate of 16°C/Ma. (2) As zircon fission track ages of these samples could not be determined, the following assumptions were made: (a) From crystallisation ages of the intrusives of the Shyok arc it is known that the Cretaceous magmatism was episodic (chap. 3, Schwab et al. in press) with peaks at ~120 Ma and ~80 Ma. (b) Hence, a constrain was set at ~80 Ma in case of sample P2. (c) A further major thermal event was assumed with the onset of the collision between India and Asia at ~55 Ma and (d) another constrain was set in the early Miocene, the initiation of the major exhumation phase in the whole Pamirs as reconstructed by low-T geochronology in this study. Interestingly, the modelling results of samples P2 and P5 are very similar (Fig. C2i,k): After emplacement (P2 ~120 Ma, P5 probably ~80 Ma or also at 120 Ma) both samples cooled relatively fast to temperatures below 150°C with 18-35°C/Ma. With the onset of the India-Asia collision, samples were reheated down to the zircon partial annealing zone (ZPAZ) with a comparable heating rate of 2.5-4.0°C/Ma. In both cases, reheating reaches temperatures of around 210°C which should totally anneal older fission tracks. From this result it becomes clear that the models interpret the track length distribution of sample P5 not as a bimodal distribution, because in such a case the reheating temperature should be in the range of the PAZ. Sample P2 enters the PAZ at ~14 Ma and leaves the PAZ at ~7 Ma. Cooling through the PAZ is with an average rate of 12.5°C/Ma. Sample P5 cools through the PAZ from 16-2 Ma with an average rate of 3.6°C/Ma. If the model (2) solution is reasonable for both samples, might be clarified with zircon fission track data from these samples.

Other dating methods

Beside fission track dating, further methods were applied to constrain the Tertiary thermal evolution of the southernmost Tien Shan and eastern Pamirs i.e. U/Pb zircon dating (Appendix A, Tab. A7), Rb/Sr whole rock-muscovite dating, Ar/Ar dating of

amphibole, white mica, and biotite as well as K/Ar dating of sericite (Appendix A, Tab. A3, A4, A5). These dating methods were determined on samples from the Muzkol and Sares domes (Fig. 4.1):

(1) Rb/Sr whole rock-muscovite ages of basement rocks, e.g. biotite schists and gneisses, were determined on two samples from the southern side of the Sares dome. Sample 96A5i yielded 37.1±0.4 Ma and sample A96A5k 30.0±1.2 Ma. The sample 96Ak3d from the northern side of the Muzkol dome obtained an age of 68.0±7.7 Ma. As the error is very high, the date will not be included into the discussion or conclusion.

(2) Several intrusions and dykes of likely Tertiary age were probed in the Muzkol and Sares domes. Sample P17, an undeformed aplite dyke that cuts high-grade biotite gneiss in the Muzkol dome is already described in chap. 3: the sample contains inherited zircons with spot ages in the range of 561 to 424 Ma, which are attributed to characterise the Qiangtang basement. Conventional U/Pb zircon dating points to an upper intercept age of 539±5 Ma with assumed Pb-loss at 44±22 Ma. Such a crystallisation/Recent Pb-loss model infers Tertiary disturbance of the U/Pb system, even so no Tertiary rims could be detected with SHRIMP analyses. Nevertheless, it was suggested that the dike was emplaced in the Tertiary (Schwab et al. in press). Another Tertiary intrusion (P15) into the Muzkol dome and a dyke of the Sares dome (96A6b) yielded conventional U/Pb zircon upper intercept ages of 540±4 Ma and 570±230 Ma, respectively. The lower intercept age is around 31±2 Ma in case of sample P15, and around 17±8 Ma for sample 96A6b. The U/Pb data are included in Appendix A, Tab. A7.

(3) Rb/Sr whole rock-muscovite dating of sample L96A11a, a pegmatitic dyke cross-cutting basement units of the Sares dome, gave an age of 13.7±0.1 Ma (see Appendix A, Tab. A5).

(4) Ar/Ar amphibole, muscovite, and biotite ages of the Muzkol and Sares domes were obtained from basalts, basement, and intrusive rocks. The data are summarised in Appendix A, Tab. A3. The metamorphic mineral ages are in the range of 28 to 14 Ma. Tertiary basalts crosscut the Muzkol and Sares domes and extruded in an extensional setting as indicated by structural analyses and preliminary geochemical classifications (see Appendix A, Tab. A2). The basalts yield Ar/Ar whole rock ages of about 20 Ma.

(5) Sandstones from Tertiary sediments from the Murgab profile (Fig. 4.4) show anchi- to greenschist facies overprint. Five samples of metamorphic grown sericite were dated by the K/Ar method (see Appendix A, Tab. A4). The ages range from 14 Ma in the north of the section to 33 Ma further to the south.

4.3 Discussion

South Tien Shan

Fission track ages of Tertiary sediments from the southernmost Tien Shan confirm the Palaeozoic and Mesozoic history of the Tien Shan as suggested in chapter 3: the basement of the Tien Shan is composed of different terranes which were originally sutured together during two collisions in Late Devonian-Early Carboniferous and Late

Carboniferous-Early Permian time. The oldest peak age of 333±56 Ma, determined from the above mentioned sediments, is from apatite sample TS8a (Appendix C, Tab. C7, Fig. C4). The peak contains only 13.4% (2 grains) of the whole grain fraction and interpretations should be taken with care. Nevertheless, this age may mirror the Early Carboniferous collisional phase along the southern margin of the Tien Shan (e.g. Allen et al. 1993). Collision ceased in the Tien Shan by latest Permian times (see chapter 3). Permian cooling, most likely related to erosive denudation, is demonstrated at mid-T ranges by Ar/Ar biotite cooling ages of granitoids at 277 Ma (samples TS12b and TS20a, Appendix A, Tab. A3), and at low-T ranges by sandstone fission track peak ages at 266 Ma (TS5a zircon) and 245 Ma (TS5a apatite). During the Triassic, the whole Central Asian region was under extension, initiated by the break-up of Pangea. The opening of several Permo-Triassic basins with huge sediment accumulations suggests several high lands along the margins of these basins, which shed a vast amount of sediments. The Tarim, Tadjik and Sonpan-Ganze regions were surrounded by the rising Tien Shan and Kunlun mountains. Basin opening may have caused a high heat transfer, producing the widespread Triassic apatite and zircon fission track ages. Similar fission track results were reported from the Chinese Tien Shan (e.g. Dumitru et al. 2001).

All sediment samples from the southern Tien Shan show Middle to Late Jurassic peak ages (Appendix C, Tab. C7, Fig. C4). In case of sample TS5a the zircon and apatite peak ages are nearly identical, indicating fast hinterland cooling during Late Jurassic times. The deposition of thick Triassic and Jurassic strata in the Turfan and Junggar basins in the eastern Tien Shan and in the northern Tarim basin is associated with faulting (Burtman 1980, Hendrix et al. 1992, Burtman et al. 1996, Bullen et al. 2003). Jurassic deposits are also documented in the southwest Tarim and Ferghana basins (Sobel 1999). Other coeval deposits are restricted to isolated accumulations in a few intramontane basins (Bullen et al. 2003). From these sediment accumulations, it can be inferred that the Tien Shan experienced a modest amount of Jurassic exhumation, an event that left a discernible thermochronological imprint. Synkinematic biotite from a north vergent thrust in the western Kunlun mountains south-west of Wuyitake yield an Ar/Ar age of 146±0.7 Ma (Arnaud et al. 1993). This suggests a compressional setting during Late Jurassic time. Sobel (2000) published apatite fission track data of a N-S transect across the whole Tien Shan. Palaeozoic sedimentary and magmatic rocks from the Atbashi range 60 km north of the Chinese border yield Jurassic ages and belong to a single grain age population. This confirms the relevance and extent of this Mid to Late Jurassic depositional and cooling event. Here, it is suggested that this thermal event is geodynamically related to the amalgamation of the Qiangtang and Lhasa blocks to the Eurasian margin. The docking to the south, gave a major exhumation impulse in the Tien Shan range, most likely under compressional setting like indicated in the Kunlun and Tien Shan mountains.

To determine the significance of the Late Cretaceous peak of apatite sample TS5a, more Neogene sediment samples must be analysed. Coeval Late Cretaceous tectonism in the hinterland might be inferred from the closure of the Shyok suture (~80 Ma) with widespread magmatic intrusions. So far, only Cretaceous apatite fission track age populations could be detected in this study, but no Cretaceous zircon fission track grain age population. Probably the Tertiary erosion level was not deep enough to reach

the zircon PAZ.

The apparent apatite fission track age from granitoid sample TS1 may indicate that exhumation following the India-Asia collision may have initiated around 11 Ma in the southernmost Tien Shan. Similar fission track ages are known from the northern Tien Shan, where detrital fission track thermochronology indicates that the north-western Tien Shan was tectonically calm for much of the Cenozoic (Bullen et al. 2001). In contrast, Sobel (2000) reported several Oligocene-Miocene apatite cooling ages (both basement rocks and sediments) at different places across the Tien Shan, which he interpreted to slightly post-dating the initiation of Cenozoic thrusting. The estimated 11-10 Ma onset of exhumation is in agreement with the initiation of compressive range building deducted from GPS measurements (e.g. Abdrakhmatov et al. 1996, Sobel 2000). Sobel (2000) suggests that during the earlier Oligocene to Early Miocene exhumation event the samples did not reached the surface. He concludes that during the Middle to Late Miocene the exhumation rate decreased until rapid final exhumation to the surface in Late Miocene.

The southernmost Tien Shan was the distal, northern edge of the Alay foreland basin, which developed in front of the rising Pamir mountains; its deposits thicken towards the south. As the Tien Shan began to rise in the Late Miocene, the old foreland basin was deformed and uplifted along its northern margin.

N-Kunlun

Geochronological studies within the Northern and Central Pamirs traced the Palaeozoic and Mesozoic Kunlun belt from Tibet into the Pamirs (chap. 3, Schwab et al. in press). In the northernmost Pamirs (Altyndara section), U/Pb zircon ages of metavolcanic rocks range between ~370 and 320 Ma and give evidence for Devonian/Carboniferous arc activity (north Kunlun arc). Devonian and Carboniferous zircon fission track grain ages are badly represented in the Tertiary intramontane basins within the northernmost Pamirs (Appendix C, Tab. C7, Fig. C4). More distinct is a Permian/Triassic grain age population at ~243 Ma (sample AD7d). Like in the Central Pamirs, this age population is most likely related to rifting processes, namely the opening of the Sonpan-Ganze ocean. Although this ocean was subducting in the Triassic along its northern margin beneath the Kunlun arc, and along its southern margin beneath the Qiangtang block, the widespread batholith occurrence in the Karakul-Mazar and south Kunlun range is post-dating (~220 Ma) the peak-ages, and therefore are excluded as source for this ages. Nevertheless, Pan (1996) reported Permian arc related volcanic rocks in the Kunlun mountains, which could also be the source for such fission track peak ages. Consequently, the Permian/Triassic grain age population gives evidence for low-T cooling of zircons related to the second arc stage, proposed for the late Palaeozoic-Triassic (south Kunlun arc; see chap. 3). The youngest zircon fission track grain ages of sample AD7d cluster around 131 Ma, whereas the detrital zircons of sample AD8a seem to consist of only one grain population with an age of ~152 Ma, pointing to a mid-Jurassic thermal event. As the stratigraphic age of both samples is badly constrained, it is unclear whether the age difference between samples AD7d and AD8a is due to different levels of erosion in the hinterland or whether the two samples derived from different catchment areas with different thermal

histories. The Mid-Jurassic zircon grain age group may originate from the like aged closure of the Rushan Pshart/Bangong-Nujiang suture and associated, arc-related magmatites of the Rushan Pshart arc along the southern margin of the Qiangtang block. The Early Cretaceous zircon grains may have been influenced by a reheating event in the South Pamirs and Karakoram. During the Cretaceous, the Hindu Kush-Karakoram-South Pamirs were the active margin arc of the northward subducting Shyok suture. The subduction/accretion processes led to widespread metamorphism and most likely bimodal magmatism in the Cretaceous times (~120 Ma and ~80 Ma).
Only few fission track data were published from northern Tibet. Jolivet et al. (2001) provided zircon fission track ages from basement rocks of the Kunlun mountains, ranging from Late Triassic (220-200 Ma) to Middle and Late Jurassic (172-143 Ma), to Late Cretaceous (~96 Ma). Apatite fission track data from the same samples were separated into two groups >50 Ma and <50 Ma. For comparison with data in this study, I divided the group >50 Ma into subgroups of Middle to Late Jurassic (167 to 147 Ma), Early Cretaceous (138 to 97 Ma) and Early to Middle Eocene (55-48 Ma). The Late Triassic zircon fission track ages of the basement rocks post-date the Permian/Triassic peak detected by the Tertiary sediment samples from the northernmost Pamirs, but matches very well with the post-tectonic emplacement ages of the Karakul and Sailiak batholiths. However, the Late Jurassic and Early Cretaceous peak ages from the Altyndara valley correspond well to the zircon and apatite age groups from basement rocks of Jolivets et al. (2001) study. These authors interpret all zircon ages to represent a Jurassic cooling event, with the Middle to Late Jurassic cooling ages exhumed from deeper crustal levels due to their hanging wall structural positions. From apatite fission track ages Jolivet et al. (2001) suggest slow long term erosion in Jurassic time with low cooling rates of 0.1°C/Ma to 1.3°C/Ma. The Cretaceous in north Tibet is characterised by sedimentation and in some places by a reheating of rocks to 60°C to 70°C, probably around 120±20 Ma (Jolivet et al. (2001). The authors conclude that there was either a previously formed relief initiated in the Jurassic and which experienced differential subsidence in the Cretaceous and/or weak tectonic activity in the Cretaceous after the collision of the Qiangtang and Lhasa blocks.

Karakul-Mazar granitoid belt, Northern Pamirs

Five different granitoid locations were probed across the Triassic/Jurassic Karakul-Mazar batholith belt. Two zircon fission track samples yielded late Early Cretaceous cooling around 122-108 Ma, which can be interpreted as a thermal event related to Cretaceous arc magmatism in the south (e.g. Shyok arc), or as slow denudational cooling following the emplacement of the Triassic/Jurassic granitoids. Apparent apatite fission track ages range from Eocene to Miocene (56-18 Ma) and young from south to north, whereas the cooling rates increase towards the north (Fig. 4.2 and 4.3).
Detailed structural mapping is missing in the Karakul-Mazar belt and therefore the apatite fission track age distribution is difficult to interpret. As discussed in Schwab et al. (in press), the massive batholith in the Karakul-Mazar belt may have acted like a rigid backbone during the Tertiary and deformation may be confined to the margins of the batholith belt. The right-lateral transpressional Markansu fault to the north of the

belt likely operated as an out-of-sequence thrust, causing exhumation during the Middle Miocene as reflected by the fission track ages of 18 Ma. The age pattern may be explained by piggy-back thrust tectonics, in which footwall burial and hanging wall exhumation propagates towards the foreland, i.e. towards the north in the Pamirs. The evidence that the Ar/Ar biotite ages mirror a similar younging towards north trend is only weak, but could argue either for the activity of a predecessor of the Markansu fault in the Jurassic/Triassic or for a 'rotation' of the whole Markansu-Mazar belt around a horizontal E-W trending axis. The latter my be explained in terms of normal faulting in the south, probably induced by the dome exhumation, and thrusting in the north, due to the ongoing compression between India and Asia. So far, the Karakul-Mazar belt is the only region in the Pamirs where Eocene apatite fission track ages are preserved. Similar Early to Middle Eocene ages were found in the eastern Kunlun range by Jolivet et al. (2001); these authors interpreted the ages by a change of the deformation style from compressive to extensive as indicated by pull-apart basin formation in e.g. the Hexi corridor (Vincent and Allen 1999). At least since Quaternary times the Karakul basin is a pull-apart basin, but whether basin formation already started in Eocene time is not clear detected.

Qiangtang block, Central Pamirs

Zircon fission track results from a Tertiary sediment sample with peak ages around 371 Ma, 242 Ma, and 165 Ma as well as from Cretaceous magmatic rocks describe the thermal evolution of the Qiangtang block: (1) Palaeogene sediment sample A96K1e from an intramontane basin along the northern margin of the Qiangtang block and the Muzkol dome possibly defines the Palaeozoic and Mesozoic history of the Qiangtang basement (Fig. 4.2, Appendix C, Tab. C7, Fig. C4). The oldest peak age is at ~371 Ma and can be interpreted in two ways: (a) The age might reflect low-T cooling of the Qiangtang basement. In chapter 3 and Schwab et al. (in press), inherited zircons (575-425 Ma) from the Parmiran Qiangtang block granitoid P17 and published zircon ages from Qiangtang basement rocks of Central Tibet (Gangma Co gneiss, Kapp et al. 2000) were interpreted to characterise the Qiangtang basement. The results from U/Pb zircon dating of Tertiary intrusions and dykes from the Muzkol and Sares domes (P15 and 96A6b) yielded upper intercept ages of 540 Ma and 570 Ma, respectively. The interpretation is that all Tertiary melts contain inherited zircons of the Qiangtang basement. Ar/Ar amphibole ages from the same Gangma Co basement rocks of central Tibet range from 380 to 355 Ma (Kapp & Cowgill 2001). The amphibole ages are consistent with high-grade metamorphism prior to Carboniferous time (Kapp & Cowgill 2001). Assuming a similar tectono-metamorphic evolution for the Pamiran Qiangtang block, the zircon peak age of ~371 Ma from sample A96K1e may reflect the low-T cooling of the Qiangtang basement; anyhow, it is speculative whether such basement was exposed in Tertiary. (b) The second interpretation of the ~371 Ma age population is that the zircons derived from the Kunlun arc to the north. Granite intrusions around 380 Ma are known from the Kunlun of north-western Tibet (Matte et al. 1996) and 370-320 Ma old metavolcanic rocks occur in the Kunlun range of the northern Pamirs (Altyndara section). Deposition of Carboniferous to Permian passive margin strata within both, the Kunlun and Qiangtang terranes, resulted from opening of the Palaeo-

Tethyan ocean between them (Kapp & Cowgill 2001; chap. 3; Schwab et al. in press). In Late Permian/Early Triassic the closure of these ocean basins started and resulted in Triassic/Early Jurassic accretion of the Qiangtang terrane to the southern Eurasian margin. Several slices of oceanic crust and mélange rocks were subducted beneath the Qiangtang block and exhumed in fault-bounded basement domes in the Central Pamirs/Qiangtang block. In the Qiangtang, exhumation of these basement rocks was already in the Mesozoic, whereas in the Central Pamirs in the Tertiary. It is not published if Tertiary central Qiangtang sediments derived Triassic ages probably related to the Mesozoic exhumation of the basement domes.

Grain ages of the Palaeogene sediment sample A96K1e cluster around 165 Ma and are comparable with a major age component in Triassic/Jurassic granitoids of the southern margin of the Qiangtang block and may record Rushan Pshart arc activity.

(2) Cretaceous magmatic rocks and contact metamorphic hornfelses occur at the northern margin of the Qiangtang block. Sample A96S1b, a subvolcanic latite-andesite, is cropping out in the Saseksu valley (Fig. 4.2); it's lower intercept U/Pb zircon age is at ~74 Ma (Fig. 3.7k, chap. 3) and the zircon fission track cooling age is about 64 Ma. A similar zircon fission track age was also found at the southern margin of the Qiangtang block; monzogranite 96A10b yielded an apparent zircon fission track age of about 59 Ma. Both the Late Cretaceous magmatic intrusions and their low-T cooling ages thus give evidence for the regional distribution of a Late Cretaceous thermal influence, likely caused by flat-slab subduction of the Shyok suture. If this thermal overprint reached as far as to the northern part of the Qiangtang block and may explain the Late Cretaceous ages determined there, is debatable.

Shyok ocean basin subduction and Kohistan-Ladakh arc accretion caused high-grade metamorphism in the Hindu Kush-Karakoram blocks south of the South Pamirs at 80 to 50 Ma (Fraser et al. 2001). As no apatite fission track ages are on hand, it can not be inferred if the Late Cretaceous/Palaeocene cooling in the Qiangtang block led to cooling of the rocks to near surface temperatures. Additionaly, intracontinental deformation caused by the approaching India may have caused renewed lithosphere subduction of the Karakul-Mazar belt beneath the northern Qiangtang margin. This may be evidenced by the geochemical signiture of sample A96S1b close to the Karakul-Mazar substratum. In the light of such Late Cretaceous thermal influences, it would be interesting to determine whether the Early Eocene apatite cooling age of the southernmost sample of the Karakul-Mazar belt is also a result of a Late Cretaceous/Palaeocene heat source.

Muzkol and Sares domes, Central Pamirs

The Muzkol and Sares domes expose fault bound greenschist to upper amphibolite facies metamorphic rocks of Tertiary age. Monotonous, mainly siliciclastic and mafic rocks with subordinate carbonatic sequences (see chap. 3) are interpreted to characterise the Karakul-Mazar-Sonpan-Ganze accretionary wedge rocks, associated with the subduction of Jinsha oceanic crust (chap. 3, Schwab et al. in press). Whereas these rock associations were formed in Triassic/Early Jurassic times, the exhumation of the domal structure is a Tertiary feature. Metamorphic hornblende and biotite Ar/Ar ages range from 28 to 14 Ma (Appendix A, Tab. A3). Two Rb/Sr whole rock-muscovite

ages from gneissic rocks within the Sares dome are 37 and 30 Ma. Locally, metamorphic grade reached migmatisation and granitoid production. One syeno-granodiorite in the Muzkol dome (P15) gave an U/Pb zircon lower intercept age of 31±5 Ma (Appendix A, Tab. A7). The emplacement age of an aplitic dyke of the Sares dome (96A6b) is at 17±8 Ma (U/Pb zircon, Appendix A, Tab. A7); another aplitic dyke (L96A11a) gave a whole rock-muscovite Rb/Sr age of 13.7±0.1 Ma (Appendix A, Tab. A5). Tertiary melt injection is also documented by basalt dykes with Ar/Ar whole rock ages at 20±2 Ma (Appendix A, Tab. A3).

Low-T cooling of the dome is constrained by zircon and apatite fission track ages of the above mentioned intrusions (P15, P17) and dykes (96A6b) and range from 20 Ma to 15 Ma. Within the Tertiary intramontane sediment basin along the southern margin of the Muzkol dome, the herein called 'Murgab section' (Fig. 4.4), the zircon fission track ages from sandstone samples A96M6b and M96M5a are ~20 Ma and ~19 Ma, respectively. K/Ar sericite ages from the same sedimentary rocks (5 samples) range of 33 to 14 Ma (Fig. 4.4; Appendix C, Tab. C4, C6), whereby the K/Ar ages increase away from the dome (from north to south). Basalt dykes cutting through the sedimentary rocks of the section gave two Ar/Ar biotite ages of about ~20 Ma. As both zircon fission track sandstone samples show only one age population, it can be concluded that either the sandstones are reset, or that only one Miocene source area was delivering around ~19 Ma old grains. From the Geological map 1:200.000 of Tadzhikistan (1968) a Plaeogene stratigraphic age is supposed for the sedimentary rocks. Both samples come from different horizons and the whole section shows changing proximal and distal parts. Considering these stratigraphic and sedimentary aspects, I exclude a single grain age source in the hinterland. More likely, the Miocene rising thermal dome heated the Palaeogene sediment basin to temperatures ≥ the zircon PAZ (190°C to 260°C, Zaun &Wagner 1985) as the zircons from these sediments are interpreted to be reset. The older K/Ar sericite ages (> 25 Ma) are interpreted to be partly reset as the thermal influence of the dome probably decreased from north to south. Preliminary geochemical data of the basalts characterise them as within plate basalts, extruded in an extensional setting in Miocene.

Interestingly, in the correlated domal structure (Schwab et al. in press) of the Qiangtang block in Central Tibet Tertiary metamorphism and exhumation are lacking and Mesozoic ages dominate (Kapp et al. 2000).

Rushan Pshart arc and Shyok arc

The Rushan Pshart zone and the northernmost South Pamirs are strongly deformed by the splays of the dextral Karakoram fault. Triassic/Jurassic arc-type intrusions and a Triassic oceanic-basin-arc sequence in the eastern Pshart and southern Qiangtang constitute the Rushan Pshart arc. Sample L96M25a, a monzogranite, yielded a zircon fission track age of about 69 Ma, suggesting Late Cretaceous low-T cooling. Late Cretaceous granodiorites (P2 and P5) are the southernmost samples dated in this study and are related to the Shyok arc. Apatite fission track ages of these samples are around 11-10 Ma and so far the youngest fission track ages in the Pamirs. This is likely due to Miocene activation along dextral transpressional strike-slip faults, the Karakorum fault splays, leading to low-T cooling and exhumation.

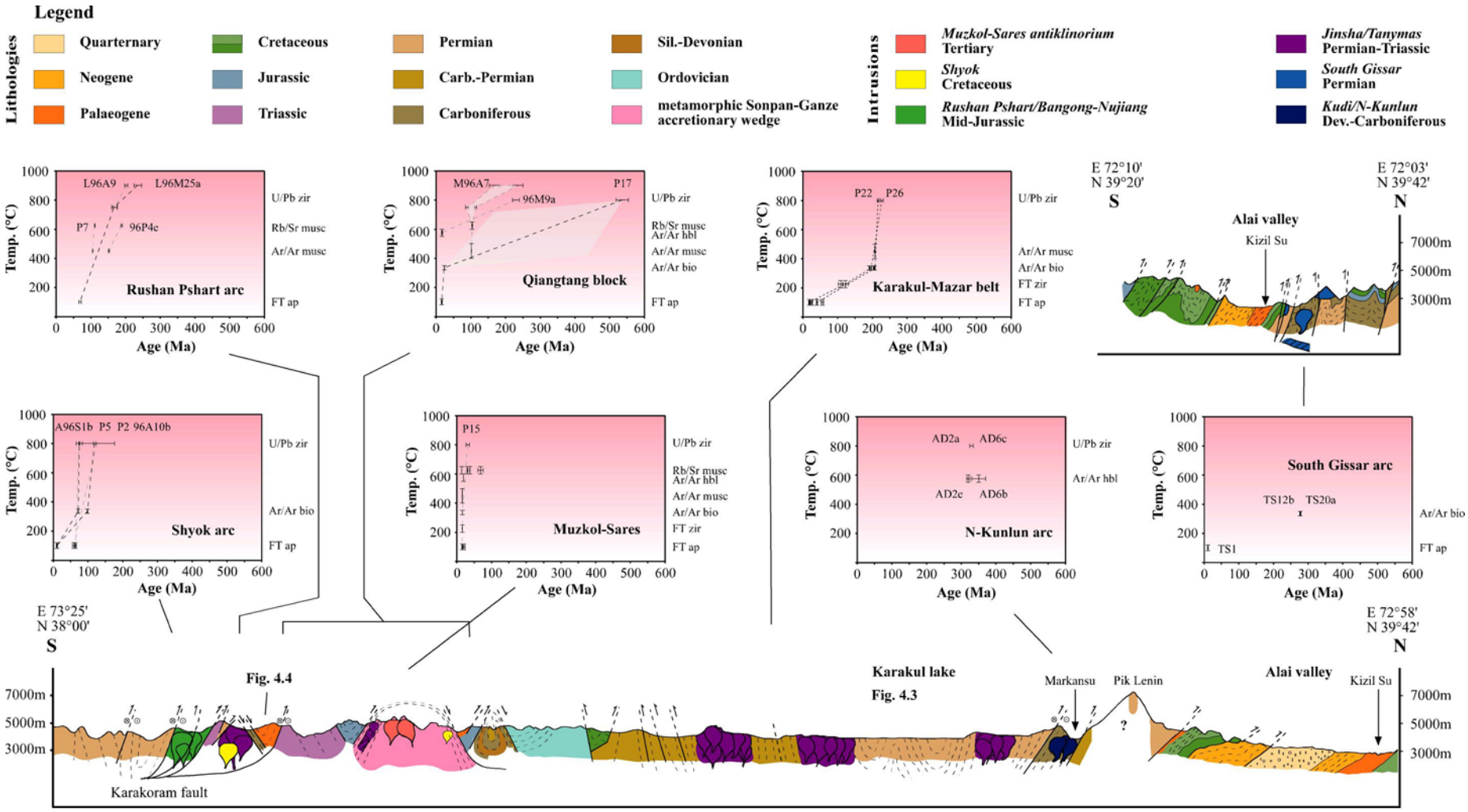

Fig. 4.5: N-S profile of the eastern Pamirs and southernmost Tien Shan with the structural units and the summary of the geochronology of the magmatic belts and basement units. The surface geology is adapted from the geological maps 1:200.000 of Tadzhikistan (1968) and Kyrgyztan (1958). For a further understanding of the subsurface geology see Fig. 3.11 (chapter 3). Not all data points are labelled with a sample name and fission track peak ages of sediments are not included.

4.4 Conclusions

This low-temperature fission track study of the southernmost Tien Shan and eastern Pamirs resulted in two major conclusions:

(1) Unreset Tertiary sediment samples trace the Palaeozoic and Mesozoic thermal history of the hinterland of the intramontane basins of the southern Tien Shan and eastern Pamirs. The reconstruction of the cooling and denudation histories constrain the thermal events, which were affecting the different tectonic units, and support the conclusions which were drawn in chapter 3.

Four major phases of tectonic activity could be traced by the decomposed apatite and zircon fission track ages:

(a) Age populations of about ~370 Ma were found in the Tertiary sedimentary basins of the northern Pamirs/Kunlun belt and northern Central Pamirs/Qiangtang block. These ages are interpreted to be related to the first, northern Kunlun arc stage, which was defined e.g. by the metavolcanic rocks of the Altyndara section (~370-330 Ma).

(b) A major Permo-Triassic peak ranging from ~266 to 242 Ma (depending on the region) was detected in all determined regions from the southern Tien Shan to the eastern Pamirs. Induced by the break-up of Pangea, the Triassic is a dominant phase of rifting and basin formation. Such large basins with thick sediment accumulations are widespread in Central Asia. Examples are the Ferghana, Turfan, Junggar, and Tadjik basins. The basins were fed from the rising Tien Shan and Kunlun mountains. Increased heat flow during basin formation is thought to be the source for the dominant occurrence of the Permo-Triassic grain ages. A further source for Triassic zircons may be derived from rocks thermally influenced by Triassic southward subduction along the Jinsha suture.

(c) Jurassic peak ages range from 170-145 Ma. They occur in the Tertiary sedimentary rocks of the South Tien Shan, Kunlun, southern Qiangtang, and Rushan Pshart zone. They are attributed to the Rushan Pshart arc and Rushan Pshart basin closure in the Mid-Jurassic, leading to the collision of the Central Pamirs/Qiangtang and SE Pamirs/Lhasa blocks. This event was coeval with Mid-Jurassic deformation determined in the Kunlun mountains.

(d) Late Cretaceous fission track ages were determined in the South Tien Shan (Tertiary sedimentary rocks) and in the Central Pamirs (Cretaceous intrusions). The occurrence of late Early Cretaceous intrusions along the southern margin of the Qiangtang block may be explained by flat-slab subduction along the Shyok suture and the Late Cretaceous zircon fission track ages as cooling ages to the emplacement ages. Late Cretaceous intrusions along the northern margin of the Shyok suture are probably induced by intracontinental renewed subduction of Karakul-Mazar and Jinsha lithosphere beneath the Qiangtang block, induced by proceeding compression due to collisional stages further to the south (Karakorum and Kohistan-Ladakh).

(2) Reset sediment samples and low-T cooling ages of basement rocks reflect the cooling history related to Tertiary tectonics, which is responsible for the modern shape and topographic pattern of the southern Tien Shan and eastern Pamirs. At least since the Tertiary (in some areas since the Late Cretaceous) the Pamir orogen was emerged above sea-level and was eroded at rates that can be approximated by fission track data:

(a) Apatite fission track ages of the Karakul-Mazar belt decrease from 56 Ma in the

south to 18 Ma in the north; the exhumation rates increase in the same direction. Such an age pattern can be explained by: (1) A piggy-back thrust tectonics in which footwall burial and hangingwall exhumation propagated towards north. (2) Since the Karakul-Mazar belt may behaved as a rigid block during the Tertiary, deformation was probably confined to the margins of the belt, e.g. to the right-lateral Markansu fault to the north of the belt. (3) The whole belt may be rotated around a horizontal axis with normal faulting in the south and thrusting in the north. (4) Cretaceous collision south of the Pamirs led to further compression and induced renewed continental subduction of the Karakul-Mazar belt beneath the Central Pamirs and thermally influenced the apatite annealing zone in the Karakul lake area.

(b) The Central Pamiran Qiangtang block is characterised by a Tertiary anticlinorium and constitute the Muzkol and Sares domes. The basement rocks exposed in the domes are interpreted as the Triassic/Jurassic Karakul-Mazar/Sonpan-Ganze accretionary wedge rocks (Schwab et al. in press). During the Tertiary, these rocks were strongly deformed and metamorphosed to upper amphibolite facies conditions with local migmatisation. Rb/Sr whole rock-muscovite ages from two gneiss samples of the Sares dome yielded 37 and 30 Ma. Emplacement ages of Tertiary melts seem to be episodic: An earlier phase with subalkaline intrusions is of Early Oligocene age (~33 Ma) and a later phase with aplitic dykes of Late Miocene ages (~14-11 Ma). Metamorphic hornblende and biotite Ar/Ar cooling ages cover ~28-14 Ma. Tertiary melt generation is also documented by widespread basalt dyke occurrence in the domes with Ar/Ar whole rock ages at ~20 Ma. Apatite and zircon fission track ages range from 20 to 15 Ma. The Tertiary anticlinorium is not only characterised by penetrative resetting of nearly all mineral chronometers, but also shows very fast exhumation rates. Between 22 and 15 Ma cooling rates increased to > 40°C/Ma and in some cases (e.g. P15) all mineral ages are reset to ~15 Ma. Tertiary intramontane basins along the margins of the dome contain coarse grained conglomerates mainly composed of weakly metamorphosed carbonatic and dolomitic clasts of the Mesozoic cover sequence of the dome. Reset zircons of sediments from a basin south of the dome yielded ages of 20 to 19 Ma. Basalts cutting through the section are preliminarily interpreted as of within plate origin. They yielded ~20 Ma Ar/Ar whole rock ages. K/Ar sericite ages range from 33 to 14 Ma and increase away from the dome (from north to south). The older K/Ar sericite ages (>25 Ma) are interpreted to be partly reset. Dome exhumation between 25 to 15 Ma seem to have heated the Palaeogene sedimentary basin.

(c) The southernmost samples evaluated for their low-T history are Cretaceous intrusions attributed to the Shyok arc. At least since Miocene the northernmost South Pamirs was strongly deformed along the right lateral splays of the Karakoram fault. The transpressional faults seem to be responsible for exhumation at 11-10 Ma. From Late Miocene to Recent, final cooling of the samples was at rates of 5-16°C/Ma.

(d) A coeval Late Miocene (11-10 Ma) denudation is indicated in the southernmost Tien Shan by apatite fission track data on granitoids. There, exhumation was probably induced in response to crustal thickening along major thrust faults and dextral transpressional strike slip faults.

In the Central Pamirs, future work has to determine if metamorphism, melt generation and deformation occurred in two major phases, namely in Early Oligocene and Early Miocene, and if exhumation in the whole Pamirs was a constant steady-state Tertiary process, or with distinct accelerated exhumation phases, e.g. at the beginning of the Middle and Late Miocene.

5 Summary

This thesis results in a fundamental new understanding of the pre-Tertiary accretion-collision history of the Pamirs. Based on determinations of age and origin of magmatic belts from the southernmost Tien Shan to the eastern Pamirs, it is for the first time possible to relate Pamiran units to those from Tibet and Afghanistan.

Furthermore, this study constrains the Tertiary low-T cooling history of the Pamirs induced by the India-Asia collision. In combination, the understanding of accretion, collision, and magmatic activity, the definition of distinct units and their margins, help to relate low-T cooling of the upper crust to probably rheologically weakened crust caused by older deformational and thermal events.

Successive southward enlargement of Eurasia started with the accretion of the northern, central, and southern continental and oceanic terranes in Early to Middle, and Late Palaeozoic times. The Early Permian (~277 Ma) syn- to postcollisional magmatic rocks of the southernmost Tien Shan are attributed to Early Permian closure of the South Gissar/South Tien Shan ocean and correlated with the Garm-Turkestan-Alay granitoids. The Baysunta and Garm basements are interpreted as part of the Tadjik continental block that is probably connected to the Tarim block. Further amalgamation was along the southern margins of the Tadjik/Tarim continental blocks.

The Sonpan-Ganze oceanic basin subducted northward below the composite Early and Late Palaeozoic/Triassic Kunlun arcs. The ~370-330 Ma old metavolcanic rocks (Altyndara section) are interpreted as representatives of the north Kunlun arc. These rocks likely extends into the Triassic, probably in a back-arc setting due to continued northward subduction in the second arc stage of the Permo-Triassic. Late Triassic to Early Jurassic (~227-199 Ma) post-tectonic granitoids in northwestern Tibet and a massive ~227 Ma Karakul lake batholith in the Pamirs stitch the Karakul-Mazar complex together. Like aged, widely distributed Triassic plutonites and Permo-Triassic volcano-sedimentary successions are described from the western Badakshan, western Hindu Kush, and Feroz Koh regions.

The cryptic Tanymas suture between the Northern and Central Pamirs is part of the Jinsha suture. The Tanymas/Jinsha suture developed by southward subduction of the Sonpan-Ganze ocean below the Central Pamirs/Qiangtang block. Subduction on the northern and southern margins (recent positions) of this ocean caused extensive accretion-subduction complexes, determined in the Central Pamirs as Karakul-Mazar accretionary wedge complex and is correlated with the Sonpan-Ganze mélange in Tibet. In the Central Pamirs and Qiangtang, Tanymas/Jinsha oceanic crust and metamorphosed Karakul-Mazar/Sonpan-Ganze mélange is exposed in regional anticlinoria. These basement domes may extend into the Safed Khers. Zircons from basement rocks of Central Tibet and inherited zircons from a Pamiran Qiangtang block granitoid have similar 575-425 Ma ages and may constitute typical Gondwanan crustal ages.

Arc-type granitoids that cut the southern Qiangtang block (~170-160 Ma) and granitoids that intrude into the eastern Pshart oceanic-basin-arc sequence (~190-150 Ma) constitute the Rushan Pshart arc which is correlated with the Bangong-Nujiang zone to the east and the Khas Rod in the west.

Cretaceous plutons that intrude the Central and Southern Pamirs record a long-lasting magmatic history. Their zircons and those from Late Miocene xenoliths show that the most distinct tectonic events were Cambro-Ordovician (~575-410 Ma), Triassic (~250-200 Ma, due to subduction along the Jinsha suture and/or Triassic rifting (e.g. in the Rushan Pshart/Bangong-Nujiang area and between the SW and SE Pamirs)), Middle Jurassic (~200-150 Ma, due to subduction along the Rushan Pshart suture), and mainly Cretaceous. The Cretaceous activity may have been bimodal, with peaks at ~120 Ma and ~80 Ma. The Mid-Cretaceous event may reflect arc activity in Asia prior to the accretion of the Karakorum block, probably along the Tirich Mir fault. The Late Cretaceous magmatism may be a sign of flat-slab subduction along the Shyok suture north of the Kohistan-Ladakh arc. Before India and Asia collided, the Pamir region from the south Tien Shan to the Indus-Yarlung was an Andean-style plate margin. From the Kunlun arc in the north to the southern Qiangtang block in the south, the Pamirs and Tibet seem to have dominantly (meta)sedimentary crust, characterised by the Karakul-Mazar/Sonpan-Ganze accretionary wedge rocks. The crust south of the southern Qiangtang block is of likely granodioritic composition, reflecting long-lived subduction, arc formation and Cretaceous/Tertiary underthrusting of arc segments beneath the Qiangtang block.

The accretion history was accomplished by the final collision of India with Eurasia at ~55 Ma. The long lasting history as an active continental margin ended and the Pamirs came into an intracontinental position. Crustal stacking in the Pamirs region initiated shortly after the India-Asia collision and led to much more thickened crust than previously thought (70-80 km). Due to crust thickening and successive melt generation, several Tertiary intrusions penetrated the Pamirs. More widespread are leucogranites in the South Pamirs, whereas localised migmatisation and melt generation led to subalkaline and alkaline intrusions into Central Pamiran basement domes in the Tertiary. The Tertiary magmatism was probably episodic with subalkaline intrusions in Late Eocene/Oligocene and aplitic and basalt dyke emplacement around ~20-11 Ma. Medium to high-grade metamorphism was about 20-15 Ma. Crustal shortening was most extreme in the Pamiran region and strain is mostly concentrated along rheologically weakened zone along the margins of the accreted crustal blocks. One exception is the Central Pamirs with its basement anticlinoriums.

Apatite and zircon fission track ages support the above outlined accretion history. Tertiary sedimentary rock samples and their determined grain ages highlight the exhumation and cooling of the rising Kunlun after Early to Mid Palaeozoic arc accretion and subduction related magmatism (peak ages in the Kunlun ~ 370 Ma). The Tien Shan range was subject of two collisions in the Palaeozoic: an Early to Mid Palaeozoic collision was only weakly detected in Tertiary Tien Shan sedimentary basins, but Late Palaeozoic/Triassic cooling and exhumation after collision together with coeval basin formation catching the sediments of the rising Tien Shan and Kunlun mountains is well detectable in the Tien Shan (~266-245 Ma). Triassic ages around ~242 Ma are also recorded in Tertiary northern Qiangtang intramontane basins and can be related to subduction of the Jinsha oceanic crust beneath the Qiangtang block and/or be related to increased heat flow due to basin formation in several areas surrounding the Qiangtang, Lhasa, and Kunlun regions. Mid-Jurassic peak ages, coupled with Jurassic

compressive tectonics and the shedding of a huge amount of Tertiary sediments into the adjacent basins, are most likely sourced by Mid-Jurassic collision of the SE Pamirs and Lhasa blocks along the Rushan Pshart and Bangong-Nujiang zones. Few Late Cretaceous fission track ages of sedimentary rocks and hardrocks imply a thermal event affecting the Qiangtang block and the Tien Shan. At least for the Qiangtang, a thermal influence is suggested from the Late Cretaceous collision of the Kohistan Ladakh arc along the Shyok suture. All other fission track ages are related to India-Asia post collisional tectonics. In the southermost Tien Shan, apatite fission track ages of granitoids point to Late Miocene exhumation (~11 Ma). Exhumation was probably induced in response to crustal stacking along major thrust faults and dextral transpressional strike-slip faults. Fission track ages of the Karakul lake batholith gave ages from 56 to 18 Ma with a younging towards the north. Either Tertiary tectonics (e.g. piggy-back thrust teconics in which footwall burial and hangingwall exhumation propagated towards north) or cooling after a Late Cretaceous reheating event, induced by underthrusting of the Karakul-Mazar belt beneath the northern Qiangtang, may have caused this age distribution. The most penetrative exhumation event is localised in the Muzkol and Sares domes of the Central Pamirs and occurred between ~25-15 Ma. Between 22 to 15 Ma the cooling rates increased to >40°C/Ma. Tertiary intramontane basins along the margins of the dome contain coarse grained conglomerates composed of the Mesozoic cover sequence of the dome. Reset zircons of sediments from a basin south of the dome yielded ages of 20 to 19 Ma. Basalts cutting through the section are preliminary interpreted as within plate origin. They yielded ~20 Ma Ar/Ar whole rock ages. K/Ar sericite ages range from 33 to 14 Ma and increase in age away from the dome (from north to south). The older K/Ar sericite ages (>25 Ma) are interpreted to be partly reset. Dome exhumation between 25 to 15 Ma seem to have heated the Palaeogene sedimentary basin.

Cretaceous granitoids intruding Late Palaeozoic to Jurassic rocks in blocks rimmed by Tertiary dextral transpressional faults. At least since Miocene the area was strongly deformed along the right lateral splays of the Karakoram fault, which seem to be responsible for exhumation at 11-10 Ma. From Late Miocene to Recent, final cooling of the samples was at rates of 5-16°C/Ma.

Obviously, deformation did not propagate continuously from south to north. Instead, it might have been concentrated into rheologically weak zones like the Central Pamirs where probably intracontinental subduction along the Jinsha suture facilitated deformation and melt generation. Coeval with the fast Early Miocene dome exhumation, the northern margin of the Karakul-Mazar belt was exhumed along the right-lateral transpressional Markansu fault. After the Early Miocene exhumation, deformation seems to have shifted to locations dominated by large strike slip faults responsible for lateral rock transportation and compensating for continuous N-S compression between India and Asia; these are e.g. the Karakoram fault, dextral transpressional faults along the southern margin of the Tien Shan and along the Pamiran frontal range. These are active at least since 11-10 Ma.

6 References

Allègre C.J., Coutillot V., Tapponnier P. Hirn A., Mattauer M., Coulon C., Jaeger J.J., Achache J., Schaerer U., Marcoux J., Burg J.P., Girardeau J., Armijo R., Gariepy C., Goepel C., Li T., Xiao X., Chang C., Li G., Lin B., Teng J.W., Wang N., Chen G., Han T., Wang X., Den W., Sheng H., Cao Y., Zhou J., Qiu H., Bao P., Wang S., Wang B., Zhou Y., and Xu R., 1984. Structure and evolution of the Himalaya-Tibet orogenic belt. Nature, 307, pp. 17-22.

Allen M.B., Windley B.F., and Chi Z., 1993. Palaeozoic collisional tectonics and magmatism of the Chinese Tien Shan, central Asia. Tectonophysics, 220, pp. 89-115.

Ansdell K.M. and Kyser T.K., 1993. Textural and chemical changes undergone by zircon during the Pb-evaporation technique. American Mineralogist, 78, 1-2, pp. 36-41.

Arnaud N. (Ed.), 1992. Contribution of $^{40}Ar/^{39}Ar$ thermochronology on potassic feldspar to the knowledge of Cenozoic tectonics in Asia; study of the accommodation mechanisms involved in continental collision (in french). Thesis Doctoral, Monographic, Université de Clermont-Ferrand II, Clermont-Ferrand, France (FRA).

Arnaud N.O., Brunel M., Cantagrel J.M., and Tapponnier P., 1993. High cooling and denudation rates at Kongur Shan, eastern Pamir (Xinjiang, China) revealed by $^{40}Ar/^{39}Ar$ alkali feldspar thermochronology. Tectonics, 12, 6, pp. 1335-1346.

Arndt N.T. and Goldstein S.L., 1987. Use and abuse of crust-formation ages. Geology, 15, 10, pp. 893-895.

Arrowsmith J.R. and Strecker M.R., 1999. Seismotectonic range-front segmentation and mountain-belt growth in the Pamir-Alai region, Kyrgyzstan (India-Eurasia collision zone). GSA Bulletin, 111, 11, pp. 1665-1683.

Bailey J.C., 1981. Geochemical criteria for a refined tectonic discrimination of orogenic andesites. Chem. Geol., 32, pp. 139-154.

Bassoullet J.P., Boulin J., Colchen M., Marcoux J., Mascle G., and Montenat C., 1980. L'évolution des domaines téthysiens au pourtour du Bouclier indien du Carbonifère au Crétacé. Mém. B.R.G.M., 115, pp. 180-198.

Bazhenov M.L., Chauvin A., Audibert M., and Levashova N.M., 1993. Permian and Triassic paleomagnetism of the southwestern Tien Shan; timing and mode of tectonic rotations. Earth and Planetary Science Letters, 118, 1-4, pp. 195-212.

Bevington P.R., 1969. Data reduction and error analysis for the Physical Sciences. New York, McGraw-Hill Book Company, 336 pp.

Borchers P. (ed.) 1931. Berge und Gletscher im Pamir. Verlag Strecker und Schröder, Stuttgart.

Brandon M.T., 2002. Decomposition of mixed grain age distributions using BINOMFIT. On Track, 24, pp. 13-18.

Brookfield M.E., 1993. The Himalayan passive margin from Precambrian to Cretaceous times. Sedimentary Geology, 84, 1-4, pp. 1-35.

Brookfield M.E., 2000. Geological development and Phanerozoic crustal accretion in the western segment of the southern Tien Shan (Kyrgyzstan, Uzbekistan, Tajikistan). Tectonophysics, 328, pp. 1-14.

Brown G.C., Thorpe R.S., and Webb P.C., 1984. The geochemical characteristics of granitoids in contrasting arcs and comments on magma sources. J. Geol. Soc. Lond.,

141, pp. 411-426.

Bruguier O., Lancelot J.R., and Malavieille J., 1997. U-Pb dating on single detrital zircon grains from the Triasic Sonpan-Ganze flysch (Central China): provenance and tectonic correlations. Earth Planet. Sci. Lett., 152, pp. 217-231.

Budanov V.I. and Pashkov B.R., 1988. Scales of Dinantian and Permian volcanism in the eastern part of the northern Pamirs (in Russian). Byulleten' Moskovskogo Obshchestva Ispytateley Prirody, Otdel Geologicheskiy, 63, 1, pp. 33-38.

Bullen M.E., Burbank D.W., Garver J.I., and Abdrakhmatov K.Y., 2001. Late Cenozoic tectonic evolution of the northwestern Tien Shan; new age estimates for the initiation of mountain building. Geological Society of America Bulletin, 113, 12, pp. 1544-1559.

Bullen M.E., Burbank D.W., and Garver J.I., 2003. Building the northern Tien Shan; integrated thermal, structural, and topographic constraints. Journal of Geology, 111, 2, pp. 149-165.

Burtman V.S., 1975. Structural geology of Variscan Tien Shan, USSR. American Journal of Science, Vol. 275-A, Tectonics and mountain ranges, pp. 157-186.

Burtman V.S., 1980. Faults of Middle Asia. American Journal of Science, 280, 8, pp. 725-744.

Burtman V.S. and Molnar P., 1993. Geological and geophysical evidence for deep subduction of continental crust beneath the Pamir. Spec. Pap. Geol. Soc. Am., 281, 76 pp.

Burtman V.S., Skobelev S.F., and Molnar P., 1996. Late Cenozoic slip on the Talas-Ferghana Fault, the Tien Shan, Central Asia. Geological Society of America Bulletin, 108, 8, pp. 1004-1021.

Carlier G. and Lorand J.P. 1997. First occurrence of diopside sanidine phlogopite lamproite in the Andean Cordillera; the Huacancha and Morojarja dikes, southern Peru. Canadian Journal of Earth Sciences = Journal Canadien des Sciences de la Terre, 34, 8, pp. 1118-1127.

Carroll A.R., Liang Y., Graham S.A., Xiao X., Hendrix M.S., Chu J., and McKnight C.L., 1990. Junggar basin, northwest China: Trapped late Paleozoic ocean. Tectonophysics, 181, pp. 1-14.

Carroll A.R., Graham S.A., Hendrix M.S., Ying D., and Zhou D., 1995. Late Paleozoic tectonic amalgamation of northwestern China; sedimentary record of the northern Tarim, northwestern Turpan, and southern Junggar basins. GSA Bulletin, 107, 5, pp. 571-594.

Chang C.F., Pan Y.S., and Sun Y.Y., 1989. The tectonic evolution of Qinghai-Tibet plateau: a review. In: Sengör A.M.C. (Ed.). Tectonic evolution of the Tethyan region. NATO ASI Series, C, 259, pp. 415-476, Kluwer, Dordrecht.

Chappell B.W. and White A.J.R., 1974. Two contrasting granite types. Pac. Geol., 8, pp. 173-174.

Che Z., Liu L., and Sun Y., 1995. U/Pb, Sm/Nd, Rb/Sr, $^{40}Ar/^{39}Ar$ and $^{18}O/^{16}O$ isotopic studies for early evolution of the structural belt in the Altun area. Acta Geosci. Sini., 3, pp. 334-337.

Chen Z., Wu N., Zhang D., Hu J., Huang H., Shen G., Wu G., Tang H., and Hu Y., 1985. Geologic map of Xinjiang Uygur autonomous region. Beijing, Geologic Publishing

House, scale 1:2 000 000.

Chen F. 1999. Variscan and pre-Variscan geochronology of the Moldanubian zone of the Black Forest, Germany. Unpublished PhD thesis.

Chen F., Hegner E., and Todt W., 2000. Zircon ages and Nd isotopic and chemical compositions of orthogneisses from the Black forest, Germany: evidence for a Cambrian magmatic arc. Int. Journal of Earth Sciences, 88, pp. 791-802.

Chen C., Lu H., Jia D., Cai D. and Wu S., 1999. Closing history of the southern Tianshan oceanic basin, western China: an oblique collisional orogeny. Tectonophysics, 302, pp. 23-40.

Cocherie A., Guerrot C., and Rossi P., 1992. Single zircon dating by step-wise evaporation: Comparison with other geochronological techniques applied to the Hercynian granites of Corsica, France. Chem. Geol., 101, pp. 131-141.

Coleman R.G, 1989. Continental growth of Northwest China. Tectonics, 8, 3, pp. 621-635.

Coulon C., Malusik H., Bolliger C., and Wang S., 1986. Mesozoic and Cenozoic volcanic rocks from central and southern Tibet: $^{39}Ar/^{40}Ar$ dating, petrological characteristics and geodynamical significance. Earth Planet. Sci. Lett., 79, pp. 281-302.

Coutand I., Strecker M.R., Arrowsmith J.R., Hilley G., Thiede R.C., Korjenkov A., and Omuraliev M., 2002. Late Cenozoic tectonic development of the intramontane Alai Valley (Pamir-Tien Shan region, Central Asia); an example of intracontinental deformation due to the Indo-Eurasia collision. Tectonics, 21, 6, pp. 1-19.

Coward M.P., Butler R.W.H., Asif Khan M., and Knipe R.J., 1987. The tectonic history of Kohistan and its implications for Himalayan structure. Journal of the Geol. Soc. of London, 144, 3, pp. 377-391.

Coward M.P., Kidd W.S.F., Pan Y. Shackleton R.M., and Zhang H., 1988. The structure of the 1985 Tibet Geotraverse, Lhasa to Golmud. Phil. Trans. Royal Soc. Lond., A, 327, pp. 307-336.

Cox K.G., Bell J.D., and Pankhurst R.J., 1979. The interpretation of igneous rocks. Allen and Unwin, London. 450 pp.

Crowley K.D., Cameron A.E., and Schaefer R.L., 1991. Experimental studies of annealing of etched fission tracks in fluorapatite. Geochimica et Cosmochimica Acta 55, pp. 1449-1465.

Debon F., Le Fort P., and Sonet J., 1983. Chemical-mineralogical typology, chronology and geodynamic setting of the western Hindu Kush-Badakhshan plutonic belt (Afghanistan). In: Shams F.A., Granites of Himalayas, Karakorum and Hindu Kush. Inst. Geol., Punjab Univ., Lahore, Pakistan (PAK).

Debon F., Le Fort P., Sheppard S.M.F., and Sonet J., 1986. The four plutonic belts of the Transhimalaya-Himalaya; a chemical, mineralogical, isotopic, and chronological synthesis along a Tibet-Nepal section. Journal of Petrology, 27, 1, pp. 219-250.

Debon F., Afzali H., Le-Fort P., and Sonet J., 1987. Major intrusive stages in Afghanistan; typology, age and geodynamic setting. Geologische Rundschau, 76, 1, pp. 245-264.

Deng S., 1995. Characterstics of the late Mesozoic monolete spore ferns from China and their paleoclimatic and evolutionary significance. Geological Review, 41, 2, pp. 135-143.

DePaolo D.J. and Wasserburg G.J. 1979. Petrogenetic mixing models and Nd-Sr isotopic patterns. Geochimica et Cosmochimica Acta, 43, pp. 615-627.

Desio A., Martina E., and Pasquare G., 1964. On the geology of central Badakhshan (north-east Afghanistan)[with discussion]. Quarterly Journal of the Geological Society of London, 120, 2, 478, pp. 127-151.

Dewey J.F., Cande S.C., and Pitman W.C., 1989. Tectonic evolution of the India/Eurasia collision zone. Eclogae Geologicae Helvetiae, 82, 3, pp. 717-734.

Ding J., Zhang Z., and Zhao M., 1996. The evolution of south passive margin of Yangtze Plate and its controlling factors. 30th International Geological Congress, Abstracts, 30, 1, p. 187.

Dronov V.I. and Leven E.Y., 1990. Permian foraminiferal complexes from olistoliths of the southeastern Pamirs (in Russian). Doklady Akademii Nauk SSSR, 311, 3, pp. 694-697.

Ducea M.N., Lutkov V., Minaev V.T., Hacker B., Ratschbacher L., Luffi, P., Schwab, M., Gehrels G.E., McWilliams M., Vervoort J., and Metcalf J., 2003. Building the Pamirs; the view from the underside. Geology, 31, 10, pp. 849-852.

Duffield W.A., Dalrymple G.B., 1990. The Taylor Creek Rhyolite of New Mexico; a rapidly emplaced field of lava domes and flows. Bulletin of Volcanology, 52, 6, pp. 475-487.

Dumitru T.A., 1993. A new computer-automated microscope stage system for fission-track analysis. Nucl. Tracks Radiat. Meas., 21, pp. 575-580.

Dumitru T.A., Zhou D., Chang E.Z., Graham S.A., Hendrix M.S., Sobel E.R., and Carroll A.R., 2001. Uplift, exhumation, and deformation in the Chinese Tian Shan. In: Hendrix M.S. and Davis G.A., Paleozoic and Mesozoic tectonic evolution of central Asia; from continental assembly to intracontinental deformation. Memoir Geological Society of America, 194, pp. 71-99.

Dunkl I., 2002. TRACKKEY: a windows program for calculation and graphical presentation of fission track data. Comuters and Geosciences, 28, 2, pp. 3-12.

Finsterwalder R., 1929. Das Expeditionsgebiet im Pamir. Zeitschrift des Deutschen und Österreichischen Alpenvereins, Verlag des DÖAV, Innsbruck.

Frank J.R., Carpenter A.B., and Oglesby T.W., 1982. Cathodoluminescence and composition of calcite cement in the Taum Sauk limestone (Upper Cambrian), southeast Missouri. J. Sediment. Petrol., 52, pp. 631-638.

Fraser J.E., Searle M.P., Parrish R.R., and Noble S.R., 2001. Chronology of deformation, metamorphism, and magmatism in the southern Karakoram Mountains. GSA Bulletin, 113, 11, pp. 1443-1455.

Frisch W., Ratschbacher L., Strecker M., Waldhör M., Klishevich V., Kornilov M., Semiletkin S., and Zamoruyev A., 1994a. Tertiary and Quaternary structures in the Eastern Pamir. J. Nepal Geol. Soc., 10, pp. 48-50, Kathmandu.

Frisch W., Ratschbacher L., Strecker M., 1994b. Känozoische Tektonik des nördlichen und östlichen Pamirs: Strukturen, Stressfeld und Heraushebung. Göttinger Arb. Geol. Paläont., Sonderband 1, pp. 209-212, Göttingen.

Gaetani M., 1997. The Karakorum Block in Central Asia, from Ordovician to Cretaceous. Sedimentary Geology, 109, 3-4, pp. 339-359.

Gaetani M., Gosso G., and Pognante U., 1990. A geological transect from Kun Lun to

Karakorum (Sinkiang, China); the western termination of the Tibetan Plateau; preliminary note. Terra Nova, 2, 1, pp. 23-30.

Gaetani M., Gosso G., and Pognante U., 1991. Geological report (Ch. IV). In: Desio A. (ED.) Ev-K2-CNR Italian expedition to the Karakorum. Geodesy, Geophysics and Geology of the Upper Shagsgam Valley (north-east Karakorum) and south Sinkiang. Scientific reports, Consiglio Nazionale delle Richerche, Milano, pp. 99-168.

Galbraith R.F., 1981. On statistical models for fission track counts. Math. Geol., 13, pp. 471-488.

Galbraith R.F., 1990. The radial plot; graphical assessment of spread in ages. Nuclear Tracks and Radiation Measurements, 17, 3, pp. 207-214.

Galbraith R.F. and Green P.F., 1990. Estimating the component ages in a finite mixture. Nucl. Tracks Radiat. Meas., 17, 3, pp. 197-206.

Galbraith R.F. and Laslett G.M., 1993. Statistical models for mixed fission track ages. Nucl. Tracks Radiat. Meas., 21, pp. 459-470.

Gao J., He G., Li M., Xiao X., Tang Y., Wang J., and Zhao M., 1995. The mineralogy, petrology, metamorphic PTDt trajectory and exhumation mechanism of blueschists, South Tianshan, northwestern China. Tectonophysics, 250, 1-3, pp. 151-168.

Gao J., Li M., Xiao X., Tang Y., and He G., 1998. Paleozoic tectonic evolution of the Tianshan Orogen, northwestern China. Tectonophysics, 287, 1-4, pp. 213-231.

Gehrels G.E., Yin A., and Wang X.F., 2003. Detrital zircon geochronology of the north-eastern Tibetan plateau. Geol. Soc. Am. Bull., 115, pp. 881-896.

Girardeau J., Marcoux J., Allegre C.J., Bassoullet J.P., Tang Y., Xiao X., Zao Y., and Wang X., 1984. Tectonic environment and geodynamic significance of the Neo-Cimmerian Donqiao Ophiolite, Bangong-Nujiang suture zone, Tibet. Nature (London), 307, 5946, pp. 27-31.

Girardeau J., Marcoux J., Fourcade J.P., Bassoullet T., and Youking T., 1985. Xainxa ultramafic rocks, central Tibet, China: tectonic environment and geodynamic significance. Geology, 13, pp. 330-333.

Girardeau J., Marcoux J., and Montenat C., 1989. The Neo-Cimmerian ophiolite belt in Afghanistan and Tibet; comparison and evolution. In: Sengor A.M.C., Yilmaz Y., Okay A.I., and Gorur N. (eds.). Tectonic evolution of the Tethyan region. NATO ASI Series. Series C: Mathematical and Physical Sciences, 259, pp. 477-504.

Gleadow A.J.W., Hurford A.J., and Quaife R.D., 1976. Fission track dating of zircon: improved etching techniques. Earth. Planet. Sci. Lett., 33, pp. 273-276.

Gleadow A.J.W., Duddy I.R., Green P.F., and Lovering J.F., 1986. Confined fission track length in apatite: a diagnostic tool for thermal history analysis. Contrib. Mineral. Petrol., 94, pp. 405-415.

Graham S.A., Brassell S.C., Carroll A.R., Xiao X., Demaison G., McKnight C.L., Liang Y., Chu J., and Hendrix M.S., 1990. Characteristics of selected petroleum source rocks, Xianjiang Uygur autonomous region, Northwest China. AAPG Bulletin, 74, 4, pp. 493-512.

Graham S.A., Hendrix M.S., Wang L.B., and Carroll A.R., 1993. Collisional successor basins of western China; impact of tectonic inheritance on sand composition. Geological Society of America Bulletin, 105, 3, pp. 323-344.

Green P.F., 1988. The relationship between track shortening and fission track age

reductionin apatite: combined influences of inherent instability, annealing anisotropy, length bias and system calibration. Earth Planet. Sci. Lett., 89, pp. 335-352.

Green P.F., Duddy I.R., Gleadow A.J.W., Tingate P.R., and Laslett G.M., 1986. Thermal annealing of fission tracks in apatite. 1. A qualitative description. Chem. Geol. (Isot. Geosc. Sect.), 59, pp. 237-253.

Green P.F., Duddy I.R., Gleadow A.J.W., and Lowering J.F., 1989. Apatite fission-track analysis as a paleotemperature indicator for hydrocarbon exploration. In: Naeser N.D. and McCulloh T.H. (eds.). Thermal history of sediment basins – methods and case histories. Springer, Berlin, Heidelberg, New York, pp. 181-196.

Harris N.B.W., Pearce J.A., and Tindle A.G., 1986. Geochemical characteristics of collision-zone magmatism. In: Coward M.P. and Ries A.C. (eds.). Collision tectonics. Geological Society Special Publications, 19, pp. 67-81.

Hendrix M.S., Graham S.A., Carroll A.R., Sobel E.R., McKnight C.L., Schulein B.J., and Wang Z., 1992. Sedimentary record and climatic implications of recurrent deformation in the Tian Shan; evidence from Mesozoic strata of the north Tarim, south Junggar, and Turpan basins, Northwest China. Geological Society of America Bulletin, 104, 1, pp. 53-79.

Hildebrand P.R., Noble S.R., Searle M.P., Parrish R.R., Shakirullah, 1998. Tectonic significance of 24 Ma crustal melting in the eastern Hindu Kush, Pakistan. Geology, 26, 10, pp. 871-874.

Hildebrand P.R., Searle M.P., Shakirullah, and van Heijst H.J., 2000. Geological evolution of the Hindu Kush, NW Frontier Pakistan; active margin to continent-continent collision zone. In: Khan M.A., Treloar P.J., Searle M.P., and Jan, M.Q. (eds.). Tectonics of the Nanga Parbat syntaxis and the western Himalaya. Geol. Soc. Spec. Pub., 170, pp. 277-293.

Hildebrand P.R., Noble S.R., Searle M.P., Waters D.J., and Parrish R.R., 2001. Old origin for an active mountain range; geology and geochronology of the eastern Hindu Kush, Pakistan. Geol. Soc. Am. Bull., 113, 5, pp. 625-639.

Hoffman, E.L., 1992, Instrumental neutron activation in geoanalysis. Journal of Geochemical Exploration, 44, pp. 297-319.

Hopson C., Wen J., Tilton G., Tang Y., Zhu B., and Zhao M., 1989. Paleozoic plutonism in east Junggar, Bogdashan, and eastern Tienshan, Northwest China. EOS, 70, pp. 1403-1404.

Hsü K.J., Guitang P., Sengör and others, 1995. Tectonic evolution of the Tibetan Plateau: a working hypothesis based on the archipelago model of orogenesis. Int. Geol. Rev., 37, pp. 473-508.

Hu A., Zhang Z., Liu J., Peng J., Zhang J., Zhao D., Yang S., and Zhou W., 1986. U-Pb age and evolution of Precambrian metamorphic rocks of the middle Tianshan uplift zone, eastern Tianshan, China. Geochimica (in Chinese), 1, pp. 23-35.

Hurford A.J., 1986. Cooling and uplift patterns in the Lepontine Alps, south-central Switzerland, and an age of vertical movement on the Insubric fault line. Contributions to Mineralogy and Petrology, 92, 4, pp. 413-427.

Hurford A.J. and Green P.F., 1983. The zeta age calibration of fission-track dating. Chem. Geol. (Isot. Geosci. Sect.), 41, pp. 285-317.

Hurford A.J. and Hammerschmidt K., 1985. 40Ar/39Ar and K/Ar dating of the Bishop and Fish Canyon Tuffs: calibration ages for fission track dating standards. Chem. Geol. (Isot. Geosci. Sect.), 58, pp. 23-32.

Hurford A.J. and Watkins R.T., 1987. Fission track age of the tuffs of the Buluk Member, Bakate Formation, Northern Kenya: A suitable fission-track age standard. Chem. Geol., 66, pp. 209-216.

Hurford A.J., Flisch M., and Jäger E., 1989. Unraveling the thermo-tectonic evolution of the Alps; a contribution from fission track analysis and mica dating. In: Coward M.P., Dietrich D., and Park R.G., Conference on Alpine tectonics. Geological Society Special Publications, 45, pp. 369-398.

Hurford A.J., Hunziker J.C., and Stoeckert B., 1991. Constraints on the late thermo-tectonic evolution of the Western Alps; evidence for episodic rapid uplift. Tectonics, 10, 4, pp.758-769.

Hubbard M.S., Grew K.V., Hodges M.G., Yates M.G. and Pertsev N.N., 1999. Neogene cooling and exhumation of upper-amphibolite facies "whiteschists" in the southwest Pamir mountains, Tajikistan. Tectonophysics, 305, pp. 325-337.

Jaffey A.H., Flynn K.F., Glendenin L.E., Bentley W.C., and Essling A.M., 1971. Precision measurements of half-lives and specific activities of ^{235}U and ^{238}U. Phys. Rev. C4: 1889-1906.

Jiang C.F., Yang J.S. Feng B.G., and Zhu Z.Z., 1992. Opening and closing tectonic of the Kunlun Mountains. Beijing, Geological Publishing House, pp. 1-217.

Jolivet M., Roger F., Arnaud N., Brunel M., Tapponnier P., and Seward D., 1999. Exhumation history of Altun Shan; indications of the age of the subduction of the Tarim Block beneath the Altyn Tagh System, northern Tibet (in french). Comptes Rendus de l'Academie des Sciences, Serie II. Sciences de la Terre et des Planetes, 329, 10, pp. 749-755.

Jolivet M., Brunel M., Seward D., Xu Z., Yang J., Roger F., Tapponnier P., Malavieille J., Arnaud N., and Wu C., 2001. Mesozoic and Cenozoic tectonics of the northern edge of the Tibetian Plateau; fission track constraints. Tectonophysics, 343, 1-2, pp. 111-134.

Kapp P. and Cowgill E., 2001. Does the Paleozoic tectonic history of Qiangtang record the formation and break-up of a Devonian supercontinent? Abstracts with Programs - Geological Society of America, 33, 3, p. 42.

Kapp P., Yin A., Manning C.E., Murphy M., Harrison T.M., Spurlin M., Ding L., Deng X., and Wu C.M., 2000. Blueschist-bearing metamorphic core complexes in the Qiangtang Block reveal deep crustal structure of northern Tibet. Geology (Boulder), 28, 1, pp. 19-22.

Kapp P., Murphy M.A., Yin A., Harrison T.M., Ding L., and Guo J., 2003. Mesozoic and Cenozoic tectonic evolution of the Shiquanhe area of western Tibet. Tectonics, 22, 4, pp. 3-23.

Karapetov S.S., Leleshus V.L., and Sonin I.I., 1975. Stratigraphy and Tabulata of the Silurian in Afghanistan (in Russian). Byulleten' Moskovskogo Obshchestva Ispytateley Prirody, Otdel Geologicheskiy, 50, 4, pp. 95-106.

Ketcham R.A., Donelick R.A., and Donelick M.B., 2000. AFTSolve: A program for multi-kinetic modelling of apatite fission-track data. Geol. Mat. Res., 2, 1, pp. 1-32.

Kober B., 1986. Whole-grain evaporation for $^{207}Pb/^{206}Pb$-age investigations on single zircons using a double-filament thermal ion source. Contr. Mineral. Petrol., 93, 482-490 pp.

Kober B., 1987. Single-Zircon evaporation combined with Pb+ emitter bedding for $^{207}Pb/^{206}Pb$-age investigations using thermal ion mass spectrometry, and implications to zirconology. Contr. Mineral. Petrol., 96, 63-71 pp.

Kober B., Hradetzky H., and Lippolt H.J., 1986. Radiogenblei-Evaporationsstudien an einzelnen Zirkonkristallen zur präherzynischen Entwicklung des Grundgebirges im Zentralschwarzwald, SW-Deutschland. Fortsch. Mineral. Band 64 (Beih. 1), 81 pp.

Klötzli U.S., 1997. Zircon evaporation TIMS: Method and procedure. The Analyst, 122, pp. 1239-1248.

Kravchenko K.N., 1979. Tectonic evolution of the Tien Shan, Pamir and Karakorum. Abul Farah, DeJong K.A. (eds.) Geodynamics of Pakistan. Geol. Surv. Pakistan, Quetta, Pakistan, pp. 25-40.

Kröner A. and Todt W., 1988. Single zircon dating constraining the maximum age of the Barberton greenstone belt, Southern Africa. J. Geophys. Res., 93, pp. 15329-15337.

Kröner A. and Hegner E., 1998. Geochemistry, single zircon ages and Sm-Nd systematics of granitoid rocks from the Gory Sowie (Owl Mts), Polish West Sudetes; Evidences for early Palaeozoic arc-related plutonism. J. Geol. Soc. London, 155, 4, 711-724 pp.

Laslett G.M., Green P.F., Duddy I.R., and Gleadow A.J.W., 1987. Thermal annealing of fission tracks in apatite. 2. A quantitative analysis. Chem. Geol. (Isot. Geosc. Sect.), 65, pp. 1-13.

Leeder M.R., Smith A.B., and Yin J., 1988. Sedimentology, palaeoecology and palaeoenvironmental evolution of the 1985 Lhasa to Golmud geotraverse. Phil. Trans. Royal Soc. London, A, 327, 1594, pp. 107-143.

Leith W., 1982. Rock assemblages in Central Asia and the evolution of the southern Asian margin. Tectonics, 1, 3, pp.303-318.

Le Maitre R.W., Bateman P., Dudek A., Keller J., Lameyre Le Bas M.J., Sabine P.A., Schmid R., Sorensen H., Streckeisen A., Woolley A.R. and Zanettin B., 1989. A classification of igneous rocks and glossary of terms. Blackwell, Oxford.

Le Pichon X., Fournier M., and Jolivet L., 1992. Kinematics, topography, shortening, and extrusion in the India-Eurasia collision. Tectonics, 11, 6, pp.1085-1098.

Leven E.Y., 1981. The age of the Paleozoic volcanic formations of North Pamirs (in Russian). Izvestiya Akademii Nauk SSSR. Seriya Geologicheskaya, 1981, 9, pp. 137-140.

Leven E.J., 1995. Permian and Triassic of the Rushan-Pshart Zone (Pamir). Rivista Italiana di Paleontologia e Stratigrafia, 101, 1, pp.3-16.

Li Y.A., Li X.D., Sun D.J., and Han Y.L., 1995. Tectonic evolution of Qiangtang block and Kangxiwar structure zone in Kara-Kunlun Mountains, southwestern Xinjiang, China. Chinese Xinjiang Science & Technology and Hygiene Publishing House, pp. 1-107.

Liew T.C. and Hofmann A.W., 1988. Precambrian crustal components, plutonic associations, plate environment of the Hercynian Fold Belt of central Europe: Indications from a Nd and Sr isotopic study. Contrib. Mineral. Petrol. 98, pp. 129-138.

Ludwig K.R., 2001 Eliminating mass-fractionation effects on U-Pb isochron ages

without double spiking. Geochimica et Cosmochimica Acta, 65, 18, 3139-3145 pp.

McDowell F.W. and Keizer R.P., 1977. Timing of mid-Tertiary volcanism in the Sierra Madre Ocidental between Durango City and Mazatlan, Mexico. Geol. Soc. Amer. Bull., 88, pp. 1479-1487.

Marshall D.J. 1988. Cathodoluminescence of geological materials. Unwin Hyman, London, United Kingdom, 146 pp.

Masuda, A., Nakamura, N. and Tanaka, T., 1973. Fine structures of mutually normalized rare-earth patterns of chondrites. Geochim. Cosmochim. Acta, 37: 239-248.

Mattauer M., Tapponnier P., and Proust F., 1980. Some analogies between the tectonic histories of Afghanistan and Tibet. Proceedings of Symposium on Qinghai-Zizang (Tibet) Plateau. Acad. Sinica, Peking, China (CHN).

Matte P., Tapponnier P., Arnaud N., Bourjot L., Avouac J.P., Vidal P., Qing L., Pan Y., and Wang Y., 1996. Tectonics of western Tibet, between the Tarim and the Indus. EPSL, 142, 3-4, pp. 311-330.

Mattern F. and Schneider W., 2000. Suturing of the Proto- and Paleo-Tethys oceans in the western Kunlun (Xinjiang, China). Journal-of-Asian-Earth-Sciences. 18, 6, pp. 637-650.

Mattern F., Schneider W., Li Y., and Li X., 1996. A traverse through the western Kunlun (Xinjiang, China): tentative geodynamic implications for the Paleozoic and Mesozoic. Geologische-Rundschau, 85, 4, pp. 705-722.

Mattinson J.M., 1994. Real and apparent concordance and discordance in the U-Pb systematics of zircon; limitations of "high precision" U/Pb and Pb /Pb ages. AGU 1994 fall meeting. Eos, Transactions, American Geophysical Union, 75, 44, 691 pp.

Miller C., Schuster R., Klötzli U., Frank W., and Grasemann B., 2000. Late Cretaceous-Tertiary magmatic and tectonic events in the Transhimalaya batholith (Kailas area, SW Tibet. Schweiz. Mineral. Petrogr. Mitt., 80, pp. 1-20.

Miyashiro, A., 1978. Nature of alkalic volcanic rock series. Contrb. Mineral. Petrol., 66: 91-104.

Mogarovskiy V.V., 1986. Trace elements in alkalic basaltoid rocks and lamprophyres of the southern Tien Shan and Pamirs. Transactions (Doklady) of the U.S.S.R. Academy of Sciences: Earth Science Sections, 291, pp. 170-172.

Molnar P. and Tapponnier P., 1975. Cenozoic tectonics of Asia; effects of a continental collision. Science, 189, 4201, pp.419-426.

Naeser C.W. and Faul H., 1969. Fission track annealing in apatite and sphene. Journal of Geophysical Research, 74, 2, pp.705-710.

Nöth L. 1932. *Teil II*: Geologische Untersuchungen im nordwestlichen Pamirgebiet und mittleren Transalai. *In*: Ficker von H. (ed.), 1932. Wissenschaftliche Ergebnisse der Alai-Pamir-Expedition 1928. 3 Teile in 6 Bänden, Verlag D. Reimers, Berlin.

Norin E., 1976. The "Black Slates" formations in the Pamirs, Karakoram and western Tibet. International colloquium on the geotectonics of the Kashmir Himalaya, Karakorum, Hindu Kush, Pamir orogenic belts. Atti dei Convegni Lincei, Accademia Nazionale dei Lincei, 21, pp. 245-264.

Pan Y., 1994. Discovery and evidence of the fifth suture zone of Qinghai-Xizang Plateau. Acta Geophysica Sinica, 37, 2, pp. 184-192.

Pan Y., 1996. Geological evolution of the Karakorum and Kunlun Mountains.

Seismological Press, Beijing, pp. 288.

Pan G. and Zheng H., 1983. A preliminary study on Bangong Co-Nujiang suture (in Chinese). Contrib. Geol. Qinghai-Xizang (Tibet) Plateau, 12, pp. 229-242.

Pan Y., Zheng D., and Zhang Q., 1992. Introduction to integrated scientific investigation on Karakorum and Kunlun mountains. China Meterological Press, Beijing, pp. 1-92.

Parrish R.R., 1987. An improved micro-capsule for zircon dissolution in U-Pb geochronology. *In*: Faure G. (ed.), New developments and applications in isotope geoscience. Chemical Geology; Isotope Geoscience Section, 66, 1-2, 99-102 pp.

Pashkov, B.R. and Shvol´man, V.A., 1979. Rift margins of Tethys in the Pamir (in Russian). Geotektonika, 13, 6, pp. 447-456.

Pearce J.A., 1982. Trace element characteristics of lavas from destructive plate boundaries. In: Thorpe R.S. (ed.). Andesites; orogenic andesites and related rocks. John Wiley & Sons, Chichester, United Kingdom.

Pearce J.A. and Deng W., 1988. The ophiolites of the Tibet Geotraverses, Lhasa to Golmud (1985) and Lhasa to Kathmandu (1986). Philosophical Transactions of the Royal Society of London, Series A: Mathematical and Physical Sciences, 327, 1594, pp. 215-238.

Pearce J.A. and Mei H., 1988. Volcanic rocks of the 1985 Tibet Geotraverse: Lhasa to Golmud. Phil. Trans. R. Soc. London, A, 327, pp. 169-201.

Pearce, J.A., Harris, N.B.W. and Tindle, A.G., 1984. Trace element discrimination diagrams for the tectonic interpretation of granitic rocks. J. Petrol., 25: 956-983.

Petterson M.G. and Windley B.F., 1985. Rb-Sr dating of the Kohistan arc-batholith in the Trans-Himalaya of North Pakistan, and tectonic implications. EPSL, 74, 1, pp. 45-57.

Poller U., Liebetrau V., and Todt W., 1997. U-Pb single-zircon dating under cathodo-luminescence control (CLC-method); application to polymetamorphic orthogneisses. Chemical Geology, 139, 1-4, 287-297 pp.

Portnyagin E.A., Koshlakov G.V., and Kuznetsov Y.S., 1974. The relationship between the deep Paleozoic structure of southern Tien Shan and the buried Tadzhik-Afghan Massif (in Russian). Byulleten Moskovskogo Obshchestva Ispytateley Prirody, Otdel Geologicheskiy, 49, 3, pp. 18-23.

Pospelov I.I., 1987. Formation and tectonic development of the late Variscides of southern Tien Shan and the northern Pamirs (in Russian). In: Timofeyev P.P., Gerbova V.G., Knipper A.L., Krasheninnikov V.A., Pushcharovskiy Y.M., and Khvorova I.V. (eds.). Early geosynclinal formations and structures (in Russian). Trudy - Geologicheskiy Institut (Moskva), 417, pp. 149-178.

Pospelov I.I. and Sigachev S.P., 1989. Development of retro-overthrusts in the Pamirs. Geotectonics, 22, 5, pp. 437-445.

Pupin J.P., 1980. Zircon and granite petrology. Contributions to Mineralogy and Petrology, 73, 3, pp. 207-220.

Ratschbacher L., Frisch W., and Appel E., 1996. Oligocene-Miocene crustal shortening in the northern and central Pamirs. 11th Himalaya-Karakorum-Tibet Workshop Flagstaff, p.72.

Ratschbacher L., Schwab M., Semiletkin S., Hacker B.R., and Herrmann U., 1997. The NE-edge of Tibet; intracontinental shortening and extension, basement doming, and exhumation in the Pamirs. GSA, 1997 annual meeting, Abstracts with Programs -

Geological Society of America, 29, 6, pp.144.

Ratschbacher L. and Schwab M., 1999. Cenozoic intracontinental deformation in the eastern Pamirs – an overview. Bayreuther Bodenkundl. Ber., 65, 73-78.

Rickwood, P.C., 1980. Boundary lines within petrologic diagrams which use oxides of major and minor elements. Lithos, 22: 247-263.

Roddick J.C., Sullivan R.W., and Dudas F.O.L., 1992. Precise calibration of Nd tracer isotopic compositions for Sm-Nd studies. Chemical Geology, 97, 1-2, 1-8 pp.

Rolland Y., Pecher A., and Picard C., 2000. Middle Cretaceous back-arc formation and arc evolution along the Asian margin; the Shyok suture zone in northern Ladakh (NW Himalaya). In: Brown D., Spadea P., and Anma R. (eds.). Processes of arc-continent collision. Tectonophysics, 325, 1-2, pp. 145-173.

Roger F. and Calassou S., 1997. Geochronologie U-Pb sur zircons et geochimie (Pb, Sr et Nd) du socle de la chaine de Songpan-Garze (Chine). U-Pb zircon geochronology and isotope (Pb, Sr and Nd) geochemistry of the basement in the Songpan-Garze fold belt, China. Comptes Rendus de l'Academie des Sciences, Serie II. Sciences de la Terre et des Planetes, 324, 10, pp. 819-826.

Ruzhentsev S.V., 1970. Tectonics of the Vanch range, central Pamirs. Transactions (Doklady) of the U.S.S.R. Academy of Sciences: Earth Science Sections, 190, 1-6, pp. 35-37.

Ruzhentsev S.V. and Shvol'man V.A., 1981. Tectonic zoning of the Pamirs and Afghanistan. In: Sinha A.K. (Ed.). Contemporary geoscientific researches in Himalaya, Vol. 1. Recherches geoscientifiques contemporaines dans l'Himalaya. Bishen Singh Mahendra Pal Singh, Dehra Dun, India (IND).

Ruzhentsev S.V. and Shvol´man V.A., 1982. The Pamirs. in: Alpine structural elements: Carpathian-Balkan-Caucasus-Pamir orogenic zone, edited by M. Mahel, pp. 115-130, VEDA, Bratislava.

Ruzhentsev S.V., Pospelov I.I., and Sukhov A.N., 1978. Tectonics of the Kalaykhumb-Sauksay Zone, North Pamirs (in Russian). Geotectonics, 11, 4, pp. 286-293.

Schärer U., Xu R.H., and Allègre C.J., 1984. U-Pb geochronology of Gangdese (Transhimalaya) plutonism in the Lhasa-Xigaze region, Tibet. Earth Planet. Sci. Lett., 69, pp. 311-320.

Schneider W., Mattern F., Wang P.J., and Li C., 2003. Tectonic and sedimentary basin evolution of the eastern Bangong-Nujiang zone (Tibet): a Reading cycle. Int. J. Earth Scien., 92, 2, pp. 228-254.

Schwab M., Kuhlemann J., Frisch W., Hermann U., Ratschbacher L., Semiletkin S., and Hacker B.R., 1997. Intracontinental shortening, basement doming and exhumation in the Central Pamirs. EUG 9 Strasbourg, Terra Nova, 9, Abstr. Suppl. 1, p. 105.

Schwab M., Ratschbacher L., Frisch W., 1999. Cenozoic to recent thermodynamic evolution of S-Tien Shan, NE- and Central Pamirs: evidences from U/Pb, $^{40}Ar/^{39}Ar$ and fission track dating methods combined with structural analyses. EUG 10 Strasbourg, J. Confer. Abstr., 4/1, p. 54.

Schwab M., Ratschbacher L., Kuhlemann J., Dunkl I., and Frisch W., 2000. Evolution of an active orogen within a continental interior position: examples from the Tien Shan and NE- and Central Pamirs. Geol. Soc. Australia Abs. Ser., 58, 287-288.

Schwab M., Ratschbacher L., Siebel W., McWilliams M., Minaev V., Lutkov V., Chen F.,

Stanek K., Nelson B., Frisch W., and Wooden J.L., 2004. Assembly of the Pamirs: Age and origin of magmatic belts from the southern Tien Shan to the southern Pamirs and their relation to Tibet. Tectonics, 23, doi: 10.1029/2003TC001583.

Şengör A.M.C., 1984. The Cimmeride Orogenic system and the Tectonics of Eurasia. Geol. Soc. Amer. Spec. Pap. 195, pp. 1-88.

Şengör A.M.C., 1990. A new model for the late Palaeozoic-Mesozoic tectonic evolution of Iran and implications for Oman. In: Robertson A.H.F., Searle M.P., and Ries A.C. (eds.). The geology and tectonics of the Oman region. Geol. Soc. Spec. Publ., 49, pp. 797-831, London.

Şengör A.M.C. and Okurogullari, A.H., 1991. The role of accretionary wedges in the growth of continents: Asiatic examples from Argand to plate tectonics. Eclogae geol. Helv. 84/3: 535-597 pp.

Şengör A.M.C., Natal'in B.A., and Burtman V.S.,1993. Evolution of the Altais tectonic collage and Paleozoic crustal growth in Eurasia, Nature, 364, 299-307 pp.

Shvol´man V.A., 1980. A Mesozoic ophiolite complex in the Pamirs. Geotectonics, 14, 6, pp. 465-470.

Shvol´man V.A., 1978. Relict of the Mesotethys in the Pamir. Himalayan Geology, 8, pp. 369-378, Dehra Dun.

Shvol´man V.A., 1977. Tectonic development of the Pamir in Cretaceous and Paleogene periods (in Russian). Transactions of the Geological Institute, Akademi Nauk USSR, 302: 160 pp.

Shvol´man V.A. and Pashkov B.R., 1986. Lower Mesozoic tectonic zones of Central Asia (in Russian). Doklady Akademii Nauk SSSR, 286, 4, pp. 951-954.

Sobel E.R., 1999. Basin analysis of the Jurassic-Lower Cretaceous Southwest Tarim Basin, Northwest China. Geological Society of America Bulletin, 111, 5, pp.709-724.

Sobel E.R. and Arnaud N., 1999. A possible middle Paleozoic suture in the Altyn Tagh, NW China. Tectonics, 18, 1, pp.64-74.

Sommerauer J. 1976. Die chemisch-physikalische Stabilität natürlicher Zirkone und ihr U-(Th)-Pb System. Dissertation, ETH Zürisch.

Stacey J.S. and Kramers J.D. 1975. Approximation of terrestrial lead isotope evolution by a two-stage model. Earth and Planetary Science Letters, 26, 2, 207-221 pp.

Stöcklin J., 1977. Structural correlation of the alpine ranges between Iran and Central Asia. Livre a la memoire de Albert F. de Lapparent (1905-1975) consacre aux Recherches geologiques dans les chaines alpines de l'Asie du Sud-Ouest. Memoire Hors Serie - Societe Geologique de France, 8, pp. 333-353.

Streckeisen A., 1976. Classification of the common igneous rocks by means of their chemical composition; a provisional attempt. Neues Jahrbuch für Mineralogie, Monatshefte, 1, pp. 1-15.

Strecker M., Frisch W., and Ratschbacher l., 1994a. Die aktive Tektonik im nördlichen Pamir (Kirgistan, Tadschikistan, 38-40°N, 70-75°E). Göttinger Arb. Geol. Paläont., Sonderband 1, 207-208, Göttingen.

Strecker M., Ratschbacher l., Frisch W., Hamburger M.W., Semiletkin S., and Zamoruyev A., 1994b. Quaternary deformation in the Eastern Pamirs. Eos, 75/44, p. 631.

Strecker M., Frisch W., Hamburger M.W., Ratschbacher l., Semiletkin S., Sturchio N.,

Zamoruyev A., 1995a. Neotectonics in the eastern Pamirs, Tadzhikistan and Kyrgytan. 10th Himalaya Karakorum Tibet Workshop, Ascona, Mitt. Geol. Inst. ETH & Univ. Zürich, N.F. 298, 1p.

Strecker M., Frisch W., Hamburger M.W., Ratschbacher L., and Semiletkin S., 1995b. Quaternary deformation in the Eastern Pamirs Tadzhikistan and Kyrgyztan. Tectonics, 14, pp. 1061-1079.

Strecker M.R., Hilley G.E., Arrowsmith J.R., and Coutand I., 2003. Differential structural and geomorphic mountain-front evolution in an active continental collision zone; the Northwest Pamir, southern Kyrgyzstan. GSA Bulletin, 115, 2, pp. 166-181.

Tagami T., Lal N., Sorkhabi R.B., Ito H., and Nishimura S., 1988. Fission track dating using the external detector method: a laboratory procedure. Mem. Fac. Sci. Kyoto Univ., Geology and Mineralogy, 53, pp. 1-30.

Taner I. and Meyerhoff A.A., 1990. Petroleum at the roof of the world. The regional evolution of Tibet (Qinghai-Xizang) Plateau. J. Petrol. Geol., 13, pp. 157-178, 289-314.

Tapponnier P. and Molnar P., 1977. Active faulting and tectonics in China. Journal of Geophysical Research, 82, 20, pp. 2905-2930.

Tapponnier P. and Molnar P., 1979. Active faulting and Cenozoic tectonics of the Tien Shan, Mongolia, and Baykal regions. Journal of Geophysical Research, 84, B7, pp. 3425-3459.

Tapponnier P., Mattauer M., Proust F., and Cassaigneau C., 1981. Mesozoic ophiolites, sutures, and large-scale tectonic movements in Afghanistan. EPSL, 52, 2, pp. 355-371.

Thompson R.N., Morrison M.A., Hendry G.L., and Parry S.J., 1984. An assessment of the relative roles of crust and mantle in magma genesis; an elemental approach. In: Moorbath S., Thompson R.N., and Oxburgh E.R. (eds.). The relative contributions of mantle, oceanic crust and continental crust to magma genesis. Phil. Trans. Royal Society of London, Series A, 310, 1514, pp. 549-590.

Vavra G., Gebauer D., Schmid R., and Compston W., 1996. Multiple zircon growth and recrystallisation during polyphase Late Carboniferous to Triassic metamorphism in granulites of the Ivrea Zone (Southern Alps): an ion microprobe (SHRIMP) study. Contrib. Mineral. Petrol., 122, 337-358 pp.

Vincent S.J. and Allen M.B., 1999. Evolution of the Minle and Chaoshui Basins, China: Implications for Mesozoic strike-slip basin formation in Central Asia. Geol. Soc. Of America Bull., 111, 5, pp. 725-742.

Vlasov N.G., Dyakov Y.A., and Cherev E.S. (editors), 1991. Geological map of the Tajik SSR and adjacent territories, 1:500 000, Leningrad.

Wagner G.A., 1969. Spuren der spontanen Kernspaltung des (super 238) Urans als Mittel zur Datierung von Apatiten und ein Beitrag zur Geochronologie des Odenwaldes. Neues Jahrbuch fuer Mineralogie. Abhandlungen, 110, 3, pp.252-286.

Wang G.P., Wu G.T., Lun Z.Q., and Zhu Y.Y., 1995. Regional Geology of Xinjiang Uygur Autonomous Region. Geol. Mem. Ser., I, 32, pp. 1-841.

Wang Z.H., Li J.L., Hou Q.L., and Chen H.H., 2000. Geology, geochemistry and genesis of the Kuda ophiolite, western Kunlun, China (in Chinese with English abstract). Sci. Geol. Sin., 35, pp. 151-160.

Wang Z.H., Sun S., Hou Q.L., and Li J.L., 2001. Effect of melt-rock interaction on geochemistry in the Kudi ophiolite (western Kunlun Mountains, northwestern China): implication for ophiolite origin. Earth Planet. Sci. Lett., 191, pp. 33-48.

Wang Z.H., Sun S., Li J.L., and Hou Q.L., 2002. Petrogenesis of tholeiite associations in Kudi ophiolite (wetsern Kunlun Mountains, northwetsern China): implications for the evolution of back-arc basins). Contrib. Mineral. Petrol., 143, pp. 471-483.

Wendt I., 1986. Radiometrische Methoden in der Geochronologie. Clausthaler Tektonische Hefte, 23, pp. 170.

Wendt J.I. and Todt W., 1991. A vapour digestion method for dating single zircons by direct measurement of U and Pb without chemical separation. Sixth meeting of the European Union of Geosciences. Terra Abstracts, 3, 1, 507-508 pp.

Whalen J.B., Currie K.L., and Chappell B.W., 1987. A-type granites; geochemical characteristics, discrimination and petrogenesis. Contributions to Mineralogy and Petrology, 95, 4, pp. 407-419.

Windley B.F., Allen M.B., Zhang C., Zhao Z.Y., and Wang G.R., 1990. Paleozoic accretion and Cenozoic redeformation of the Chinese Tien Shan Range, Central Asia. Geology, 18, 2, pp.128-131.

Wittekindt H., 1973. Erläuterungen zur geologischen Karte von Zentral- und Süd-Afghanistan 1:500 000. Explanatory text for the geologic map of central and southern Afghanistan; 1:500,000. Bundesanst. Bodenforsch., Hanover, Federal Republic of Germany (DEU).

Xiao W., Windley B.F., Chen H., Zhang G., and Li J., 2002. Carboniferous-Triassic subduction and accretion in the western Kunlun, China; implications for the collisional and accretionary tectonics of the northern Tibetan Plateau. Geology, 30, 4, pp.295-298.

Xu R., Schärer U., and Allegre C.J., 1985. Magmatism and metamorphism in the Lhasa block (Tibet): a geochronological study. J. Geol., 93, pp. 41-57.

Xu R.H., Zhang Y.Q., Vidal P., and Arnaud N., 1992. Two plutonic belts in western Kunlun. Abstr. Int. Symp. On the Karakorum and Kunlun Mountains, Kashi, p. 61.

Xu R.H., Zhang Y.Q., Xie Y.W., Chen F.K., Vidal P., Arnaud N., Zhang Q.D., and Zhao D.M., 1994. A discovery of an early Palaeozoic tectonomagmatic belt in the northern part of west Kunlun mountains (in Chinese with English abstract). Sci. Geol. Sin., 4, pp. 313-328.

Xu R.H., Zhang Y.Q., Xie Y.W., Vidal P., Arnaud N., Zhang Q.D., and Zhao D.M., 1996. Isotopic geochemistry of plutonic rocks. In: Pan Y. (Ed.), Geological Evolution of the Karakorum and Kunlun mountains. Seismol. Press, Beijing, pp. 137-186.

Yang J.S., Robinson P.T., Jiang C.F., and Xu Z.Q., 1996. Ophiolites of the Kunlun mountains, China and their tectonic implications. Tectonophysics, 258, pp. 215-231.

Yaohui J., Zhou X., Rui X., Guo K., He J., and Yang W., 2001. Ocean ridge granite and its geochemical characteristics in western Qinghai-Xizang Plateau. Chinese Journal of Geochemistry, 20, 2, pp. 177-183.

Yin A. and Nie S., 1996. A Phanerozoic palinspastic reconstruction of China and its neighboring regions. In: Yin A. and Harrison M. (eds.). The tectonic evolution of Asia. Cambridge Univ. Press, USA, pp. 442-485.

Yin A. and Harrison T.M., 2000. Geologic evolution of the Himalayan-Tibetan orogen.

Ann. Rev. of Earth and Planetary Sciences, 28, pp. 211-280.

Yin J., Xu J., Liu C., and Li H., 1988. The Tibetan plateau: regional stratigraphic context and previous work. Phil. Trans. Royal. Soc. London., A, 327, pp. 5-52.

Yu G., Wang C., Zhang S., 1991. The charcteristic of Jurassic sedimentary basin of Bangong Co-Dêngqên fault belt in Xizang (in Chinese). Bull. Cengdu Inst. Geol. Miner. Resour., 13, pp. 33-44.

Yuan C., Sun M., Zhou M., and Li J., 1999. Quiescence of arc magmatism in the West Kunlun in the period of Devonian and Carboniferous and its significance to amalgamation and accretion history of Eurasia. Eos, Transactions American Geophysical Union, 80, 46, pp. 1019.

Zanchi A., Gaetani M., and Poli S., 1997. The Rich Gol metamorphic complex; evidence of separation between Hindu Kush and Karakorum (Pakistan). Comptes Rendus de l'Academie des Sciences, II, Sciences de la Terre et des Planetes, 325, 11, pp. 877-882.

Zaun P.E. and Wagner G.A., 1985. Fission track stability in zircons under geological conditions. Nucl. Tracks, 10, pp. 303-307.

Zhang Y.Q. and Xie Y., 1989. A study on the Rb/Sr biotite isochron ages of the granitoid in Shanshiliyingfang area of the Karakorum and Kunlun Mts. region. Journal of Natural Resources, 4, pp. 222-227.

Zhang Y.Q. and Zhou G.Q., 2001. Ophiolites of China (in Chinese with English abstract). Science Press, Beijing, China.

Zhang Y., Xie Y., Xu R., Vidal P., and Arnaud N., 1992. Elements geochemistry of granitoid rocks in the west Qingahi-Xizang Plateau. Int. Symp. On the Karakorum and Kunlun Mountains, Abstracts, Kashi, p. 64.

Zheng Y., Xu K., Yang and others, 1984. Geological charcteristics of ophiolite-melange in Ali region and its relationship with regional tectonics (in Chinese). J. Changchun College Geol., 4, pp. 29-37.

Zonenshain L.P., Kuzmin M.I., Natapov L.M. and Page B.M. (editor), 1990. Geology of the USSR: A plate-tectonic synthesis. Geodynamic Series, 21: 242 pp.

Acknowledgements

It was very challenging to have the chance to visit and study the "roof of the world", like the Pamirs are called. This thesis wouldn't have come to an end without the support of many persons. The first ones to be sincerely thanked are my two supervisors, Prof. Dr. Lothar Ratschbacher (TU Bergakademie Freiberg) and Prof. Dr. Wolfgang Frisch (Eberhard-Karls-Universität Tübingen). Both revised ideas and manuscripts and encouraged me to visit international conferences.
I also want to thank the Deutsche Forschungsgemeinschaft (DFG) for financial support in the frame of the project Fr 610/11 "Tertiäre und quartäre Strukturentwicklung im östlichen Pamir: Kontinentdeformation vor der Spitze des indischen Indenters". A "Jubiläumsstiftung" grant from the University of Würzburg enabled the second travelling to the Pamirs.
During field work I benefited from logistical and geological support of the Russian colleagues Sergei Semiletkin, Micha Kornilov, and Sascha Zamouryev. Physical conditions were kept up in the best field kitchen I ever experienced under the leadership of Irina. Field time was partly joined by other working group members like Manfred Strecker, Ramon Arrowsmith, Peter Blisniuk, Martin Waldhör, and Achim Kuhlemann - we had many stimulating discussions or just relaxing humorous evenings.
Numerous kindly help from colleagues and friends of the Institut für Geowissenschaften der Universität Tübingen are gratefully acknowledged. Gerlinde Höckh, Dagmar Kost, Doris Mühlbayer-Renner, Ulrich Alt-Epping, Steffi Braun and Thomas Piepenbrink are thanked for the preparation of rocks. I sincerely thank I. Gill-Kopp and J. Mällich for the preparation of thin sections, as well as M. Schumann and G. Bartholomä for the XRF analyses. H.P. Meier (Mineralogisches Institut, Universität Tübingen) and M. Westphal (Institut für Geowissenschaften, Universität Tübingen) introduced me into the application of the microprobe for analyses of apatites and zircons. The Activation Laboratory Ltd. in Ancaster, Ontario, Canada is thanked for providing the INAA data. Istvan Dunkl taught me the fission track dating method, whereas Wolfgang Siebel and Fokun Chen guided me in the application of the U/Pb dating method. I thank Yury D. Pushkarev from the Institute of Geology and Geochronology of the Precambrian, Russian Academy of Science, St. Petersburg, Russia for K/Ar dating. Lothar Ratschbacher is thanked for providing me the SHRIMP and Ar/Ar data. Mass spectrometer measurements of Rb, Sr, Nd were done by Elmar Reitter and Wolfgang Siebel.
During my work I benefited many times from discussions or enjoyed the friendly and pleasant atmosphere created also by the other colleagues like Petra Angelmaier, Achim Brügel, Ines Dünkel, Radu Girbacea, Kirsten Gräfe, Dieter Hubich, Achim Kuhlemann, Andreas Läufer, Franz Moser, Thomas Most, Renato Pagliuca, John Reinecker, Cornelia Spiegel, and Britta Trautwein. During the time of finishing our theses motivation was kept up by weekly meetings with Siegfried Kraft and Martin Staiger. I'm thankful for this mutual support. Arndt Peterhänsel, Cornelia Spiegel, Britta Trautwein and Gregor Markl are thanked for their constructive review of parts of the manuscript.
Last but not least, I thank all those people who never lost interest in the progress of

this work, especially all members of the Schwab and Schmalholz families, Tina Schaber, Britta Trautwein, and Manuela Traxler.
My heartiest thanks are going to my husband Andreas. He was patiently supporting and encouraging me.

Appendix

Appendix A

Appendix B

Appendix C

Appendix A

Tab. A1 Sample description and location of magmatic and basement rocks

Sample	Rock	N-latitude	E-latitude
TS1	granite, southern Tien Shan	40°06.3’	73°31.5’
TS2	granite, southern Tien Shan	40°08.4’	73°30.5’
TS12a	granite, southern Tien Shan	39°46.3’	73°37.1’
TS12b	granodiorite, southern Tien Shan	39°46.08’	73°36.72’
TS18a	diorite, southern Tien Shan	39°32.2’	72°06.2’
TS20a	diorite, southern Tien Shan	39°33.77’	72°04.64’
AD1a	metaandesite, Altyndara valley	39°19.3’	72°15.6’
AD2a	metarhyolithe, Altyndara valley	39°12.5’	72°14.3’
AD2e	hornblende-rich metavolcanic rock, Altyndara v.	39°13.64’	72°15.18’
AD2f	metabasalt, Altyndara valley	39°15.4’	72°15.1’
AD5a	metaandesite, Altyndara valley	39°16.8’	72°16’
AD6b	hornblende-rich metaandesite, Altyndara valley	39°17.68’	72°16.08’
AD6c	metaandesite, Altyndara valley	39°18.1’	72°16.01’
AD6d	metabasalt, Altyndara valley	39°18.4’	72°15.9’
AD6e	metaandesite, Altyndara valley	39°18.2’	72°16.6’
AD6f	metadacite, Altyndara valley	39°18.8’	72°15.2’
AD7c	metaandesite, Altyndara valley	39°15.7’	72°18.1’
M3	metaandesite, Altyndara valley	39°17.2’	72°16.05’
AD11b	phyllitic shale	39°21.995’	72°19.619’
P20	two-mica granite, southwestern Karakul lake	38°48.1’	73°17.03’
P22	granite, Karakul lake	38°55.93’	73°22.87’
P24	granite, Karakul lake	38°56.1’	73°26.56’
P25	granite, Karakul lake	39°11.42’	73°26.59’
P26	granite, Karakul lake	39°12’	73°25’
P17	anatectic granite, Akbai valley	38°32.73’	73°31.27’
96M18a	Silurian phyllite, Rankul lake	38°15.05‘	74°02.27‘
96M9a	metaleucogabbro, south of Rankul lake	38°20.84’	74°02.28’
L96M25a	biotite granodiorite, Phart valley	38°12.48’	74°01.724’
L96A9	biotite granite, Aksu valley	38°11.8’	74°14.5’
96P4e	granite pebble in Lower Miocene red beds, Pshart valley	38°16.46’	73°44.53’
A96M18h	chlorite-muscovite-staurolithe-garnet schist, Pshart valley		
P2	granodiorite, western Murgab valley	38°07.67’	73°51.13’
P5	metagranodiorite, western Murgab valley	38°10.2’	73° 34.1’
P7	white-mica bearing granite, eastern Murgab valley	38°11.75’	74°15.33’
96A10b	granodiorite, Aksu valley	38°08.10’	74°28.11’
M96A7	biotite granite intruding Jurassic sed. Rocks, Aksu val.	38°09.2’	74°24.6’
A96S1b	subvolcanic diorite, Saseksu valley	38°31.9’	73°40.7’
96Ak3d	high-grade biotite gneiss, Akbai valley		
P15	granite, Muzkol dome	38°30.4’	73°42.6‘
96A6b	undeformed aplite dike from a leucogranite, Sares dome	38°13.52’	74°29.67’
A96A5k	high-grade biotite gneis, Muzkol dome		
96A5i	high-grade biotite gneis		
96P2a	basalt, Pshart valley	38°16.37’	73°52.08’
A96S2d	basalt in Tertiary red beds, Saseksu valley	38°30’	73°46.3’
L96M7b	basalt in Tertiary red beds, Muzkol dome	38°15.298’	74°02.815’
L96M25b	basalt, Pshart valley	38°12.48’	74°01.724’
L96M27a	basalt, Murgab valley	38°06.62’	73°36.59’
M96M28a	basalt, Muzkol dome		
A96M31b	basalt sill in basement, Pshart valley	38°16.6’	73°56.7’

Tab. A2 Major and trace element concentrations of magmatic rocks

	South Tien Shan/Gissar arc						Pamir frontal range/Kunlun arc					
	subvolcanic		plutonic				volcanic					
	diorite		granite				basalt		basaltic andesite			andesite
Sample	TS20a	TS18a	TS12a	TS2	TS1	TS12b	AD2f	AD6d	AD6b	M3	AD1a	AD7c
SiO_2	58.37	60.60	69.43	70.1	70.80	71.23	46.41	46.91	52.12	52.71	54.55	55.24
TiO_2	0.74	0.78	0.33	0.29	0.33	0.28	0.87	0.72	0.76	0.79	0.61	0.69
Al_2O_3	18.21	16.93	15.17	14.8	14.4	14.8	15.05	15.18	18.50	16.71	17.73	17.03
Fe_2O_3	6.10	5.88	2.53	2.47	2.44	2.07	8.47	9.16	9.13	8.21	7.60	7.15
MnO	0.10	0.11	0.05	0.05	0.06	0.03	0.15	0.15	0.15	0.15	0.15	0.15
MgO	2.11	2.60	0.59	0.46	0.55	0.52	6.73	6.89	5.52	4.83	4.59	3.19
CaO	6.36	5.78	2.20	1.74	1.81	2.02	11.09	9.16	3.48	8.12	7.82	6.66
Na_2O	2.63	2.24	3.69	3.72	2.90	3.35	4.29	2.24	2.27	2.23	2.53	4.15
K_2O	2.77	2.96	4.37	3.77	4.35	4.01	0.11	0.68	4.27	1.35	0.95	0.30
P_2O_5	0.15	0.16	0.08	0.11	0.10	0.06	0.05	0.09	0.10	0.10	0.07	0.10
Ba	1507	1830	585	657	402	686	38.0	172.0	615.0	312.0	389.0	159.0
Cr	15	14	20	82	149	6	355	270	58	70	42	4
Nb	12	12	13	21	18	13	0.5	bdl	bdl	0.0	0.0	2.0
Ni	7	0	22	50	49	2	165.0	64.0	19.0	5.0	13.5	0.5
Rb	116	117	167	147	201	150	1.5	23.0	95.0	32.0	19.0	8.0
Sr	554	409	251	352	199	251	96.5	207.0	609.0	464.0	479.5	498.5
V	31	57	15	17	25	13	181.0	231.0	199.0	212.0	172.0	135.0
Y	25	25	18	17	22	15	20.0	21.0	18.0	22.0	18.0	22.0
Zn	113	124	34	39	40	28	61.0	85.0	84.0	82.0	68.4	78.5
Zr	175	156	163	183	162	159	59.5	52.0	52.0	104.0	91.0	121.0
Total	99.12	99.01	99.10	99.25	99.24	99.15	99.34	99.81	99.83	99.04	99.56	99.37
LOI	1.31	0.74	0.52	1.43	1.07	0.67	6.00	8.63	3.49	3.71	2.83	4.58
A/CNK	0.97	0.97	1.02	1.11	1.13	1.10	0.55	0.72	1.26	0.84	0.91	0.88
Th	8.8	10.7	18.0	18.0	25.0	17.4	0.3	0.9	0.6	3.1	1.5	1.7
Ta	<0.3	1.0	1.5	2.8	1.2	1.2	<0.3	<0.3	<0.3	0.6	<0.3	<0.3
Hf	4.5	4.2	4.3	4.7	4.5	4.5	1.6	1.4	1.3	2.9	2.3	3.0
La	29.4	33.1	38.9	36.8	37.3	38.2	1.95	4.93	4.82	10.20	7.29	9.71
Ce	52	53	64	54	62	65	6.0	12.0	12.0	23.0	18.0	20.0
Nd	20	22	23	20	21	22	5.0	7.0	7.0	12.0	10.0	12.0
Sm	4.41	4.48	4.21	3.60	4.33	4.06	1.91	2.15	2.01	3.05	2.55	3.06
Eu	1.24	1.19	0.94	0.73	0.70	0.94	0.74	0.75	0.57	0.80	0.80	0.94
Tb	0.7	0.7	0.5	0.4	0.5	0.5	0.5	0.4	0.4	0.4	0.4	0.5
Yb	1.93	2.03	0.85	1.39	1.71	0.76	1.97	1.74	1.49	1.98	1.95	2.35
Lu	0.30	0.31	0.14	0.22	0.26	0.12	0.31	0.27	0.23	0.31	0.30	0.38

LOI = loss of ignition
A/CNK = molar concentration of (Al_2O_3/CaO + Na_2O + K_2O)
bdl or < = below detection limit
n.d. = not determined
K. l. = Karakul lake
RPZ = Rushan Pshart zone

Tab. A2 continued

	Pamir frontal range/Kunlun arc					Karakul-Mazar belt			Triassic/Jurassic at Qiangtang and RPZ			
	volcanic					plutonic			plutonic			
	andesite		dacite	rhyolite		granite			leucogab.	granite		
Sample	AD5a	AD6e	AD6c	AD6f	AD2a	P22	P24	P25	96M9a	L96M25a	96P4e	L96A9
SiO_2	55.63	55.96	62.67	67.00	72.93	68.42	69.47	71.96	59.94	68.65	70.14	71.84
TiO_2	0.61	0.65	0.60	0.55	0.23	0.33	0.31	0.25	1.21	0.57	0.30	0.30
Al_2O_3	14.76	17.63	15.02	14.50	13.85	15.92	15.56	14.49	18.34	13.05	15.22	14.18
Fe_2O_3	7.47	7.21	5.58	4.74	2.80	3.06	2.87	2.27	2.50	3.42	1.94	2.04
MnO	0.14	0.14	0.09	0.06	0.05	0.07	0.07	0.06	0.03	0.09	0.04	0.04
MgO	3.45	3.80	2.34	1.32	0.66	0.93	0.76	0.64	1.58	1.49	0.54	0.72
CaO	7.46	7.34	4.49	2.20	1.83	3.05	2.59	2.09	3.68	2.95	1.64	1.90
Na_2O	3.50	3.34	3.95	4.39	6.16	2.63	2.61	2.60	8.59	2.53	3.41	2.63
K_2O	0.48	0.46	1.16	2.45	0.10	3.50	3.85	4.02	0.61	4.10	3.79	4.38
P_2O_5	0.05	0.10	0.05	0.05	0.02	0.11	0.10	0.09	0.19	0.11	0.22	0.07
Ba	73.0	237.0	348.0	660.0	14.0	466	519	422	308	932	237	403
Cr	32	24	33	26	0	34	28	50	109	138	9	115
Nb	0.0	2.0	2.5	6.0	2.5	11.0	9.5	7.0	107	12	23	11
Ni	0.0	11.5	12.0	2.0	3.5	32.0	20.0	41.0	94	9	4	48
Rb	9.0	9.0	41.0	76.5	2.0	154.0	163.5	162.5	15	155	250	183
Sr	163.0	518.5	442.0	248.5	77.0	227.0	209.0	164.5	496	218	119	162
V	169.0	136.5	99.5	74.0	21.5	33.0	29.5	23.5	50	39	29	20
Y	17.0	21.0	14.0	22.0	18.0	24.4	26.0	24.0	27	22	16	29
Zn	73.0	76.0	53.0	57.0	26.0	59.5	55.0	43.5	18	127	37	74
Zr	70.0	105.0	129.5	150.0	99.5	148.0	141.5	119.0	1488	188	111	125
Total	99.47	99.39	99.49	99.30	99.63	99.15	99.05	99.18	98.34	99.53	99.31	99.11
LOI	5.88	2.63	3.39	1.93	0.96	0.79	0.59	0.47	1.20	2.4	1.99	0.69
A/CNK	0.74	0.91	0.94	1.05	1.02	1.17	1.18	1.17	0.85	0.93	1.20	1.13
Th	0.9	1.4	6.7	11.2	1.3	13.3	16.2	12.6	13.8	13.8	10.7	22.6
Ta	<0.3	<0.3	0.3	0.5	<0.3	1.3	1.2	1.1	6.5	1.2	2.5	1.6
Hf	2.1	2.5	3.3	3.9	2.8	4.0	4.2	3.3	24.6	5.0	3.1	3.6
La	3.63	9.06	15.10	23.80	4.77	32.90	38.70	22.80	80.5	39.0	14.0	28.0
Ce	9.0	20.0	28.0	40.0	11.0	58.0	67.0	42.0	128	68	27	49
Nd	6.0	11.0	12.0	17.0	6.0	24.0	27.0	17.0	49	25	13	20
Sm	2.10	2.90	2.75	3.60	1.71	5.03	5.62	4.21	8.67	5.19	3.17	4.72
Eu	0.68	0.88	0.77	0.81	0.45	1.07	1.04	0.72	3.33	1.06	0.66	0.75
Tb	0.5	0.5	0.3	0.4	0.4	0.6	0.6	0.5	0.8	0.5	0.4	0.6
Yb	2.20	1.94	1.25	1.77	1.85	1.98	2.15	2.26	2.67	1.57	0.76	2.47
Lu	0.33	0.30	0.20	0.26	0.29	0.31	0.33	0.33	0.40	0.24	0.11	0.37

LOI = loss of ignition
A/CNK = molar concentration of (Al_2O_3/CaO + Na_2O + K_2O)
bdl or < = below detection limit
n.d. = not determined
K. l. = Karakul lake
RPZ = Rushan Pshart zone

Tab. A2 continued

	Cretaceous at Qiangtang and RPZ						Tertiary extensional phase in the Murgab-Sares domes				
	subvolc.	plutonic					volcanic				
	andesite	granodiorite			granite		basalts				
Sample	A96S1b	P5	96A10b	P2	M96A7	P7	L96M27a	96P2a	A96M31b	A96S2d	L96M7b
SiO_2	53.67	61.68	64.58	68.84	70.51	75.50	46.03	48.21	50.22	50.27	50.36
TiO_2	0.76	0.85	0.83	0.55	0.41	0.22	0.96	1.54	1.52	1.17	1.68
Al_2O_3	19.08	16.61	15.67	15.06	15.02	14.20	16.85	17.88	16.17	17.02	17.41
Fe_2O_3	6.65	3.87	6.21	2.96	2.60	0.63	9.49	9.75	8.25	3.14	8.93
MnO	0.15	0.09	0.04	0.08	0.09	0.00	0.16	0.15	0.08	0.09	0.13
MgO	2.55	1.24	1.42	0.95	0.70	0.14	8.29	8.98	6.2	1.71	5.49
CaO	5.96	2.84	1.08	3.19	1.61	0.19	10.42	3.88	5.67	8.53	6.82
Na_2O	4.51	0.38	2.59	2.04	2.65	2.16	2.42	4.01	3.8	6.98	3.77
K_2O	3.51	5.21	3.99	3.93	3.97	5.51	1.09	0.34	1.11	1.29	1.67
P_2O_5	0.29	0.19	0.19	0.13	0.10	0.07	0.18	0.36	0.41	0.28	0.46
Ba	577	379	1480	881	843	259	359	135	223	181	716
Cr	9	53	0	1	4	129	380	187	163	168	161
Nb	6	15	10	12	22	22	14	16	21	18	22
Ni	0	32	0	22	0	45	143	74	62	44	59
Rb	104	189	122	139	210	318	21	6	26	46	33
Sr	749	42	299	324	210	90	355	535	374	351	518
V	132	84	72	35	28	13	227	181	163	101	168
Y	23	25	18	25	16	16	23	37	42	38	41
Zn	85	15	30	59	90	29	83	160	70	31	106
Zr	139	254	270	200	118	100	96	269	290	335	328
Total	99.18	99.07	99.02	99.06	99.17	99.75	98.78	99.38	99.57	99.23	99.69
LOI	1.85	5.82	2.25	1.07	1.15	0.90	2.71	4.28	6.14	8.75	2.97
A/CNK	0.87	1.45	1.50	1.12	1.26	1.44	0.70	1.28	0.91	0.60	0.85
Th	8.3	24.4	26.9	22.2	13.7	16.8	n.d.	6.1	4.7	13.6	5.6
Ta	1.2	0.8	0.9	1.1	3.0	2.6	n.d.	1	0.7	1.1	1
Hf	3.2	6.6	7.0	5.5	3.4	2.9	n.d.	6.2	6.5	7.3	7.5
La	35.9	60.9	78.4	60.1	25.6	32.0	n.d.	40.4	35.2	49.6	44.6
Ce	61	97	133	100	42	52	n.d.	77	74	95	85
Nd	25	40	50	39	17	20	n.d.	33.00	33.00	44	41
Sm	5.14	7.43	8.57	7.93	4.0	3.52	n.d.	7.67	7.8	7.55	8.89
Eu	1.49	1.36	1.42	1.43	0.68	0.44	n.d.	1.81	1.59	1.94	1.95
Tb	0.6	0.8	0.8	0.7	0.5	0.4	n.d.	0.9	1	1	1
Yb	1.80	1.60	1.23	1.42	1.10	1.00	n.d.	3.68	3.41	3.02	3.6
Lu	0.28	0.24	0.2	0.22	0.16	0.15	n.d.	0.55	0.52	0.45	0.55

LOI = loss of ignition
A/CNK = molar concentration of (Al_2O_3/CaO + Na_2O + K_2O)
bdl or < = below detection limit
n.d. = not determined
K. l. = Karakul lake
RPZ = Rushan Pshart zone

Tab. A2 continued

	Tertiary extensional phase in the Murgab-Sares domes					
	volcanic			plutonic		?
	basalts			granodiorite	granite	?
Sample	M96M28c	M96M28a	L96M25b	P15	96A6b	96P4d
SiO_2	50.44	51.44	53.66	66.01	74.12	81.96
TiO_2	1.57	1.58	1.02	0.38	0.12	0.46
Al_2O_3	16.24	16.47	16.46	17.48	14.05	6.11
Fe_2O_3	8.95	8.82	7.46	2.26	0.85	3.66
MnO	0.08	0.08	0.11	0.01	0.02	0.03
MgO	6.64	6.64	4.53	0.33	0.12	2.12
CaO	6.86	6.92	4.07	1.30	1.16	0.82
Na_2O	3.36	3.35	3.74	4.90	3.91	0.53
K_2O	0.13	0.12	3.97	5.63	4.29	1.09
P_2O_5	0.46	0.45	0.21	0.09	0.02	0.09
Ba	40	70	402	1094	1003	195
Cr	159	156	93	53	60	31
Nb	24	21	10	25	2	11
Ni	61	60	44	13	0	38
Rb	<3	<5	193	106	222	29
Sr	591	559	308	348	438	25
V	158	165	146	22	10	41
Y	41	42	29	18	8	12
Zn	37	33	78	16	17	50
Zr	321	308	149	455	95	253
Total	98.75	99.6	99.84	98.99	99.16	99.21
LOI	3.89	3.73	4.61	0.24	0.29	2.27
A/CNK	0.90	0.90	0.92	1.06	1.06	1.72
Th	n.d.	4.9	7.4	16.9	13.9	n.d.
Ta	n.d.	1.3	1	1.9	0.5	n.d.
Hf	n.d.	6.8	3.9	8.8	3.0	n.d.
La	n.d.	42.6	40.2	83.4	23.5	n.d.
Ce	n.d.	81	72	120	36	n.d.
Nd	n.d.	38	32	40	11	n.d.
Sm	n.d.	8.6	5.74	5.84	2.0	n.d.
Eu	n.d.	1.72	1.85	1.60	0.47	n.d.
Tb	n.d.	1	0.9	0.4	0.2	n.d.
Yb	n.d.	3.75	2.4	1.77	0.53	n.d.
Lu	n.d.	0.56	0.36	0.26	0.08	n.d.

LOI = loss of ignition
A/CNK = molar concentration of (Al_2O_3/CaO + Na_2O + K_2O)
bdl or < = below detection limit
n.d. = not determined
K. l. = Karakul lake
RPZ = Rushan Pshart zone

Tab. A3 Summary of $^{40}Ar/^{39}Ar$ data

Sample	Mineral	J	Weight (mg)	GS (μm)	TFA (Ma)	WMA (Ma)	IA (Ma)	MSWD	$^{40}Ar/^{36}Ar$	% ^{39}Ar used
South Tien Shan/Gissar arc										
TS12b	bio	0.0007562	5	125-250	260.2 ± 0.8	277 ± 0.8[1]	**277.2 ± 1.8**	5/1.7	279 ± 3	92
TS20a	bio	0.0007592	4.7	125-250	277 ± 0.8	**277 ± 0.8**	277.9 ± 1.5	102/1.9	288 ± 8	98
N-Pamirs (Altyndara Valley)/Kunlun arc										
AD2e	hbl	0.0007632	63	125-250	371.6 ± 1.1	357.2 ± 1.0[2]	357.1 ± 2.5	13/3.8	503 ± 9	40
AD6b	hbl	0.0007678	5	125-250	319.9 ± 4.6[3]	na	na	na	na	na
N-Pamirs (Karakul lake)/Songpan-Ganze belt										
P20	bio	0.0014516	2.2	63-200	202.6 ± 1.1	**203.1 ± 1.1**	203.6 ± 1.2	3.7/1.8	274	98
P20	mus	0.0014668	4.4	63-355	206.9 ± 1.1	**206.9 ± 1.0**	207 ± 1.1	1.1/1.9	294	97
P22	bio	0.0014649	0.4	63-355	206.2 ± 1.3	**206.8 ± 1.3**	205.1 ± 2.5	5.2/1.8	338	97
P22	kfs-high-T	0.004509	11.3		176 ± 2	166.7 ± 1.6	167.1 ± 1.7	16.7/2.2	271 ± 19	24
P24	bio	0.0014638	2.7	125-250	203.6 ± 1.1	**204.1 ± 1.1**	203.1 ± 1.1	1.4/1.9	309	67
P24	kfs-laser	0.004427	9.6	63-355	**166.2 ± 1.6**	166.7 ± 1.6	na			100
P25	bio	0.0014555	0.4	125-250	190.1 ± 1.1	**191 ± 1.1**	192.4 ± 2.9	7/1.7	261	96
P26	bio	0.0014722	3.9	63-250	195.7 ± 1.0	**196.2 ± 1**	196.5 ± 1.1	3.7/1.7	288	99
P26	kfs-low-T	0.004512	16.8		122.4 ± 1.2	38.9 ± 0.4	38.8 ± 2.4	579/3.9	294 ± 73	2
P26	kfs-high-T	0.004512	16.8		122.4 ± 1.2	155.4 ± 1.5	151.1 ± 6.8	743/2.2	464 ±156	47
Jurassic in Rushan Pshart Zone										
96P4e	mus-laser	0.000707	4.9	125-250	164.2 ± 1.8	**151.4 ± 1.7**[4]	151.4 ± 5.1	1.33/1.8	436	100
A96M18h	mus	0.0006961	3.4	125-250	162.5 ± 1.0	**166.2** ± 0.5	166.5 ± 1.5	56/2.3	293	5
Cretaceous at Qiangtang and Rushan Pshart Zone										
P7	mus	0.001511	0.2	125-250	**105.3 ± 1.2**	110 ± 0.9	100.9 ± 6.0	4.4/1.8	266	100
P7	kfs-high-T	0.0015081	19	125-250	107.4 ± 1.1	118 ± 1.2	110.7 ± 3.0	146/3	895 ± 215	53
P7	kfs-low-T	0.0015081	19	125-250	107.4 ±1.1	57.8 ± 0.6	57.9 ± 0.7	21/2.7	282.± 12	2
M96A7	mus	0.0007469	4.8	125-250	101 ± 0.3	**101.2 ± 0.3**	101.9 ± 0.3	9.9/1.6	288 ± 1	100
P8	hbl-mid-T	0.0014376	28.4	125-250	78.4 ± 0.6	74.5 ± 0.6	**74.4 ± 1.2**	7.7/3.0	311	42
Shyok arc										
P2	bio	0.0015132	4.6	125-250	98.5 ± 0.6	98.2 ± 0.6	98.3 ± 0.7	4/1.9	295	99
P2	kfs-md	0.004544	28.8	125-250	main domains: 105 Ma and <20 Ma; lovera to be calculated					
P5	bio	0.0015132	1.5	125-250	71.3 ± 0.6	***70 ± 0.7***	69.7 ± 1.0	5/2.4	284	82
Cenozoic reactivation phase										
P9	hbl-fib	0.0015036	10	125-250	23.3 ± 1	21.5 ± 0.3	**21.5 ± 0.3**	0.5/2.2	373	84
P10	hbl	0.0015003	2.7	125-250	14.0 ± 0.2	**14.9 ± 0.2**	14.9 ± 0.4	1.2/2.3	311	68
P14	hbl	0.0014943	47.8	125-250	16.2 ± 0.3	**15.5 ± 0.2**	15.2 ± 0.5	3.0/1.8	301	63
P14	bio	0.004228	0.8	125-250	17.9 ± 0.2	**15.8 ± 0.2**	16 ± 0.4	15.8/2.4	248	92
P15	hbl-low-T	0.00456	10.6	125-250	25.2 ± 0.3	**19.2 ± 0.3**	20 ± 0.6	1.9/3	285	10
P15	hbl-high-T	0.00456	10.6	125-250	10.4 ± 0.3	25.4 ± 0.3	**25.4 ± 1**	9.1/2.4	715	56
P15	bio	0.0014911	5.6	125-250	16 ± 0.1	**16 ± 0.1**	15.9 ± 0.2	2.9/1.9	300	97
P15	kfs-lovera	0.0014574	16.1		17.1 ± 0.2	**15 ± 0.15**[5]	15 ± 0.16	3.8/1.9	339 ± 3	37
P17	bio	0.004239	1.2	125-250	22.6 ± 0.3	**23.3 ± 0.3**	23.5 ± 1.1	5.9/2.4	281	46
Pa4460	bio	0.00455	1.5	125-250	16.9 ± 0.2	**15.4 ± 0.2**	15.3 ± 0.2	7.3/2.3	303	77

J is the irradiation parameter; MSWD is the mean square weighted deviation (Wendt and Carl 1991), which expresses the goodness of fit of the isochron (Roddick 1978); isochron and weighted mean ages are based on fraction of ^{39}Ar listed in the last column. Abbreviations are as follows: TFA, total fusion age; WMA, weighted mean age; IA, isochrone age; bio, biotite; mus, K-white mica; hbl, hornblende; wrb, whole rock basalt; na, not analysed. Italics: weighted mean plateau age; bold: preferred are interpretation.

[1] Weighted mean age recalculated with $^{40}Ar/^{36}Ar$ of 279; [2] Weighted mean age recalculated with $^{40}Ar/^{36}Ar$ of 503, youngest steps down to ~40 Ma, possibly homogenously distributed excess ^{40}Ar; [3] Highest temperature step at ~354 Ma; [4] Weighted mean age recalculated with $^{40}Ar/^{36}Ar$ of 436; [5] Weighted mean age recalculated with $^{40}Ar/^{36}Ar$ of 339; [6] Weighted mean age recalculated with $^{40}Ar/^{36}Ar$ of 338; [7] Weighted mean age recalculated with $^{40}Ar/^{36}Ar$ of 392; [8] Weighted mean age recalculated with $^{40}Ar/^{36}Ar$ of 428, [9] Weighted mean age recalculated with $^{40}Ar/^{36}Ar$ of 466, preferred age interpretation 23 ± 5 Ma; [10] Weighted mean age recalculated with $^{40}Ar/^{36}Ar$ of 313; [11] Preferred age interpretation 25 ± 10 Ma. Data were provided by L. Ratschbacher.

Tab. A3 continued

Sample	Mineral	J	Weight (mg)	GS (μm)	TFA (Ma)	WMA (Ma)	IA (Ma)	MSWD	$^{40}Ar/^{36}Ar$	% ^{39}Ar used
Cenozoic reactivation phase (continued)										
Pa5360	bio	0.004514	1.8	125-250	15.7 ± 0.2	**15.7 ± 0.2**	15.7 ± 0.2	0.2/3	299	39
Pa5360	kfs-lov	0.004471	6.5		15.5 ± 0.15	**15.4 ± 0.15**	15.5 ± 0.16	1.6/1.7	295 ± 1	93
96A6c	bio	0.0007328	2.2		15.4 ± 0.05	***15.3 ± 0.05***	15.3 ± 0.05	1/2.6	296 ± 3	90
96A11d	bio	0.0007357	7	125-250	16.4 ± 0.1	16.1 ± 0.1	**16.1 ± 0.2**	0.67/2.1	337	100
A96A5i	mus	0.0007398	5		15.7 ± 0.1	***15.7 ± 0.05***	15.7 ± 0.05	3.8/2.6	295 ± 2	62
A96A5k	bio	0.0007435	5.9		15.5 ± 0.1	**15.7 ± 0.05**	15.7 ± 0.06	6.6/1.7	302 ± 7	86
A96A5k	mus	0.0007452	2.7		15.8 ± 0.1	**15.8 ± 0.05**	15.7 ± 0.08	2.1/2.3	306 ± 7	84
L96A11a	mus	0.0007365	7		15.5 ± 0.1	**15.4 ± 0.05**	15.4 ± 0.1	69/1.8	298 ± 4	96
M96A8e	bio	0.0007501	3.5		13.5 ± 0.1	**13.5 ± 0.1**	13.3 ± 0.1	31/1.6	315 ± 7	98
96Ak2c	bio	0.0007138	4.8		15.8 ± 0.1	**15.9 ± 0.1**	15.8 ± 0.1	3.1/2.4	314 ± 7	99
96Ak3f	hbl	0.0007232	16.6		18.3 ± 0.1	**18.7 ± 0.06**	18.7 ± 0.07	5.5/2.4	297 ± 3	80
96M9c	hbl-low-T	0.0006875	3.6		54.2 ± 0.2	16.6 ± 0.5[6]	**16.6 ± 1.2**	0.9/3	338 ± 6	10
96M9c	hbl-mid-T	0.0006875	3.6		54.2 ± 0.2	29.0 ± 0.2[7]	**28.9 ± 0.6**	3.6/3	392 ± 6	35
96M10a	bio	0.0006899	2.2		14.4 ± 0.5	14.7 ± 0.3[8]	**14.7 ± 0.4**	0.7/2.3	428 ± 56	96
96M11b	bio	0.0006914	1	63-125	16.1 ± 0.2	15.4 ± 0.3	**15.4 ± 0.5**	0.52/2.3	616	100
96M16d	hbl-mid-T	0.0006927	25.5		156.1± 0.5	23.9 ± 0.3[9]	23.8 ± 1.2	2.8/3.8	466	7
L96M21a	hbl	0.0006978	5.9		17 ± 0.1	15.9 ± 0.05[10]	**15.9 ± 0.07**	1.6/1.9	313 ± 6	76
L96M18c	bio	0.0007026	4.2		19.2 ± 0.1	**18.8 ± 0.1**	18.8 ± 0.2	5/2.7	295 ± 3	93
96S6c	hbl-low-T	0.0007531	6.4		19.5 ± 0.1	15.7 ± 0.2	17.2 ± 0.8	4.4/2.3	292 ± 2	25
96S6c	hbl-high-T	0.0007531	6.4		19.5 ± 0.1	20.5 ± 0.1	19.6 ± 0.4	11.3/2.3	310 ± 5	59
96S6d	hbl	0.0007544	26		17.3 ± 0.1	**18.2 ± 0.1**	18.6 ± 0.2	6.4/1.7	285 ± 2	99
Central Pamirian basalts										
A96M31b	wrb	0.0007853	31.7		24.4 ± 0.1	**19.5 ± 0.1**	20.6 ± 1.0	42/2.5	292 ± 4	81
L96M7b	wrb	0.0007819	60.2		20.3 ± 0.1	**20.4 ± 0.1**	20.2 ± 0.15	13/1.6	297 ± 1	92
L96M27a	wrb	0.0007048	20.1		37.1 ± 8.5	22.6 ± 8.7[11]	31.2 ± 14	38037	295 ± 2	32
A96S2d	wrb	0.0007709	29.3		19.3 ± 0.2	**18.0 ± 0.2**	25.1 ± 1.4	4.8/1.8	282 ± 3	92

J is the irradiation parameter; MSWD is the mean square weighted deviation (Wendt and Carl 1991), which expresses the goodness of fit of the isochron (Roddick 1978); isochron and weighted mean ages are based on fraction of ^{39}Ar listed in the last column. Abbreviations are as follows: TFA, total fusion age; WMA, weighted mean age; IA, isochrone age; bio, biotite; mus, K-white mica; hbl, hornblende; wrb, whole rock basalt; na, not analysed. Italics: weighted mean plateau age; bold: preferred are interpretation.

[1] Weighted mean age recalculated with $^{40}Ar/^{36}Ar$ of 279; [2] Weighted mean age recalculated with $^{40}Ar/^{36}Ar$ of 503, youngest steps down to ~40 Ma, possibly homogenously distributed excess ^{40}Ar; [3] Highest temperature step at ~354 Ma; [4] Weighted mean age recalculated with $^{40}Ar/^{36}Ar$ of 436; [5] Weighted mean age recalculated with $^{40}Ar/^{36}Ar$ of 339; [6] Weighted mean age recalculated with $^{40}Ar/^{36}Ar$ of 338; [7] Weighted mean age recalculated with $^{40}Ar/^{36}Ar$ of 392; [8] Weighted mean age recalculated with $^{40}Ar/^{36}Ar$ of 428, [9] Weighted mean age recalculated with $^{40}Ar/^{36}Ar$ of 466, preferred age interpretation 23 ± 5 Ma; [10] Weighted mean age recalculated with $^{40}Ar/^{36}Ar$ of 313; [11] Preferred age interpretation 25 ± 10 Ma. Data were provided by L. Ratschbacher.

Tab. A4 Summary of K/Ar data

Sample	Mineral	%K	^{40}Ar (ng/g)	Age (Ma)
Basement				
AD11b	illite	5.03 ± 0.04	10.8 ± 0.15	31 ± 1.5
96M18a	sericite	5.57 ± 0.04	35.3 ± 0.4	89 ± 2
Basalts				
L96M7b	wrb	1.37 ± 0.03	2.45 ± 0.1	25.0 ± 1.5
96P2a	wrb	0.35 ± 0.015	0.7 ± 0.03	29 ± 2
A96S2d	wrb	1.27 ± 0.03	1.6 ± 0.1	18 ± 2
A96M31b	wrb	1.16 ± 0.03	1.8 ± 0.1	22 ± 2
Sediments				
M96M6b	sericite	4.17 ± 0.04	6.2 ± 0.2	21.5 ± 1.5
96M8c	sericite	5.50 ± 0.4	12.5 ± 0.15	32.5 ± 1.5
96M13a	sericite	3.90 ± 0.04	3.90 ± 0.15	14.0 ± 1.0
M96M5a	sericite	5.13 ± 0.04	10.0 ± 0.15	28.0 ± 1.5
A96M4c	sericite	4.45 ± 0.04	5.6 ± 0.2	18.0 ± 1.0

wrb = whole rock basalt

Tab. A5 Rb/Sr Geochronology

Sample	Mineral	Rb (ppm)	Sr (ppm)	^{87}Rb/^{86}Sr[1]	^{87}Sr/^{86}Sr	^{87}Sr/^{86}Sr$_{(i)}$	Age (Ma)
96Ak3d	whole rock	287	28	29.727	0.732202 ± 0.000009		
	muscovite	264.7	22.88	33.576	0.735898 ± 0.000012	0.703652 ± 0.0035	68.0 ± 7.7
96A5i	whole rock	224	140	4.63	0.709417 ± 0.000010		
	muscovite	427.1	36.06	34.327	0.725058 ± 0.000011	0.706978 ± 0.000042	37.1 ± 0.4
A96A5k	whole rock	115	59	5.6461	0.719875 ± 0.000010		
	muscovite	250.6	85.99	8.4415	0.721067 ± 0.000010	0.717467 ± 0.000113	30.0 ± 1.2
L96A11a	whole rock	62	116	1.5485	0.721664 ± 0.000013		
	muscovite	472.7	14.75	92.985	0.739416 ± 0.000012	0.721363 ± 0.000015	13.7 ± 0.1
M96A7	whole rock	209	212	2.8547	0.716054 ± 0.000010		
	muscovite	458.3	19.97	67.058	0.810614 ± 0.000012	0.711850 ± 0.000063	103.6 ± 1.1
96P4e	whole rock	250	121	5.9928	0.733269 ± 0.000010		
	muscovite	937.4	13.47	212.77	1.287214 ± 0.000015	0.717215 ± 0.000229	188.4 ± 1.9
P7	whole rock	318	91	10.129	0.726648 ± 0.000011		
	muscovite	1001	12.94	232.08	1.077421 ± 0.000011	0.710640 ± 0.000233	111.2 ± 1.1

[1] The maximum error is ± 0.5%.

Tab. A6 Rb/Sr and Sm/Nd isotopic ratios

Sample	Age (Ma)	Sr ppm	Rb ppm	Sm ppm	Nd ppm	$^{87}Rb/^{86}Sr$	$^{87}Sr/^{86}Sr$	$^{87}Sr/^{86}Sr(i)$	$^{147}Sm/^{144}Nd$	$^{143}Nd/^{144}Nd$	$^{143}Nd/^{144}Nd(i)$	εNd (T)	εNd (0)	TDM[1]	εSr (0)	εSr (T)
AD2a	329 ± 5	74.32	1.148	1.796	6.478	0.045	0.705596 ± 08	0.705384	0.1676	0.512869 ± 10	0.5125080	5.73	4.51	0.60	16	18.16
AD6b	355 ± 2	533.5	108.7	1.830	6.534	0.590	0.708277 ± 09	0.705264	0.1728	0.512646 ± 10	0.5122443	1.24	0.16	0.99	54	16.89
AD6c	329 ± 5	427.0	41.45	2.680	12.70	0.281	0.706972 ± 09	0.705642	0.1276	0.512466 ± 09	0.5121912	-0.45	-3.36	1.11	35	21.81
P22	216 ± 2	216.4	148.6	5.174	27.88	1.987	0.713857 ± 08	0.707623	0.1122	0.512308 ± 09	0.5121479	-4.09	-6.44	1.32	133	48.05
P26	216 ± 2	198.4	175.2	4.530	34.84	2.557	0.715323 ± 09	0.706974	0.0786	0.512276 ± 11	0.5121592	-3.64	-7.06	1.29	154	38.99
L96M25a	235 ± 11	217.5	155	5.151	27.22	2.087	0.714926 ± 10	0.707951	0.1168	0.512228 ± 08	0.5120484	-5.60	-8.00	1.46	148	52.99
96M9a	230 ± 10	495.5	15	8.679	55.37	0.089	0.705601 ± 10	0.705311	0.0967	0.512623 ± 07	0.5124774	2.64	-0.29	0.78	16	15.43
L96A9	205 ± 2	161.5	183	5.147	25.29	3.319	0.718987 ± 10	0.709310	0.1256	0.512222 ± 10	0.5120535	-6.62	-8.11	1.49	206	71.78
M96A7	131 ± 2	212	209	4.575	24.38	2.887	0.716052 ± 10	0.710717	0.1158	0.512081 ± 10	0.5119825	-9.53	-10.87	1.70	164	90.48
96A10b	126 ± 50	296	120	11.78	88.01	1.187	0.711870 ± 10	0.709745	0.0826	0.512039 ± 10	0.5119709	-9.85	-11.68	1.72	105	76.60
P2	119 ± 3.6	324	139	19.46	46.99	1.256	0.713211 ± 10	0.711105	0.2555	0.512017 ± 09	0.5118197	-13.00	-12.11	1.97	124	95.77
P7	111.2 ± 1.1	90	317.5	8.168	53.32	10.34	0.726548 ± 10	0.710234	0.0945	0.512070 ± 09	0.5120014	-9.64	-11.08	1.69	313	83.29
96Ak3d	68 ± 7.7	28	287	5.921	76.19	30.07	0.732255 ± 10	0.703210	0.0480	0.511860 ± 06	0.5118387	-13.89	-15.18	2.01	394	-17.16
96A5i	37.1 ± 0	140	224	2.241	13.00	4.683	0.709403 ± 10	0.706942	0.1037	0.512145 ± 10	0.5121199	-9.18	-9.62	1.60	70	35.29
A96A5k	30 ± 1.2	59	115	54.12	311.2	5.710	0.719806 ± 10	0.717373	0.1073	0.512157 ± 07	0.5121359	-9.04	-9.38	1.58	217	183.2
L96A11a	13.7 ± 0.1	113.0	59.62	2.474	11.98	1.529	0.721966 ± 23	0.721659	0.1274	0.512111 ± 11	0.5120993	-10.16	-10.28	1.66	248	243.8
P15	32 ± 8	348	106	6.196	48.69	0.891	0.707082 ± 10	0.706677	0.0785	0.512482 ± 09	0.5124656	-2.56	-3.04	1.06	37	31.44
96A6b	30 ± 8	437.5	221.5	2.731	20.78	1.481	0.707607 ± 10	0.706976	0.0811	0.512291 ± 10	0.5122751	-6.33	-6.77	1.36	44	35.65

Errors are two standard deviations (2σ). [1] TDM = depleted mantle model ages calculated with the formula of Liew & Hofmann (1988) for a two component reservoir of continental crust and depleted mantle.

Tab. A7 U/Pb analytical data for zircons

Sample	Atomic ratios					Apparent ages (Ma)		
	$^{206}Pb/^{204}Pb$[1]	$^{207}Pb/^{206}Pb$	$^{208}Pb/^{206}Pb$	$^{206}Pb/^{238}U$	$^{207}Pb/^{235}U$	$^{206}Pb/^{238}U$	$^{207}Pb/^{235}U$	$^{207}Pb/^{206}Pb$
AD2a								
F1	1091.5 ± 27.6	0.06434 ± 0.000066	0.19890 ± 0.000084	0.053759 ± 0.00068	0.37999 ± 0.0056	337.6	327.0	252.7
F3	197.4 ± 0.4	0.12637 ± 0.000140	0.34773 ± 0.000240	0.052418 ± 0.00064	0.38309 ± 0.0053	329.4	329.3	329.0
F5	171.0 ± 0.5	0.13793 ± 0.000072	0.04089 ± 0.000013	0.052200 ± 0.00056	0.38186 ± 0.0094	328.0	328.4	331.2
AD6c								
F2	1480.9 ± 15.8	0.06379 ± 0.000010	0.17416 ± 0.000066	0.050814 ± 0.00019	0.37985 ± 0.0016	319.5	326.9	380.0
P22								
F1	1688.6 ± 3.2	0.05907 ± 0.000032	0.14225 ± 0.000046	0.033808 ± 0.00026	0.23505 ± 0.0019	214.3	214.4	214.6
F2	353.4 ± 2.0	0.09141 ± 0.000180	0.21970 ± 0.000029	0.035145 ± 0.00019	0.24210 ± 0.0026	222.7	220.1	193.1
P26								
2a	4073.0 ± 15.9	0.05516 ± 0.000003	0.10380 ± 0.000052	0.03314 ± 0.00019	0.23615 ± 0.00023	210.2	215.3	271.5
2b	2065.0 ± 30.3	0.05547 ± 0.000100	0.08864 ± 0.000057	0.03278 ± 0.00026	0.21909 ± 0.000023	207.9	201.2	122.5
F2	4789.0 ± 4.7	0.05387 ± 0.000008	0.09955 ± 0.000058	0.03368 ± 0.00023	0.23648 ± 0.0016	213.6	215.5	237.1
P17								
D2	5778.0 ± 18.8	0.06049 ± 0.000035	0.14620 ± 0.000089	0.07532 ± 0.00059	0.60340 ± 0.0048	468.1	479.4	533.6
DE2	4315.0 ± 19.3	0.06121 ± 0.000033	0.14890 ± 0.000078	0.06703 ± 0.00036	0.53580 ± 0.0030	418.3	435.7	528.8
96m9a								
F2	241.3 ± 0.3	0.11582 ± 0.000037	0.54962 ± 0.000220	0.036537 ± 0.00022	0.27864 ± 0.0028	231.3	249.6	424.8
F3	99.7 ± 0.2	0.20707 ± 0.000300	0.75496 ± 0.000380	0.03193 ± 0.00025	0.27340 ± 0.00043	202.6	245.4	677.7
F4	931.9 ± 7.6	0.06700 ± 0.000230	0.42996 ± 0.000460	0.032206 ± 0.00003	0.23406 ± 0.0039	204.3	213.6	316.4
F5	571.8 ± 1.9	0.07805 ± 0.000031	0.38006 ± 0.000061	0.031057 ± 0.00018	0.22511 ± 0.0017	197.2	206.2	310.2
L96M25a								
F1	3302.9 ± 19.1	0.06021 ± 0.000099	0.09534 ± 0.000170	0.032832 ± 0.00034	0.25336 ± 0.0027	208.2	229.3	451.1
F2	1766.1 ± 26.5	0.06170 ± 0.000068	0.08657 ± 0.000130	0.033633 ± 0.00035	0.24865 ± 0.0027	213.3	225.5	355.0
F3	830.7 ± 2.3	0.07335 ± 0.000044	0.11968 ± 0.000055	0.041391 ± 0.00054	0.31933 ± 0.0046	216.5	281.4	450.6
F5	488.4 ± 5.6	0.08331 ± 0.000063	0.16047 ± 0.000087	0.038997 ± 0.00043	0.28813 ± 0.0038	246.6	257.1	353.7
L96A9								
F1	489.2 ± 2.4	0.09627 ± 0.000035	0.15725 ± 0.000063	0.034989 ± 0.00360	0.32300 ± 0.0034	221.7	284.2	836.3
F2	176.9 ± 0.2	0.13606 ± 0.000014	0.27477 ± 0.000027	0.029998 ± 0.00031	0.22073 ± 0.0025	190.5	202.5	344.4
F3	326.0 ± 0.9	0.09608 ± 0.000013	0.18269 ± 0.000022	0.032588 ± 0.00058	0.22984 ± 0.0042	206.7	210.1	247.7
F4	129.0 ± 0.1	0.16460 ± 0.000020	0.36389 ± 0.000080	0.028210 ± 0.00034	0.19775 ± 0.0028	179.3	183.2	233.7
F5	706.1 ± 1.9	0.07213 ± 0.000012	0.12812 ± 0.000028	0.032436 ± 0.00033	0.22986 ± 0.0028	205.8	210.1	258.7

Tab. A7 continued

Sample	Atomic ratios					Apparent ages (Ma)		
	$^{206}Pb/^{204}Pb$[1]	$^{207}Pb/^{206}Pb$	$^{208}Pb/^{206}Pb$	$^{206}Pb/^{238}U$	$^{207}Pb/^{235}U$	$^{206}Pb/^{238}U$	$^{207}Pb/^{235}U$	$^{207}Pb/^{206}Pb$
M96A7								
F1	1371.2 ± 9.6	0.06552 ± 0.000054	0.13679 ± 0.00015	0.024878 ± 0.00025	0.18856 ± 0.0020	158.4	175.4	411.0
F2	7023.4 ± 17.8	0.06658 ± 0.000013	0.09581 ± 0.000023	0.021452 ± 0.00021	0.19103 ± 0.0019	136.8	177.5	760.8
F3	3604.9 ± 16.3	0.05872 ± 0.000027	0.12013 ± 0.000062	0.021038 ± 0.00021	0.15883 ± 0.0016	134.2	149.7	402.4
F4	4410.9 ± 23.0	0.05862 ± 0.000035	0.10097 ± 0.000067	0.020883 ± 0.00023	0.15948 ± 0.0018	133.2	150.2	427.9
F5	6301.6 ± 15.0	0.06926 ± 0.000007	0.07398 ± 0.000013	0.021902 ± 0.00021	0.20241 ± 0.0020	139.7	187.2	838.5
96A10b								
F1	116.8 ± 1.0	0.17452 ± 0.001	0.49216 ± 0.0027	0.017315 ± 0.00013	0.11520 ± 0.0045	110.7	110.7	111.8
F2	564.7 ± 8.9	0.07579 ± 0.00017	0.12394 ± 0.00019	0.019374 ± 0.00024	0.12977 ± 0.0033	123.7	123.9	127.6
F3	1859.9 ± 8.5	0.05745 ± 0.000090	0.08616 ± 0.00011	0.017593 ± 0.00012	0.11914 ± 0.0012	112.4	114.3	153.4
A96S1b								
F2	467.8 ± 2.1	0.08096 ± 0.00045	0.56322 ± 0.00056	0.01208 ± 0.00014	0.08455 ± 0.0014	77.4	82.4	230.2
F3	790.9 ± 7.4	0.06884 ± 0.000084	0.49607 ± 0.00017	0.01206 ± 0.00016	0.08434 ± 0.0012	77.3	82.2	227.3
F5	282.6 ± 2.1	0.10097 ± 0.00039	0.59945 ± 0.00097	0.005785 ± 0.00009	0.04009 ± 0.0011	37.2	39.9	207.1
F6	637.8 ± 9.0	0.06904 ± 0.00015	0.55967 ± 0.00054	0.011566 ± 0.00025	0.07468 ± 0.0018	74.1	73.1	40.5
F7	834.7 ± 20.4	0.06406 ± 0.000049	0.54728 ± 0.00020	0.011653 ± 0.00024	0.07537 ± 0.0018	74.7	73.8	44.8
F8	626.2 ± 2.3	0.09037 ± 0.000046	0.40724 ± 0.00024	0.016405 ± 0.00036	0.15429 ± 0.0035	104.9	145.7	875.0
P2								
D3	4349.2 ± 19.5	0.05610 ± 0.00015	0.10745 ± 0.00052	0.017842 ± 0.00010	0.13002 ± 0.00081	114.0	124.1	322.6
P5								
E3	1059.0 ± 2.0	0.06681 ± 0.000025	0.1851 ± 0.000083	0.017330 ± 0.00011	0.12710 ± 0.00081	110.8	121.5	337.0
EF2	2315.0 ± 3.2	0.05990 ± 0.00042	0.1453 ± 0.000038	0.018160 ± 0.00017	0.13450 ± 0.0013	116.0	128.1	359.4
P15								
E2	542.7 ± 1.6	0.07409 ± 0.000037	0.2657 ± 0.00022	0.005133 ± 0.00003	0.03344 ± 0.00035	33.0	33.4	62.2
E3a	738.4 ± 1.1	0.06684 ± 0.000020	0.2784 ± 0.000060	0.004997 ± 0.00003	0.03247 ± 0.00026	32.1	32.4	55.6
E3b	578.7 ± 1.0	0.07232 ± 0.000048	0.2923 ± 0.0033	0.004638 ± 0.00004	0.03014 ± 0.00031	29.8	30.2	56.2
F2b	456.4 ± 1.8	0.07916 ± 0.000061	0.3008 ± 0.00012	0.005084 ± 0.00003	0.03306 ± 0.00028	32.7	33.0	57.7
F3	373.4 ± 0.3	0.08551 ± 0.000026	0.3341 ± 0.000043	0.005068 ± 0.00004	0.03239 ± 0.3	32.6	32.4	15.7
96A6b								
F1	255.3 ± 2.9	0.10561 ± 0.00037	0.31258 ± 0.00072	0.003320 ± 0.00006	0.02265 ± 0.00060	21.4	22.7	170.6
F3	982.9 ± 46.3	0.06397 ± 0.00029	0.24555 ± 0.00045	0.002952 ± 0.00004	0.02032 ± 0.00040	19.0	20.4	191.0
F4	718.7 ± 137.6	0.06339 ± 0.000057	0.16489 ± 0.00088	0.002534 ± 0.00008	0.01522 ± 0.0015	16.3	15.3	-135.45

Tab. A8 Isotope data for single grain $^{207}Pb/^{206}Pb$ evaporation analyses of zircons of sample 96M9a

Sample	No. of ratios	$^{204}Pb/^{206}Pb$	$^{206}Pb/^{208}Pb$	$^{207}Pb/^{206}Pb$	Age (Ma)
96M9a-1	226	0.000323	2.5	0.050720 ± 48	228.2 ± 2.2
96M9a-2	260	0.000447	2.3	0.050772 ± 53	230.5 ± 2.4
Weighted average					**229.3 ± 1.6**

Errors are given at the 95% confidence level and refer to the last digits.

Tab. A9 U/Pb isotopic ratios from SHRIMP measurements

Sample-Grain-Spot	U ppm	Th ppm	Pb* ppm	^{204}Pb ppm	Atomic ratios						Apparent ages (Ma)			
					^{204}Pb/^{206}Pb	^{208}Pb/^{206}Pb	^{208}Pb/^{232}Th	^{206}Pb/^{238}U	^{207}Pb/^{235}U	^{207}Pb/^{206}Pb	^{208}Pb/^{232}Th	^{206}Pb/^{238}U	^{207}Pb/^{235}U	^{207}Pb/^{206}Pb
P26-1.1	336	171	12	0	0.00001± 0.00004	0.16327± 0.00664	0.01110± 0.00050	0.03454± 0.00062	0.24075± 0.00910	0.05055± 0.00157	223±10	219±4	219±8	220±75
P26-1.2	2844	282	91	12	0.00014± 0.00013	0.03028± 0.00506	0.01053± 0.00184	0.03448± 0.000156	0.24726± 0.01611	0.05200± 0.00217	212±37	219±10	224±13	286±98
P26-2.1	170	54	6	0	0.00001± 0.00000	0.10470± 0.00581	0.01123± 0.00069	0.3402± 0.00076	0.23632± 0.01470	0.05038± 0.00279	226±14	216±5	215±12	213±134
P26-3.1	1246	253	44	5	0.00013± 0.00005	0.06182± 0.00237	0.01112± 0.00044	0.3655± 0.00022	0.25418± 0.00571	0.05044± 0.00105	224±9	231±1	230±5	215±49
P26-3.2	295	87	10	1	0.00007± 0.00013	0.09451± 0.00855	0.01095± 0.00137	0.03434± 0.00267	0.21675± 0.03281	0.04578± 0.00552	220±27	218±17	199±28	0±0
P26-4.1	169	87	6	0	0.00001± 0.00000	0.18579± 0.01371	0.01287± 0.00103	0.03552± 0.00096	0.24285± 0.01465	0.04959± 0.00251	258±21	225±6	221±12	176±123
P26-5.1	369	139	12	3	0.00025± 0.00015	0.11224± 0.01080	0.01008± 0.00099	0.03383± 0.00055	0.21612± 0.01385	0.04633± 0.00278	203±20	215±3	199±12	16±137
P26-6.1	1277	174	44	-1	-0.00003± 0.00002	0.04588± 0.00174	0.01234± 0.00050	0.03673± 0.00047	0.26876± 0.00566	0.05307± 0.00081	248±10	233±3	242±5	332±35
P26-6.2	142	56	5	0	0.00001± 0.00006	0.12402± 0.00989	0.01160± 0.00115	0.03649± 0.00188	0.26405± 0.02669	0.05248± 0.00424	233±23	231±12	238±22	306±195
P26-7.1	151	49	5	0	0.00011± 0.00021	0.09032± 0.01064	0.00969± 0.00124	0.03498± 0.00149	0.23666± 0.03004	0.04907± 0.00561	195±25	222±9	216±25	151±248
P26-7.2	308	98	11	1	0.00006± 0.00011	0.10166± 0.00639	0.01151± 0.00075	0.03593± 0.00052	0.23829± 0-01231	0.04810± 0.00230	231±15	228±3	217±10	104±109
P26-8.1	283	71	10	0	0.00001± 0.00000	0.08077± 0.00338	0.01134± 0.00079	0.03527± 0.00125	0.24954± 0.01235	0.05131± 0.00156	228±16	224±8	226±10	254±71
P26-9.1	210	65	13	-2	-0.00020± 0.00019	0.11667± 0.01115	0.02434± 0.00908	0.06433± 0.01956	0.35696± 0.12706	0.04025± 0.00608	486±180	402±120	310±100	0±0
P26-10.1	251	111	8	2	0.00027± 0.00019	0.13549± 0.00979	0.00912± 0.00084	0.02971± 0.00144	0.18274± 0.01932	0.04461± 0.00393	183±17	189±9	170±17	0±0
P26-11.1	421	193	15	-2	-0.00020± 0.00014	0.16453± 0.00842	0.01189± 0.00079	0.03308± 0.00118	0.24664± 0.01608	0.05408± 0.00271	239±16	210±7	224±13	374±117
P26-12.1	202	97	7	-1	-0.00021± 0.00015	0.15176± 0.01291	0.01073± 0.00097	0.03402± 0.00099	0.24944± 0.02178	0.05318± 0.00419	216±19	216±6	226±18	337±189

Data were provided by L. Ratschbacher.

Tab. A9 continued

Sample-Grain-Spot	U ppm	Th ppm	Pb* ppm	^{204}Pb ppm	Atomic ratios						Apparent ages (Ma)			
					^{204}Pb/^{206}Pb	^{208}Pb/^{206}Pb	^{208}Pb/^{232}Th	^{206}Pb/^{238}U	^{207}Pb/^{235}U	^{207}Pb/^{206}Pb	^{208}Pb/^{232}Th	^{206}Pb/^{238}U	^{207}Pb/^{235}U	^{207}Pb/^{206}Pb
P17-1.1	172	67	16	-1	-0.00006± 0.00006	0.15850± 0.00495	0.03706± 0.00152	0.09101± 0.00203	0.71902± 0.02969	0.05730± 0.00184	736±30	562±12	550±18	503±72
P17-1.2	135	99	13	1	0.00007± 0.00016	0.23699± 0.00899	0.02806± 0.00135	0.08690± 0.00233	0.71034± 0.04397	0.05928± 0.00312	559±27	537±14	545±27	578±119
P17-2.1	173	70	14	-1	-0.00005± 0.00011	0.14294± 0.00666	0.02699± 0.00145	0.07662± 0.00178	0.61706± 0.03961	0.05841± 0.00333	538±29	476±11	488±25	545±130
P17-3.1	258	120	21	1	0.00006± 0.00006	0.15718± 0.00391	0.02686± 0.00084	0.07953± 0.00134	0.62841± 0.02867	0.05731± 0.00231	536±17	493±8	495±18	504±91
P17-4.1	133	49	12	0	0.00001± 0.00001	0.13556± 0.00501	0.03198± 0.00202	0.08697± 0.00378	0.75082± 0.04874	0.06261± 0.00270	636±40	538±22	569±29	695±95
P17-5.1	146	81	11	0	0.00001± 0.00004	0.21387± 0.00851	0.02630± 0.00120	0.06814± 0.00137	0.52842± 0.02280	0.05625± 0.00201	525±24	425±8	431±15	462±81
P17-6.1	82	41	8	0	0.00001± 0.00000	0.15905± 0.00529	0.02788± 0.00142	0.08904± 0.00295	0.74375± 0.03783	0.06058± 0.00210	556±28	550±18	565±22	625±77
P17-7.1	145	104	14	-1	-0.00008± 0.00017	0.22956± 0.00961	0.02727± 0.00131	0.08555± 0.00173	0.70368± 0.03958	0.05966± 0.00299	544±26	529±10	541±24	591±112
P17-8.1	191	99	19	-1	-0.00006± 0.00014	0.17385± 0.00696	0.03161± 0.00135	0.09449± 0.00124	0.76598± 0.03619	0.05879± 0.00257	629±27	582±7	578±21	559±98
P17-9.1	115	62	10	0	0.00001± 0.00005	0.16787± 0.00506	0.02670± 0.00094	0.08585± 0.00137	0.65010± 0.03833	0.05492± 0.00301	533±19	531±8	509±24	409±128
P17-10.1	171	114	16	1	0.00006± 0.00011	0.20617± 0.00863	0.02717± 0.00291	0.08811± 0.00562	0.72966± 0.06223	0.06006± 0.00296	542±57	544±33	556±37	606±110
P17-11.1	107	52	10	0	0.00001± 0.00001	0.15682± 0.00432	0.02876± 0.00104	0.08812± 0.00170	0.71267± 0.02500	0.05866± 0.00158	573±20	544±10	546±15	555±60
P17-12.1	90	56	9	0	0.00001± 0.00008	0.21273± 0.01165	0.02968± 0.00184	0.08674± 0.00218	0.69490± 0.03429	0.05811± 0.00229	591±36	536±13	536±21	534±89
P17-13.1	95	47	9	0	0.00001± 0.00004	0.17339± 0.00493	0.03157± 0.00110	0.09078± 0.00150	0.73394± 0.03138	0.05864± 0.00219	628±22	560±9	559±19	554±84
P17-14.1	97	51	9	0	0.00001± 0.00004	0.16465± 0.00661	0.02623± 0.00121	0.08373± 0.00170	0.71881± 0.04357	0.06227± 0.00340	523±24	518±10	550±26	683±121

Data were provided by L. Ratschbacher.

Tab. A9 continued

Sample-Grain-Spot	U ppm	Th ppm	Pb* ppm	^{204}Pb ppm	Atomic ratios						Apparent ages (Ma)			
					^{204}Pb/^{206}Pb	^{208}Pb/^{206}Pb	^{208}Pb/^{232}Th	^{206}Pb/^{238}U	^{207}Pb/^{235}U	^{207}Pb/^{206}Pb	^{208}Pb/^{232}Th	^{206}Pb/^{238}U	^{207}Pb/^{235}U	^{207}Pb/^{206}Pb
L96A9-1.1	1835	461	56	70	0.00135± 0.00017	0.05611± 0.00688	0.00718± 0.00088	0.03219± 0.00026	0.22120± 0.01269	0.04984± 0.00278	145±18	204±2	203±11	188±135
L96A9-1.2	2545	410	75	3	0.00005± 0.00011	0.05140± 0.00426	0.00996± 0.00084	0.03119± 0.00047	0.21752± 0.00871	0.05058± 0.00178	200±17	198±3	200±7	222±84
L96A9-2.1	1994	461	59	2	0.00004± 0.00003	0.07089± 0.00207	0.00943± 0.00056	0.03074± 0.00130	0.21214± 0.01048	0.05006± 0.00104	190±11	195±8	195±9	198±49
L96A9-2.2	2775	352	83	-1	-0.00001± 0.00001	0.04302± 0.00129	0.01084± 0.00037	0.03192± 0.00045	0.22724± 0.00511	0.05163± 0.00082	218±8	203±3	208±4	269±37
L96A9-3.1	539	188	17	1	0.00004± 0.00004	0.11818± 0.00526	0.01092± 0.00092	0.03218± 0.00208	0.21981± 0.02124	0.04953±0. 00319	219±19	204±13	202±18	173±156
L96A9-4.1	2500	1990	73	1024 1	0.04284± 0.00078	0.41339± 0.07634	0.01192± 0.00236	0.02295± 0.00165	0.19143± 0.09904	0.06049± 0.03045	240±47	146±10	178±88	621±1776
L96A9-5.1	1896	592	48	568	0.01054± 0.00053	0.05840± 0.02785	0.00499± 0.00256	0.02666± 0.00432	0.17282± 0.05879	0.04701± 0.01314	101±52	170±27	162±52	50±851
L96A9-6.1	2304	421	72	5	0.00007± 0.00005	0.06298± 0.00204	0.01124± 0.00047	0.03262± 0.00073	0.23365± 0.00860	0.05195± 0.00139	226±9	207±5	213±7	283±62
L96A9-7.1	2505	394	82	2	0.00003± 0.00002	0.05366± 0.00139	0.01169± 0.00036	0.03428± 0.00047	0.24085± 0.00500	0.05096± 0.00071	235±7	217±3	219±4	239±32
L96A9-7.2	1221	165	35	2171	0.02967± 0.00097±	0.02594± 0.06373	0.00605± 0.01487	0.03158± 0.00284	0.11042± 0.11105	0.02536± 0.02512	122±297	200±18	106±106	0±0
L96A9-8.1	2666	908	63	3207	0.02798± 0.00106	0.09898± 0.07684	0.00701± 0.00554	0.02411± 0.003010	0.12058± 0.10572	0.03627± 0.03091	141±112	154±19	116±101	0±0
L96A9-8.2	6836	1451	196	2581	0.01102± 0.00044	0.00897± 0.02063	0.00135± 0.00310	0.03183± 0.00055	0.16773± 0.03579	0.03822± 0.00805	270±62	202±3	157±32	0±0
L96A9-9.1	1174	831	36	41	0.00131± 0.00042	0.11951± 0.01707	0.00516± 0.00074	0.03058± 0.00031	0.22792± 0.02916	0.05406± 0.00683	104±15	194±2	209±24	374±313
L96A9-9.2	3172	1691	79	1538	0.01561± 0.00039	0.06684± 0.01833	0.00323± 0.00090	0.02575± 0.00087	0.19730± 0.02804	0.05556± 0.00744	65±18	164±6	183±24	435±330
L96A9-10.1	7187	4533	160	6773	0.02324± 0.00042	-0.05009± 0.02198	-0.00214± -0.00094	0.02695± 0.00075	0.04082± 0.03440	0.01099± 0.00922	0±0	171±5	41±34	0±0
L96A9-10.2	1662	229	48	48	0.00108± 0.00016	0.03880± 0.00704	0.00864± 0.00157	0.03065± 0.00045	0.21221± 0.01297	0.05022± 0.00289	174±32	195±3	195±11	205±139
L96A9-11.1	2936	1011	74	656	0.00818± 0.00032	0.03044± 0.01738	0.00239± 0.00136	0.02703± 0.00036	0.19662± 0.03027	0.05275± 0.00801	48±28	172±2	182±26	318±318
L96A9-12.1	2204	696	64	159	0.00267± 0.00040	0.07585± 0.01645	0.00718± 0.00161	0.02990± 0.00144	0.23081± 0.03171	0.05599± 0.00687	145±32	190±9	211±27	452±299

Data were provided by L. Ratschbacher.

Tab. A9 continued

Sample-Grain-Spot	U ppm	Th ppm	Pb* ppm	^{204}Pb ppm	Atomic ratios					Apparent ages (Ma)			
					^{204}Pb/^{206}Pb	^{208}Pb/^{206}Pb	^{208}Pb/^{232}Th	^{206}Pb/^{238}U	^{207}Pb/^{235}U	^{207}Pb/^{206}Pb	^{208}Pb/^{232}Th	^{206}Pb/^{238}U	^{207}Pb/^{235}U	^{207}Pb/^{206}Pb
M96A7-1.1	1383	1017	27	5	0.00026± 0.00014		0.00579± 0.00021	0.01778± 0.00023	0.11343± 0.00635	0.04626± 0.00245	117±4	114±1	109±6	13±121
M96A7-1.2	1572	292	27	1	0.00005± 0.00006		0.00614± 0.00031	0.01795± 0.00012	0.12338± 0.00353	0.04985± 0.00135	124±6	115±1	118±3	188±64
M96A7-2.1	1266	95	19	2	0.00009± 0.00010		0.00494± 0.00105	0.01652± 0.00058	0.10391± 0.00606	0.04562± 0.00194	100±21	106±4	100±6	0±0
M96A7-3.1	1753	480	29	48	0.00180± 0.00038		0.00524± 0.00099	0.01719± 0.00023	0.10412± 0.01517	0.04393± 0.00630	106±20	110±1	101±14	0±0
M96A7-4.1	1303	186	20	1	0.00005± 0.00006		0.00535± 0.00035	0.01632± 0.00018	0.11211± 0.00434	0.04982± 0.00178	108±7	104±1	108±4	187±85
M96A7-5.1	2233	857	43	1	0.00003± 0.00004		0.00614± 0.00015	0.01887± 0.00017	0.12490± 0.00284	0.04801± 0.00095	124±3	120±1	119±3	100±47
M96A7-6.1	1261	470	15	2	0.00018± 0.00026		0.00440± 0.00053	0.01206± 0.00034	0.07562± 0.00836	0.4548± 0.00470	89± 11	77±2	74±8	0±0
M96A7-7.1	536	51	15	0	0.00001± 0.00003		0.01586± 0.00163	0.02859± 0.00038	0.21158± 0.00750	0.05368± 0.00168	318±33	182±2	195±6	358±72
M96A7-7.2	4227	1000	77	202	0.00267± 0.00020		0.00230± 0.00067	0.01978± 0.00013	0.11728± 0.00914	0.04300± 0.00331	46±14	126±1	113±8	0±0
M96A7-8.1	2700	3726	59	18	0.00045± 0.00013		0.00563± 0.00016	0.01683± 0.00034	0.10997± 0.00706	0.04740± 0.00277	113±3	108±2	106±6	69±134
M96A7-8.2	8185	2479	108	688	0.00613± 0.00031		0.00168± 0.00061	0.01419± 0.00013	0.09801± 0.01042	0.05009± 0.00525	34±12	91±1	95±10	199±227
M96A7-9.1	2770	792	47	2	0.00004± 0.00004		0.00567± 0.00017	0.01742± 0.00021	0.11703± 0.00407	0.04874± 0.00152	114±3	111±1	112±4	135±75
M96A7-10.1	1085	88	14	8	0.00057± 0.00053		0.00029± 0.00375	0.01463± 0.00053	0.08638± 0.01788	0.04282± 0.00854	6±76	94±3	84±17	0±0
M96A7-11.1	3506	1308	90	231	0.00272± 0.00020		0.00516± 0.00061	0.02682± 0.00047	0.17478± 0.01287	0.04726± 0.00328	104±12	171±3	164±11	62±157
M96A7-11.2	6721	817	103	428	0.00404± 0.00028		0.00031± 0.00161	0.01699± 0.00020	0.11345± 0.01141	0.04844± 0.00477	6±32	109±1	109±10	121±217
M96A7-12.1	1206	1218	25	6	0.00035± 0.00014		0.00565± 0.00020	0.01710± 0.00036	0.10844± 0.00653	0.04599± 0.00247	114±4	109±2	105±6	0±0
M96A7-13.1	630	264	25	0	0.00001± 0.00000		0.01248± 0.00055	0.03947± 0.00053	0.27094± 0.00937	0.04979± 0.00151	251±11	250±3	243±8	185±72
M96A7-13.2	2365	1045	60	178	0.00335± 0.00024		0.00765± 0.00056	0.02456± 0.00023	0.20951± 0.01424	0.06188± 0.00409	154±11	156±1	193±12	670±148

Data were provided by L. Ratschbacher.

Tab. A9 continued

Sample-Grain-Spot	U ppm	Th ppm	Pb* ppm	^{204}Pb ppm	Atomic ratios						Apparent ages (Ma)			
					^{204}Pb/^{206}Pb	^{208}Pb/^{206}Pb	^{208}Pb/^{232}Th	^{206}Pb/^{238}U	^{207}Pb/^{235}U	^{207}Pb/^{206}Pb	^{208}Pb/^{232}Th	^{206}Pb/^{238}U	^{207}Pb/^{235}U	^{207}Pb/^{206}Pb
M96A7-14.1	274	175	5	1	0.00037± 0.00025		0.00554± 0.00051	0.01669± 0.00024	0.09906± 0.01090	0.04306± 0.00462	112±10	107±2	96±10	0±0
M96A7-15.1	452	285	18	0	0.00001± 0.00000		0.01267± 0.00035	0.03666± 0.00057	0.26460± 0.01076	0.05235± 0.00187	254±7	232±4	238±9	301±84
M96A7-15.2	6664	1999	105	410	0.00406± 0.00028		0.00376± 0.00063	0.01633± 0.00015	0.11375± 0.01091	0.05052± 0.00477	76±13	104±1	109±10	219±218
M96A7-16.1	2250	584	55	111	0.00217± 0.00047		0.00653± 0.00183	0.02538± 0.00047	0.19683± 0.02714	0.05625± 0.00755	131±37	162±3	182±23	462±329
M96A7-16.2	1381	746	27	27	0.00119± 0.00026		0.00623± 0.00040	0.01867± 0.00023	0.12556± 0.01162	0.04878± 0.00440	125±8	119±1	120±11	137±199
M96A7-16.2	1912	2314	52	0	0.00001± 0.00004		0.00836± 0.00039	0.02031± 0.00040	0.13845± 0.00478	0.04944± 0.00128	168±8	130±3	132±4	169±62
M96A7-19.1	956	231	414	1	0.00000± 0.00000		0.13792± 0.00230	0.40395± 0.00283	904.780± 0.09401	0.16245± 0.00111	2612±41	2187±13	2343±10	2481±12
M96A7-19.2	5619	2488	78	342	0.00445± 0.00077		0.00177± 0.00105	0.01464± 0.00026	0.09077± 0.02594	0.04498± 0.01273	36±21	94±2	88±24	0±0
M96A7-20.1	1082	448	19	1	0.00005± 0.00009		0.00551± 0.00029	0.01772± 0.00016	0.11717± 0.00473	0.04796± 0.00184	111±6	113±1	112±4	97±89
M96A7-21.1	1238	327	21	0	0.00001± 0.00001		0.00534± 0.00031	0.01707± 0.00055	0.11723± 0.00520	0.04981± 0.00134	108±6	109±3	113±5	186±64
M96A7-22.1	954	580	40	-1	-0.00003± 0.00005		0.01281± 0.00031	0.03866± 0.00048	0.27005± 0.00852	0.05066± 0.00139	257±6	245±3	243±7	225±65
M96A7-23.1	1951	4521	67	12	0.00034± 0.00024		0.00789± 0.00045	0.02031± 0.00079	0.13968± 0.01412	0.04987± 0.00441	159±9	130±5	133±13	189±194
M96A7-24.1	2866	492	92	6	0.00007± 0.00004		0.01187± 0.00035	0.03376± 0.00023	0.23411± 0.00470	0.05029± 0.00091	239±7	214±1	214±4	209±43
P2-1.1	113	133	2	1	0.00075± 0.00080	0.3725± 0.03553	0.00537± 0.00053	0.01692± 0.00044	0.0864± 0.03108	0.03703± 0.01317	108±11	108±3	84±30	0±0
P2-2.1	293	46	19	0	0.00001± 0.00005		0.02798± 0.00215	0.06684± 0.00127	0.52464± 0.02382	0.05693± 0.00222	558±42	417±8	428±16	489±88
P2-2.2	2800	2975	43	4	0.00009± 0.00016		0.00122± 0.00013	0.01594± 0.00054	0.10738± 0.00775	0.04885± 0.00291	25±3	102±3	104±7	141±137
P2-3.1	1249	457	22	1	0.00006± 0.00005		0.00555± 0.00017	0.01727± 0.00019	0.10948± 0.00594	0.04597± 0.00238	112±3	110±1	105±5	0±0
P2-4.1	91	106	2	0	0.00001± 0		0.00613± 0.00044	0.01681± 0.00069	0.11426± 0.01760	0.04929± 0.00707	124±9	107±4	110±16	162±305
P2-5.1	293	252	6	20	0.00419± 0.00138		0.00699± 0.00123	0.01755± 0.00069	0.21513± 0.05959	0.08888± 0.02394	141±25	112±4	198±51	1402±629

Data were provided by L. Ratschbacher.

Tab. A9 continued

Sample-Grain-Spot	U ppm	Th ppm	Pb* ppm	^{204}Pb ppm	Atomic ratios						Apparent ages (Ma)			
					^{204}Pb/^{206}Pb	^{208}Pb/^{206}Pb	^{208}Pb/^{232}Th	^{206}Pb/^{238}U	^{207}Pb/^{235}U	^{207}Pb/^{206}Pb	^{208}Pb/^{232}Th	^{206}Pb/^{238}U	^{207}Pb/^{235}U	^{207}Pb/^{206}Pb
P2-5.2	1985	562	37	16	0.00049± 0.00016		0.00616± 0.00047	0.01895± 0.00023	0.12748± 0.00804	0.04879± 0.00294	124±9	121±1	122±7	138±136
P2-6.1	396	304	9	-1	-0.00014± 0.00020		0.00690± 0.00033	0.01895± 0.00026	0.13891± 0.01000	0.05317± 0.00367	139±7	121±2	132±9	336±165
P2-6.1	1388	429	27	0	0.00001± 0.0003		0.00664± 0.00018	0.01981± 0.00021	0.13011± 0.00587	0.04763± 0.00203	134±4	126±1	124±5	81±98
P2-7.1	1108	419	63	2	0.00004± 0.00004		0.01799± 0.00075	0.05669± 0.00068	0.42316± 0.00961	0.05414± 0.00097	360±15	355±4	358±7	377±41
P2-7.2	1981	920	36	12	0.00037± 0.00014		0.00392± 0.00026	0.01827± 0.00023	0.12681± 0.00671	0.05034± 0.00251	79±5	117±1	121±6	211±120
P2-8.1	1609	2221	42	6	0.0023± 0.00009		0.00756± 0.00059	0.01896± 0.00055	0.11985± 0.00687	0.04584± 0.00210	152±12	121±4	115±6	0±0
P2-8.2	1308	725	23	4	0.00021± 0.00014		0.00341± 0.00025	0.01781± 0.00047	0.12980± 0.00745	0.05287± 0.00254	69±5	114±3	124±7	323±113
P2-9.1	365	61	53	-1	-0.00002± 0.00001		0.04739± 0.00181	0.15013± 0.00262	149.615± 0.04171	0.07228± 0.00142	936±35	902±15	929±17	994±40
P2-10.1	803	123	14	-2	-0.00019± 0.00038		0.00602± 0.00202	0.01823± 0.00236	0.13086± 0.02870	0.05206± 0.00840	121±41	116±15	125±26	288±332
P2-11.1	1092	1448	16	251	0.01560±0.0 0195		0.00281± 0.00105	0.01221± 0.00083	0.11898± 0.08185	0.07070± 0.04780	57±21	78±5	114±77	949±3031
P2-11.2	818	129	13	1	0.00009± 0.00013		0.00478± 0.00067	0.01660± 0.00031	0.10701± 0.00626	0.04675± 0.00248	96±14	106±2	103±6	37±122
P2-12.1	1160	316	339	9	0.00003± 0.00001		0.07215± 0.00105	0.28657± 0.00237	465.311± 0.05271	0.11777± 0.00080	1408±20	1624±12	1759±10	1923±12
P2-13.1	734	126	14	0	0.00001± 0		0.00468± 0.00027	0.01962± 0.00022	0.13459± 0.00433	0.04974± 0.00144	94±5	125±1	128±4	183±69
P2-14.1	645	407	20	124	0.00640± 0.00115		0.00609± 0.00237	0.03094± 0.00082	0.22714± 0.08542	0.05325± 0.01980	123±48	196±5	208±73	339±1176
P2-14.2	1497	417	28	10	0.00040± 0.00014		0.00622± 0.0047	0.01881± 0.00011	0.12544± 0.00804	0.04837± 0.00305	125±9	120±1	120±7	117±142
P2-15.1	1184	141	28	6	0.00025± 0.00010		0.00759± 0.00087	0.02483± 0.00023	0.18219± 0.00755	0.05322± 0.00209	153±18	158±1	170±7	338±91

Data were provided by L. Ratschbacher.

Appendix B

Plate B1 Cathodoluminescence images of zircons

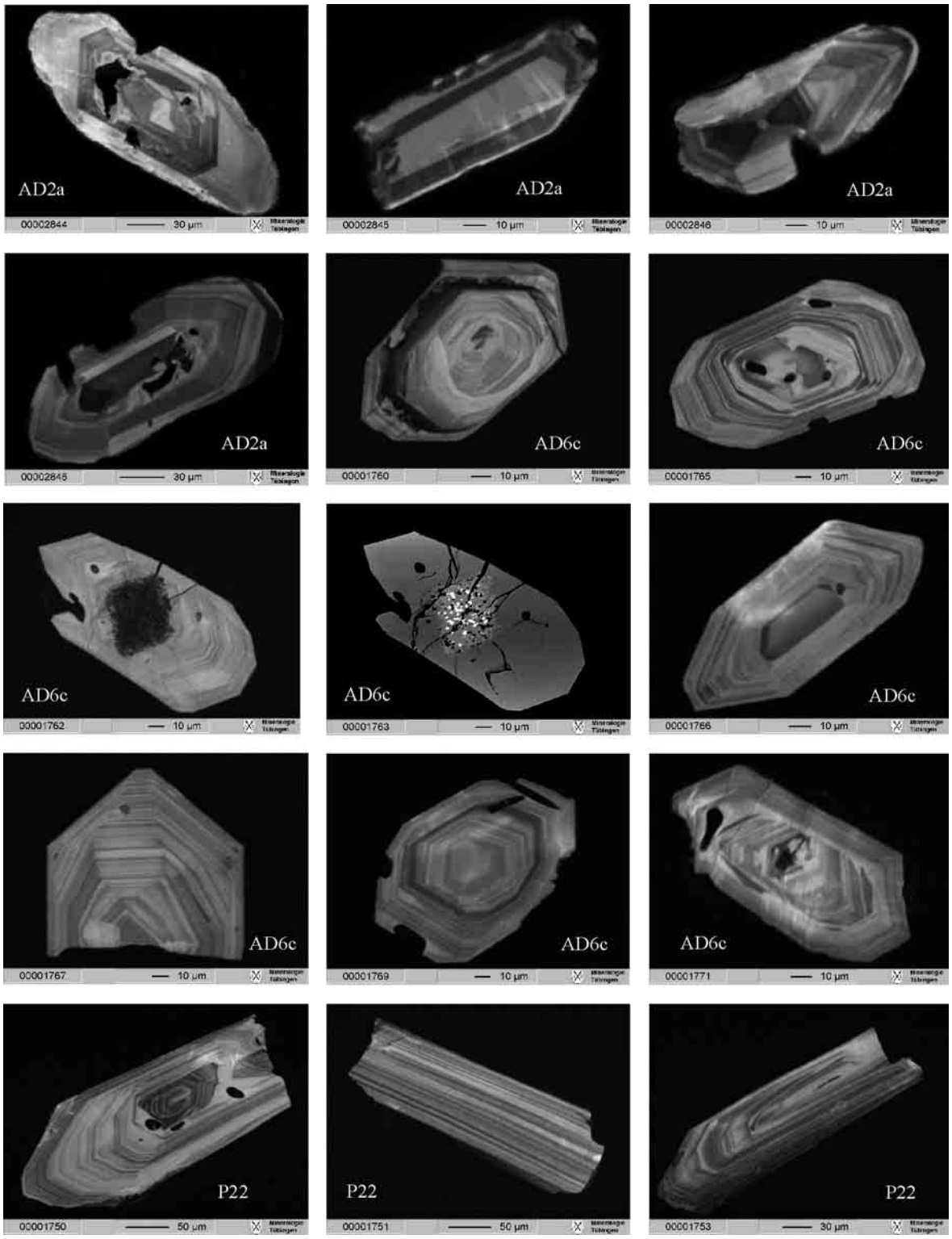

Plate B2 Cathodoluminescence images of zircons[1]

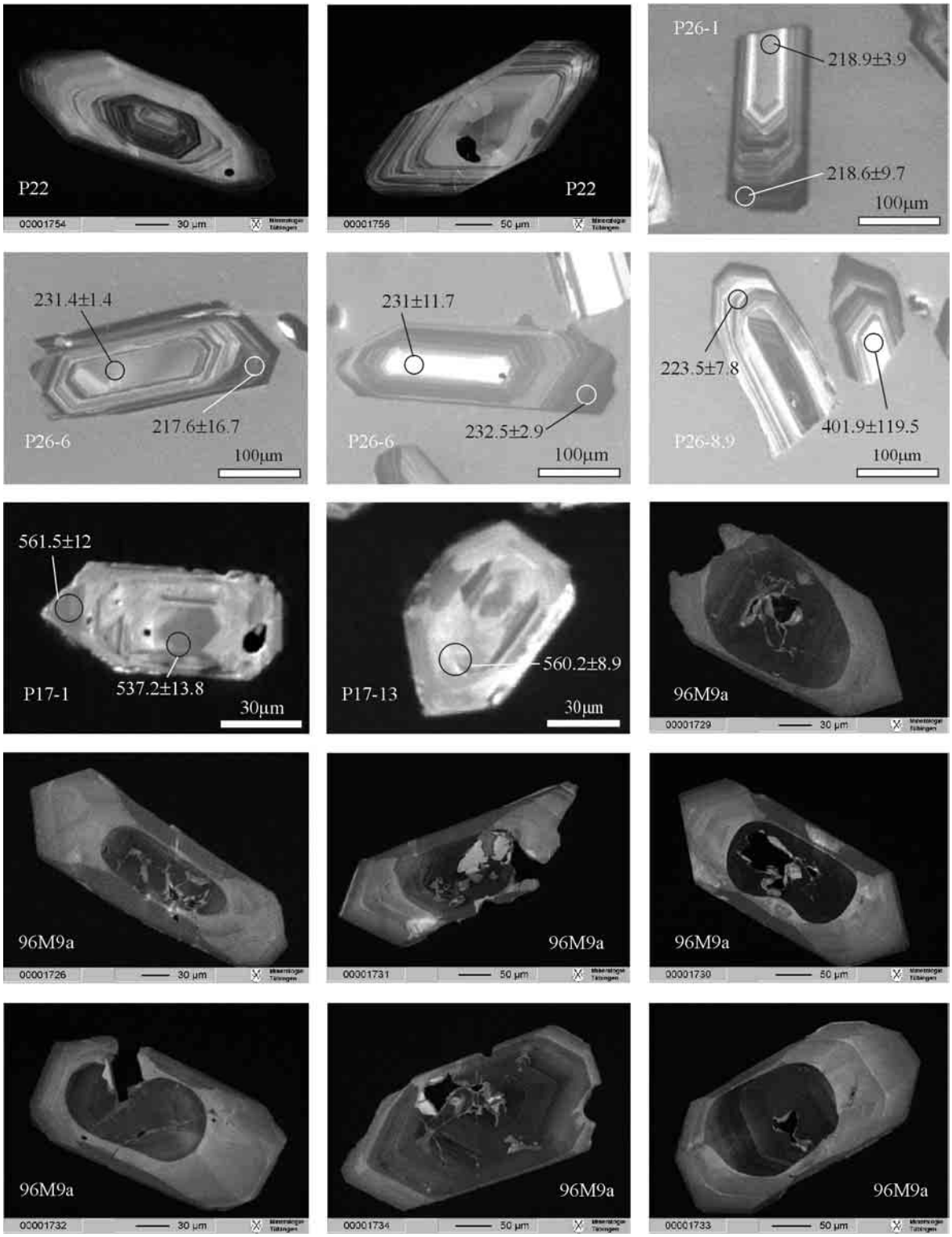

[1] Cathodoluminescence images with age data determined by SHRIMP analyses were provided by L. Ratschbacher.

Plate B3 Cathodoluminescence images of zircons[1]

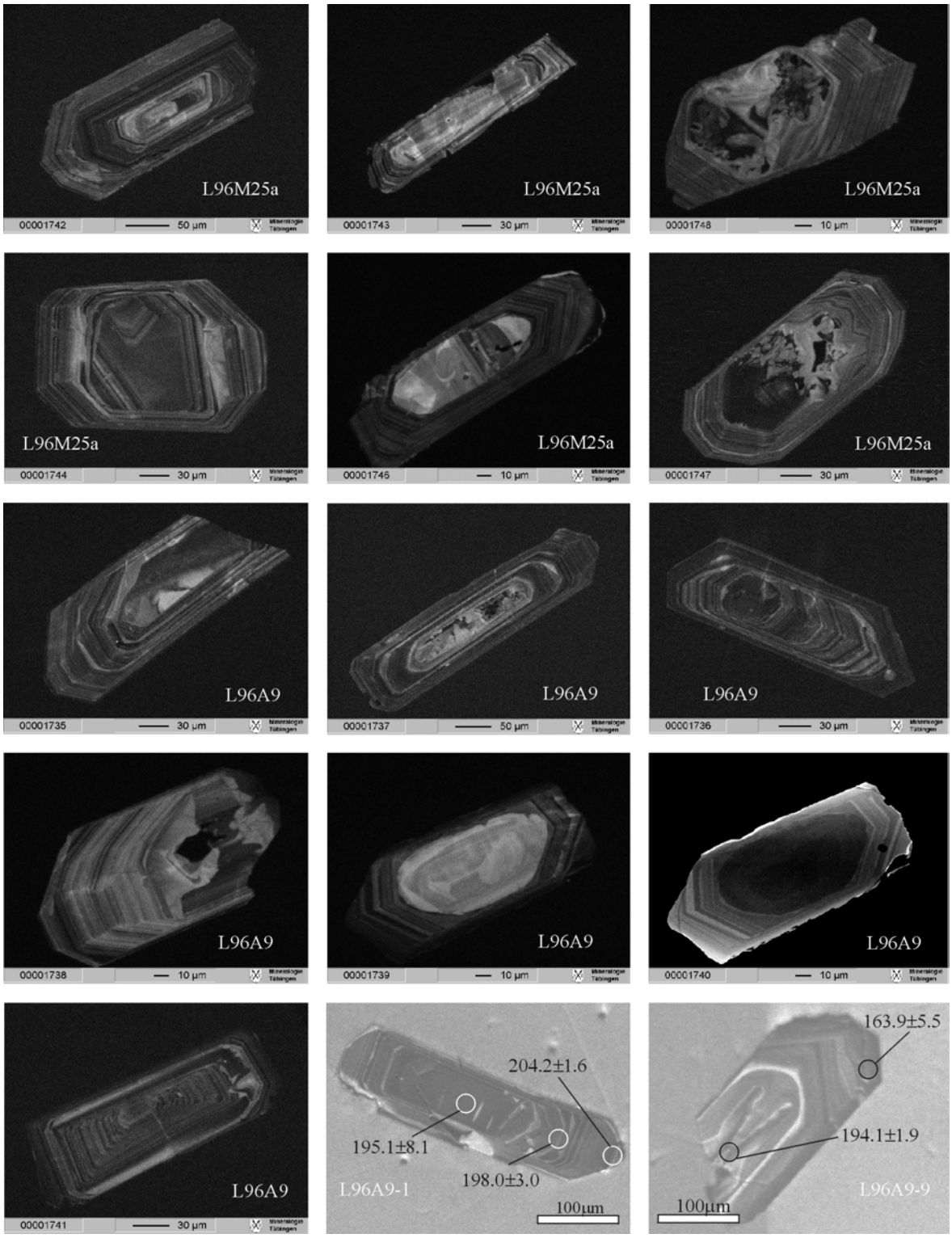

[1] Cathodoluminescence images with age data determined by SHRIMP analyses were provided by L. Ratschbacher.

Plate B4 Cathodoluminescence images of zircons[1]

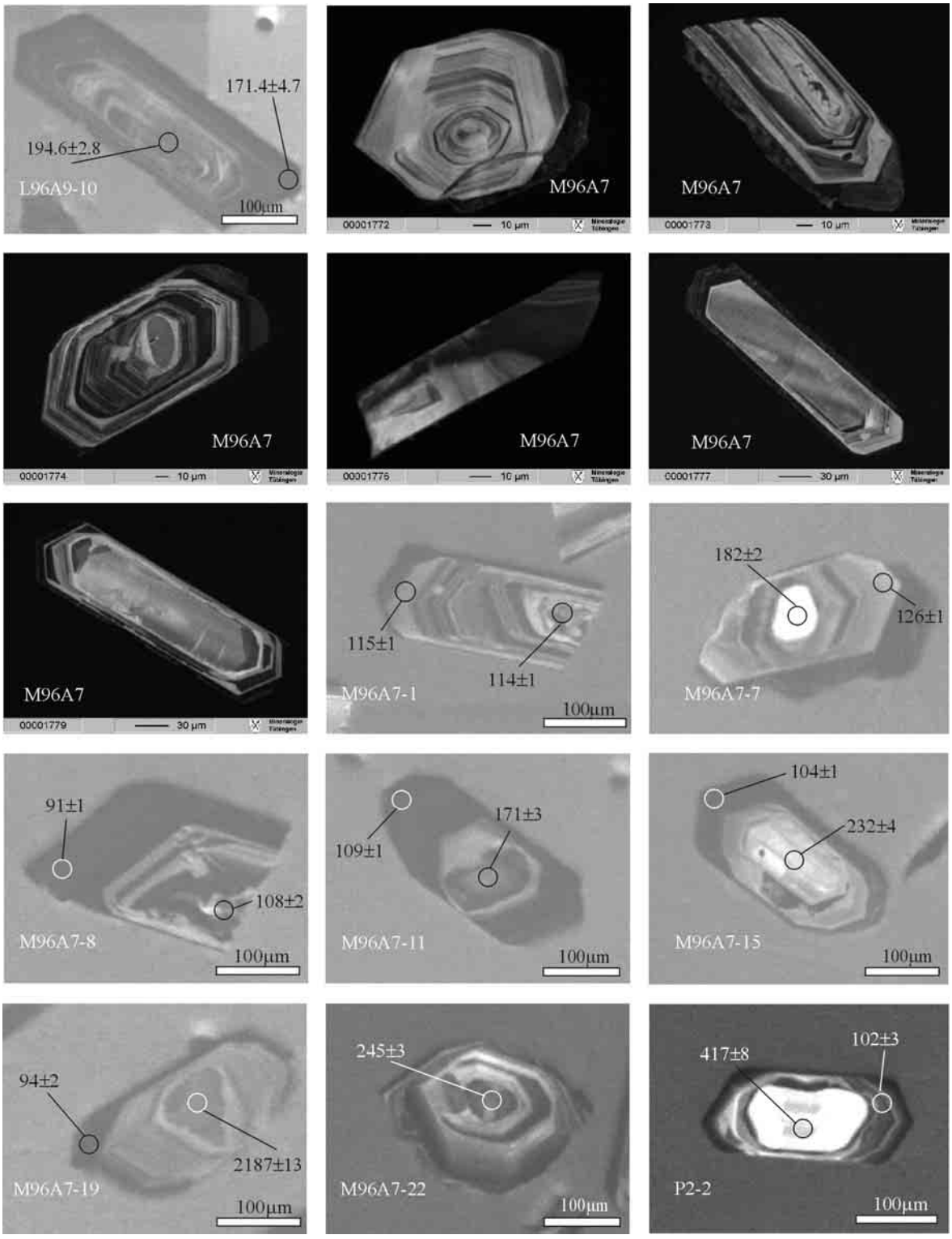

[1] Cathodoluminescence images with age data determined by SHRIMP analyses were provided by L. Ratschbacher.

Plate B5 Cathodoluminescence images of zircons[1]

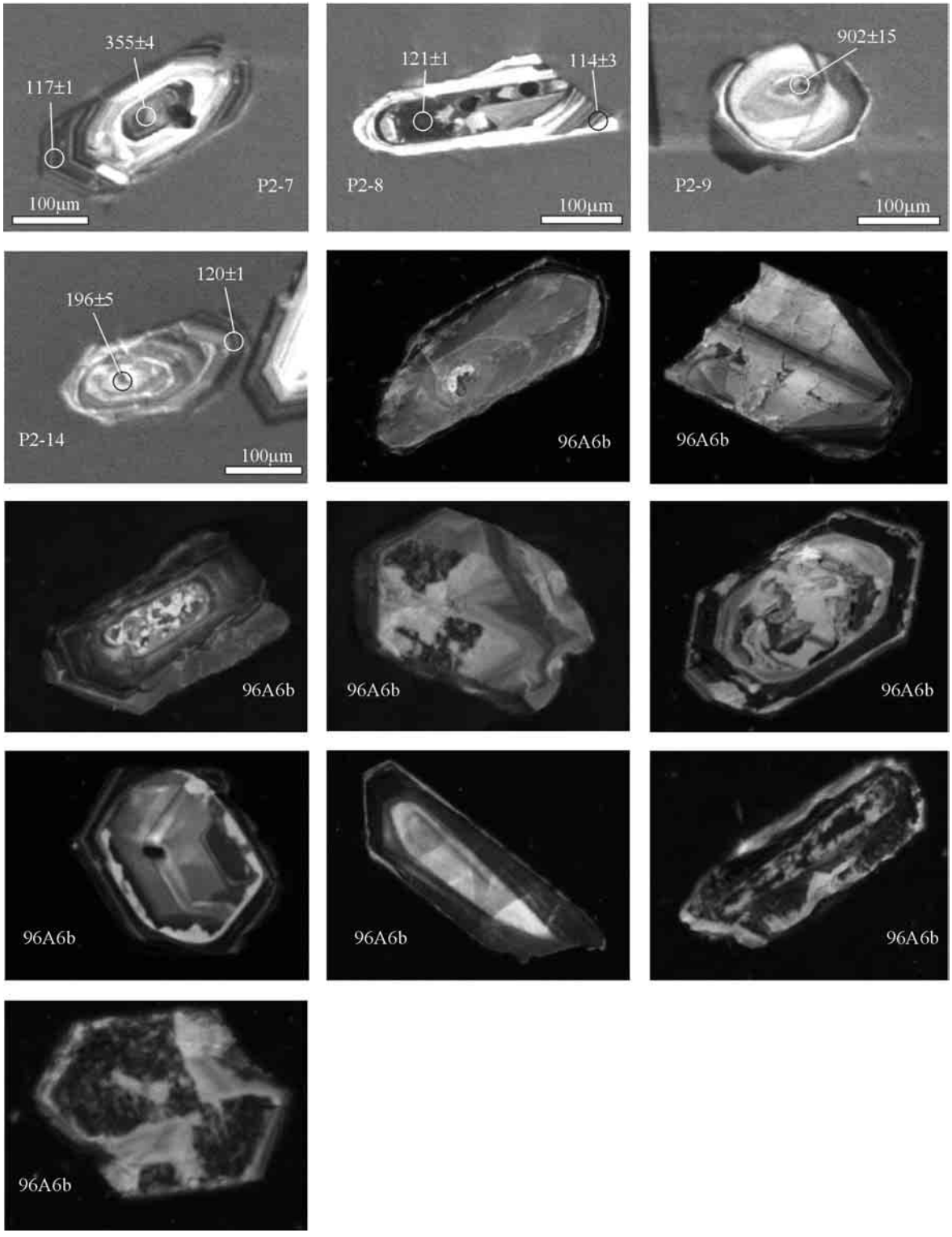

[1] Cathodoluminescence images with age data determined by SHRIMP analyses were provided by L. Ratschbacher.

Appendix C

Tab. C1 Sample description and location of samples investigated for the Tertiary cooling history

Sample	Rock	Mineral	Method	N-latitude	E-latitude
Hard rocks					
Tien Shan					
TS1	weakly deformed granite	apatite	FT	40°06.30'	73°31.50'
Karakul lake					
P20	two-mica granite	apatite	FT	38°48.10'	73°17.03'
P22	granite	apatite	FT	38°55.93'	73°22.87'
P24	granite	apatite	FT	38°56.10'	73°26.56'
P25	granite	apatite, zircon	FT	39°11.42'	73°26.59'
P26	granite	apatite, zircon	FT	39°12.00'	73°25.00'
Central Pamirs					
A96S1b	latite-andesite	zircon	FT	38°31.90'	73°40.70'
P15	granodiorite	apatite, zircon	U/Pb zircon, FT	38°30.40'	73°42.35'
P17	aplite dike in high-grade biotitegneiss	apatite	FT	38°32.73'	73°31.27'
96A6b	aplite vein	apatite	U/Pb zircon, FT	38°13.52'	74°29.67'
L96A11a	aplitic dyke	WR-muscovite	Rb/Sr	38°11.323'	74°35.992'
96A5i	basement	WR-muscovite	Rb/Sr	38°12.29'	74°27.47'
A96A5k	basement	WR-muscovite	Rb/Sr	38°14.00'	74°27.00'
96Ak3d	basement	WR-muscovite	Rb/Sr	38°28.74'	73°32.93'
96A10b	granite	zircon	FT	38°08.10'	74°28.11'
Rushan Pshart					
L96M25a	granite	zircon	FT	38°12.48'	74°01.724'
Shyok arc					
P2	granodiorite	apatite	FT	38°07.67'	73°51.13'
P5	granodiorite	apatite	FT	38°10.20'	73°34.10'
Soft rocks					
Tien Shan					
TS5a	sandstone	apatite, zircon	FT	39°51.909'	73°21.436'
TS8a	sandstone	apatite	FT	39°55.516'	73°25.808'
Altyndara valley					
AD7d	sandstone	zircon	FT	39°20.916'	72°17.672'
AD8a	sandstone	zircon	FT	39°24.563'	72°19.009'
Central Pamirs					
A96K1e	sandstone	zircon	FT	38°31.20'	73°33.90'
A96M4b	sandstone	zircon	FT	38°18.20'	74°02.00'
M96M6b	sandstone	zircon, sericite	FT, K/Ar	38°17.33'	74°01.43'
96M8c	sandstone	sericite	K/Ar	38°16.49'	74°02.15'
96M13c	sandstone	sericite	K/Ar	38°19.89'	73°58.83'
A96M4c	sandstone	sericite	K/Ar	38°18.28'	74°02.10'
M96M5a	sandstone	sericite	K/Ar	38°16.85'	74°01.44'

Tab. C2 Determination of the ζ-value for dosimeter glass CN5 for apatites

Age standard	Number of grains	Spontaneous		Induced		$P\chi^2$(%)	Dosimeter		ζ ± 1σ
		ρ_s	N_s	ρ_i	N_i		ρ_d	N_d	
AD-2-40	25	2.417	507	8.767	1839	97.68	5.336	10407	427.46±22.88
AF-3-40	25	1.635	252	6.859	1057	77.00	5.333	10407	440.33±32.15
AF-5-42	25	1.621	282	6.381	1110	8.54	5.26	10388	416.92±29.08
AD-4-43	25	2.587	444	7.371	1265	73.85	4.61	9253	389.05±22.70
AF-3-43	25	1.483	251	5.139	870	1.7	4.61	9253	403.00±30.06
AD-5-46	14	2.215	89	6.248	251	34.08	4.60	4537	383.35±48.02
AF-5-36	20	1.780	182	6.221	636	97.38	5.305	5235	368.57±32.09
AF-7-55	8	2.098	57	6.219	169	83.57	4.85	9566	342.14±52.88
AF-4-59	9	1.885	137	6.4	465	66.19	4.58	14919	413.89±41.05
AD-6-59	12	2.665	230	7.219	623	15.55	4.58	14919	370.49±29.35
weighted mean									**401.21±9.89**

Track densities (ρ) are measured as ($x10^5$ tr/cm^2); N is the number of tracks counted; ρs = spontaneous track density; ρi = induced track density, ρd = track density of the dosimeter glass (CN5); $P\chi^2$ is the probability to obtain the chi-square value for n degree of freedom (n is the number of crystals –1). AD = Durango apatite, AF = Fish Canyon Tuff apatite.

Tab. C3 Determination of the ζ-value for dosimeter glass CN2 for zircons

Age standard	Number of grains	Spontaneous		Induced		$P\chi^2$(%)	Dosimeter		ζ ± 1σ
		ρ_s	N_s	ρ_i	N_i		ρ_d	N_d	
ZB-3-38	25	10.468	834	21.45	1709	11.78	5.52	10895	123.69±5.57
ZF-5-38	25	57.237	1154	77.622	1565	13.04	5.526	10895	137.46±6.02
ZT-2-38	21	69.854	1075	43.082	663	35.33	5.52	10895	131.64±7.07
ZB-5-48	24	11.4	684	24.351	1461	15.86	6.57	6484	106.36±5.26
ZF-4-49	25	56.814	1887	62.746	2084	21.57	5.40	10665	114.55±4.32
ZB-3-49	25	11.195	736	21.766	1431	71.52	5.40	10665	118.32±5.67
ZT-3-51	25	66.951	1865	52.124	1452	30.24	6.51	6427	140.87±5.86
weighted mean									**122.91±2.09**

Track densities (ρ) are measured as ($x10^5$ tr/cm^2); N is the number of tracks counted; ρs = spontaneous track density; ρi = induced track density, ρd = track density of the dosimeter glass (CN2); $P\chi^2$ is the probability to obtain the chi-square value for n degree of freedom (n is the number of crystals –1). ZB = Buluk Member zircon, ZF = Fish Canyon Tuff zircon, ZT = Tardree Rhyolite zircon.

Tab. C4 Apatite fission track ages determined with the program TRACKKEY 4.0 (Dunkl 2002).

sample	Elev. (m)	Number of grains	Spontaneous ρ_s	Spontaneous N_s	Induced ρ_i	Induced N_i	$P\chi^2$(%)	Dosimeter ρ_d	Dosimeter N_d	Age (Ma) ± 1σ
Hard rocks										
Tien Shan										
TS1-59	n.d.	31	0.994	83	8.722	728	81.29	4.75	14919	10.9±1.3
Karakul lake										
P20-40	3950	34	9.597	344	18.079	648	48.05	5.258	10407	55.7±4.1
P22-40	3950	49	2.993	855	8.24	2354	0.3	5.252	10407	*39.8±2.2
P24-43	3950	34	2.485	167	9.315	626	71.58	4.71	9253	25.2±2.3
P25-40	4230	34	1.956	137	10.81	757	48.95	5.246	10407	18.8±1.9
P26-40	4100	35	1.488	109	8.67	635	18.91	5.249	10407	18.0±2.1
Central Pamirs										
P15-43	4365	34	1.217	138	7.471	847	19.91	4.67	9253	15.4±1.7
P17-40	4560	31	1.008	159	6.766	1067	93.71	5.263	10407	15.7±1.4
96A6b-59	n.d.	7	0.743	34	3.495	160	95.5	4.686	14919	19.9±3.8
Rushan Pshart										
P2-43	3600	62	0.929	57	8.214	504	99.28	4.71	9253	10.7±1.5
P5-40	3550	49	0.726	57	10.05	789	3.92	5.255	10407	*10.1±1.7
Soft rocks										
Tien Shan										
TS5a-43	2570	106	18.829	3617	12.15	2334	0.0	4.66	9253	*169±9
TS8a-59	n.d.	11	19.977	574	8.875	255	2.17	4.66	14919	*209±23

The track densities (ρ) are measures as $x10^5 tr/cm^2$. $P\chi^2$ is the probability obtaining a chi-square value for n degrees of freedom (where n = no. of crystals –1). The ages were calculated as central ages, where $P\chi^2$ is >5%, and as mean ages (indicated by *), where $P\chi^2$ is <5%. Abbreviation n.d.= not determined.

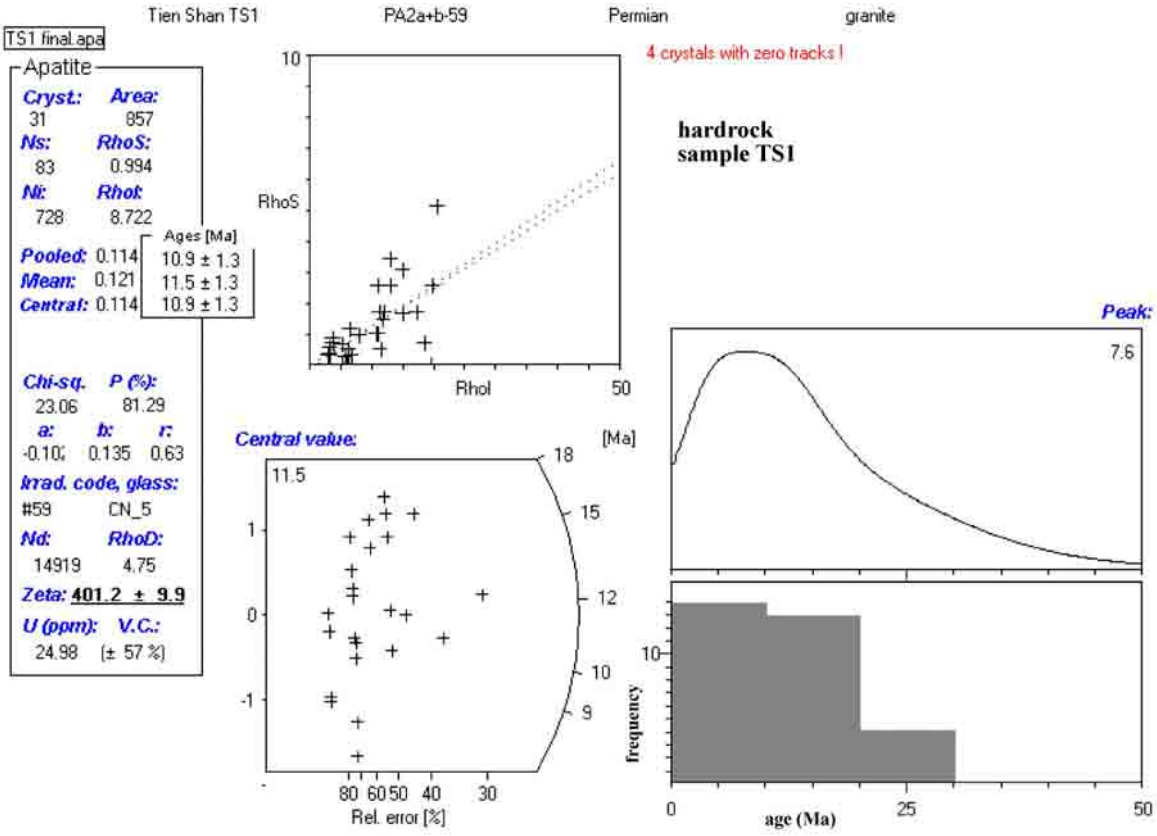

Fig. C1: Apatite fission track ages determined with the Program TRACKKEY 4.0 (Dunkl 2002). The radial plot is after Galbraith (1990).

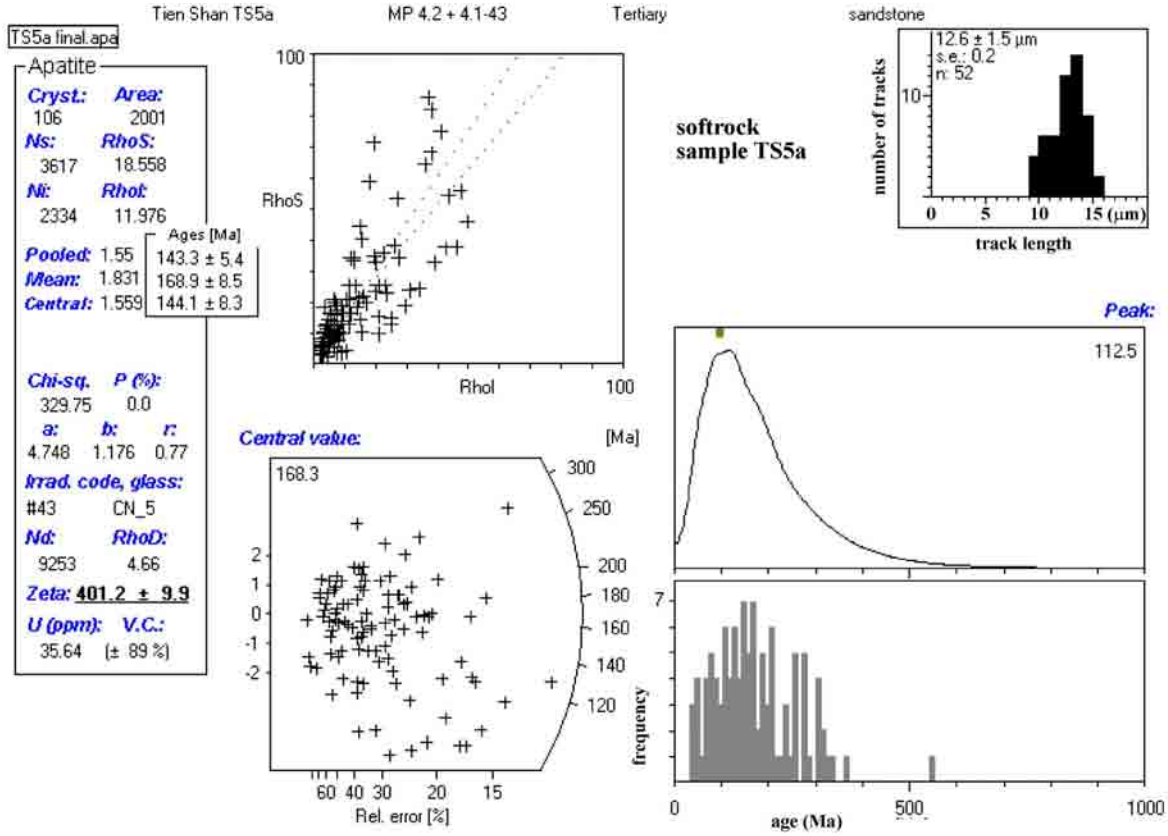

Fig. C1, continued: Apatite fission track ages determined with the Program TRACKKEY 4.0 (Dunkl 2002). The radial plot is after Galbraith (1990). Abbreviations: s.e.=standard deviation, n=number of tracks.

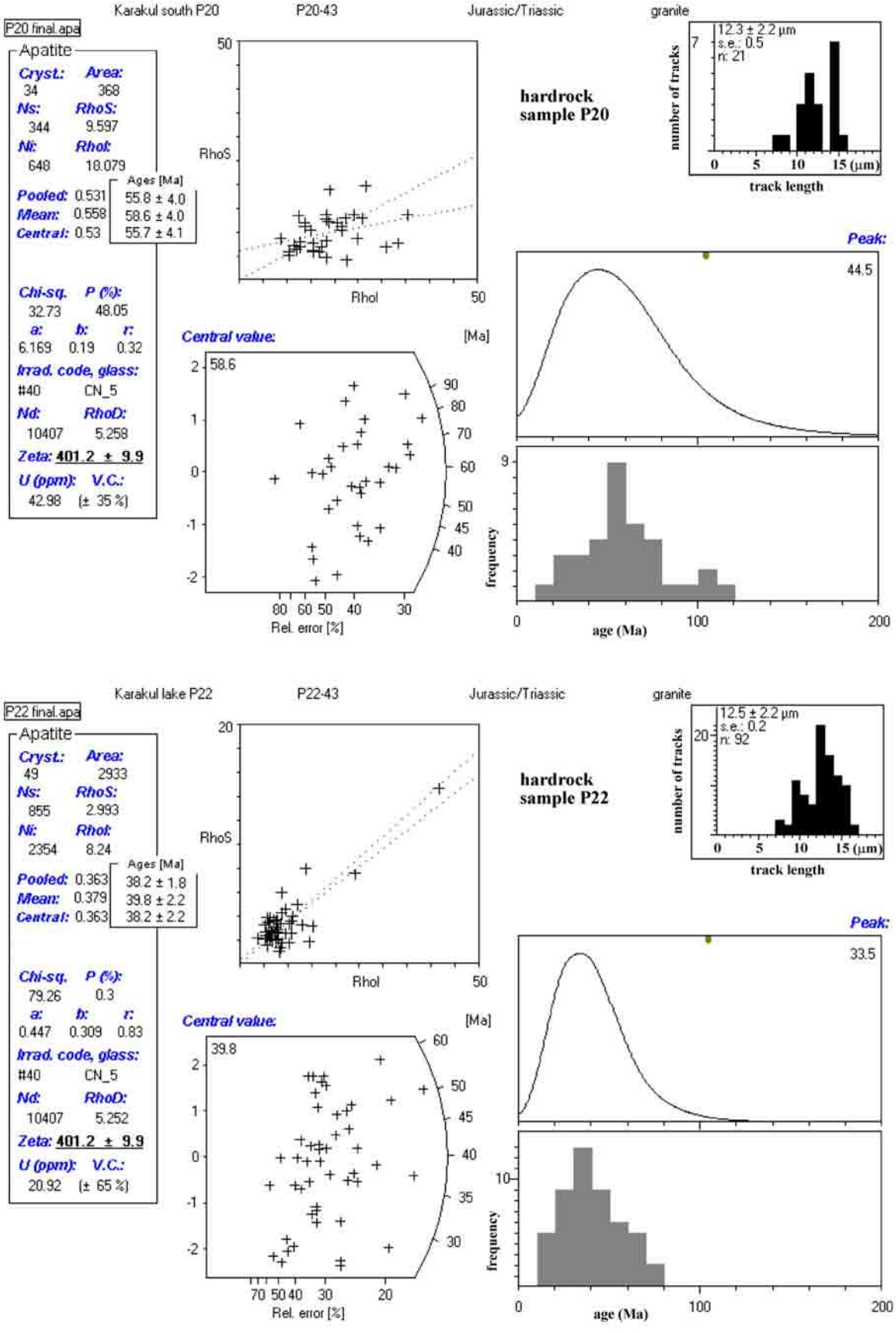

Fig. C1, continued: Apatite fission track ages determined with the Program TRACKKEY 4.0 (Dunkl 2002). The radial plot is after Galbraith (1990). Abbreviations: s.e.=standard deviation, n=number of tracks.

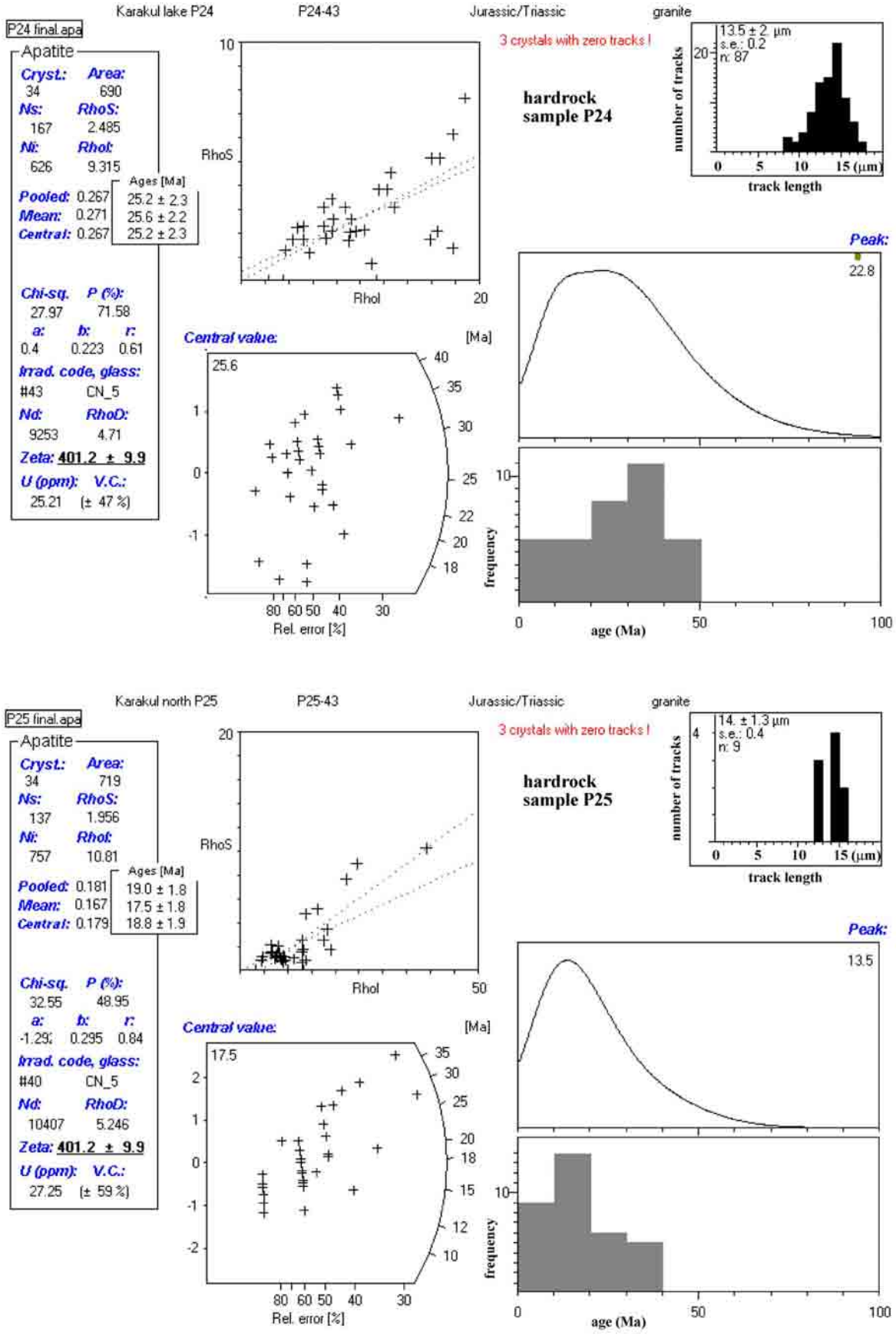

Fig. C1, continued: Apatite fission track ages determined with the Program TRACKKEY 4.0 (Dunkl 2002). The radial plot is after Galbraith (1990). Abbreviations: s.e.=standard deviation, n=number of tracks.

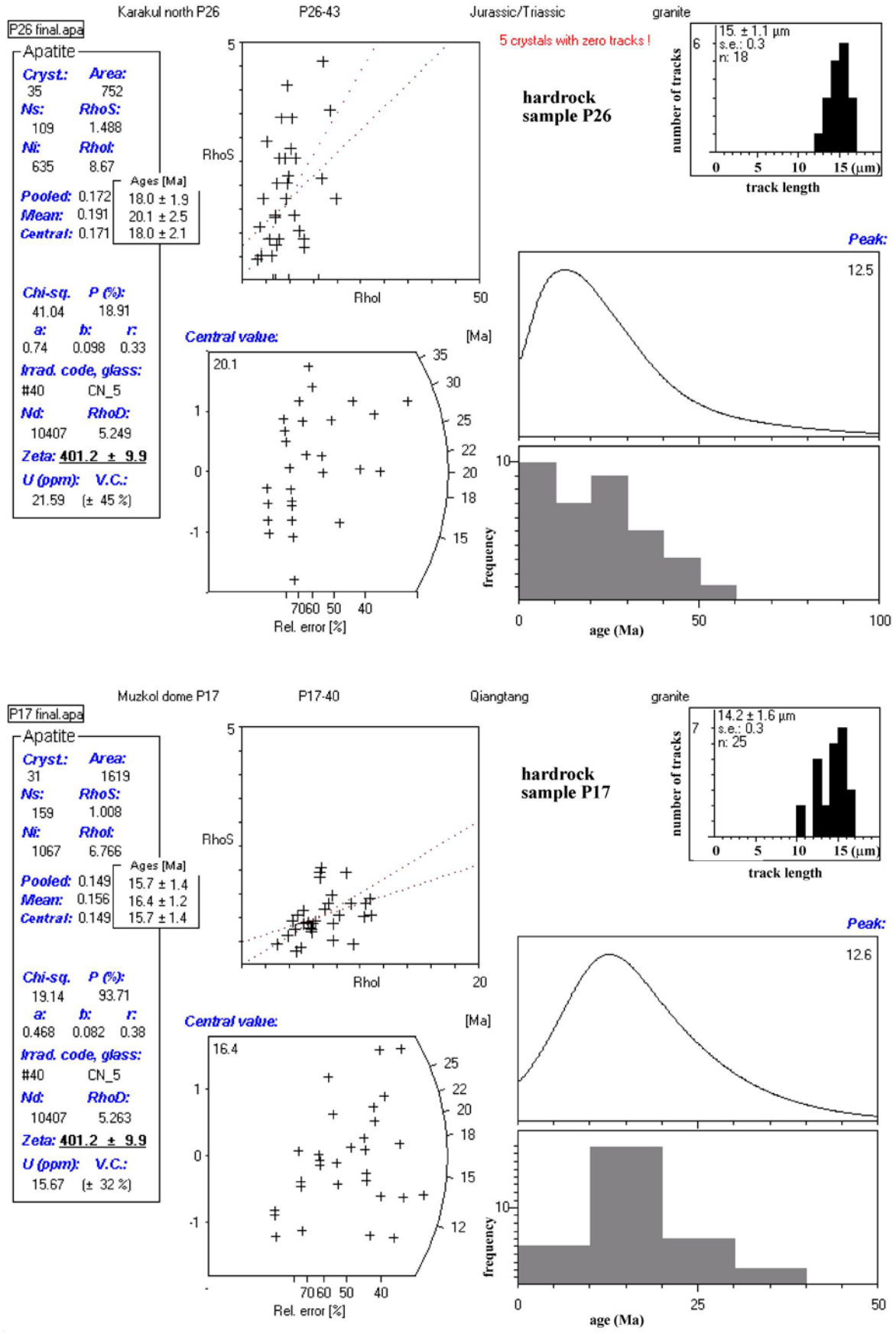

Fig. C1, continued: Apatite fission track ages determined with the Program TRACKKEY 4.0 (Dunkl 2002). The radial plot is after Galbraith (1990). Abbreviations: s.e.=standard deviation, n=number of tracks.

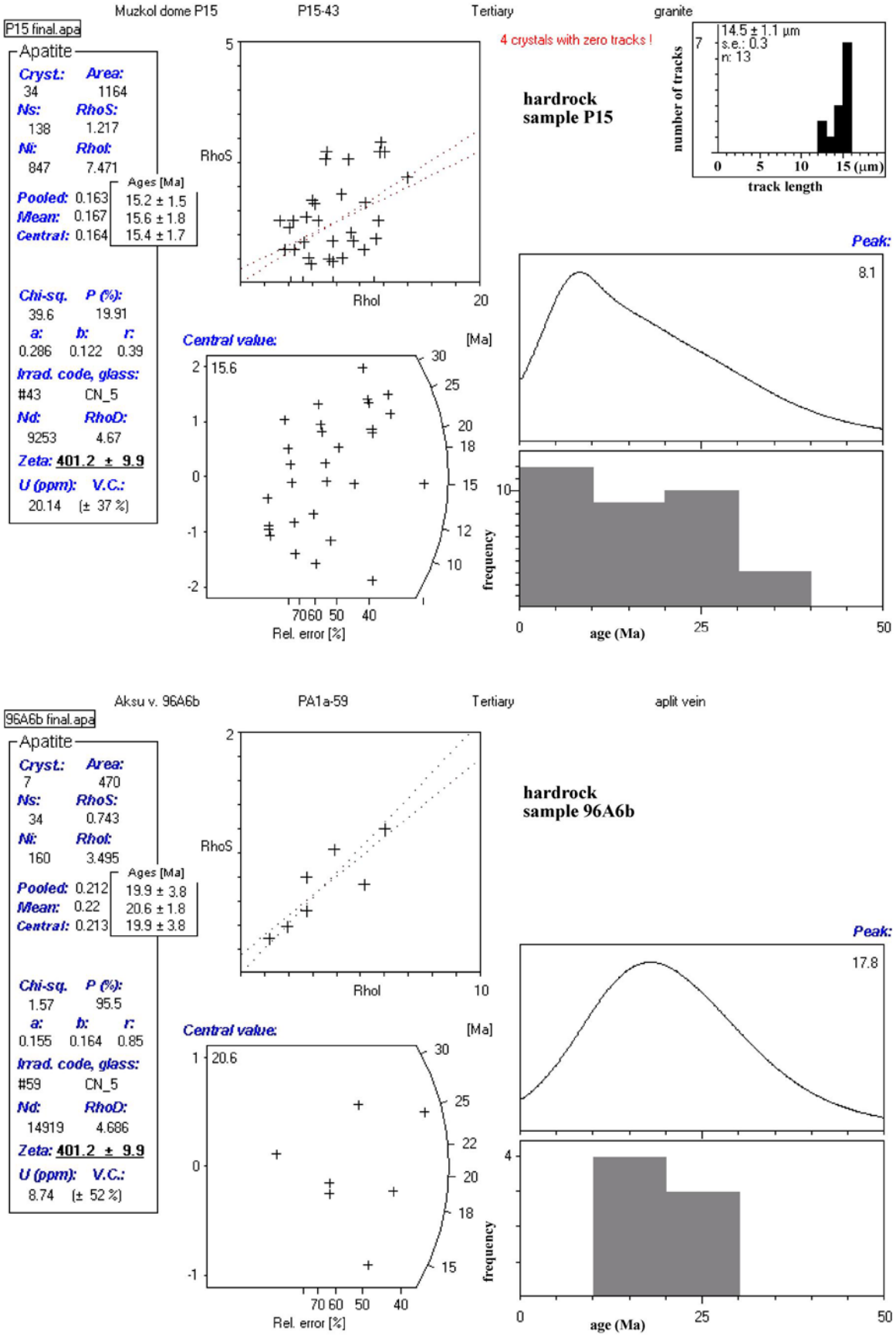

Fig. C1, continued: Apatite fission track ages determined with the Program TRACKKEY 4.0 (Dunkl 2002). The radial plot is after Galbraith (1990). Abbreviations: s.e.=standard deviation, n=number of tracks.

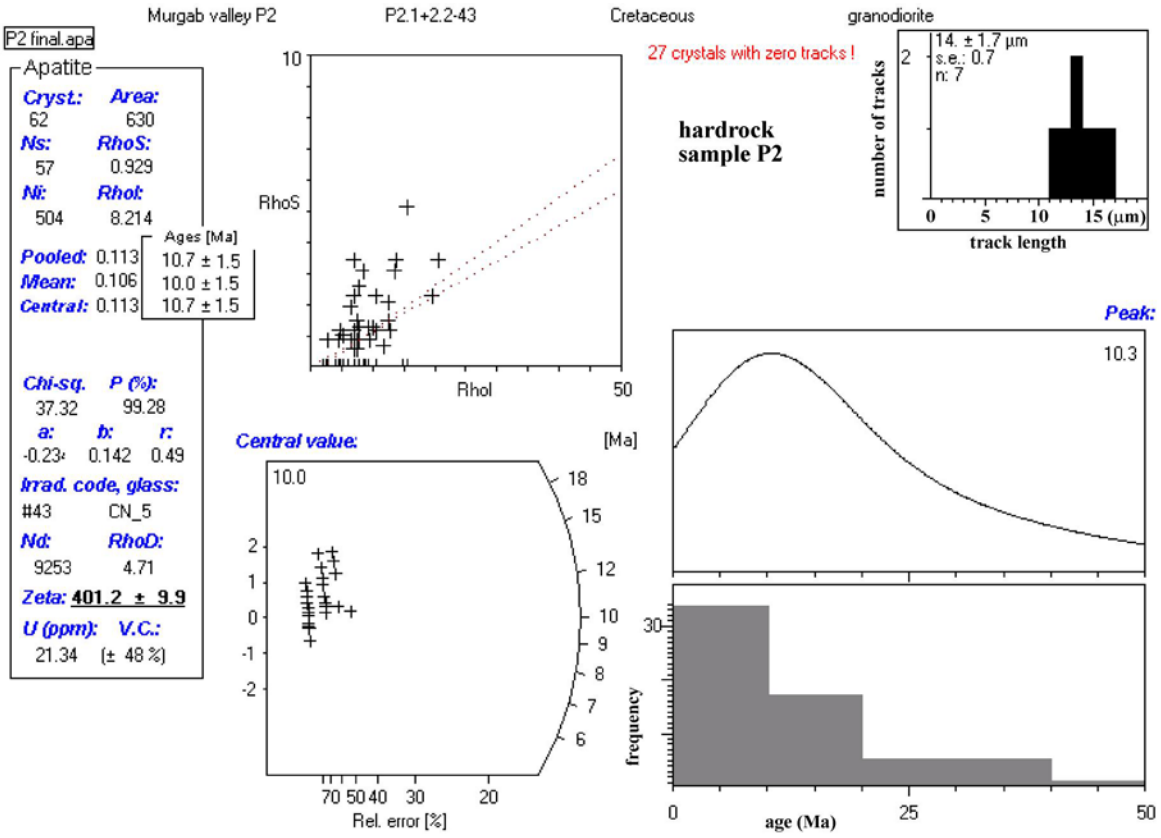

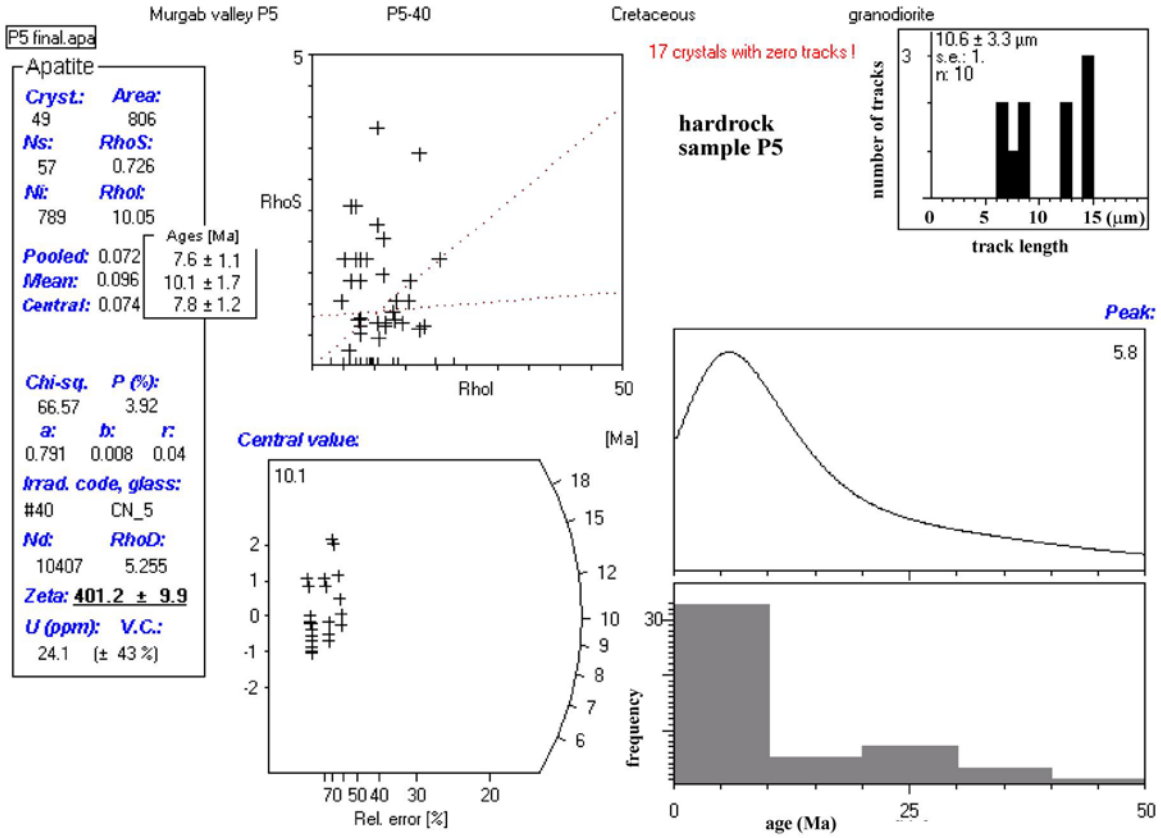

Fig. C1, continued: Apatite fission track ages determined with the Program TRACKKEY 4.0 (Dunkl 2002). The radial plot is after Galbraith (1990). Abbreviations: s.e.=standard deviation, n=number of tracks.

Tab. C5 Electron microprobe analyses of selected apatite samples

Sample grain-no.	P_2O_5 wt%	SiO_2 wt%	MgO wt%	CaO wt%	MnO wt%	FeO wt%	SrO wt%	Na_2O wt%	H_2O wt%	F wt%	Cl wt%	Total wt%
P20												
P20-1	41.71	0.31	0.00	55.22	0.56	0.03	0.04	0.08	0.11	3.53	0.00	101.60
P20-2	41.76	0.08	0.00	55.22	0.65	0.10	0.03	0.09	0.09	3.57	0.00	101.59
P20-3	41.05	0.09	0.00	55.07	0.54	0.09	0.02	0.13	0.08	3.55	0.00	100.61
P20-3	41.98	0.07	0.00	54.86	0.69	0.14	0.02	0.13	0.05	3.64	0.01	101.59
P20-3	42.01	0.03	0.00	54.97	0.74	0.12	0.00	0.09	0.10	3.54	0.00	101.60
P20-4	41.75	0.02	0.00	55.17	0.73	0.12	0.03	0.12	0.08	3.58	0.00	101.59
P20-4	41.31	0.13	0.00	55.26	0.72	0.18	0.01	0.12	0.00	3.94	0.00	101.66
P20-8	41.68	0.06	0.00	55.43	0.52	0.03	0.02	0.10	0.01	3.74	0.00	101.58
P20-14	41.84	0.06	0.00	55.37	0.41	0.02	0.00	0.08	0.00	3.82	0.00	101.61
P20-14	41.95	0.02	0.00	55.44	0.39	0.06	0.01	0.09	0.11	3.53	0.01	101.60
P20-13	42.01	0.06	0.00	55.42	0.30	0.07	0.02	0.10	0.11	3.53	0.00	101.60
P20-17	41.97	0.02	0.00	55.24	0.43	0.10	0.00	0.14	0.06	3.64	0.00	101.59
P20-17	42.11	0.02	0.00	55.14	0.54	0.10	0.01	0.09	0.15	3.45	0.01	101.60
P20-25	41.73	0.01	0.00	55.55	0.49	0.05	0.01	0.12	0.12	3.51	0.00	101.59
P20-24	41.79	0.04	0.00	55.26	0.58	0.07	0.01	0.14	0.05	3.65	0.01	101.58
P20-24	41.76	0.02	0.00	55.30	0.42	0.09	0.02	0.08	0.00	3.98	0.00	101.68
P20-23	41.83	0.05	0.00	55.13	0.47	0.10	0.01	0.08	0.00	4.03	0.01	101.70
P20-23	41.97	0.04	0.00	55.29	0.47	0.08	0.03	0.10	0.12	3.51	0.00	101.60
P20-22	42.17	0.02	0.00	55.19	0.47	0.07	0.01	0.08	0.16	3.43	0.00	101.60
P20-22	42.23	0.03	0.00	55.05	0.45	0.08	0.00	0.10	0.09	3.57	0.00	101.60
P20-18	42.33	0.02	0.00	54.78	0.57	0.08	0.02	0.13	0.10	3.57	0.01	101.60
P20-18	41.99	0.10	0.00	54.77	0.66	0.08	0.01	0.13	0.00	3.90	0.00	101.64
P20-11	41.78	0.05	0.00	55.06	0.64	0.10	0.01	0.09	0.00	3.92	0.00	101.65
P20-12	42.07	0.02	0.00	54.75	0.70	0.09	0.00	0.07	0.00	3.95	0.00	101.66
P20-9	41.91	0.02	0.00	54.97	0.57	0.06	0.04	0.11	0.00	4.03	0.01	101.70
P20-9	42.03	0.05	0.00	55.30	0.32	0.10	0.03	0.11	0.09	3.56	0.01	101.59
P20-7	42.28	0.06	0.00	55.17	0.29	0.04	0.02	0.10	0.11	3.55	0.00	101.60
P20-7	42.25	0.03	0.00	55.20	0.30	0.03	0.00	0.08	0.05	3.66	0.00	101.59
P20-10	42.40	0.03	0.00	55.01	0.33	0.08	0.00	0.09	0.10	3.56	0.01	101.60
P20-10	42.14	0.06	0.00	54.87	0.64	0.11	0.00	0.18	0.15	3.45	0.01	101.60
P20-21	42.18	0.02	0.00	54.88	0.65	0.13	0.02	0.08	0.12	3.51	0.01	101.60
P20-21	41.73	0.03	0.00	55.74	0.31	0.04	0.00	0.09	0.10	3.55	0.00	101.59
P20-16	41.97	0.04	0.00	55.34	0.44	0.02	0.00	0.13	0.10	3.55	0.00	101.59
P20-20	42.36	0.06	0.00	54.85	0.48	0.06	0.01	0.10	0.09	3.58	0.01	101.60
P20-19	41.94	0.07	0.00	55.32	0.38	0.08	0.00	0.14	0.09	3.57	0.01	101.59
P20-15	41.68	0.07	0.00	55.44	0.55	0.07	0.01	0.12	0.10	3.55	0.00	101.59
P20-15	41.87	0.03	0.00	55.17	0.49	0.06	0.04	0.10	0.00	3.86	0.01	101.63
P20-6	42.31	0.02	0.00	54.90	0.32	0.05	0.02	0.12	0.00	3.92	0.00	101.65
P20-6	41.62	0.04	0.00	55.52	0.28	0.01	0.01	0.09	0.00	4.19	0.00	101.77
P20-5	41.90	0.13	0.00	55.31	0.18	0.00	0.01	0.12	0.00	4.07	0.00	101.71
P20-5	41.94	0.02	0.00	55.06	0.63	0.14	0.01	0.11	0.06	3.62	0.00	101.59
P20-26	42.01	0.04	0.00	55.03	0.59	0.13	0.00	0.11	0.08	3.59	0.01	101.59
P20-26	40.96	0.34	0.00	54.78	0.58	0.09	0.02	0.11	0.00	3.91	0.01	100.81
P20-28	42.03	0.07	0.00	54.82	0.58	0.05	0.00	0.10	0.00	4.05	0.01	101.71
P20-28	41.53	0.13	0.00	55.62	0.30	0.01	0.00	0.10	0.00	4.01	0.00	101.69
P20-27	41.85	0.10	0.00	55.40	0.21	0.00	0.02	0.07	0.00	4.06	0.00	101.71
P20-29	42.04	0.12	0.00	55.08	0.31	0.01	0.01	0.12	0.00	3.97	0.01	101.67
P20-29	41.78	0.03	0.00	55.84	0.15	0.03	0.01	0.07	0.06	3.63	0.01	101.59

Tab. C5 continued

Sample grain-no.	P_2O_5 wt%	SiO_2 wt%	MgO wt%	CaO wt%	MnO wt%	FeO wt%	SrO wt%	Na_2O wt%	H_2O wt%	F wt%	Cl wt%	Total wt%
P20-30	41.79	0.04	0.00	55.52	0.46	0.06	0.01	0.09	0.11	3.53	0.01	101.60
P20-30	41.27	0.42	0.00	55.31	0.44	0.08	0.02	0.11	0.14	3.44	0.00	101.24
P20-31	41.56	0.21	0.00	55.94	0.06	0.03	0.01	0.09	0.06	3.62	0.01	101.59
P20-33	41.53	0.30	0.00	54.84	0.64	0.09	0.03	0.12	0.11	3.52	0.00	101.17
P20-32	42.39	0.13	0.00	54.66	0.60	0.06	0.02	0.13	0.13	3.50	0.00	101.60
P20-32	42.00	0.06	0.00	54.89	0.59	0.10	0.02	0.12	0.00	3.85	0.01	101.62
P20-35	41.62	0.40	0.00	54.97	0.54	0.11	0.00	0.11	0.04	3.67	0.00	101.45
P20-35	42.17	0.08	0.00	54.80	0.53	0.00	0.00	0.12	0.00	3.96	0.01	101.67
P20-34	41.86	0.04	0.00	54.96	0.59	0.09	0.02	0.14	0.00	3.97	0.01	101.67
P20-34	41.76	0.02	0.00	55.30	0.39	0.10	0.01	0.12	0.00	3.95	0.00	101.67
P20-34	41.94	0.04	0.00	55.10	0.43	0.10	0.01	0.11	0.00	3.93	0.00	101.66
P22												
P22-5	41.26	0.03	0.00	56.11	0.43	0.12	0.03	0.09	0.21	3.29	0.04	101.60
P22-16/3	41.25	0.10	0.00	55.78	0.50	0.11	0.02	0.10	0.20	3.28	0.06	101.40
P22-15	41.47	0.04	0.00	55.30	0.63	0.16	0.02	0.16	0.20	3.29	0.08	101.32
P22-6	41.57	0.09	0.00	55.24	0.67	0.16	0.02	0.11	0.03	3.65	0.05	101.60
P22-7	41.38	0.11	0.00	55.56	0.67	0.21	0.01	0.14	0.22	3.25	0.06	101.60
P22-15	41.94	0.12	0.00	54.98	0.64	0.16	0.03	0.11	0.14	3.45	0.05	101.60
P22-8	41.37	0.12	0.00	55.54	0.58	0.20	0.00	0.13	0.09	3.54	0.02	101.60
P22-18	41.00	0.12	0.00	55.77	0.56	0.19	0.00	0.14	0.16	3.36	0.07	101.36
P22-19	41.25	0.12	0.00	55.51	0.70	0.20	0.02	0.16	0.11	3.52	0.00	101.60
P22-4	41.40	0.13	0.00	55.43	0.73	0.19	0.04	0.12	0.18	3.34	0.05	101.60
P22-14	41.38	0.11	0.00	55.61	0.52	0.09	0.02	0.12	0.02	3.70	0.01	101.60
P22-9	41.38	0.13	0.00	55.32	0.67	0.22	0.02	0.10	0.01	3.70	0.03	101.60
P22-6	41.17	0.10	0.00	55.87	0.58	0.12	0.02	0.14	0.15	3.41	0.03	101.60
P22-17	41.45	0.13	0.00	55.57	0.51	0.15	0.01	0.11	0.09	3.56	0.02	101.60
P22-24	41.68	0.11	0.00	55.28	0.60	0.14	0.06	0.12	0.14	3.45	0.04	101.60
P24												
P24-35	41.40	0.03	0.00	55.82	0.45	0.12	0.00	0.14	0.11	3.50	0.03	101.59
P24-1	40.31	0.25	0.02	54.54	0.39	0.09	0.00	0.14	0.10	3.45	0.01	99.29
P24-2	41.48	0.16	0.00	55.38	0.64	0.13	0.02	0.09	0.06	3.62	0.01	101.58
P24-34	41.81	0.12	0.00	55.16	0.56	0.18	0.04	0.09	0.10	3.54	0.00	101.59
P24-3	41.87	0.23	0.00	55.17	0.34	0.06	0.02	0.08	0.00	3.85	0.00	101.62
P24-33	41.55	0.12	0.00	55.68	0.43	0.08	0.01	0.10	0.12	3.49	0.01	101.59
P24-5	40.85	0.20	0.00	54.96	0.47	0.14	0.01	0.12	0.05	3.59	0.01	100.41
P24-4	41.45	0.12	0.00	55.49	0.58	0.12	0.00	0.11	0.03	3.68	0.00	101.58
P24-32	41.65	0.20	0.00	55.77	0.35	0.06	0.01	0.07	0.24	3.23	0.05	101.61
P24-7	41.20	0.14	0.00	55.56	0.36	0.07	0.00	0.08	0.06	3.60	0.00	101.09
P24-8	41.01	0.20	0.00	55.68	0.48	0.10	0.00	0.13	0.12	3.48	0.00	101.19
P24-31	41.35	0.11	0.00	55.57	0.65	0.21	0.00	0.13	0.16	3.42	0.00	101.60
P24-30	41.20	0.16	0.00	55.12	0.62	0.21	0.03	0.12	0.10	3.51	0.01	101.09
P24-9	41.22	0.03	0.00	55.88	0.46	0.07	0.04	0.12	0.10	3.52	0.01	101.45
P24-10	40.99	0.17	0.00	55.80	0.52	0.10	0.00	0.13	0.11	3.51	0.01	101.34
P24-29	41.62	0.12	0.00	55.12	0.65	0.26	0.00	0.09	0.02	3.69	0.02	101.58
P24-28	41.83	0.14	0.00	55.58	0.25	0.07	0.02	0.13	0.15	3.46	0.00	101.60
P24-27	41.10	0.16	0.01	54.58	0.61	0.15	0.00	0.14	0.13	3.44	0.00	100.31
P24-11	41.65	0.12	0.00	55.59	0.39	0.10	0.02	0.10	0.12	3.51	0.01	101.59
P24-26	41.32	0.13	0.00	55.40	0.71	0.15	0.02	0.12	0.02	3.71	0.01	101.58
P25												

Tab. C5 continued

Sample grain-no.	P_2O_5 wt%	SiO_2 wt%	MgO wt%	CaO wt%	MnO wt%	FeO wt%	SrO wt%	Na_2O wt%	H_2O wt%	F wt%	Cl wt%	Total wt%
P25-1	40.95	0.21	0.00	54.41	0.30	0.06	0.00	0.14	0.07	3.53	0.01	99.68
P25-15	40.14	0.31	0.00	53.97	0.22	0.04	0.00	0.13	0.10	3.43	0.01	98.33
P25-14	41.56	0.10	0.00	56.06	0.19	0.00	0.00	0.10	0.14	3.46	0.00	101.60
P25-2	41.26	0.29	0.00	55.60	0.14	0.02	0.00	0.06	0.11	3.48	0.05	101.02
P25-4	40.14	0.39	0.00	54.95	0.25	0.03	0.00	0.10	0.15	3.35	0.01	99.36
P25-34	41.58	0.26	0.00	55.73	0.24	0.04	0.00	0.10	0.12	3.50	0.01	101.57
P25-33	41.44	0.17	0.00	55.66	0.43	0.12	0.00	0.10	0.08	3.57	0.04	101.59
P25-16	41.59	0.28	0.00	55.62	0.22	0.01	0.00	0.14	0.09	3.56	0.00	101.50
P25-5	41.30	0.19	0.00	56.07	0.26	0.02	0.00	0.11	0.09	3.55	0.01	101.59
P25-6	41.38	0.18	0.00	55.94	0.29	0.09	0.02	0.10	0.14	3.45	0.00	101.60
P25-7	41.31	0.20	0.00	56.04	0.24	0.04	0.02	0.11	0.12	3.50	0.01	101.59
P25-17	41.52	0.12	0.00	56.01	0.23	0.02	0.03	0.09	0.16	3.41	0.01	101.60
P25-32	41.25	0.17	0.00	56.04	0.27	0.07	0.02	0.14	0.10	3.53	0.01	101.59
P25-31	41.55	0.14	0.00	55.83	0.25	0.05	0.04	0.12	0.13	3.49	0.00	101.60
P25-23	40.63	0.84	0.00	55.73	0.30	0.04	0.04	0.17	0.05	3.64	0.00	101.43
P25-18	41.87	0.32	0.00	55.39	0.25	0.02	0.02	0.09	0.15	3.44	0.00	101.57
P25-8	40.55	0.54	0.00	55.79	0.14	0.03	0.03	0.10	0.15	3.40	0.01	100.72
P25-9	41.67	0.19	0.00	55.76	0.24	0.04	0.00	0.10	0.15	3.45	0.01	101.60
P25-24	41.45	0.30	0.00	55.64	0.26	0.04	0.00	0.11	0.07	3.60	0.00	101.48
P25-35	40.45	0.41	0.00	54.82	0.25	0.05	0.01	0.10	0.10	3.46	0.01	99.65
P26												
P26-4	42.64	0.13	0.00	55.02	0.13	0.04	0.00	0.10	0.21	3.33	0.01	101.62
P26-4	42.25	0.13	0.00	55.33	0.15	0.05	0.00	0.12	0.18	3.39	0.01	101.61
P26-4	42.54	0.22	0.00	54.94	0.14	0.06	0.02	0.13	0.21	3.34	0.01	101.62
P26-3	42.23	0.37	0.00	55.16	0.12	0.02	0.00	0.13	0.19	3.38	0.02	101.61
P26-19	42.36	0.22	0.00	54.94	0.19	0.04	0.02	0.12	0.07	3.64	0.00	101.60
P26-19	42.42	0.11	0.00	55.04	0.16	0.06	0.00	0.09	0.06	3.65	0.00	101.60
P26-25	42.69	0.13	0.00	54.94	0.16	0.04	0.02	0.12	0.25	3.25	0.02	101.62
P26-25	42.59	0.13	0.00	55.05	0.15	0.04	0.01	0.15	0.25	3.25	0.01	101.62
P26-18	42.41	0.11	0.00	55.28	0.11	0.01	0.01	0.09	0.17	3.41	0.01	101.61
P26-18	42.65	0.13	0.00	54.97	0.13	0.01	0.00	0.11	0.15	3.47	0.00	101.61
P26-5	42.06	0.29	0.00	55.25	0.18	0.08	0.01	0.13	0.15	3.45	0.02	101.60
P26-5	42.48	0.26	0.00	54.97	0.13	0.05	0.01	0.11	0.17	3.43	0.01	101.61
P26-2	41.88	0.10	0.00	55.81	0.15	0.05	0.00	0.12	0.23	3.28	0.00	101.61
P26-2	41.89	0.12	0.00	55.78	0.19	0.04	0.00	0.11	0.24	3.26	0.00	101.61
P26-1	42.32	0.29	0.00	55.05	0.13	0.04	0.01	0.11	0.11	3.54	0.01	101.60
P26-1	42.83	0.18	0.00	54.80	0.10	0.01	0.02	0.11	0.20	3.38	0.00	101.62
P26-26	42.19	0.16	0.00	55.16	0.18	0.06	0.00	0.10	0.02	3.72	0.01	101.59
P26-26	42.29	0.27	0.00	55.05	0.11	0.03	0.01	0.11	0.05	3.67	0.01	101.60
P26-27	42.57	0.21	0.00	54.97	0.14	0.03	0.03	0.12	0.21	3.34	0.01	101.62
P26-27	41.92	0.34	0.00	55.34	0.17	0.15	0.01	0.13	0.20	3.34	0.01	101.61
P26-28	42.86	0.24	0.00	54.77	0.10	0.02	0.01	0.07	0.23	3.31	0.01	101.62
P26-28	42.06	0.31	0.00	55.49	0.10	0.00	0.00	0.07	0.17	3.42	0.00	101.61
P26-28	42.26	0.31	0.00	55.43	0.04	0.00	0.00	0.00	0.19	3.38	0.01	101.61
P26-17	42.58	0.12	0.00	55.14	0.05	0.01	0.02	0.07	0.14	3.49	0.00	101.61
P26-17	42.85	0.12	0.00	54.70	0.14	0.05	0.02	0.13	0.17	3.44	0.01	101.62
P26-16	42.26	0.24	0.00	55.31	0.12	0.02	0.00	0.08	0.18	3.39	0.00	101.61
P26-16	41.25	0.24	0.00	55.93	0.15	0.02	0.00	0.12	0.17	3.37	0.01	101.27
P26-15	42.48	0.22	0.00	55.25	0.03	0.00	0.02	0.05	0.20	3.36	0.01	101.62

Tab. C5 continued

Sample grain-no.	P_2O_5 wt%	SiO_2 wt%	MgO wt%	CaO wt%	MnO wt%	FeO wt%	SrO wt%	Na_2O wt%	H_2O wt%	F wt%	Cl wt%	Total wt%
P26-15	42.23	0.23	0.00	55.40	0.07	0.00	0.01	0.07	0.16	3.43	0.01	101.61
P26-14	42.02	0.21	0.00	55.58	0.10	0.04	0.02	0.08	0.19	3.36	0.01	101.61
P26-14	42.11	0.15	0.00	55.55	0.11	0.03	0.02	0.09	0.19	3.36	0.00	101.61
P26-29	42.61	0.11	0.00	55.04	0.16	0.06	0.01	0.11	0.25	3.26	0.01	101.62
P26-29	42.49	0.11	0.00	55.18	0.16	0.02	0.00	0.12	0.24	3.28	0.02	101.62
P26-30	42.58	0.21	0.00	54.94	0.16	0.04	0.00	0.10	0.18	3.41	0.01	101.61
P26-30	42.50	0.15	0.00	55.16	0.09	0.03	0.03	0.10	0.20	3.36	0.01	101.62
P26-31	42.54	0.16	0.00	55.14	0.11	0.05	0.00	0.08	0.22	3.33	0.01	101.62
P26-31	42.24	0.16	0.00	55.38	0.13	0.02	0.02	0.05	0.16	3.44	0.01	101.61
P26-6	42.23	0.13	0.00	55.49	0.06	0.00	0.01	0.06	0.14	3.49	0.01	101.61
P26-6	42.65	0.15	0.00	54.91	0.12	0.04	0.01	0.12	0.16	3.44	0.01	101.61
P26-20	42.56	0.13	0.00	55.07	0.16	0.01	0.00	0.11	0.19	3.38	0.01	101.61
P26-20	42.40	0.10	0.00	55.25	0.14	0.03	0.04	0.12	0.21	3.32	0.01	101.62
P26-24	42.34	0.20	0.00	55.20	0.17	0.04	0.01	0.10	0.19	3.37	0.00	101.61
P26-24	42.18	0.23	0.00	55.38	0.13	0.02	0.02	0.10	0.20	3.35	0.00	101.61
P26-7	42.37	0.03	0.00	55.43	0.14	0.00	0.00	0.09	0.21	3.33	0.02	101.62
P26-7	42.90	0.05	0.00	54.82	0.15	0.04	0.02	0.13	0.25	3.27	0.01	101.63
P26-8	42.41	0.11	0.00	55.21	0.15	0.06	0.00	0.11	0.19	3.37	0.00	101.61
P26-8	42.19	0.16	0.00	55.50	0.07	0.03	0.01	0.03	0.15	3.46	0.00	101.60
P26-8	42.42	0.12	0.00	55.23	0.12	0.05	0.00	0.12	0.20	3.36	0.00	101.62
P26-9	42.73	0.25	0.00	54.58	0.10	0.04	0.01	0.09	0.27	3.22	0.01	101.30
P26-9	41.80	0.27	0.00	55.51	0.09	0.02	0.02	0.12	0.22	3.30	0.01	101.34
P26-32	42.57	0.14	0.00	55.08	0.13	0.01	0.01	0.09	0.18	3.39	0.01	101.61
P26-32	42.41	0.15	0.00	55.17	0.17	0.03	0.00	0.12	0.20	3.36	0.01	101.61
P26-23	42.98	0.35	0.00	54.49	0.09	0.05	0.00	0.09	0.21	3.36	0.01	101.63
P26-23	42.24	0.32	0.00	55.24	0.09	0.02	0.00	0.10	0.16	3.45	0.00	101.61
P26-23	42.10	0.38	0.00	55.34	0.10	0.02	0.00	0.09	0.22	3.32	0.00	101.57
P26-13	42.48	0.11	0.00	55.20	0.14	0.00	0.02	0.11	0.21	3.32	0.02	101.62
P26-13	42.44	0.11	0.00	55.21	0.13	0.01	0.02	0.08	0.16	3.45	0.01	101.61
P26-13	42.31	0.13	0.00	55.37	0.09	0.01	0.01	0.10	0.17	3.41	0.01	101.61
P26-10	43.08	0.15	0.00	54.63	0.09	0.00	0.02	0.13	0.24	3.29	0.01	101.63
P26-10	42.37	0.21	0.00	55.19	0.10	0.02	0.03	0.12	0.19	3.37	0.01	101.61
P26-22	42.38	0.31	0.00	54.80	0.17	0.05	0.02	0.12	0.02	3.73	0.00	101.59
P26-22	42.27	0.18	0.00	55.07	0.16	0.04	0.00	0.12	0.02	3.72	0.01	101.59
P26-33	42.26	0.01	0.00	55.75	0.03	0.00	0.00	0.00	0.20	3.36	0.00	101.61
P26-33	42.18	0.02	0.00	55.72	0.04	0.03	0.02	0.01	0.16	3.43	0.00	101.61
P26-34	41.83	0.25	0.00	55.69	0.11	0.06	0.01	0.09	0.18	3.38	0.00	101.61
P26-34	41.63	0.26	0.00	56.00	0.07	0.02	0.02	0.06	0.21	3.31	0.01	101.59
P26-35	42.39	0.03	0.00	55.35	0.13	0.01	0.02	0.10	0.18	3.39	0.01	101.61
P26-35	42.16	0.03	0.00	55.57	0.15	0.01	0.00	0.10	0.17	3.41	0.00	101.61
P26-11	41.94	0.24	0.00	55.62	0.09	0.05	0.00	0.10	0.19	3.36	0.01	101.61
P26-11	42.31	0.17	0.00	55.44	0.08	0.00	0.00	0.07	0.21	3.34	0.00	101.62
P26-12	42.19	0.23	0.00	55.21	0.17	0.01	0.00	0.13	0.10	3.55	0.01	101.60
P26-12	42.20	0.45	0.05	54.81	0.11	0.24	0.00	0.10	0.12	3.53	0.01	101.61
P26-21	42.22	0.27	0.00	55.23	0.14	0.05	0.03	0.10	0.19	3.37	0.01	101.61
P26-21	42.24	0.24	0.00	55.26	0.14	0.01	0.00	0.14	0.18	3.39	0.01	101.61
P15												
P15-1	41.05	0.61	0.00	55.93	0.07	0.05	0.05	0.07	0.02	3.66	0.08	101.58
P15-2	41.46	0.10	0.00	56.12	0.05	0.04	0.06	0.08	0.07	3.59	0.04	101.59

Tab. C5 continued

Sample grain-no.	P_2O_5 wt%	SiO_2 wt%	MgO wt%	CaO wt%	MnO wt%	FeO wt%	SrO wt%	Na_2O wt%	H_2O wt%	F wt%	Cl wt%	Total wt%
P15-3	40.65	0.26	0.00	56.75	0.04	0.00	0.06	0.08	0.02	3.67	0.04	101.57
P15-4	40.79	0.39	0.00	56.35	0.01	0.04	0.04	0.28	0.08	3.55	0.06	101.58
P15-6	41.02	0.49	0.00	55.99	0.06	0.07	0.05	0.10	0.00	3.76	0.06	101.60
P15-7	41.25	0.13	0.00	56.34	0.04	0.00	0.00	0.09	0.03	3.67	0.04	101.58
P15-15	40.51	0.57	0.00	56.63	0.00	0.02	0.09	0.08	0.08	3.52	0.08	101.58
P15-17	40.31	0.43	0.00	56.29	0.00	0.04	0.05	0.13	0.00	3.73	0.04	101.01
P15-18	40.95	0.15	0.00	56.52	0.04	0.03	0.07	0.05	0.00	3.74	0.04	101.59
P15-16	40.82	0.40	0.00	56.18	0.03	0.03	0.06	0.13	0.00	3.96	0.06	101.68
P15-19	40.58	0.45	0.00	56.36	0.01	0.00	0.08	0.11	0.03	3.64	0.05	101.31
P15-20	40.86	0.32	0.00	56.39	0.03	0.00	0.05	0.09	0.00	3.84	0.05	101.63
P15-32	41.62	0.03	0.00	55.98	0.03	0.04	0.08	0.02	0.00	3.72	0.05	101.58
P15-32	41.18	0.36	0.00	56.05	0.01	0.00	0.02	0.09	0.00	3.88	0.06	101.65
P15-34	41.16	0.24	0.00	56.06	0.04	0.03	0.08	0.10	0.00	3.88	0.04	101.64
P15-22/31	40.95	0.35	0.00	56.12	0.00	0.02	0.07	0.09	0.00	4.10	0.04	101.73
P15-35	40.87	0.43	0.00	56.26	0.02	0.03	0.03	0.15	0.00	3.70	0.07	101.57
P15-21	41.05	0.12	0.00	56.37	0.01	0.05	0.04	0.11	0.00	3.81	0.05	101.61
P15-14	40.87	0.21	0.00	56.63	0.02	0.01	0.04	0.05	0.00	3.73	0.02	101.57
P15-30	40.79	0.39	0.00	56.14	0.01	0.06	0.00	0.10	0.00	4.26	0.05	101.81
P15-23	40.57	0.15	0.00	56.51	0.02	0.01	0.06	0.11	0.00	4.39	0.03	101.86
P15-11	40.87	0.10	0.00	56.73	0.04	0.03	0.09	0.05	0.09	3.52	0.04	101.58
P15-13/24	40.60	0.43	0.00	56.35	0.04	0.01	0.07	0.11	0.00	3.76	0.05	101.42
P15-25	40.85	0.41	0.00	56.15	0.04	0.04	0.07	0.10	0.00	3.99	0.06	101.69
P15-29	40.83	0.41	0.00	56.25	0.01	0.04	0.06	0.06	0.00	3.91	0.05	101.62
P15-28	40.76	0.12	0.00	56.82	0.02	0.02	0.04	0.08	0.01	3.68	0.04	101.57
P15-12	40.67	0.36	0.00	56.03	0.01	0.00	0.04	0.13	0.00	3.78	0.05	101.08
P15-26	41.06	0.37	0.00	56.22	0.03	0.01	0.06	0.11	0.04	3.65	0.03	101.58
P15-27	40.71	0.36	0.00	56.45	0.01	0.03	0.04	0.05	0.00	4.01	0.04	101.70
P17												
P17-1	41.99	0.38	0.00	55.23	0.01	0.03	0.02	0.17	0.13	3.33	0.31	101.60
P17-1	41.47	0.20	0.00	55.87	0.02	0.09	0.02	0.19	0.15	3.27	0.31	101.60
P17-1	41.59	0.37	0.00	55.68	0.02	0.01	0.01	0.14	0.11	3.35	0.31	101.59
P17-8	42.10	0.18	0.00	55.49	0.02	0.05	0.02	0.14	0.26	3.07	0.28	101.62
P17-8	42.34	0.12	0.00	55.33	0.02	0.06	0.01	0.14	0.27	3.05	0.30	101.62
P17-9	42.14	0.05	0.00	55.62	0.03	0.03	0.00	0.12	0.25	3.12	0.25	101.61
P17-9	42.28	0.05	0.00	55.48	0.06	0.00	0.02	0.10	0.24	3.10	0.29	101.62
P17-17	41.73	0.05	0.00	56.02	0.00	0.04	0.03	0.19	0.29	3.00	0.27	101.62
P17-17	42.23	0.06	0.00	55.57	0.02	0.04	0.04	0.10	0.30	2.99	0.27	101.62
P17-7	42.30	0.16	0.00	55.28	0.02	0.03	0.01	0.16	0.22	3.18	0.25	101.61
P17-7	42.32	0.16	0.00	55.14	0.02	0.04	0.03	0.23	0.20	3.22	0.26	101.61
P17-18	42.33	0.21	0.00	55.26	0.02	0.06	0.00	0.07	0.23	3.14	0.30	101.62
P17-18	42.52	0.34	0.00	54.88	0.03	0.06	0.02	0.13	0.25	3.10	0.30	101.62
P17-16	42.08	0.17	0.00	55.49	0.02	0.04	0.05	0.14	0.24	3.10	0.29	101.62
P17-16	42.03	0.43	0.00	55.24	0.05	0.05	0.02	0.14	0.24	3.09	0.32	101.62
P17-16	41.79	0.13	0.00	55.79	0.01	0.06	0.01	0.18	0.24	3.10	0.32	101.61
P17-10	42.18	0.08	0.00	55.46	0.01	0.07	0.02	0.11	0.20	3.18	0.30	101.61
P17-10	42.06	0.07	0.00	55.56	0.03	0.06	0.03	0.12	0.21	3.16	0.30	101.61
P17-11	42.34	0.26	0.00	54.95	0.04	0.07	0.03	0.22	0.18	3.24	0.30	101.61
P17-11	42.01	0.27	0.00	55.25	0.02	0.04	0.04	0.24	0.17	3.25	0.32	101.61
P17-11	42.11	0.32	0.00	55.19	0.03	0.07	0.00	0.20	0.20	3.17	0.32	101.61

Tab. C5 continued

Sample grain-no.	P_2O_5 wt%	SiO_2 wt%	MgO wt%	CaO wt%	MnO wt%	FeO wt%	SrO wt%	Na_2O wt%	H_2O wt%	F wt%	Cl wt%	Total wt%
P17-15	41.78	0.33	0.00	55.67	0.04	0.05	0.00	0.12	0.26	3.06	0.32	101.62
P17-15	42.31	0.05	0.00	55.43	0.02	0.07	0.04	0.11	0.29	2.99	0.31	101.62
P17-6	42.51	0.06	0.00	55.09	0.00	0.05	0.02	0.15	0.17	3.25	0.32	101.61
P17-6	42.26	0.06	0.00	55.29	0.03	0.10	0.02	0.13	0.16	3.27	0.30	101.61
P17-6	41.70	0.07	0.00	55.87	0.02	0.05	0.04	0.11	0.15	3.27	0.32	101.60
P17-2	42.42	0.07	0.00	55.38	0.03	0.05	0.00	0.07	0.29	2.98	0.33	101.62
P17-2	41.85	0.04	0.00	55.83	0.01	0.04	0.03	0.15	0.24	3.05	0.36	101.61
P17-2	42.31	0.06	0.00	55.50	0.00	0.07	0.01	0.07	0.29	2.99	0.34	101.62
P17-19	42.07	0.07	0.00	55.58	0.04	0.09	0.02	0.12	0.24	3.11	0.29	101.61
P17-19	41.82	0.06	0.00	55.95	0.00	0.05	0.02	0.12	0.27	3.05	0.29	101.62
P17-35	42.10	0.05	0.00	55.49	0.03	0.05	0.01	0.12	0.12	3.37	0.26	101.60
P17-35	42.34	0.07	0.00	55.20	0.00	0.08	0.00	0.17	0.15	3.32	0.28	101.61
P17-14	41.97	0.19	0.00	55.65	0.03	0.03	0.00	0.14	0.27	3.05	0.29	101.62
P17-14	42.14	0.12	0.00	55.58	0.03	0.03	0.01	0.10	0.27	3.06	0.29	101.62
P17-33	42.09	0.15	0.00	55.52	0.03	0.06	0.05	0.09	0.24	3.11	0.29	101.62
P17-33	42.29	0.11	0.00	55.33	0.00	0.05	0.03	0.16	0.23	3.13	0.29	101.62
P17-34	41.94	0.11	0.00	55.73	0.01	0.04	0.02	0.16	0.25	3.11	0.25	101.62
P17-34	42.50	0.38	0.00	54.90	0.02	0.06	0.02	0.13	0.27	3.08	0.29	101.63
P17-34	42.23	0.07	0.00	55.51	0.04	0.05	0.01	0.12	0.27	3.07	0.26	101.62
P17-32	42.45	0.08	0.00	55.22	0.03	0.03	0.02	0.16	0.28	3.02	0.34	101.62
P17-32	42.34	0.25	0.00	55.12	0.06	0.07	0.01	0.16	0.29	2.99	0.36	101.62
P17-31	42.32	0.32	0.00	55.14	0.03	0.03	0.01	0.18	0.30	2.97	0.33	101.63
P17-31	41.78	0.28	0.00	55.63	0.00	0.08	0.02	0.24	0.30	2.96	0.33	101.62
P17-30	42.09	0.13	0.00	55.56	0.03	0.08	0.02	0.13	0.27	3.06	0.26	101.62
P17-30	42.32	0.12	0.00	55.40	0.02	0.06	0.03	0.10	0.29	3.05	0.24	101.62
P17-30	41.90	0.13	0.00	55.79	0.04	0.04	0.03	0.08	0.25	3.11	0.24	101.62
P17-12	42.29	0.12	0.00	55.55	0.03	0.02	0.01	0.05	0.30	3.00	0.28	101.62
P17-12	42.20	0.07	0.00	55.58	0.01	0.05	0.02	0.11	0.28	3.04	0.25	101.62
P17-20	41.93	0.25	0.00	55.49	0.01	0.04	0.03	0.14	0.16	3.28	0.28	101.60
P17-20	42.45	0.18	0.00	55.06	0.01	0.07	0.03	0.15	0.23	3.14	0.30	101.62
P17-20	42.29	0.21	0.00	55.13	0.04	0.08	0.01	0.18	0.20	3.18	0.31	101.61
P17-21	42.03	0.33	0.00	55.26	0.01	0.06	0.04	0.16	0.15	3.34	0.23	101.61
P17-21	42.21	0.14	0.00	55.34	0.01	0.02	0.02	0.14	0.14	3.34	0.25	101.60
P17-29	41.95	0.13	0.00	55.66	0.04	0.02	0.02	0.16	0.25	3.06	0.32	101.61
P17-29	41.93	0.15	0.00	55.60	0.06	0.07	0.02	0.16	0.25	3.09	0.29	101.61
P17-5	42.61	0.10	0.00	55.05	0.02	0.06	0.03	0.13	0.26	3.08	0.29	101.62
P17-5	41.97	0.38	0.00	55.33	0.03	0.07	0.01	0.18	0.24	3.11	0.30	101.62
P17-4	42.24	0.21	0.00	55.21	0.01	0.07	0.02	0.23	0.27	3.02	0.33	101.62
P17-4	42.02	0.43	0.00	55.13	0.05	0.09	0.02	0.26	0.28	3.00	0.34	101.62
P17-22	42.56	0.19	0.00	54.90	0.02	0.08	0.03	0.22	0.29	2.99	0.34	101.63
P17-22	42.04	0.41	0.00	55.23	0.01	0.06	0.03	0.21	0.28	2.99	0.36	101.62
P17-28	42.41	0.07	0.00	55.37	0.00	0.03	0.04	0.14	0.29	3.03	0.27	101.62
P17-28	42.43	0.19	0.00	55.11	0.03	0.06	0.03	0.11	0.23	3.16	0.28	101.62
P17-27	42.35	0.07	0.00	55.35	0.04	0.03	0.01	0.13	0.25	3.11	0.28	101.62
P17-27	41.28	0.40	0.00	56.15	0.03	0.06	0.00	0.07	0.24	3.12	0.27	101.61
P17-26	42.32	0.05	0.00	55.47	0.02	0.04	0.04	0.10	0.26	3.12	0.20	101.62
P17-26	42.02	0.30	0.00	55.51	0.02	0.05	0.02	0.07	0.23	3.16	0.24	101.61
P17-23	41.82	0.36	0.00	55.55	0.00	0.03	0.04	0.07	0.15	3.32	0.26	101.60
P17-23	42.62	0.10	0.00	55.02	0.04	0.04	0.03	0.08	0.19	3.24	0.25	101.61

Tab. C5 continued

Sample grain-no.	P_2O_5 wt%	SiO_2 wt%	MgO wt%	CaO wt%	MnO wt%	FeO wt%	SrO wt%	Na_2O wt%	H_2O wt%	F wt%	Cl wt%	Total wt%
P17-24	42.42	0.14	0.00	55.09	0.04	0.07	0.02	0.17	0.22	3.14	0.31	101.61
P17-24	41.85	0.54	0.00	55.20	0.02	0.10	0.02	0.20	0.23	3.11	0.35	101.61
P17-13	42.79	0.08	0.00	54.93	0.04	0.05	0.02	0.12	0.27	3.09	0.24	101.63
P17-13	42.19	0.28	0.00	55.27	0.01	0.04	0.03	0.18	0.27	3.06	0.29	101.62
P17-3	42.12	0.15	0.00	55.52	0.05	0.05	0.00	0.10	0.24	3.13	0.26	101.61
P17-3	42.18	0.16	0.00	55.40	0.00	0.08	0.01	0.15	0.23	3.15	0.27	101.62
P17-25	41.92	0.35	0.00	55.17	0.02	0.05	0.04	0.25	0.10	3.37	0.33	101.60
P17-25	42.33	0.13	0.00	55.13	0.00	0.03	0.05	0.16	0.12	3.37	0.29	101.60
P17-25	42.08	0.37	0.00	54.96	0.03	0.11	0.03	0.22	0.11	3.36	0.33	101.60
P2												
P2.1-1	41.80	0.20	0.00	55.78	0.15	0.04	0.03	0.10	0.24	3.26	0.02	101.61
P2.1-1	42.34	0.17	0.00	55.24	0.13	0.08	0.01	0.07	0.19	3.38	0.02	101.61
P2.1-2	42.57	0.15	0.00	54.95	0.12	0.02	0.00	0.11	0.10	3.56	0.03	101.60
P2.1-2	42.04	0.14	0.00	55.45	0.15	0.05	0.03	0.09	0.10	3.54	0.01	101.60
P2.1-3	42.51	0.10	0.00	55.10	0.14	0.07	0.01	0.08	0.18	3.40	0.02	101.61
P2.1-3	42.31	0.15	0.00	55.22	0.17	0.04	0.04	0.06	0.14	3.46	0.03	101.61
P2.1-3	42.24	0.21	0.00	55.23	0.15	0.09	0.03	0.06	0.16	3.44	0.02	101.61
P2.1-4	42.36	0.15	0.00	55.28	0.11	0.04	0.03	0.05	0.17	3.41	0.02	101.61
P2.1-4	42.08	0.18	0.00	55.46	0.13	0.04	0.02	0.08	0.15	3.45	0.02	101.60
P2.1-4	42.48	0.14	0.00	55.07	0.13	0.06	0.04	0.08	0.16	3.43	0.03	101.61
P2.1-5	41.91	0.20	0.00	55.55	0.13	0.08	0.03	0.08	0.13	3.47	0.04	101.60
P2.1-5	42.35	0.13	0.00	55.24	0.14	0.03	0.02	0.05	0.12	3.50	0.02	101.60
P2.1-6	41.98	0.16	0.00	55.34	0.14	0.03	0.01	0.09	0.00	3.85	0.02	101.63
P2.1-6	42.24	0.17	0.00	55.06	0.15	0.04	0.05	0.07	0.00	3.83	0.02	101.62
P2.1-8	42.02	0.17	0.00	55.52	0.10	0.04	0.01	0.06	0.10	3.54	0.03	101.60
P2.1-8	42.09	0.18	0.00	55.40	0.13	0.03	0.01	0.09	0.09	3.56	0.02	101.60
P2.1-8	41.47	0.20	0.00	54.71	0.09	0.04	0.04	0.12	0.09	3.52	0.03	100.31
P2.1-9	42.46	0.15	0.00	55.04	0.14	0.00	0.01	0.06	0.05	3.66	0.02	101.60
P2.1-9	41.97	0.16	0.00	55.46	0.13	0.07	0.01	0.07	0.05	3.64	0.03	101.59
P2.1-9	42.33	0.21	0.00	54.78	0.17	0.06	0.01	0.09	0.06	3.63	0.02	101.34
P2.1-10	42.11	0.20	0.00	55.15	0.14	0.01	0.04	0.08	0.00	3.90	0.03	101.65
P2.1-10	42.53	0.23	0.00	54.82	0.13	0.03	0.01	0.05	0.00	3.78	0.02	101.59
P2.1-10	41.84	0.20	0.00	55.44	0.09	0.03	0.02	0.07	0.00	3.95	0.03	101.67
P2.1-11	42.38	0.12	0.00	55.17	0.14	0.04	0.01	0.06	0.11	3.54	0.02	101.60
P2.1-11	42.39	0.14	0.00	55.21	0.13	0.03	0.01	0.06	0.14	3.47	0.02	101.61
P2.1-12	42.12	0.11	0.00	55.11	0.17	0.06	0.02	0.06	0.00	4.04	0.02	101.71
P2.1-12	41.98	0.17	0.00	55.24	0.11	0.08	0.02	0.05	0.00	4.04	0.02	101.70
P2.1-13	41.91	0.42	0.00	55.44	0.12	0.02	0.00	0.06	0.13	3.49	0.02	101.60
P2.1-13	42.08	0.42	0.00	55.21	0.15	0.06	0.01	0.08	0.16	3.42	0.02	101.61
P2.1-14	42.12	0.14	0.00	55.46	0.10	0.06	0.02	0.09	0.15	3.46	0.01	101.61
P2.1-14	42.13	0.20	0.00	55.42	0.10	0.03	0.03	0.10	0.15	3.45	0.01	101.61
P2.1-16	42.45	0.16	0.00	54.98	0.18	0.02	0.03	0.10	0.10	3.56	0.02	101.60
P2.1-16	42.21	0.20	0.00	55.19	0.13	0.09	0.00	0.10	0.09	3.57	0.02	101.60
P2.1-17	41.53	0.39	0.00	55.04	0.10	0.12	0.01	0.10	0.15	3.42	0.03	100.89
P2.1-17	41.84	0.37	0.01	55.41	0.12	0.11	0.03	0.09	0.14	3.46	0.03	101.60
P2.1-18	42.57	0.11	0.00	54.98	0.13	0.07	0.03	0.09	0.15	3.45	0.03	101.61
P2.1-18	42.01	0.23	0.00	55.54	0.11	0.04	0.00	0.07	0.16	3.43	0.02	101.61
P2.1-19	42.34	0.12	0.00	55.23	0.12	0.05	0.01	0.06	0.11	3.53	0.02	101.60
P2.1-19	42.62	0.11	0.00	54.93	0.15	0.05	0.04	0.08	0.14	3.48	0.02	101.61

Tab. C5 continued

Sample grain-no.	P_2O_5 wt%	SiO_2 wt%	MgO wt%	CaO wt%	MnO wt%	FeO wt%	SrO wt%	Na_2O wt%	H_2O wt%	F wt%	Cl wt%	Total wt%
P2.1-21	42.07	0.15	0.00	55.26	0.19	0.05	0.03	0.10	0.03	3.70	0.02	101.59
P2.1-21	42.40	0.15	0.00	55.07	0.15	0.03	0.04	0.07	0.08	3.61	0.02	101.60
P2.1-22	42.22	0.17	0.00	55.45	0.13	0.01	0.00	0.07	0.19	3.36	0.02	101.61
P2.1-22	42.41	0.15	0.00	55.23	0.12	0.02	0.02	0.06	0.17	3.41	0.02	101.61
P2.1-22	40.72	0.38	0.00	55.28	0.09	0.14	0.01	0.05	0.19	3.30	0.03	100.18
P2.1-23	42.25	0.15	0.00	55.31	0.14	0.04	0.02	0.05	0.11	3.53	0.01	101.60
P2.1-23	42.37	0.18	0.00	55.15	0.12	0.03	0.02	0.08	0.12	3.52	0.01	101.60
P2.1-23	42.35	0.13	0.00	55.17	0.16	0.02	0.02	0.13	0.13	3.50	0.01	101.60
P2.1-24	41.68	0.21	0.04	55.72	0.13	0.10	0.03	0.07	0.14	3.46	0.03	101.60
P2.1-24	42.34	0.14	0.00	55.23	0.12	0.04	0.01	0.08	0.13	3.49	0.02	101.60
P2.1-25	41.65	0.09	0.00	55.91	0.14	0.03	0.05	0.09	0.12	3.49	0.02	101.59
P2.1-25	42.23	0.16	0.00	55.35	0.11	0.07	0.01	0.07	0.16	3.42	0.02	101.61
P2.1-26	41.71	0.52	0.03	54.59	0.15	0.23	0.02	0.08	0.22	3.28	0.01	100.84
P2.1-28	41.75	0.23	0.00	55.43	0.13	0.06	0.00	0.12	0.13	3.48	0.02	101.34
P2.1-28	42.49	0.15	0.00	55.04	0.14	0.07	0.01	0.09	0.16	3.44	0.03	101.61
P2.1-30	42.56	0.15	0.00	55.06	0.13	0.00	0.01	0.07	0.14	3.47	0.02	101.61
P2.1-30	41.90	0.22	0.00	55.53	0.13	0.03	0.02	0.09	0.08	3.58	0.02	101.59
P2.1-32	41.23	0.61	0.12	54.85	0.17	0.49	0.01	0.10	0.01	3.71	0.03	101.32
P2.1-33	42.02	0.11	0.00	55.52	0.13	0.04	0.03	0.10	0.11	3.53	0.01	101.60
P2.1-34	40.84	0.19	0.00	55.34	0.18	0.05	0.03	0.10	0.15	3.37	0.02	100.27
P2.1-35	42.13	0.26	0.00	55.07	0.12	0.15	0.00	0.09	0.00	3.76	0.02	101.59
P5												
P5-8	41.14	0.08	0.00	55.76	0.14	0.04	0.02	0.06	0.15	3.37	0.06	100.84
P5-9	41.60	0.13	0.00	55.83	0.12	0.04	0.00	0.13	0.19	3.31	0.06	101.41
P5-10	40.15	0.12	0.00	54.52	0.12	0.05	0.00	0.14	0.22	3.14	0.05	98.52
P5-11	40.35	0.45	0.00	54.36	0.18	0.08	0.03	0.12	0.13	3.35	0.09	99.13
P5-12	41.25	0.21	0.00	55.32	0.21	0.06	0.08	0.05	0.00	4.51	0.09	101.75
P5-12	41.29	0.16	0.00	55.95	0.23	0.08	0.03	0.09	0.01	3.70	0.05	101.58
P5-12	40.59	0.18	0.00	55.04	0.21	0.03	0.04	0.08	0.00	3.73	0.07	99.97
P5-24	41.03	0.30	0.00	55.94	0.14	0.05	0.03	0.09	0.22	3.22	0.11	101.13
P5-24	41.73	0.17	0.00	55.83	0.13	0.09	0.04	0.08	0.24	3.21	0.09	101.61
P5-35	41.08	0.24	0.00	55.56	0.15	0.05	0.01	0.11	0.16	3.36	0.05	100.77
P5-36	40.22	0.22	0.00	55.65	0.15	0.10	0.00	0.11	0.27	3.06	0.09	99.86
P5-37	41.73	0.23	0.00	55.44	0.15	0.14	0.03	0.08	0.20	3.30	0.07	101.36
P5-38	39.47	0.51	0.08	54.29	0.07	0.44	0.04	0.08	0.12	3.36	0.04	98.49
P5-39	41.89	0.10	0.00	55.68	0.17	0.05	0.05	0.13	0.22	3.26	0.06	101.61
P5-44	40.98	0.21	0.00	55.66	0.12	0.03	0.03	0.12	0.19	3.30	0.04	100.68
P5-45	40.73	0.28	0.00	55.95	0.17	0.08	0.01	0.14	0.20	3.24	0.10	100.89
P5-46	41.32	0.27	0.00	56.08	0.10	0.07	0.02	0.12	0.20	3.30	0.05	101.52
P5-50	40.65	0.19	0.00	56.35	0.03	0.04	0.00	0.03	0.05	3.60	0.03	100.97

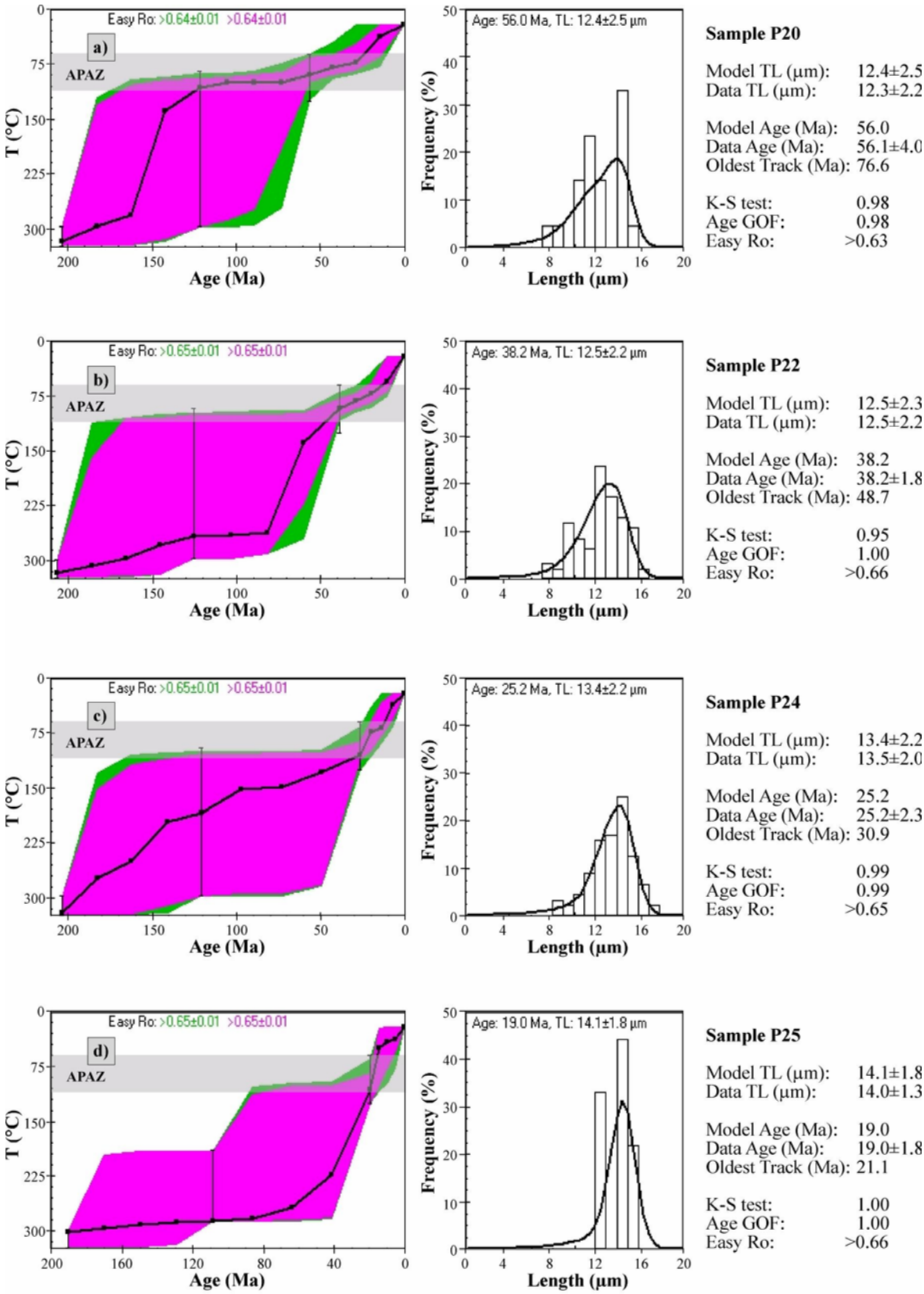

Fig. C2: Time-temperature paths and fission track length distributions of apatite samples modelled with AFTSolve 1.2.2 (Ketcham et al. 2000). APAZ=Apatite partial annealing zone. Track length distributions are normalised to n=100. The fit between the observed and modelled data (t-T paths, left side) is indicated as follows: solid black line=best fit, dark gray area=good fit, light gray area=acceptable fit. Age GOF=goodness of fit between modelled and calculated age, K-S Test=Kolmogorov-Smirnov statistical test, TL=track length.

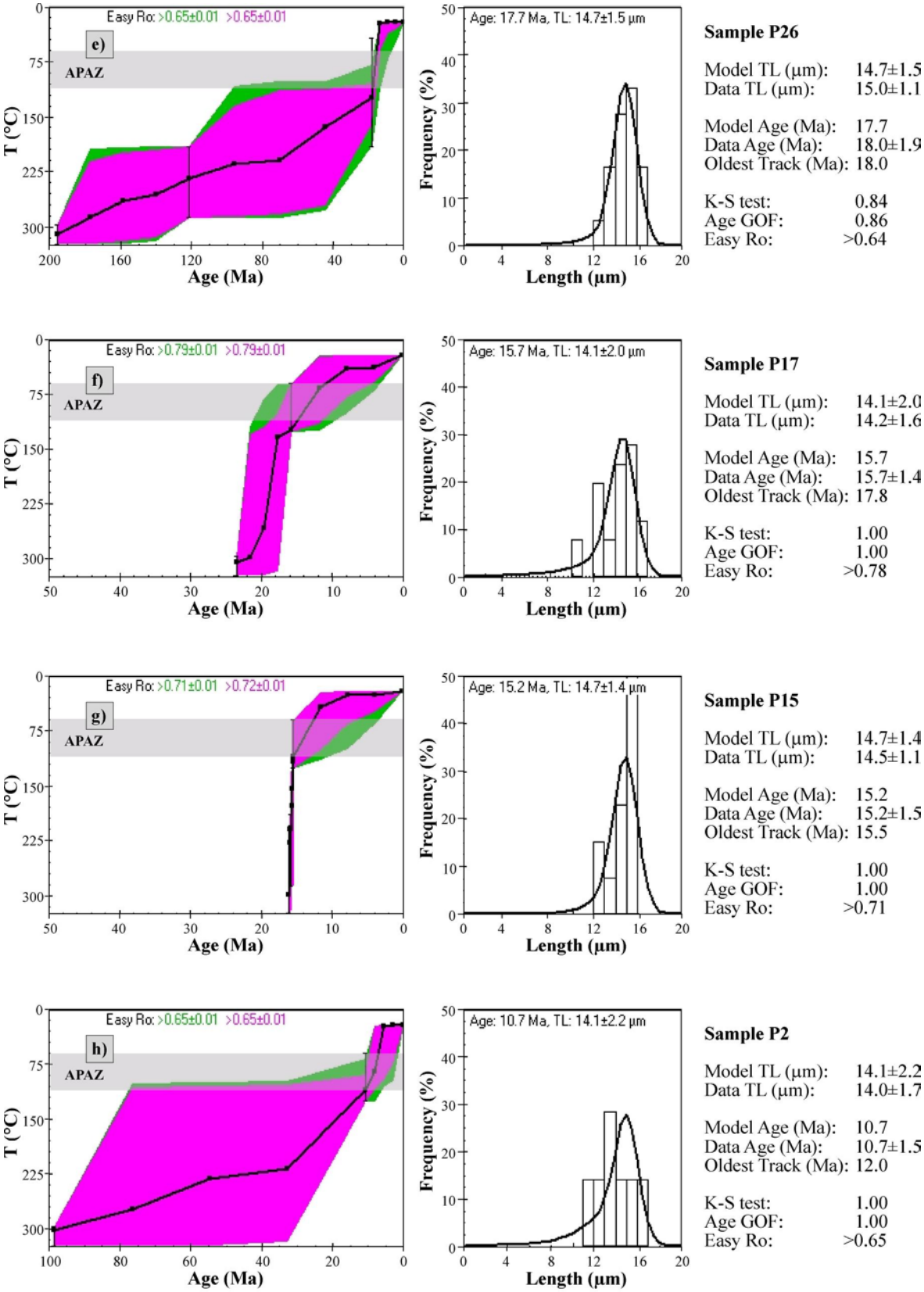

Fig. C2, continued: Time-temperature paths and fission track length distributions of apatite samples modelled with AFTSolve 1.2.2 (Ketcham et al. 2000). APAZ=Apatite partial annealing zone. Track length distributions are normalised to n=100. The fit between the observed and modelled data (t-T paths, left side) is indicated as follows: solid black line=best fit, dark gray area=good fit, light gray area=acceptable fit. Age GOF=goodness of fit between modelled and calculated age, K-S Test=Kolmogorov-Smirnov statistical test, TL=track length.

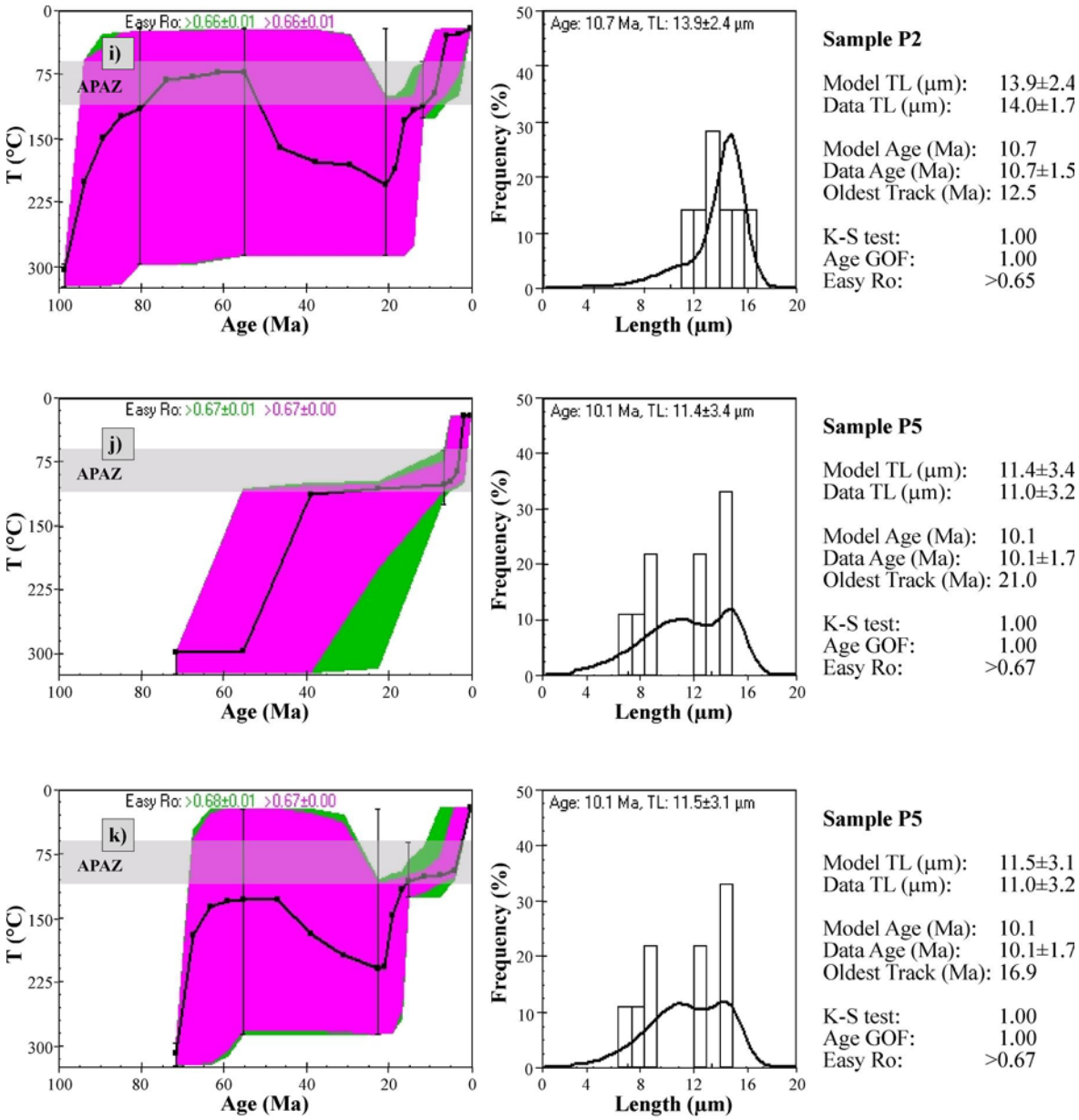

Fig. C2, continued: Time-temperature paths and fission track length distributions of apatite samples modelled with AFTSolve 1.2.2 (Ketcham et al. 2000). APAZ=Apatite partial annealing zone. Track length distributions are normalised to n=100. The fit between the observed and modelled data (t-T paths, left side) is indicated as follows: solid black line=best fit, dark gray area=good fit, light gray area=acceptable fit. Age GOF=goodness of fit between modelled and calculated age, K-S Test=Kolmogorov-Smirnov statistical test, TL=track length.

Tab. C6 Zircon fission track ages determined with the program TRACKKEY 4.0 (Dunkl 2002).

sample	Elev.. (m)	Number of grains	Spontaneous ρ_s	Spontaneous N_s	Induced ρ_i	Induced N_i	$P\chi^2$(%)	Dosimeter ρ_d	Dosimeter N_d	Age (Ma) ± 1σ
Hard rocks										
Karakul lake										
P25-38	4230	24	180.739	1516	56.153	471	7.57	5.52	10895	108±7
P26-38	4100	14	158.762	1081	43.766	298	38.43	5.52	10895	122±9
Central Pamirs										
A96S1b-49	n.d.	23	241.372	2445	125.474	1271	98.94	5.4	10665	63.5±2.5
P15-38	4365	40	20.84	2111	45.935	4653	2.38	5.52	10895	*15.6±0.5
Rushan Pshart										
L96M25a-49	n.d.	17	241.108	1456	116.248	702	25.09	5.4	10665	68.5±3.6
96A10b-49	n.d.	33	129.079	2087	77.868	1259	0.0	5.4	10665	*59.4±4.6
Soft rocks										
Tien Shan										
TS5a-49	2570	61	221.267	5237	35.026	829	0.0	5.4	10665	*239±13
Altyndara valley										
AD7d-49	n.d.	43	206.785	4290	37.79	784	0.0	5.4	10665	*204±14
AD8a-49	n.d.	6	245.082	740	52.991	160	64.94	5.4	10665	152±14
Qiangtang										
A96K1e-49	n.d.	59	333.768	9070	44.416	1207	0.0	5.4	10665	*285±17
Muzkol dome										
M96M6b-49	n.d.	47	33.435	1726	56.643	2924	11.59	5.4	10665	19.7±0.8
A96M4b-49	n.d.	51	36.668	1375	64.562	2421	44.3	5.4	10665	18.8±0.8

The track densities (ρ) are measured as $x10^5 tr/cm^2$. $P\chi^2$ is the probability obtaining a chi-square value for n degrees of freedom (where n = no. of crystals –1). The ages were calculated as central ages, where $P\chi^2$ is >5%, and as mean ages (indicated by *), where $P\chi^2$ is <5%. Abbreviation n.d.= not determined.

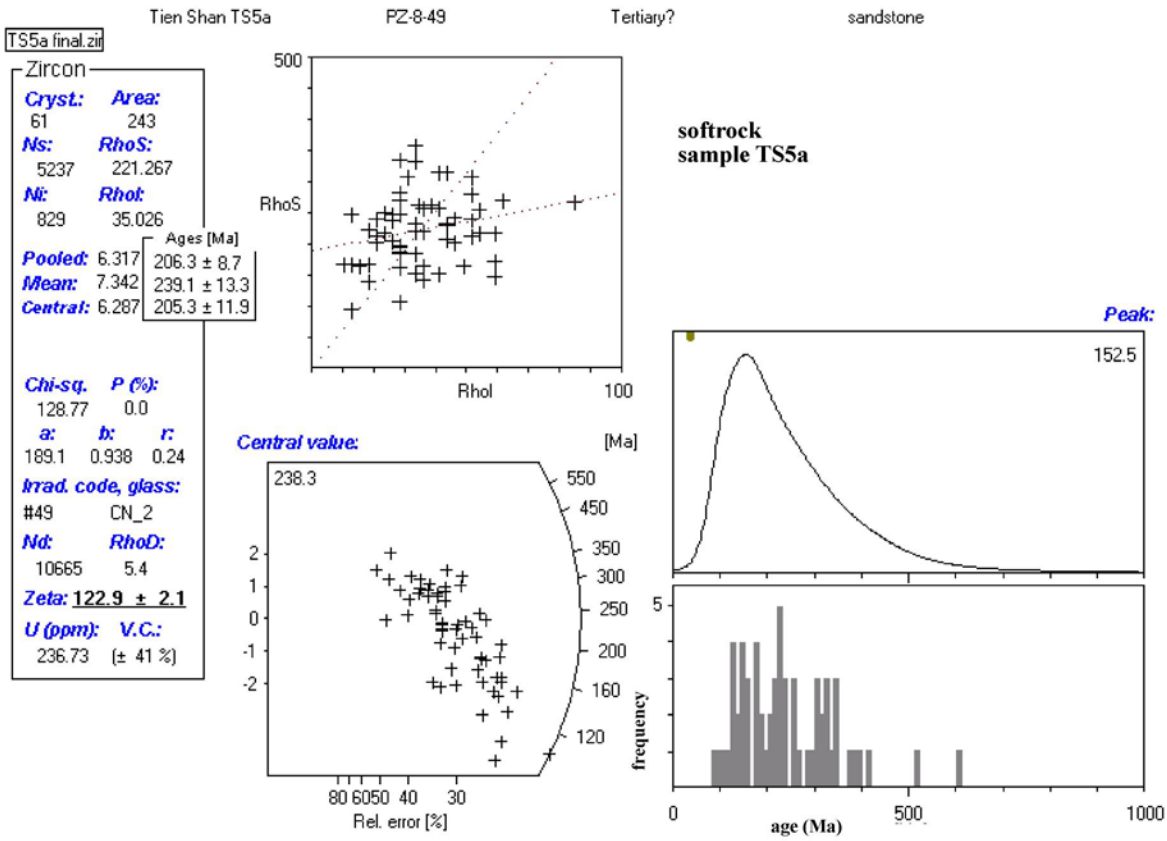

Fig. C3: Zircon fission track ages determined with the Program TRACKKEY 4.0 (Dunkl 2002). The radial plot is after Galbraith (1990).

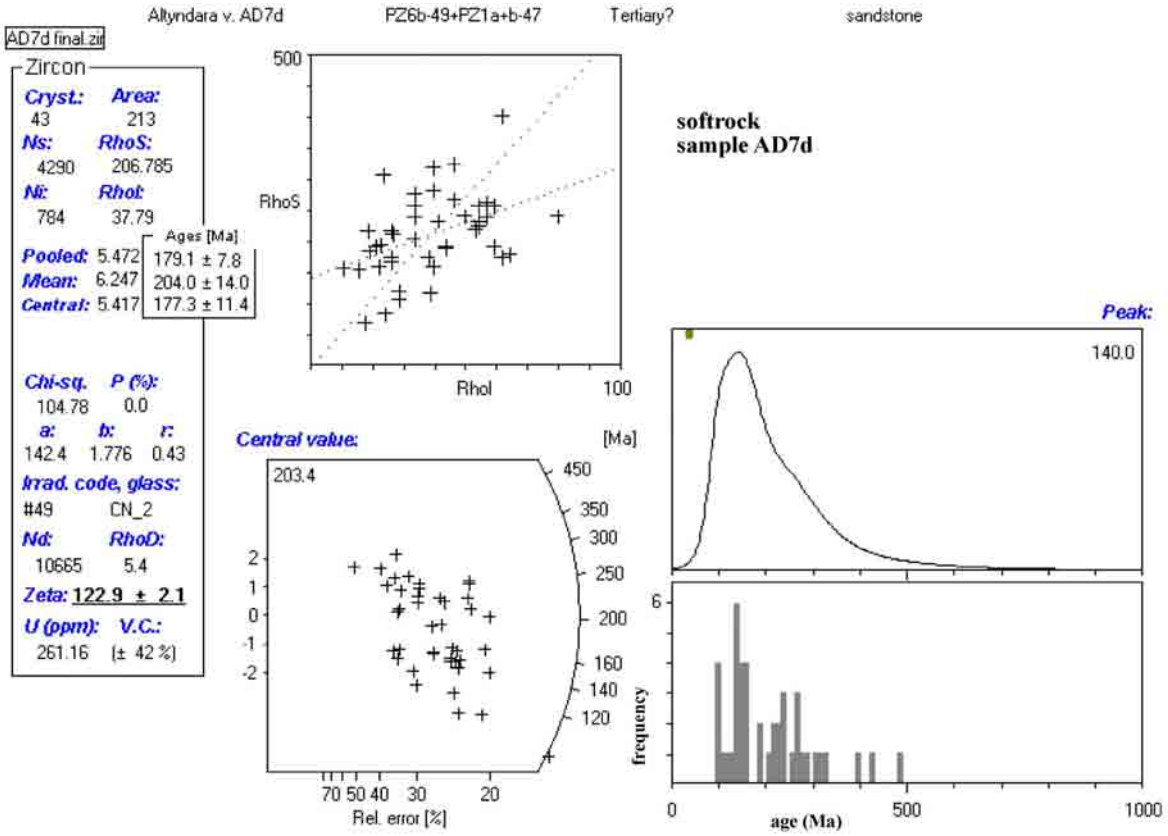

Fig. C3, continued: Zircon fission track ages determined with the Program TRACKKEY 4.0 (Dunkl 2002). The radial plot is after Galbraith (1990).

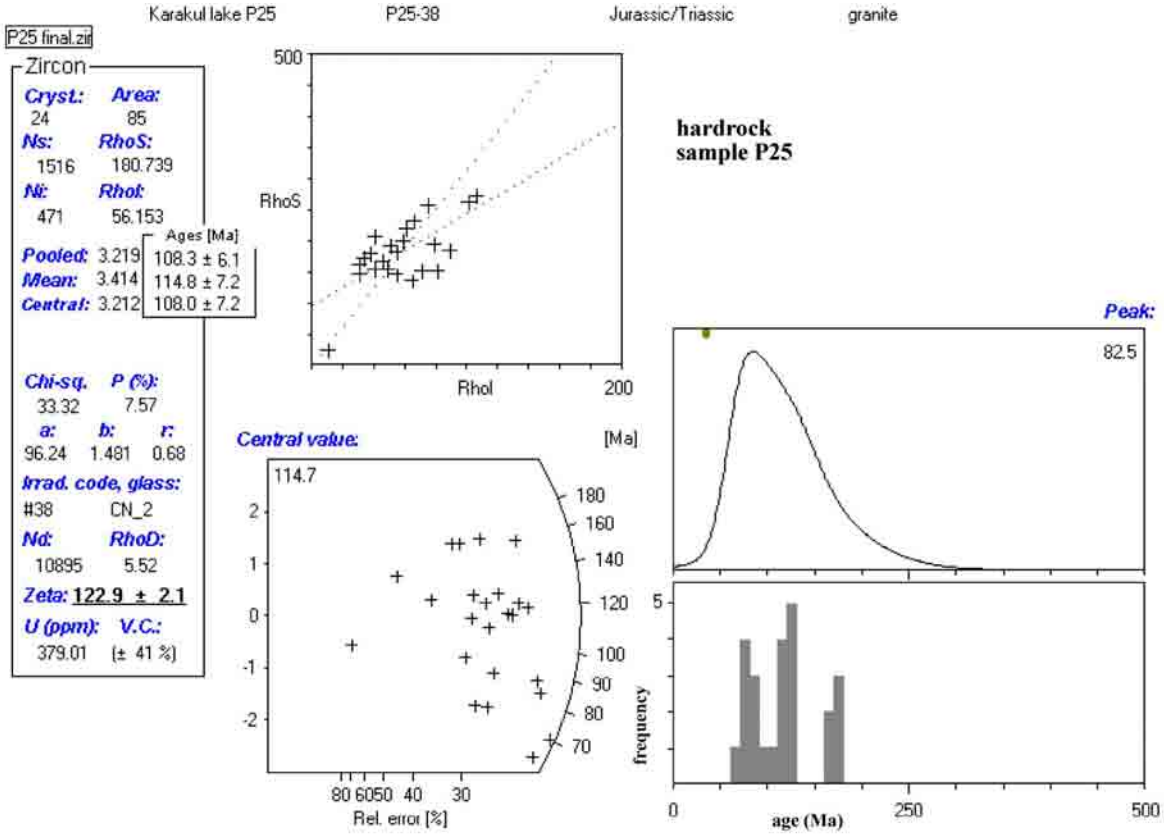

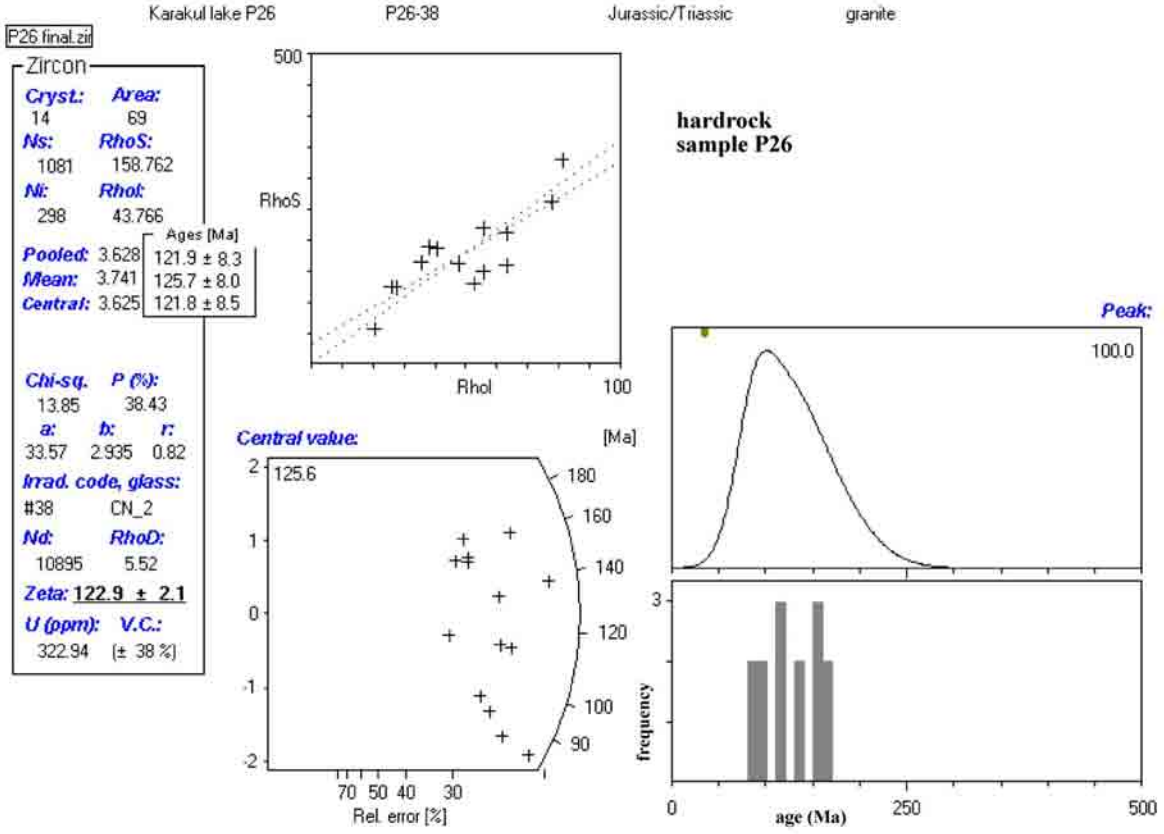

Fig. C3, continued: Zircon fission track ages determined with the Program TRACKKEY 4.0 (Dunkl 2002). The radial plot is after Galbraith (1990).

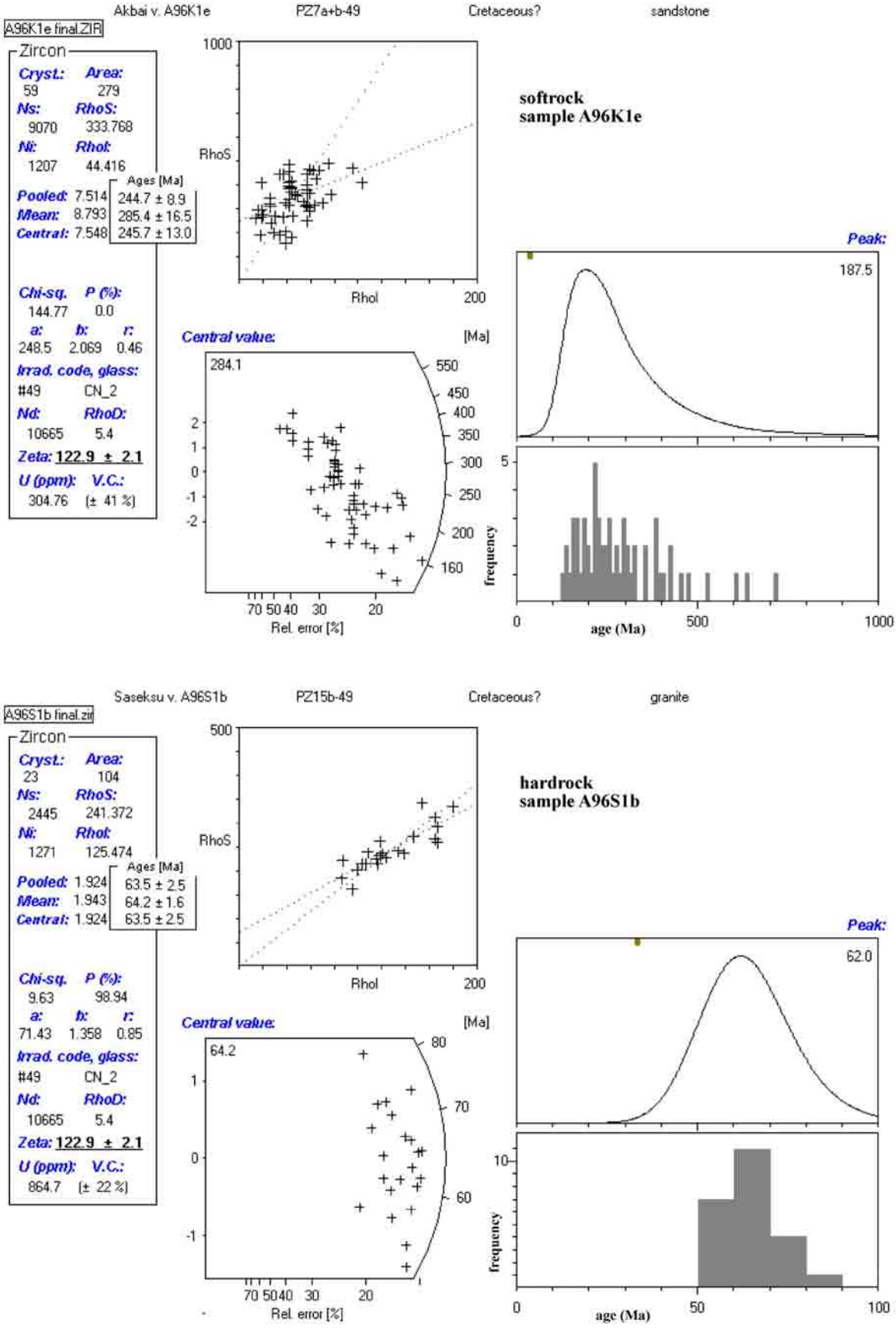

Fig. C3, continued: Zircon fission track ages determined with the Program TRACKKEY 4.0 (Dunkl 2002). The radial plot is after Galbraith (1990).

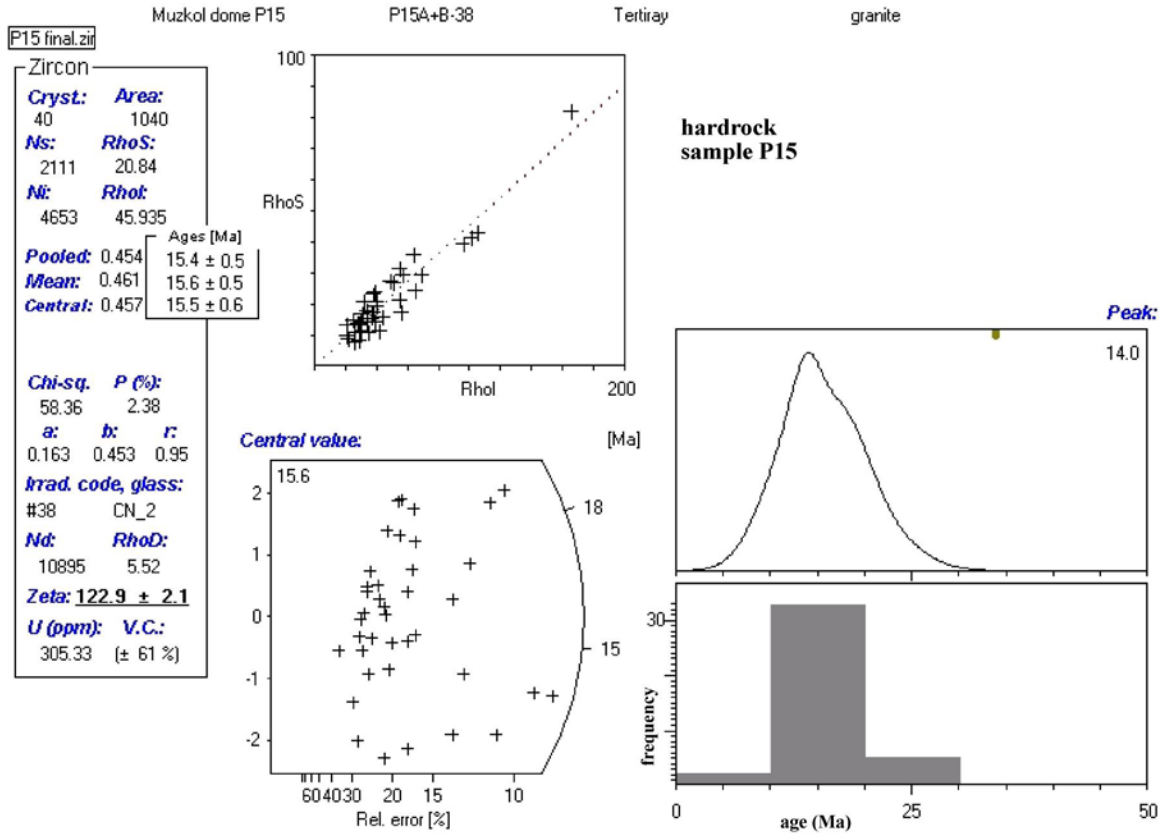

Fig. C3, continued: Zircon fission track ages determined with the Program TRACKKEY 4.0 (Dunkl 2002). The radial plot is after Galbraith (1990).

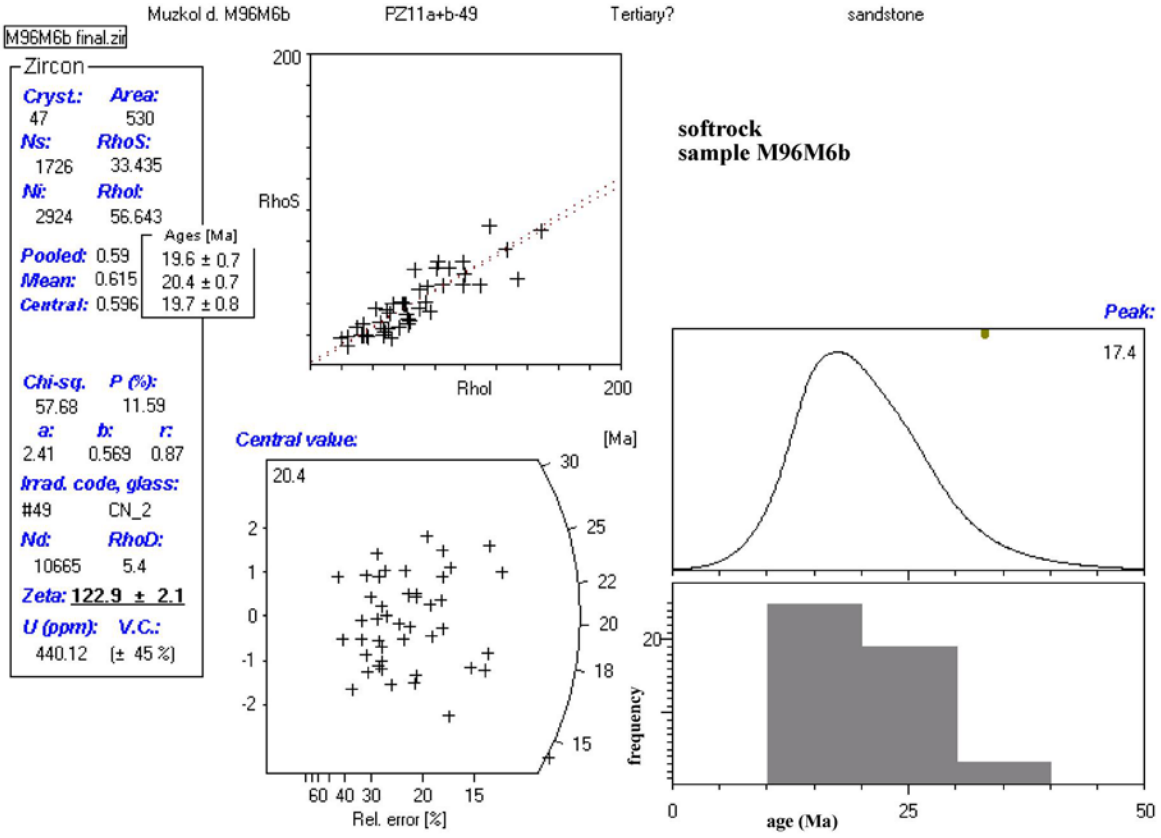

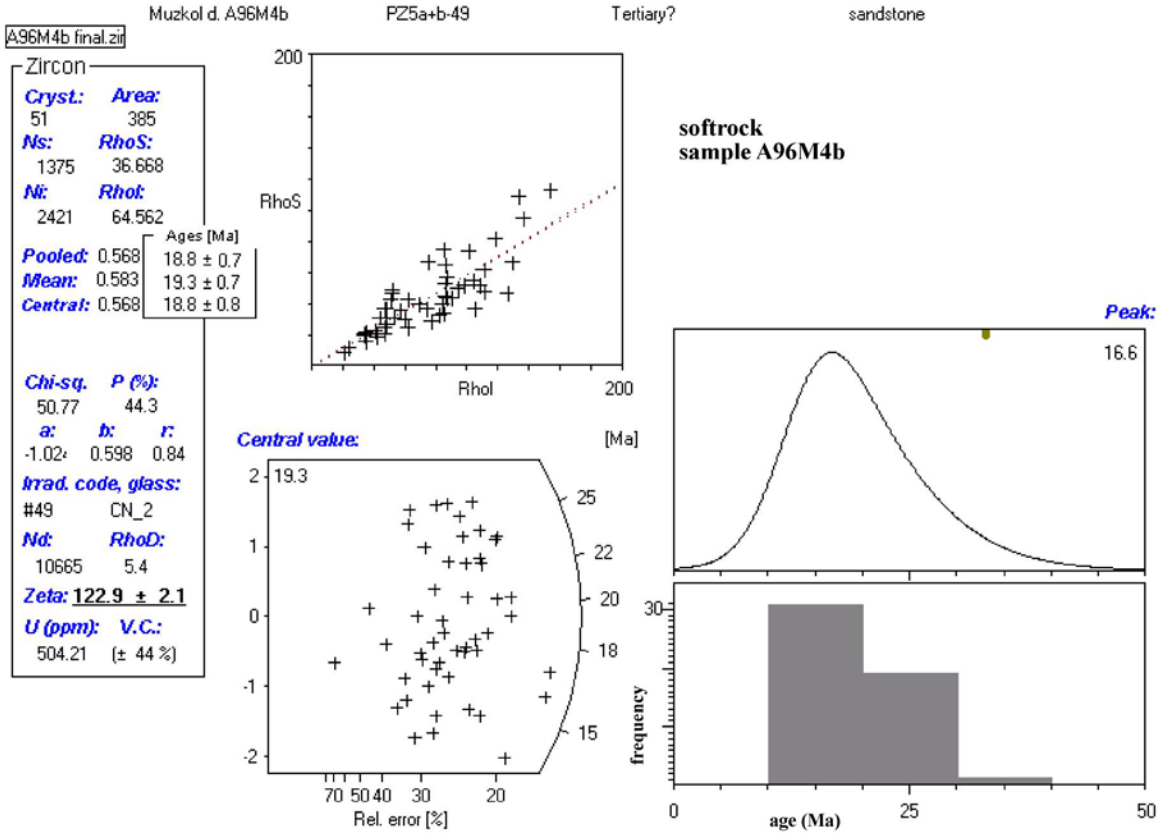

Fig. C3, continued: Zircon fission track ages determined with the Program TRACKKEY 4.0 (Dunkl 2002). The radial plot is after Galbraith (1990).

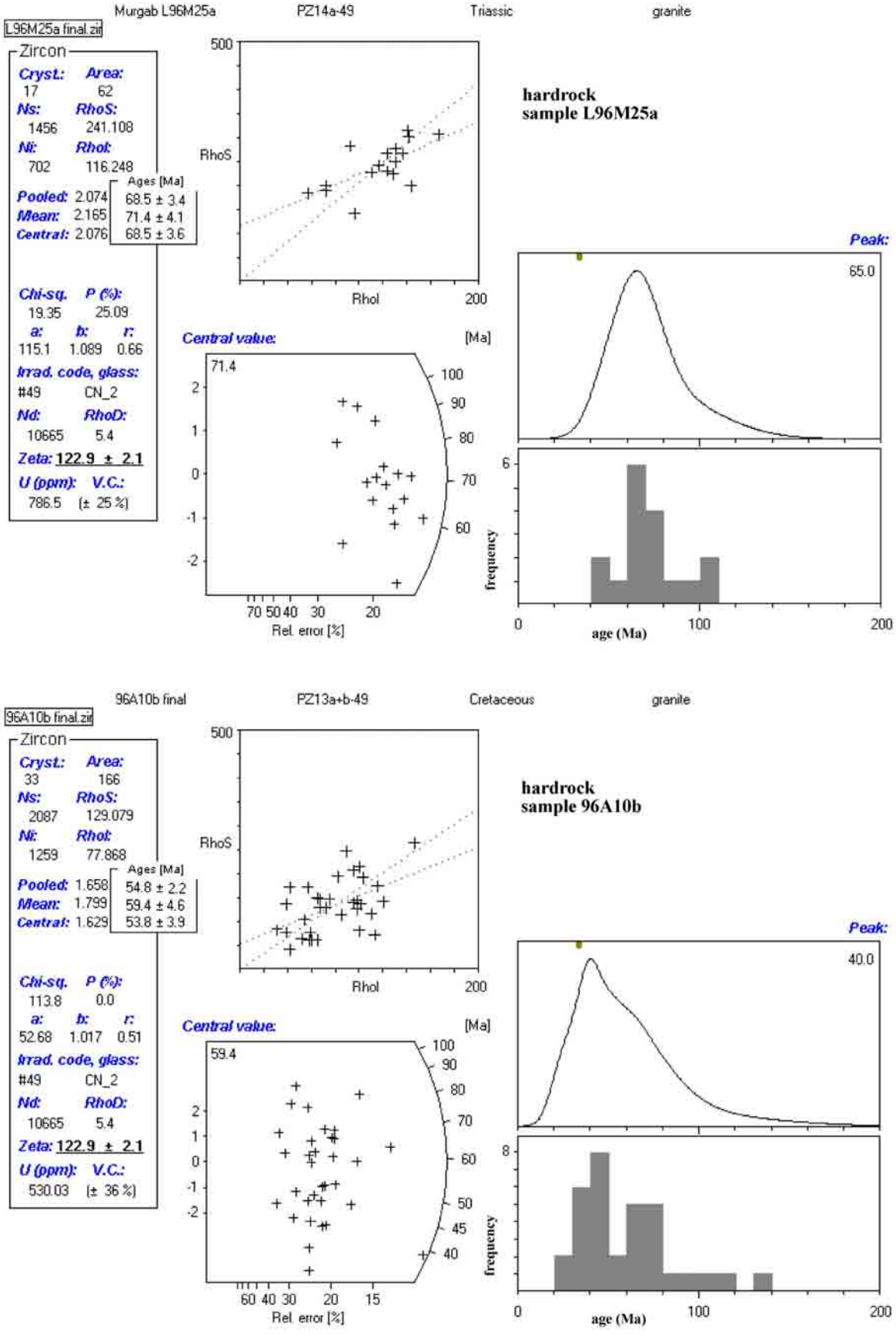

Fig. C3, continued: Zircon fission track ages determined with the Program TRACKKEY 4.0 (Dunkl 2002). The radial plot is after Galbraith (1990).

Tab. C7 Apatite and zircon fission track data and calculated age clusters

Sample	sedimentation	no. of	Spontaneous		Induced		Dosimeter		$P(\chi^2)$	best-fit peak-ages (Ma)			Fit statistics	
	age (Ma)	crystals	ρ_s	N_s	ρ_i	N_i	ρ_d	N_d	(%)	1	2	3	χ^2	P(F)
TS5a apatite	?Neogene	106	18.829	3617	12.15	2334	4.66	9253	0.0	**75.6±6.5**	**144±14**	**245±39**	106.3	0%
										N_f=21.1	N_f=56.2	N_f=28.7		
										Frac.%=19.9	Frac.%=53.0	Frac.%=27.1		
TS8a apatite	?Upper Paleogene	10	15.218	375	8.197	202	4.66	14919	87.43	**170±16**	**333±56**		8.15	0%
										N_f=9.5	N_f=1.5			
										Frac.%=86.6	Frac.%=13.4			
TS5a zircon	?Neogene	61	221.267	5237	35.026	829	5.4	10665	0.0	**145±15**	**266±22**		61.15	0%
										N_f=20.8	N_f=40.2			
										Frac.%=34.0	Frac.%=66.0			
AD7d zircon	no data	43	206.785	4290	37.79	784	5.4	10665	0.0	**131±10**	**243±20**		41.49	0%
										N_f=20.5	N_f=22.5			
										Frac.%=47.8	Frac.%=52.2			
A96K1e zircon	?Neogene	59	333.768	9070	44.416	1207	5.4	10665	0.0	**165±19**	**242±33**	**371±50**	59.08	0%
										N_f=13.1	N_f=28.9	N_f=16.9		
										Frac.%=22.3	Frac.%=49.0	Frac.%=28.7		

The modelled peak-ages are calculated with the BINOMFIT program (Brandon 2002), based on the binomial "peak-fitting" method of Galbraith & Green (1990). The uncertainty of the peak-ages is given at 68% confidence level (1σ). The size of the individual peaks is reported as a fraction in percent (Frac.%) and as number of grains in the peak-age population (N_f). χ^2=Chi-squared value for best fit, P(F) is the improvement if the fit in peaks is significant. P(F) < ~5% indicate that the improvement in fit is very good. ρ=track density, N=number of counted tracks, $\sum N_f$=total number of grains.

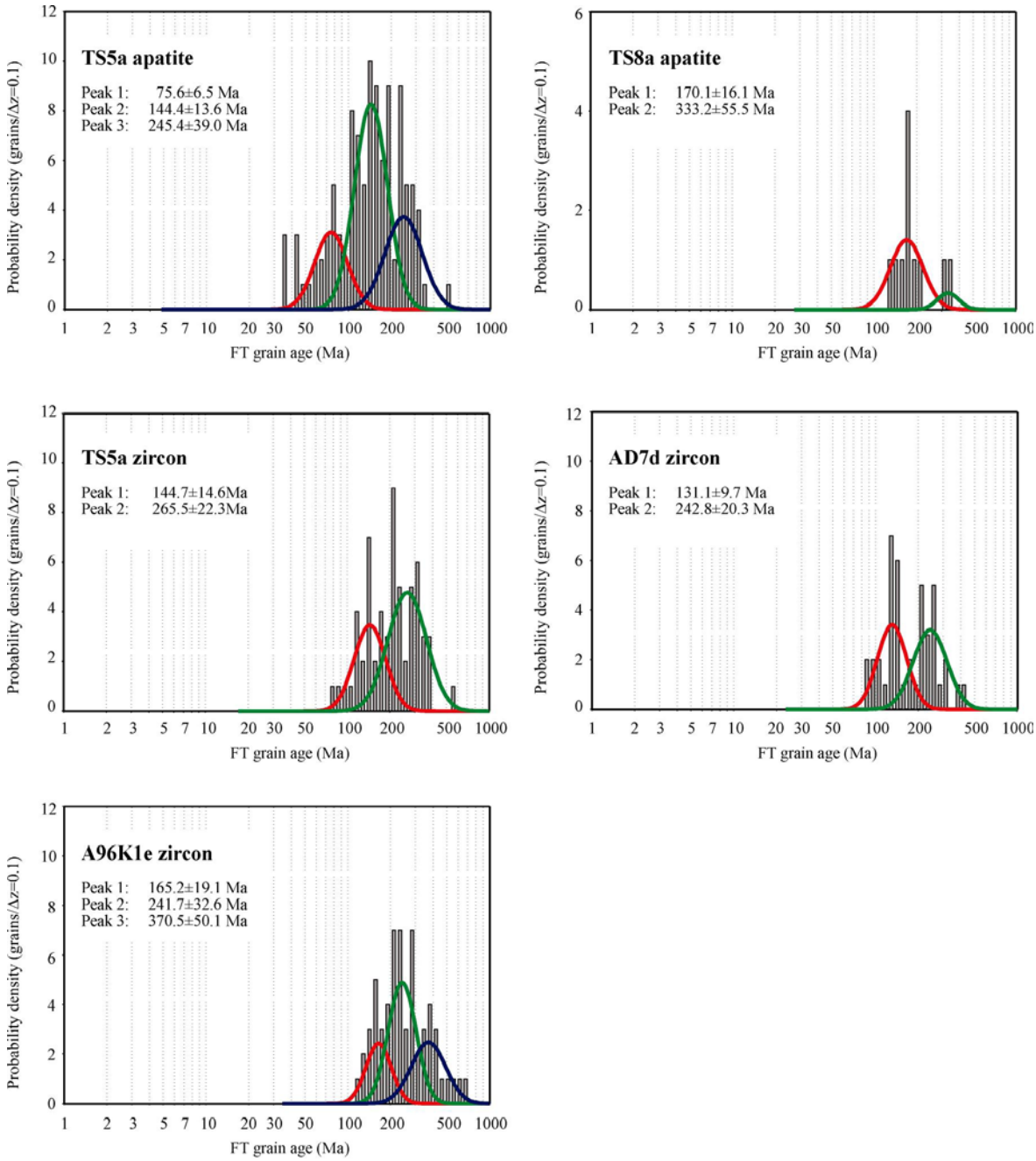

Fig. C4: Apatite and zircon fission track age spectra decomposed with the Program BINOMFIT (Brandon 2002).